

PROCEEDINGS OF THE 2003 ANTENNA APPLICATIONS SYMPOSIUM VOLUME II

**Dr. Daniel Schaubert
University of Massachusetts at Amherst
College of Engineering
Amherst MA 01003**

FINAL TECHNICAL REPORT SEPTEMBER 2003

APPROVED FOR PUBLIC RELEASE: DISTRIBUTION UNLIMITED



**AIR FORCE RESEARCH LABORATORY
Sensors Directorate
Electromagnetics Technology Division
80 Scott Drive
Hanscom AFB MA 01731-2909**

TECHNICAL REPORT

TITLE: 2003 ANTENNA APPLICATIONS SYMPOSIUM

APPROVED FOR PUBLIC RELEASE
DISTRIBUTION UNLIMITED

VOLUME II

NOTICE

USING GOVERNMENT DRAWINGS, SPECIFICATIONS, OR OTHER DATA INCLUDED IN THIS DOCUMENT FOR ANY OTHER PURPOSE OTHER THAN GOVERNMENT PROCUREMENT DOES NOT IN ANY WAY OBLIGATE THE US GOVERNMENT. THE FACT THAT THE GOVERNMENT FORMULATED OR SUPPLIED THE DRAWINGS, SPECIFICATIONS, OR OTHER DATA DOES NOT LICENSE THE HOLDER OR ANY OTHER PERSON OR CORPORATION; OR CONVEY ANY RIGHTS OR PERMISSION TO MANUFACTURE, USE, OR SELL ANY PATENTED INVENTION THAT MAY RELATE TO THEM.

THIS TECHNICAL REPORT HAS BEEN REVIEWED AND IS APPROVED FOR PUBLICATION.

\\SIGNED\\

HARVEY E. TOBIN
Antenna Technology Branch
Electromagnetics Technology Division

\\SIGNED\\

LIVIO D. POLES
Chief, Antenna Technology Branch
Electromagnetics Technology Division

\\SIGNED\\

MICHAEL ALEXANDER
Technical Advisor
Electromagnetics Technology Division

REPORT DOCUMENTATION PAGE					Form Approved OMB No. 0704-0188	
<p>The public reporting burden for this collection of information is estimated to average 1 hour per response, including the time for reviewing instructions, searching existing data sources, gathering and maintaining the data needed, and completing and reviewing the collection of information. Send comments regarding this burden estimate or any other aspect of this collection of information, including suggestions for reducing the burden, to Department of Defense, Washington Headquarters Services, Directorate for Information Operations and Reports (0704-0188), 1215 Jefferson Davis Highway, Suite 1204, Arlington, VA 22202-4302. Respondents should be aware that notwithstanding any other provision of law, no person shall be subject to any penalty for failing to comply with a collection of information if it does not display a currently valid OMB control number.</p> <p>PLEASE DO NOT RETURN YOUR FORM TO THE ABOVE ADDRESS.</p>						
1. REPORT DATE (DD-MM-YYYY) 16 January		2. REPORT TYPE Final		3. DATES COVERED (From - To) September 2003		
4. TITLE AND SUBTITLE Proceedings of the 2003 Antenna Applications Symposium Volume II				5a. CONTRACT NUMBER GSA TASK NUMBER R15701320		
				5b. GRANT NUMBER		
				5c. PROGRAM ELEMENT NUMBER		
6. AUTHOR(S) Daniel Schaubert et, al.				5d. PROJECT NUMBER		
				5e. TASK NUMBER		
				5f. WORK UNIT NUMBER		
7. PERFORMING ORGANIZATION NAME(S) AND ADDRESS(ES) University of Massachusetts at Amherst College of Engineering Amherst, MA 01003				8. PERFORMING ORGANIZATION REPORT NUMBER Volume II		
9. SPONSORING/MONITORING AGENCY NAME(S) AND ADDRESS(ES) Air Force Research Laboratory 80 Scott Rd Electromagnetics Technology Division Sensors Directorate Hanscom AFB, MA 01731				10. SPONSOR/MONITOR'S ACRONYM(S)		
				11. SPONSOR/MONITOR'S REPORT NUMBER(S)		
12. DISTRIBUTION/AVAILABILITY STATEMENT Approved for Public Release; Distribution Unlimited						
13. SUPPLEMENTARY NOTES Volume I contains pages 1-230 Volume II contains pages 231-429						
14. ABSTRACT The Proceedings of the 2003 Antenna Applications Symposium is a collection of state-of-the-art papers relating to antenna arrays, millimeter wave antennas, simulation and measurement of antennas, integrated antennas, and antenna bandwidth and radiation improvements.						
15. SUBJECT TERMS Antennas, Arrays, Genetic Antennas, Bandwidth, Impedance Bandwidth, Spaced-Based Arrays						
16. SECURITY CLASSIFICATION OF:			17. LIMITATION OF ABSTRACT UL	18. NUMBER OF PAGES 198	19a. NAME OF RESPONSIBLE PERSON	
a. REPORT	b. ABSTRACT	c. THIS PAGE			19b. TELEPHONE NUMBER (Include area code)	

2003 ANTENNA APPLICATIONS SYMPOSIUM

17 – 19 September 2003

Monticello, Illinois

Multi-Beam Transmit Receive Module for USB and SGLS Band Satellite Links	1
S. S. Bharj, P. Oleski, B. Tomasic, J. Turtle, S. Liu, N. Patel, A. Merzhevskiy, Li. Qu and M. Thaduri	
A Novel Approach of a Planar Multi-Band Hybrid Series Feed Network for Use in Antenna Systems Operating at Millimeterwave Frequencies	15
M. W. Elsallal and B. L. Hauck	
Multibeam Spatially-Fed Antenna Array with Amplitude-Controlled Beam Steering	25
S. Rondineau, S. Romisch, D. Popovic. And Z. Popovic	
Rectenna Arrays for Recycling Statistical Broadband Radiation	38
J. Hagerty and Z. Popovic	
Space-Based E-Textile Arrays	52
M. Dcaett, P. Dufilic and W. Weedon	
A Computer-Aided Approach for Designing Edge-Slot Waveguide Arrays	67
R. B. Gosselin	
New Variable for Fresnel Zone Plate Antennas	92
G. W. Webb	
Frequency Selective Surfaces: Design of Broadband Elements and New Frequency Stabilization Techniques	107
A. Raiva, F. Harackiewicz and J. Lindsay III	
Genetic Antenna Optimization: A Tale of Two Chromosomes	131
T. O'Donnell, S. Best, E. Altshuler, J. Hunter, T. Bullett and R. Barton	

A Small Array of Boresight to Endfire Radiation Reconfigurable Antennas	147
G. H. Hu(T), J. Feng and J. T. Bernhard	
Effect of Dielectric Substrate on Infinite Arrays of Single-Polarized Vivaldi Antennas	162
S. Kasturi and D. H. Schaubert	
A Novel Approach for Bandwidth Enhancement of Slot Antennas	176
N. Behdad and K. Sarabandi	
A Commemoration of Deschamps' and Sichak's "Microstrip Microwave Antennas": 50 Years of Development, Divergence and New Directions	189
J. T. Bernhard, P. E. Mayes, D. Schaubert and R. J. Mailloux	
Broadband Dual-Mode Slot Antenna	231
A. Bhobe, T. Cencich, J. Burford and D. Filipovic	
Truncated Versions of Modified Parany Gasket Monopole Antenna and Its Frequency Allocation	244
K. Han and F. Harackiewicz	
Impedance and Gain Bandwidths of Broadband, Electrically Small, Stacked Conical Resonator Antennas	256
P. E. Mayes and P. W. Klock	
Bandwidth Enhancement and Comparison between Square Micro strip Patch Antenna	269
S. V. Khobragade and S. N. Talbar	
Analysis of Modified Diamond Dipole for Ultra-Wideband Communication Using FDTD Method	278
S. Desamsetty, E. Lule, T. Babij and K. Siwiak	
The Coaxial Cavity Antenna Implementation in the N-Port (Four and Eight) Feed Configuration	298
T. Holzheimer	

Investigation of Wideband Low-Profile Canted Antennas for Broadside Radiation in Aperiodic Arrays	318
J. T. Bernhard, B. Herting, J. Fladie, D. Chen and P. Mayes	
Some Lessons Learned About Truncation Effects in Wideband Vivaldi Arrays	327
A. O. Boryssenko and D. H. Schaubert	
Electronically Controlled Beam-Steering Antenna (Demo)	355
V. A. Manasson, L. Sadovnik, M. Aretskin, A. Brailovsky, P. Grabice, D. Eliyahu, M. Felman, V. Khodos, V. Litvinov, J. Marczewski and R. Mino	
A Ka-Band Electronically Scanned Antenna for Multi-Function RF Applications	360
R. Dahlstrom, S. Weiss, E. Viveiros, A. Bayba and E. Adler	
Impedance, Bandwidth, and Q of the General One-Port Antenna	373
S.R. Best and A.D. Yaghjian	
On the Radiation Properties of Electrically Small Mult-Arm Folded Wire Antennas	403
S.R. Best	

Identifiers for Proceedings of Symposia

The USAF Antenna Research and Development Program

Year	Symp. No.	Identifier
1951	First	
1952	Second	ADB870006
1953	Third	ADB283180
1954	Fourth	AD63139
1955	Fifth	AD90397
1956	Sixth	AD114702
1957	Seventh	AD138500
1958	Eighth	AD301151
1959	Ninth	AD314721
1960	Tenth	AD244388 (Vol. 1) AD319613 (Vol. 2)
1961	Eleventh	AD669109 (Vol. 1) AD326549 (Vol. 2)
1962	Twelfth	AD287185 (Vol. 1) AD334484 (Vol. 2)
1963	Thirteenth	AD421483
1964	Fourteenth	AD609104
1965	Fifteenth	AD474238L
1966	Sixteenth	AD800524L
1967	Seventeenth	AD822894L
1968	Eighteenth	AD846427L
1969	Nineteenth	AD860812L
1970	Twentieth	AD875973L
1971	Twenty-First	AD888641L
1972	Twenty-Second	AD904360L
1973	Twenty-Third	AD914238L

Antenna Applications Symposium

		TR#	ADA#
1977	First	None	955413
1978	Second	None	955416
1979	Third		077167
1980	Fourth		205907
1981	Fifth		205816
1982	Sixth		129356
1983	Seventh		142003; 142754
1984	Eighth	85-14	153257; 153258
1985	Ninth	85-242	166754; 165535
1986	Tenth	87-10	181537; 181536
1987	Eleventh	88-160	206705; 206704
1988	Twelfth	89-121	213815; 211396
1989	Thirteenth	90-42	226022; 226021
1990	Fourteenth	91-156	237056; 237057
1991	Fifteenth	92-42	253681; 253682
1992	Sixteenth	93-119	268167; 266916
1993	Seventeenth	94-20	277202; 277203
1994	Eighteenth	95-47	293258; 293259
1995	Nineteenth	96-100	309715; 309723
1996	Twentieth	97-189	341737
1997	Twenty First	1998-143	355120
1998	Twenty Second	1999-86	364798
1999	Twenty Third	2000-008 (I) (II)	386476; 386477
2000	Twenty Fourth	2002-001 Vol I & II	
2001	Twenty Fifth	2002-002 Vol I & II	
2002	Twenty Sixth		

Author Index

Adler, E.	360	Khodos, V.	355
Altshuler, E.	131	Klock, P.	256
Aretskin, M.	355	Lindsey III, J.	107
Babij, T.	278	Litvinov, V.	355
Barton, R.	131	Liu, S.	1
Bayba, A.	360	Lule, E.	278
Behdad, N.	176	Mailloux, R.	189
Bernhard, J.	147, 189, 318	Marczewski, J.	355
Best, S.	131	Masasson, V.	355
Bharj, S.	1	Mayes, P.	189, 256, 318
Bhode, A.	231	Merzhevskiy, A.	1
Borysenko, A.	327	Mino, R.	355
Brailovsky, A.	355	O'Donnell, T.	131
Bullett, T.	131	Oleski, P.	1
Burford, J.	231	Patel, N.	1
Cencich, T.	231	Popovic, D.	25
Chen, D.	318	Popovic, Z.	25, 38
Dahlstrom, R.	360	Qu, L.	1
Deaett, M.	52	Raiva, A.	107
Desamsetty, S.	278	Romisch, S.	25
Dufilie, P.	52	Rondineau, S.	25
Eliyahu, D.	355	Sadovnik, L.	355
Elsallal, M.	15	Sarabandi, K.	176
Felman, M.	355	Schaubert, D.	162, 189, 327
Feng, J.	147	Siwiak, K.	278
Filipovic, D.	231	Talbar, S.	269
Fladie, J.	318	Thaduri, M.	1
Gosselin, R.	67	Tomasic, B.	1
Grabiec, P.	355	Turtle, J.	1
Hagerty, J.	38	Viveiros, E.	360
Han, K.	244	Webb, G.	92
Harackiewicz, F.	107, 244	Weedon, W.	52
Hauck, B.	15	Weiss, S.	360
Herting, B.	318		
Holzheimer, T.	298		
Huff, G.	147		
Hunter, J.	131		
Kasturi, S.	162		
Khobragade, S.	269		

BROADBAND DUAL-MODE SLOT ANTENNA

Alpesh Bhobe[†], Thomas Cencich^{††}, Jason Burford^{††} and Dejan Filipović[†]

[†]Department of Electrical and Computer Engineering

The University of Colorado

425 UCB

Boulder, CO 80309-0425

^{††}Lockheed Martin Space Systems Company Astronautics Operations

P.O. Box 179

Mail Stop S4914

Denver, CO 80201

ABSTRACT: A novel cavity-backed 4-arm slot spiral antenna for broadband communications is proposed in this paper. It is designed for dual-mode, 1st/Normal mode and 2nd/Split-Beam mode, operation from 1.5–4.5GHz and 2.5–6GHz respectively. A Finite-Element Boundary-Integral (FE-BI) based numerical tool is extensively used to study effects of various antenna parameters, including slot width, dielectric loading, cavity depth, growth rate, resistive taper, etc. The slot spiral is designed for axial ratio ≤ 4 dB over the desired bandwidth for both modes. Based on the numerical analysis, cavity depth and diameter of 1.5cm and 8.5cm, respectively, were chosen. The antenna is built on a 0.0786cm thick RT/Duroid®5880 substrate of dielectric constant (ϵ_r) 2.2. Measured and numerical data are presented and discussed, and generally a very good agreement between the two is obtained.

1. INTRODUCTION

Since their introduction in the mid 1960's [1-3] spiral antennas have emerged as leading candidates for various commercial and military applications requiring broadband circularly polarized operation. They can be realized with single or a multiple arms in printed/wire [2], microstrip [4] and slot forms [1,3,5,6]. Printed and wire spirals have been studied extensively and they are particularly popular due to well established broadband feeding schemes for various radiation modes [7]. On the other hand, slot spirals, although developed first [1,3], have been less studied primarily due to a need for an infinite balun feed [1] required for establishing a traveling slot line wave. Additionally, the continuous nature of a slot line at the center disables many useful phasing

combinations thus restricting broadband multimode functionality. This is likely the main reason why slot spirals (so far) have been realized with only two arms.

In this paper, a design of a novel cavity-backed 4-arm slot spiral, shown in Fig. 1, is presented. The antenna is realized for broadband performance of its 1st (normal) and 2nd (split-beam) mode for an axial ratio of less than 4dB at beam maximum. A specialized FE-BI based numerical tool is extensively used to analyze various antenna parameters [6]. This 4-arm Archimedean slot spiral has 2x2 continuous arms, which start at the center and are separated by 90° from each other. The antenna is fed with two semi-rigid coaxial cables in the form of a two port infinite Dyson balun, as shown in Fig. 1. Thus, an *in* and *out* of phase currents at the coax to slot line transition are responsible for generating a dual-mode operation. It is important to note that the continuous nature of the slot line does not permit required 4-arm normal mode phasing conditions of {0°, 90°, 180°, 270°}. Instead, a phasing of {0°, 180°, 180°, 0°} between neighboring arms is established, which resembles phasing for a 2 arm spiral. As a consequence, lower radiation efficiency and significant 3rd mode radiation occur, thus somewhat degrading antenna performance. The phasing progression for the 2nd mode radiation is correctly established and similar split-beam patterns as with a 4-arm printed spiral are obtained.

2. PARAMETRIC STUDY

In this section the antenna performance for various parameters is discussed and relevant physics is deduced.

DIELECTRIC LOADING: provides mechanical support for the antenna structure as well as the electrical support for establishing the leaking traveling wave responsible for the radiating process. Antenna performance was analyzed for three typically used substrates with dielectric constants of $\epsilon_r = 2.2, 3.38, 6.1$. It is observed that the higher dielectric constant increases the gain at lower frequencies (antenna becomes electrically larger) but deteriorates both the gain (traveling wave is more bounded within substrate) and axial ratio (3rd mode and cavity resonance become significant) at higher bands. Also, input impedance decreases (increased capacitance of the line) and WOW (ratio of maximum to minimum field) deteriorates rapidly (3rd mode/resonance). Similar effects are observed when the thickness is increased.

GROWTH RATE: determines number of turns within a given spiral aperture size. Archimedes growth rate leads to a constant width of the metal sections between slots and its choice affects not only radiation properties of the

aperture, but also the feed line losses. Five different growth rates of $\alpha = 0.2077, 0.2395, 0.2713, 0.3349$ and 0.3668 rad/cm were studied. It is observed that the directivity improves at mid and higher frequencies with smaller growth rates for both modes. This is due to more turns in the radiation region and enhanced coupling between neighboring arms, thus more leaking. Also, the same physics contributes to the significantly reduced WOW (less energy within the non-radiated wave after it passes the radiating ring). Note that small growth rate increases the length of the infinite balun, thus higher feed line losses.

CAVITY DEPTH: adds the 3rd dimension in an antenna, and is necessary for providing uni-directional radiation. Range of (absorber free) depths between 0.5cm and 2cm was considered here. Increased cavity depth improves the lower band gain (primarily due to reduced energy in the microstrip mode), but also increases the negative effects of cavity resonances and higher modes, such as larger axial ratio and WOW.

SLOT WIDTH: affects the characteristic impedance of a quasi-TEM slot line, wave energy distribution in the slot and microstrip modes, and the diameter of the feeding cables to be used as a balun. Three slot widths of 0.0508, 0.063 and 0.0762cm were studied. As expected, the real and imaginary parts of input impedance decreased with reducing the slot width (due to increased capacitance). Additionally, small changes in both the gain and the axial ratio (for the entire frequency range) are observed.

RESISTIVE TAPER: should enable the radiation of direct traveling wave, i.e. the energy associated with the non-radiated wave (after it passes the radiating ring) should be absorbed. Traditionally, this taper is realized in a broadband Klopfenstein [5,6] configuration with more than 15 resistors per arm. To reduce this number, as well as to determine the best location for each resistor, a procedure suggested in [8] was utilized. Dependence of the axial ratio at the beam peak for both modes and various stages in the taper design is shown in Fig. 2.

3. FABRICATION AND MEASUREMENTS

Based on the numerical analysis, the 4-arm slot spiral with following parameters is designed: $\alpha=0.2713 \text{ cm/rad}$, $w=0.0508 \text{ cm}$, $D=1.5 \text{ cm}$ and $dI=8.5 \text{ cm}$. Antenna is realized on RT/Duroid ® 5880 ($\epsilon_r=2.2$) substrate of thickness $t=0.0786 \text{ cm}$. Two 0.047" semi-rigid coaxial (infinite Dyson) baluns are soldered directly on the metal between slots, as shown in Fig. 1a. The resistive taper termination is realized using resistors soldered across the slots at predetermined

locations (and resistances). To reduce effects of cavity resonances, a 5mm thick absorber (ARC LS - 11191) is placed at the cavity bottom.

Measured and simulated VSWR for 1st and 2nd modes, as depicted in Fig. 3a & 3b respectively, is less than 2 for entire frequency range. The observed disagreements are likely due to the differences between the computational and fabricated models (particularly at the feed transitions). Note the measured VSWR ripple of 176 MHz corresponds to twice the electrical length (2×85.3 cm) of the coaxial balun. For the characterization of radiation patterns, the antenna was placed in a 4ft. diameter circular aluminum ground plane. The comparison between measured and simulated gains for 1st & 2nd mode is shown in Fig. 4a, while respective elevation angles of the beam maximum are given in Fig. 4b. The results generally agree very well. For the 1st mode the gain achieves its nominal value of 3.5dBic at 2.5GHz, and it is greater than -5dBic above 1.4GHz. A slight deterioration in the simulated gain is observed around 4.5GHz caused by the cavity resonance. Note that this effect is reduced in measurement due to the cavity absorber. For the 2nd mode, the gain remains flat at approximately 3dBic above 3.5 GHz and is greater than -5dBic above 2.5GHz. The axial ratio performance, both measured and simulated, for both modes is plotted in Fig. 5. For the 1st mode the axial ratio is computed at the broadside where as for the second mode it is computed at the pattern peak, as shown in Fig. 4b.

Measured radiation patterns of the antenna with respect to elevation angle (θ) at frequencies of 3, 4 and 5GHz, for both modes are shown in Fig. 6, 7 & 8 respectively. The radiation patterns were measured for azimuth angles of $\phi = 0^\circ$ to 360° with steps of 10° . A clear broadside beam for the 1st mode and a sharp null for the 2nd demonstrate the dual-mode performance of this antenna. Measured and simulated results agree well with each other, and rippling in the measured results is due to the finite ground plane edge effects (numerical model assumes an infinite ground plane). The radiation patterns for the 1st mode show a very good axial ratio performance at the broadside. However, at wider elevation angles the axial ratio performance and WOW deteriorate and worsen as the frequency increases. This is caused by the excitation of the undesired 3rd mode. For the 2nd mode no such effects are observed for measured frequencies, and the WOW is well within 2dB at wide elevation angles.

4. SUMMARY AND CONCLUSIONS

A detailed computational and experimental study of a flush-mounted, lightweight, cavity-backed 4-arm slot spiral antenna for broadband communications is presented in this paper. The simulated and measured results

show good agreement with each other. The antenna has more than an octave broadband gain and circular polarization characteristics (near beam maximum) for both modes of operation. Further improvements in eliminating higher order modes are necessary if this antenna is to be used in monopulse direction finding systems.

7. ACKNOWLEDGMENTS

Authors would like to thank Assist. Prof. Daniel Connors, Dept. of ECEN, The University of Colorado, Boulder for allowing the use of computational facilities for simulations conducted in this work.

This work was sponsored by the Lockheed Martin Corporation under the contract No. 1536974.

8. REFERENCES

- [1] J.D. Dyson, "The Equiangular Spiral Antenna", IRE Trans. Ant. Propagat., vol. AP-7, pp. 181-188, April 1959.
- [2] J.A. Kaiser, "The Archimedean Two-Wire Spiral Antenna", IRE Trans. Ant. Propagat., vol. AP- 8, pp. 312-323, May 1960.
- [3] M. Turner, "Spiral Slot Antenna", US Patent No. 2,863,145, Issued December 2 1958.
- [4] J.J. Wang, V.K. Tripp, "Design of Multioctave Spiral-Mode Microstrip Antennas", IEEE Trans. Ant. Propagat., vol. AP-39, pp. 273-276, March 1991.
- [5] M.W. Nurnberger, J.L. Volakis, "A New Planar Feed for Slot Spiral Antennas", IEEE Trans. Ant. Propagat., vol. AP-44, pp. 130-131 , January 1996.
- [6] D. S. Filipovic, J.L. Volakis, "A Broadband Meanderline Slot Spiral Antenna", IEE Proc.,-Microw., Ant. Propagat., vol. 149, 2, April 2002.
- [7] R. Corzine and J. Mosko, Four-Arm Spiral Antennas, Norwood, MA, Artech House, 1990.
- [8] D. S. Filipovic, J.L. Volakis, "Novel Slot Spiral Antenna Designs for Dual-band/Multi-band Operation", IEEE Trans. Ant. Propagat., vol. AP-51, pp. 430-440, March 2003.

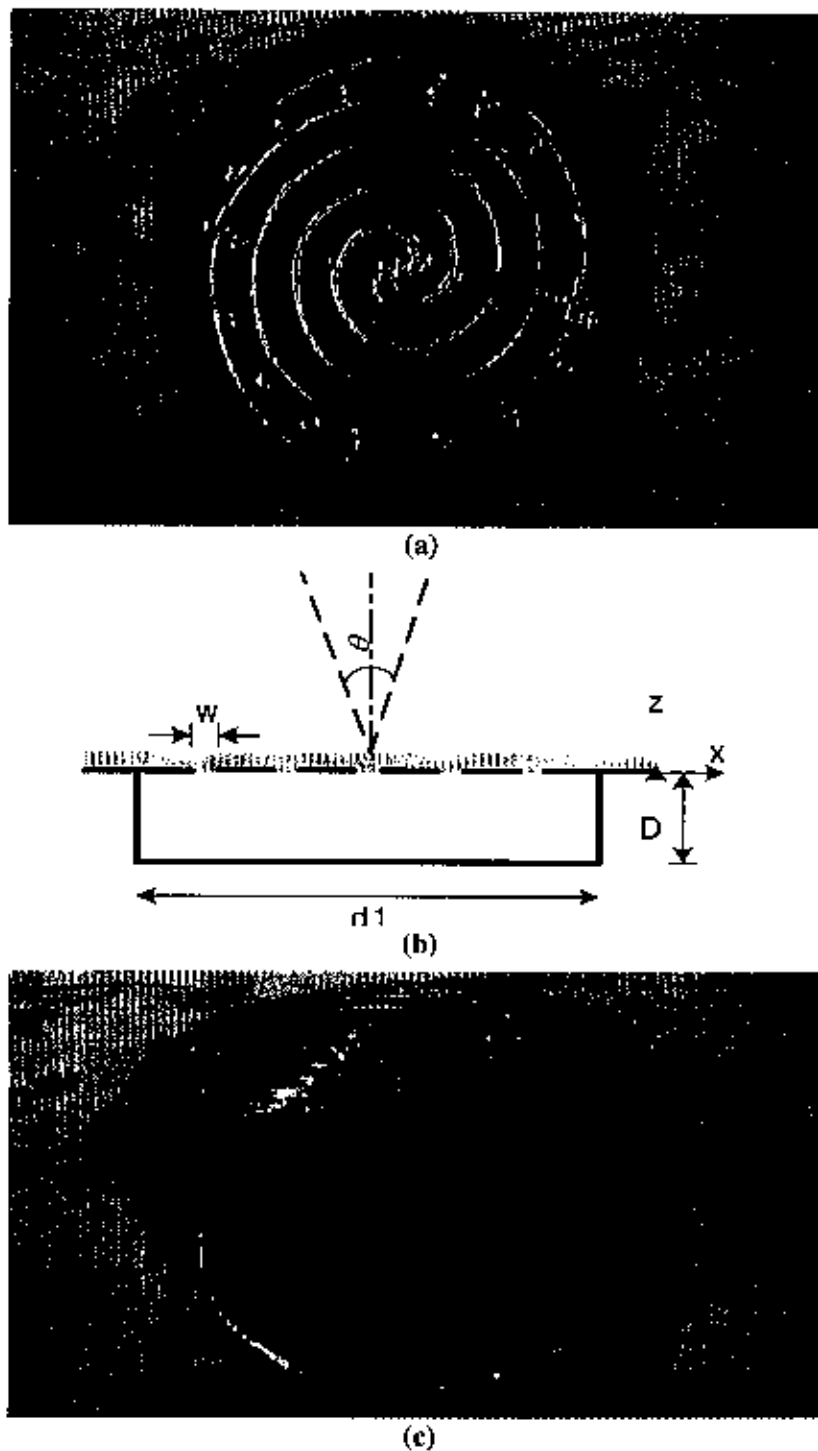
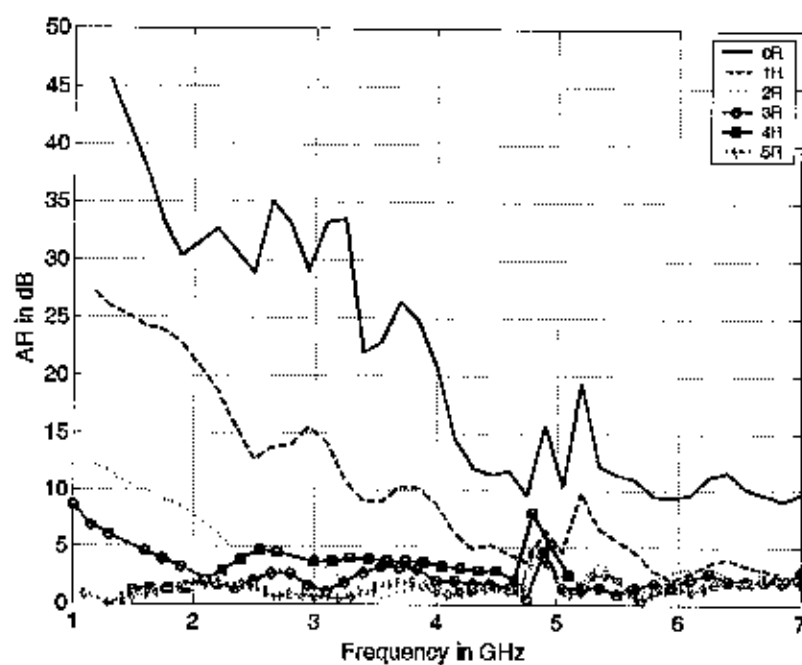
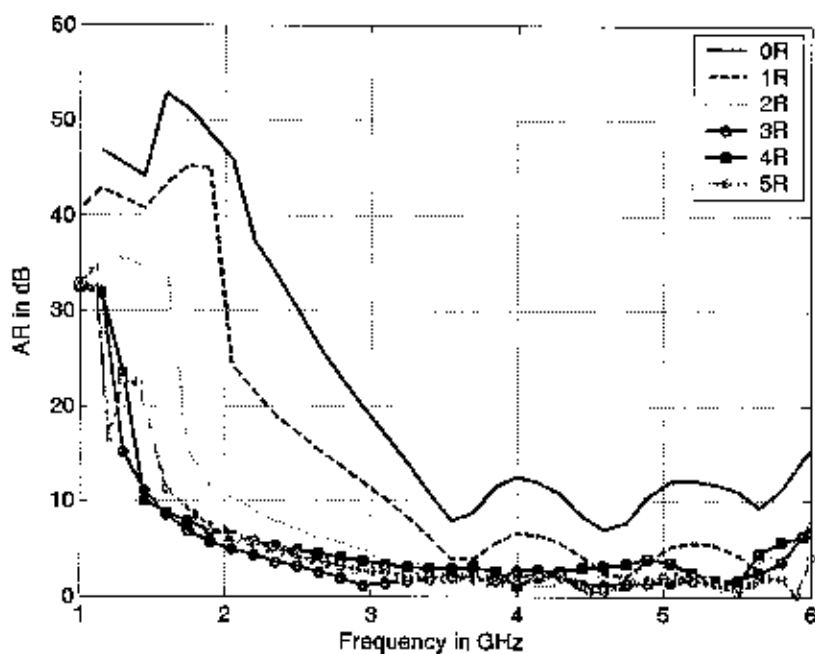


Fig. 1. Top view of the 4-arm spiral (a), Cross-section of the shallow cavity (b) and cavity of the slot spiral with the absorber (c)

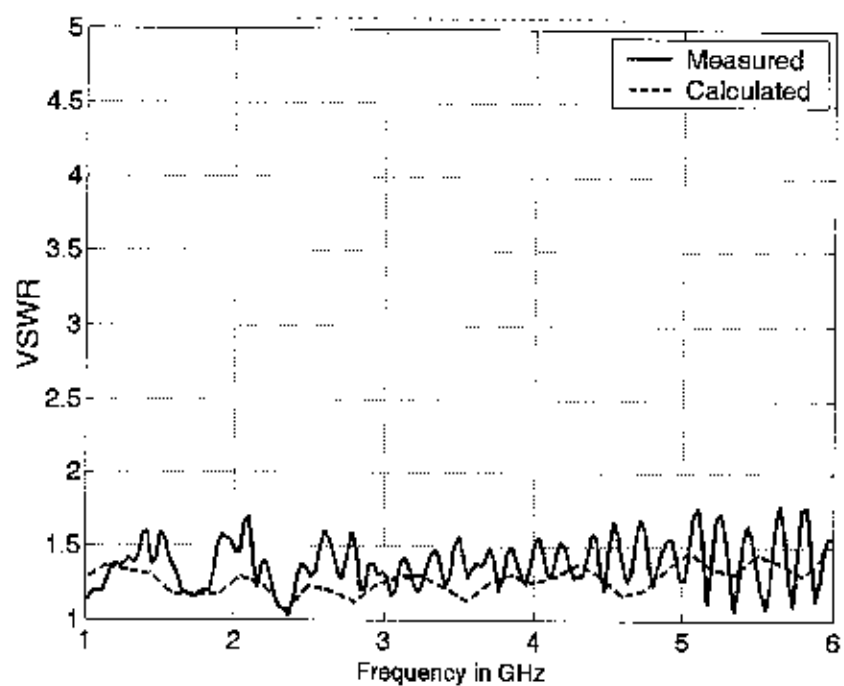


(a)

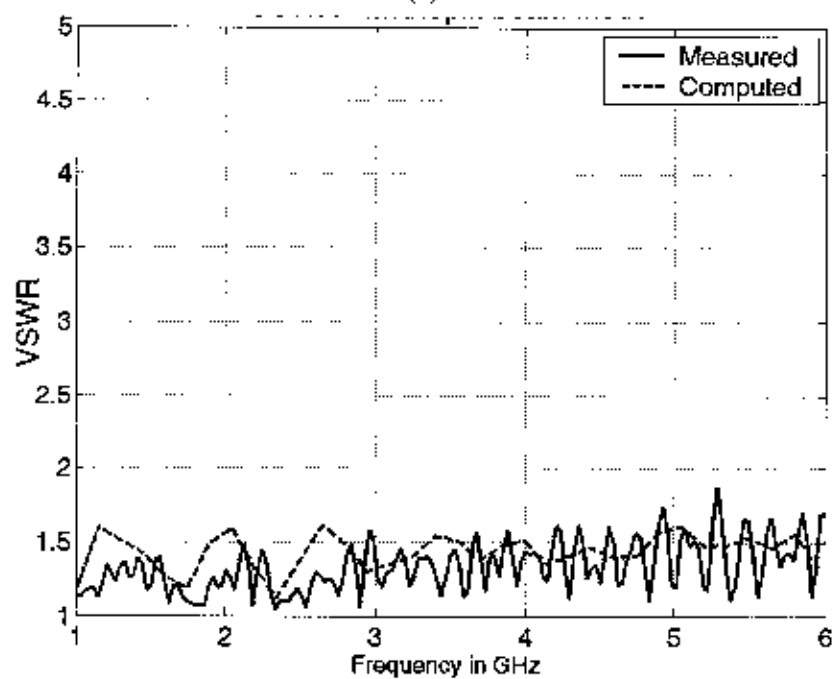


(b)

Fig. 2. Axial ratio computed at the peak-gain angle for the 1st (a) and 2nd modes (b) vs. different number of resistors

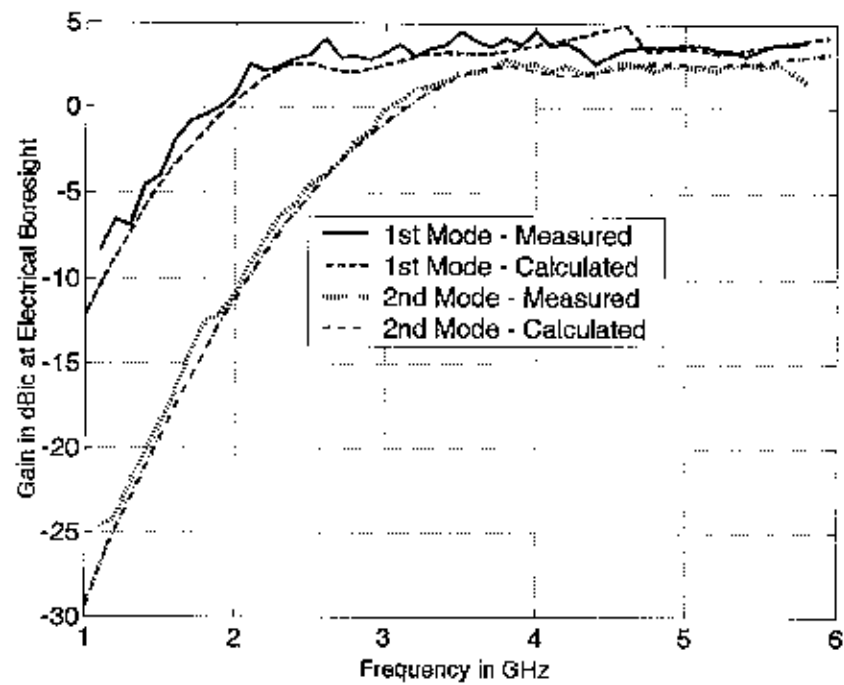


(a)

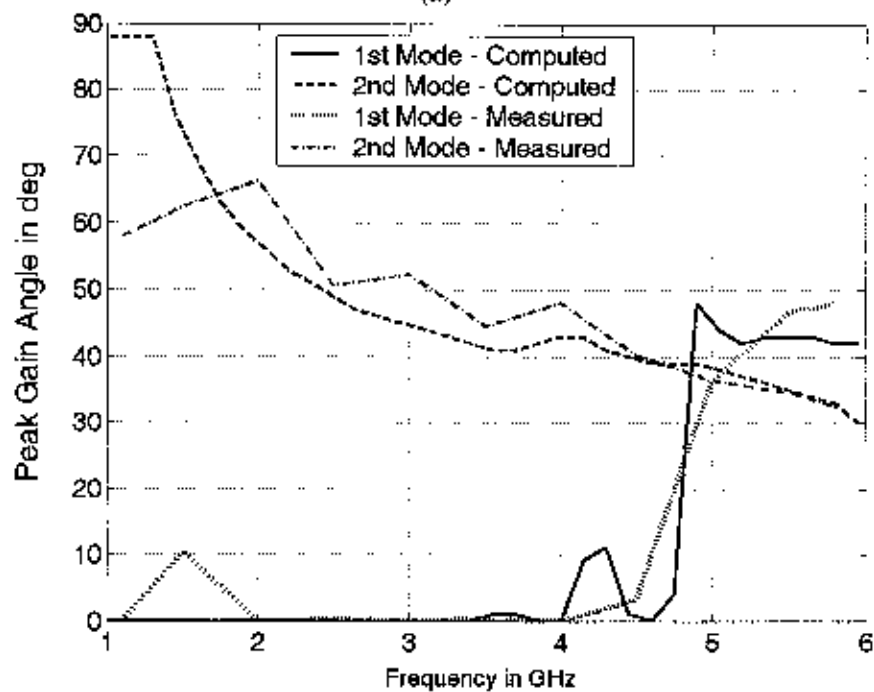


(b)

Fig. 3. VSWR for the 1st mode (a) and 2nd mode (b) vs. frequency



(a)



(b)

Fig. 4. Gain (a) and Peak-gain angle (b) for the 1st and 2nd modes vs. frequency

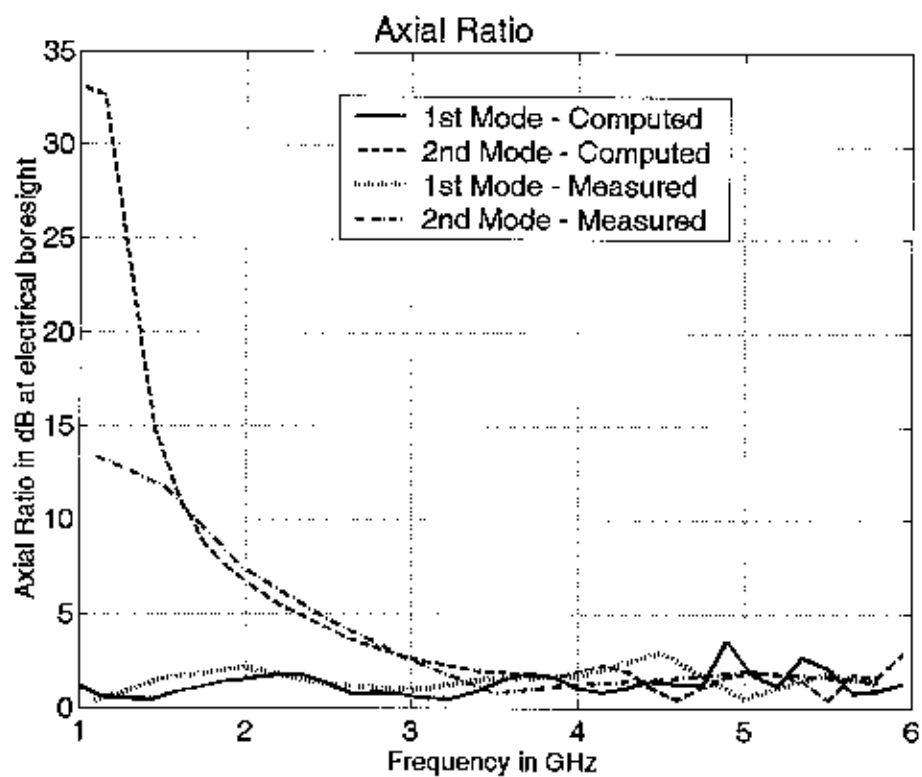


Fig. 5. Axial-ratio at the peak-gain angle for the 1st and 2nd modes vs. frequency

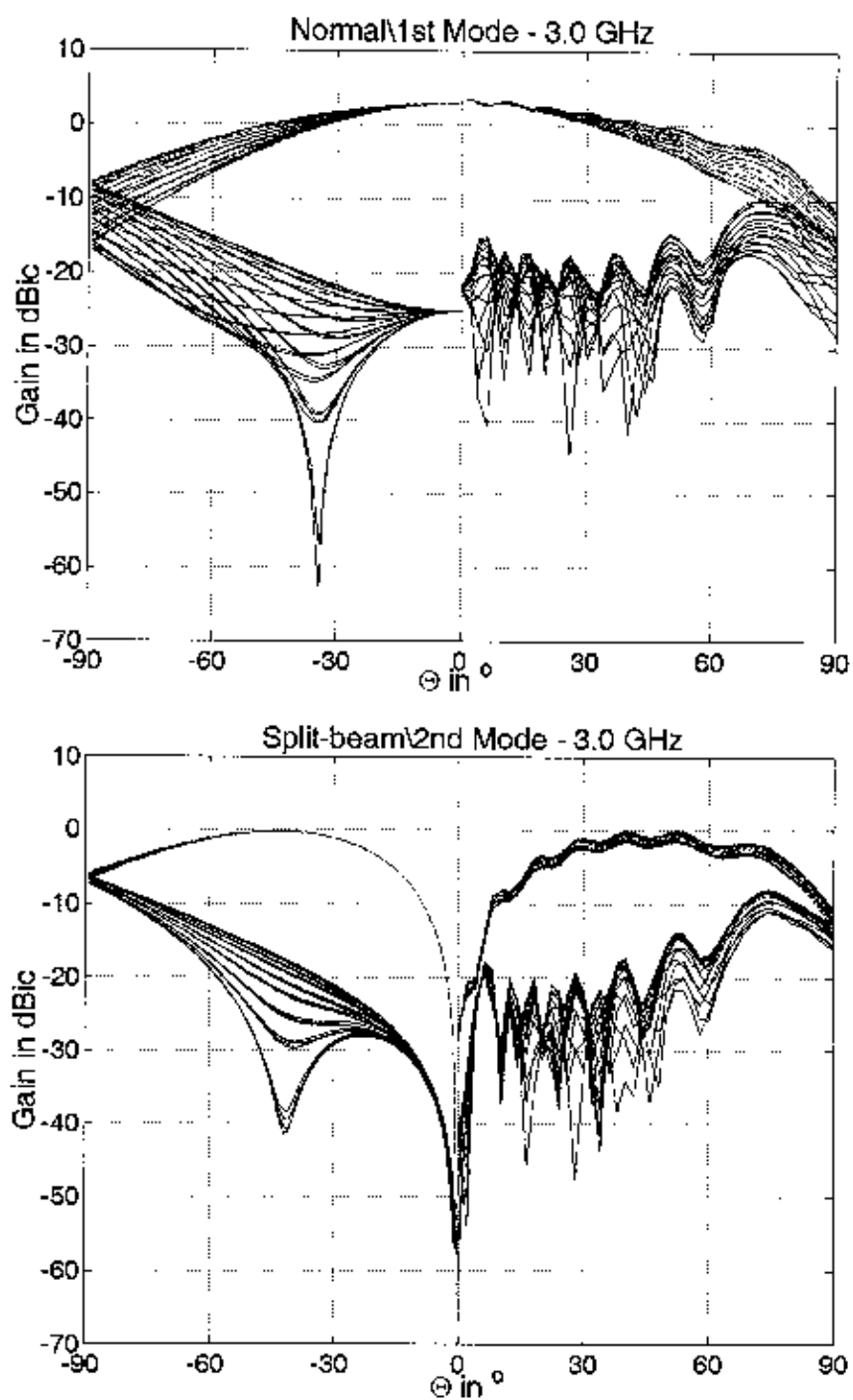


Fig. 6. Simulated (-90° to 0°) and measured (0° to 90°) co- and cross-polarization patterns at 3 GHz

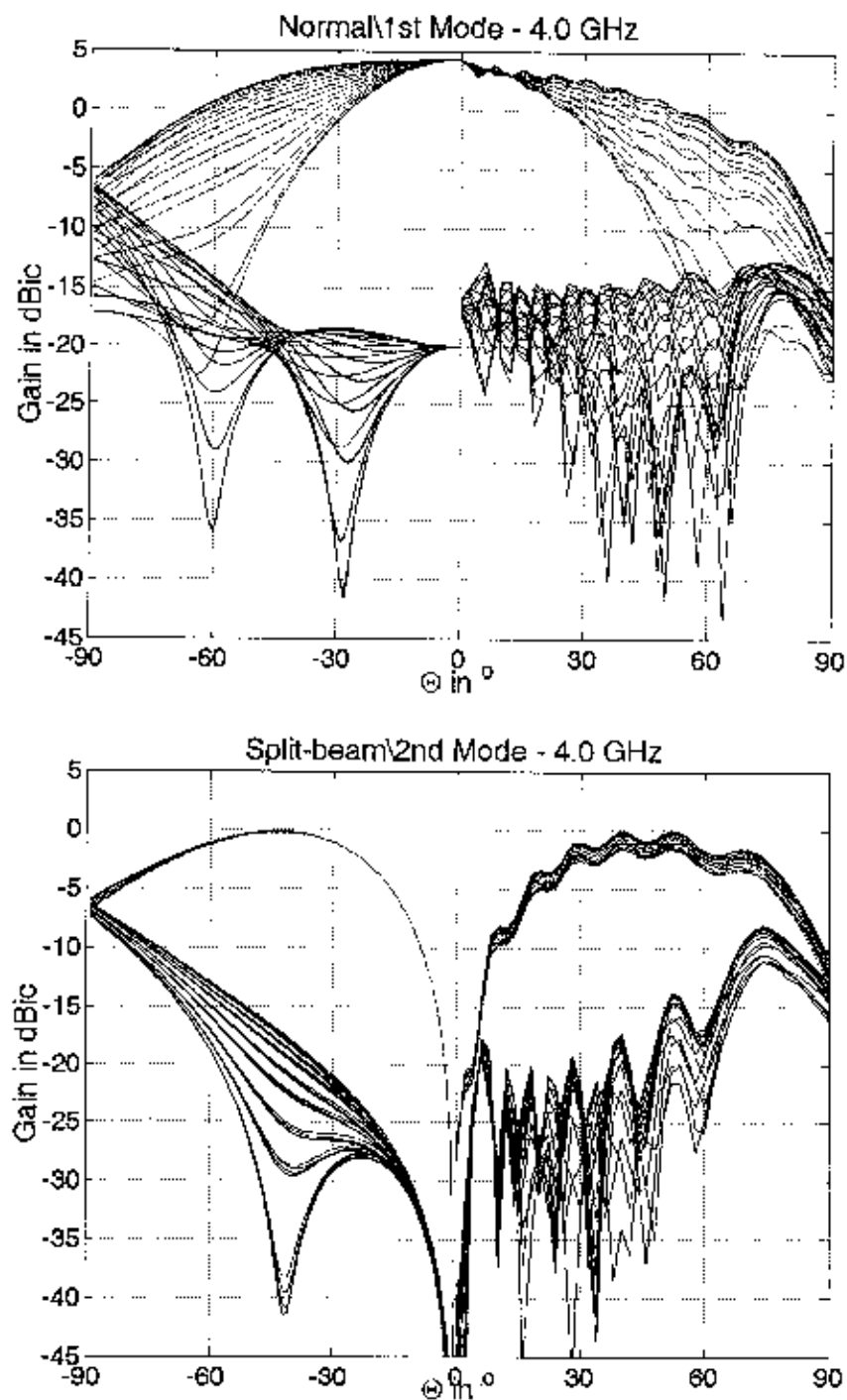


Fig. 7. Simulated (-90° to 0°) and measured (0° to 90°) co- and cross-polarization patterns at 4 GHz

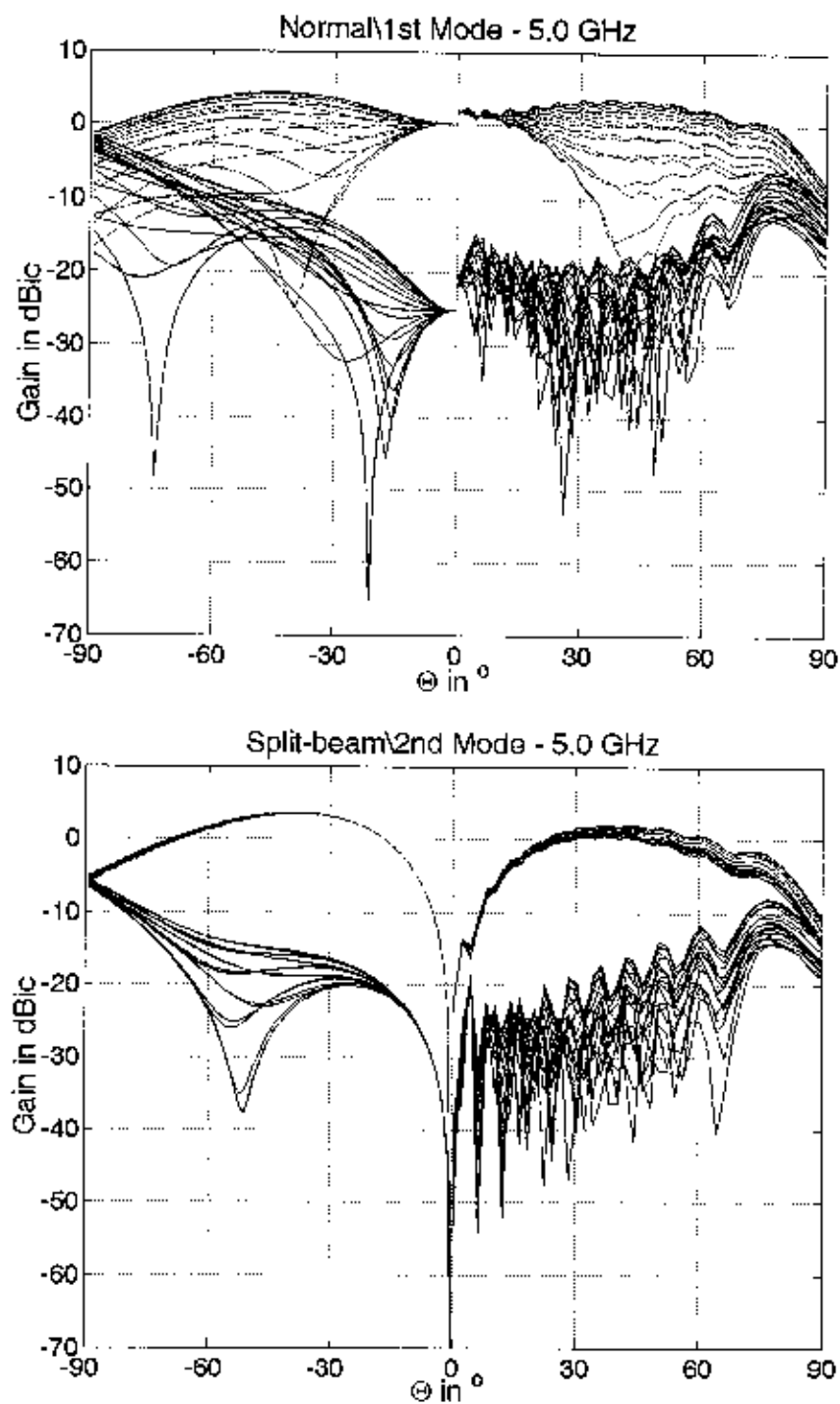


Fig. 8. Simulated (-90° to 0°) and measured (0° to 90°) co- and cross-polarization patterns at 5 GHz

TRUNCATED VERSIONS OF MODIFIED PARANY GASKET MONOPOLE ANTENNA AND ITS FREQUENCY ALLOCATION

Kiyun Han and Frances J. Harackiewicz
Antennas and Propagation Laboratory
Department of Electrical and Computer Engineering
Southern Illinois University Carbondale
Carbondale, IL 62901-6603

Abstract: To achieve multi-frequency operating bands, the Sierpinski triangle gasket fractal geometry has been applied to monopole and dipole antennas. Recently, modified 2- and 3-dimensional parany gasket monopole antennas have been introduced and the results show simpler design than the conventional Sierpinski monopole and also improved operating band characteristics.

In this paper, to reduce the size of the modified parany gasket monopole, the gasket is truncated into a couple of different shapes. The monopoles are fed by 50 Ω microstrip lines and ground plane is printed at the back of the microstrip line. The results show that truncated versions of the modified parany gasket monopole maintain multi-frequency operating bands; and due to the printed ground plane, the overall volume is smaller than that of a monopole that uses a conventional metal ground plane perpendicular to the antenna. Also, the flare angle of the proposed antennas is changed from 60 $^\circ$ to 90 $^\circ$ to study allocation of the operating bands. The results suggest that changing the flare angle is one way to control the position of multiple bands.

1. Introduction

The Sierpinski triangle monopole and dipole antennas have been studied intensively to achieve multi-frequency operating band [1]-[3]. Recently, modified 2- and 3-dimensional parany gasket monopole antennas have been introduced [4]. As a result, improved operating band characteristics have been achieved. In [5] and [6], multiple ring and parany gaskets are used instead of the conventional Sierpinski gasket. Both cases show multiband characteristics. Especially in [6],

printed ground plane with microstrip line feed have been applied for better impedance matching.

In this paper, a modified parany and two different truncated versions of modified parany gasket monopoles are introduced to reduce the size of the monopole and to study multiband behavior. The flare angle also has been changed from 60° to 90° to study frequency allocation. Section 2 demonstrates the multiband behavior of the modified parany gasket monopole and its truncated versions with microstrip feed on a printed ground plane. Section 3 demonstrates frequency allocation of monopoles in section 2 by changing the flare angle. Input return losses of three pairs of monopoles are compared between 60° and 90° flare angles.

2. Modified Parany Gasket Monopole and Its Truncated Versions

2.1 Design and configuration

Modified parany gasket monopole with 60° flare angle (hereafter 60MPARANY) is printed on a 62-mil thickness Rogers RT/Duroid 5880 ($\epsilon_r = 2.2$). The antenna is fed by a 50Ω microstrip line (4.4mm wide) and the ground plane is at the back of the microstrip line. To study the truncation effect, two more monopoles are made. First, 60MPARANY is truncated into a diamond shape (hereafter T60PARANY1) and second, the top of the T60PARANY1 is also truncated (hereafter T60PARANY2). Figure 1 shows the three different monopoles. For all three antennas, a scaling factor of approximately $\frac{1}{2}$ is applied. The heights of the 60MPARANY and T60PARANY1 are 6.5, 12, 23, and 44mm from the top of the ground plane. The heights of the T60PARANY2 are 6.5, 12, 23, and 28mm from the top of the ground plane. All the slot heights are maintained with 2mm.

All the antennas in this paper including the antennas in Figure 1 and later section are fabricated and measured at the SIUC Antennas and Propagations Laboratory.

2.2 Simulated and measured results

Measured return losses of the three antennas are shown in Figure 2. The results between simulated and measured return losses show good agreement. Except the fourth band of the T60PARANY1, the center frequencies of each band of all three antennas between the simulation and measurement are shown at the

almost the same points. The simulated results are obtained using a Finite Difference Time Domain (FDTD) commercial software package CONCERTO from Vector Fields Inc. [7]. All antennas clearly show four frequency bands. It can be seen that at the first band, the resonant frequency is shifted from 1.18 for 60MPARANY to 1.57 and 1.86GHz for T60PARANY1 and T60PARANY2 respectively. It is found that even though the height of the T60PARANY1 is same as 60MPARANY, the resonant frequency of the T60PARANY1 is shifted higher. For T60PARANY2, the frequency shift is expected because of the short height of the antenna. Bandwidth (VSWR<2) and center frequencies of each bandwidth (f_c) are summarized in Table 1.

Table 1. The center frequencies and bandwidths of the three antennas with 60° flare angle.

Band #	f_c (GHz)				Bandwidth (VSWR<2) (%)			
	1	2	3	4	1	2	3	4
60MPARANY	1.18	3.92	8.11	16.17	-	12.6	19.1	24.9
T60PARANY1	1.57	3.85	7.82	15.58	18.5	10.1	22.4	23.7
T60PARANY2	1.86	4.33	7.58	16.12	-	4.6	19.3	24.7

The bandwidths of all antennas for the second, third, and fourth band remain close except the second band of the T60PARANY2, which decreased from 12.6% to 4.6%. However the first bandwidth of the T60PARANY1 increases from 0% to 18.5%.

Radiation patterns in all four bands of the three antennas are simulated using the CONCERTO. Figure 3 compares $\phi = 90^\circ$ at the second, third, and fourth band of three antennas. It can be seen that the patterns are similar among those three antennas and bands. As the operating band increases, back lobe radiation also increases. This is because as the wavelength becomes smaller, the ground plane looks longer. The radiation patterns of $\phi = 0^\circ$ and $\theta = 90^\circ$ also show similar radiation patterns among antennas.

3. Frequency Allocation by Changing Flare Angle

3.1 Design and configuration

To study frequency allocation, the flare angle of each antenna from the previous section has been changed from 60° to 90° . Figure 4 shows 90° flare angle of 60MPARANY (hereafter 90MPARANY), T60PARANY1 (hereafter T90PARANY1), and T60PARANY2 (hereafter T90PARANY2). All antennas are printed on a 62-mil thickness Rogers RT/Duroid 5880 ($\epsilon_r = 2.2$), fed by $50\ \Omega$ microstrip line and have a ground plane at the back of the feed line. The heights of each antenna and slot height are the same as those in the previous section.

3.2 Measured results

Measured return losses of the antennas with 90° flare angle are compared with 60° flare angle in Figure 5. All three 90° flare angle antennas show four frequency operating bands however it can be seen that the resonant frequencies are shifted to lower side. It is expected because the length of antennas side has been increased. The figure also shows better impedance matching at the second and third band of the 90MPARANY and third bands of the T90PARANY1 and T90PARANY2. The input impedances $62 + j26$ and $51.5 + j14$ for the second and third band of the 60MPARANY respectively have been changed to $50.1 - j3$ and $52.7 - j1.0$ for the second and third band of the 90MPARANY respectively. The reactances at the resonant frequencies decrease almost to zero.

The center frequencies of the bandwidths of each band and bandwidths of the antennas with 90° flare angle are summarized in Table 2, 3, and 4. It shows that from the 60MPARANY to 90MPARANY, the center frequencies are shifted 8.5%, 20.4%, 22.7%, and 14.7% down for first, second, third, and fourth band respectively. The bandwidths of antennas with 90° flare angle are increased or maintained the same level as the 60° flare angle with the exception of the first and second bands of the T90PARANY1.

Table 2. The center frequencies and bandwidths of the 60MPARANY and 90MPARANY.

Band #	f_c (GHz)				Bandwidth (VSWR<2) (%)			
	1	2	3	4	1	2	3	4
60MPARANY	1.18	3.92	8.11	16.17	-	12.6	19.1	24.9
90MPARANY	1.08	3.12	6.27	13.79	-	21.8	21.7	37.3
Freq. Shift (lower)	8.5%	20.4%	22.7%	14.7%				

Table 3. The center frequencies and bandwidths of the T60PARANY1 and T90PARANY1.

Band #	f_c (GHz)				Bandwidth (VSWR<2) (%)			
	1	2	3	4	1	2	3	4
T60PARANY1	1.57	3.85	7.82	15.58	18.5	10.1	22.4	23.7
T90PARANY1	1.47	2.97	6.66	14.80	-	3.3	20.4	29.5
Freq. Shift (lower)	6.4%	22.9%	14.8%	5.0%				

Table 4. The center frequencies and bandwidths of the T60PARANY2 and T90MARANY2.

Band #	f_c (GHz)				Bandwidth (VSWR<2) (%)			
	1	2	3	4	1	2	3	4
T60PARANY2	1.86	4.33	7.58	16.12	-	4.6	19.3	24.7
T90PARANY2	1.76	3.02	6.52	15.01	-	3.3	22.2	23.3
Freq. Shift (lower)	5.4%	30.3%	14.0%	6.9%				

The simulated radiation patterns of antennas with 90° flare angle using CONCERTO also show close patterns with the antennas with 60° flare angle.

4. Conclusion

Six different monopoles including modified parany gasket monopole and a couple of truncated versions of it with 60° and 90° flare angles are fabricated and tested to study the truncation effect and allocate its operating frequency bands. All antennas are fed by microstrip line on a printed ground plane, which reduces the overall volume of the antennas. All antennas show similar multiband characteristics even when they are truncated. Especially T60PARANY1 shows better impedance matching and as a result, broader bandwidth compared to 60MPARANY. The bandwidth is increased from 0% to about 19%. The T60PARANY1 only has half the size of the 60MPARANY.

Antennas with 90° flare angle show each band shifted lower than those with 60° flare angle. This is expected because antennas with 90° flare angle have longer side length than antennas with 60° flare angle. The frequencies are shifted approximately from 5% to 30%. Some of the antennas with 90° flare angle show better impedance matching, especially in the case of the 90MPARANY. The results suggest that changing the flare angle is one way to control the position of multiple bands. Also since the truncated versions of the modified parany gasket monopole have smaller size than the modified parany gasket monopoles (half or less than half), they are attractive candidates for array and mobile communication applications.

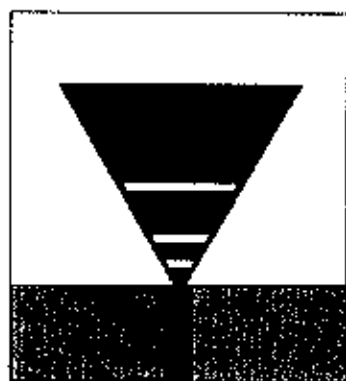
5. Acknowledgement

The authors would like to thank Vector Fields Inc. for supporting the software.

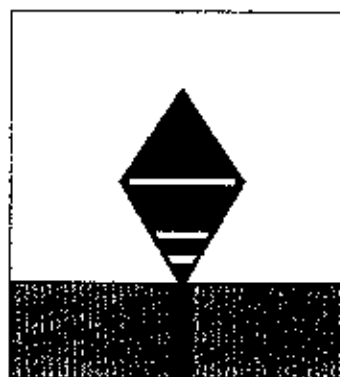
6. References

- [1] C. Puente, J. Romeu, R. Pous, X. Garcia and F. Benitez, "Fractal Multiband Antenna Based on the Sierpinski Gasket," *IEE Electron. Letters*, vol.32, no. 1, pp. 1-2, Jan. 1996.
- [2] C. Puente, J. Romeu, R. Pous and R. Cardama, "On the Behavior of the Sierpinski Multiband Fractal Antenna," *IEEE Trans. Antennas Propagat.*, vol. 46, no. 4, pp. 517-524, Apr. 1998.

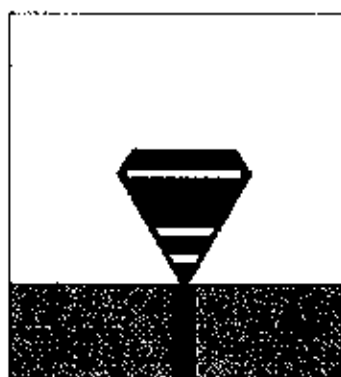
- [3] C. Puente, J. Romeu, R. Bartoleme and R. Pous, "Perturbation of the Sierpinski Antenna to Allocate Operating Bands," *IEE Electron. Lett.*, vol. 32, no. 24, pp. 2186-2188, Nov. 1996.
- [4] S. R. Best, "On the Performance of a Multiband Conical Monopole Antenna," *Proc. Of the Antenna Application Symposium*, Monticello, Illinois, pp. 320-328, Sep. 2002.
- [5] C. T. P. Song, P. S. Hall and H. Ghafouri-Shiraz, "Multiband Multiple Ring Monopole Antennas," *IEEE Trans. Antennas Propagat.*, vol. 51, no. 4, pp. 722-729, Apr. 2003.
- [6] C. T. P. Song, P. S. Hall and H. Ghafouri-Shiraz, "Perturbed Sierpinski Multiband Fractal Antenna with Improved Feeding Technique," *IEEE Trans. Antennas Propagat.*, vol. 51, no. 5, pp. 1011-1017, May 2003.
- [7] CONCERTO, version 2.0, Vector Fields Inc.



(a)

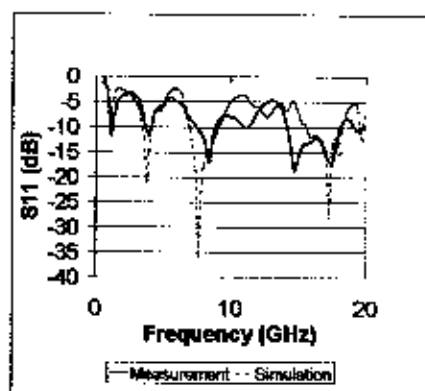


(b)

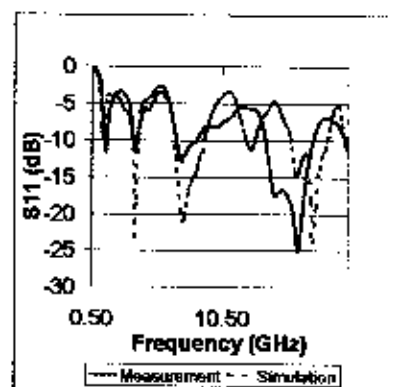


(c)

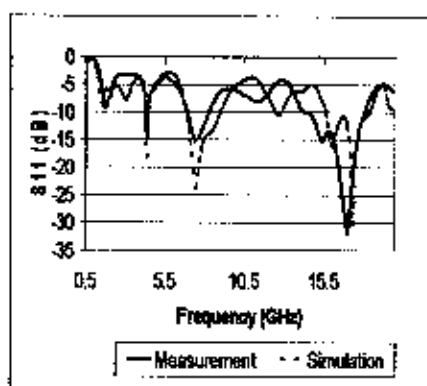
Figure 1. Modified parany gasket monopole and its truncated versions with 60° flare angle. (a) Modified parany gasket monopole (60MPARANY), (b) Truncated version of modified parany gasket monopole 1 (T60PARANY1), (c) Truncated version of modified parany gasket monopole 2 (T60PARANY2).



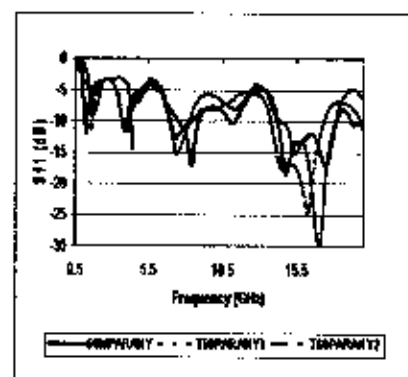
(a)



(b)



(c)



(d)

Figure 2. Simulated and measured return losses of the antennas with 60° flare angle. (a) 60MPARANY, (b) T60PARANY1, (c) T60PARANY2, (d) comparison of the measured results only.

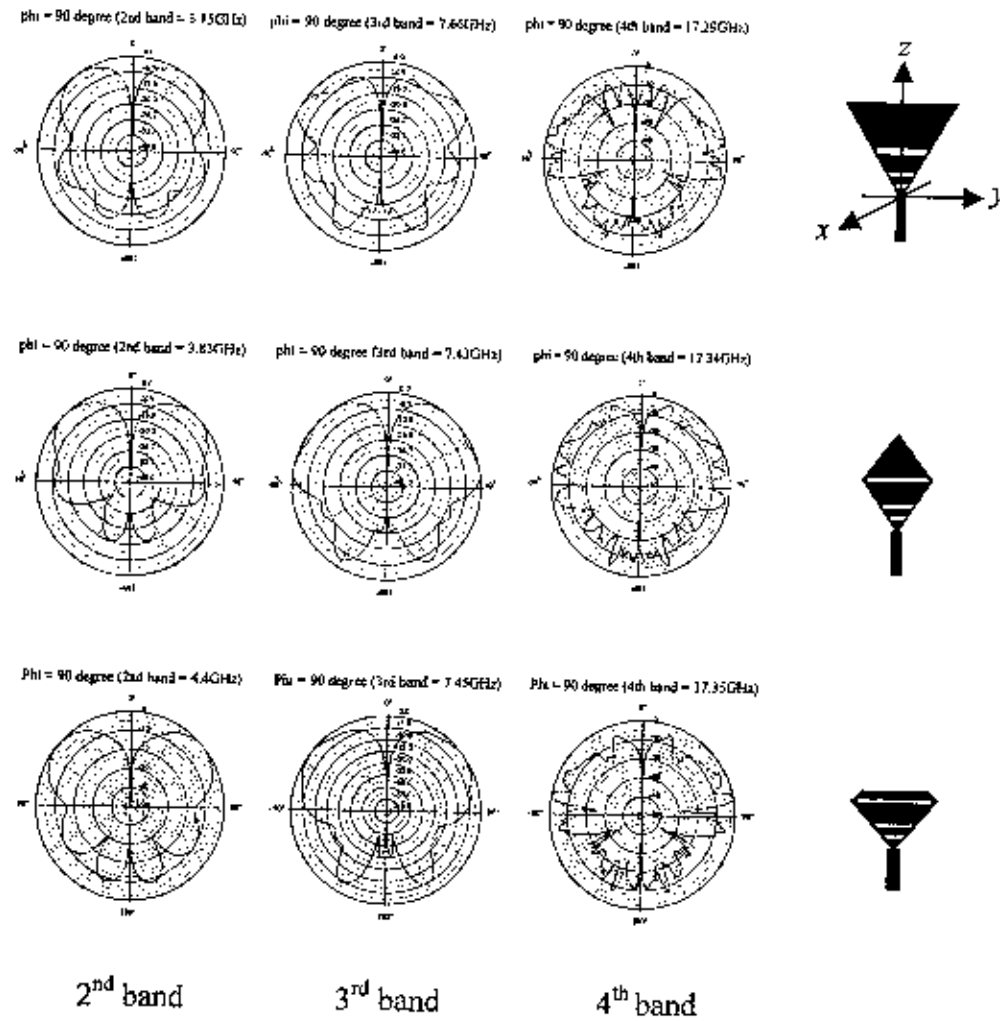
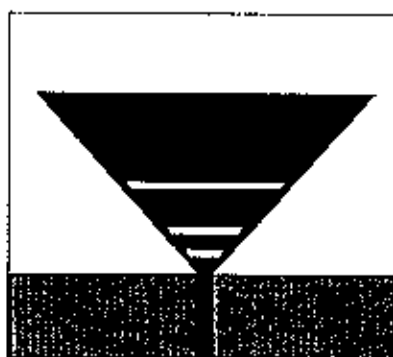


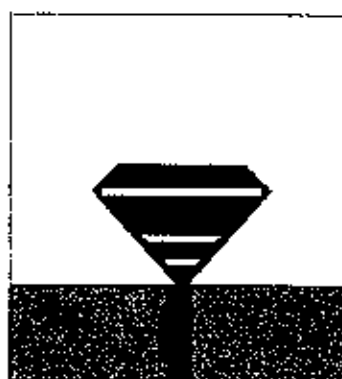
Figure 3. Radiation patterns of the 60MPARANY, T60PARANY1 and T60PARANY2 at $\phi = 90^\circ$.



(a)

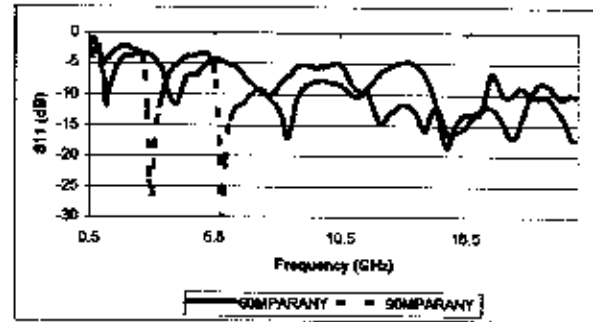


(b)

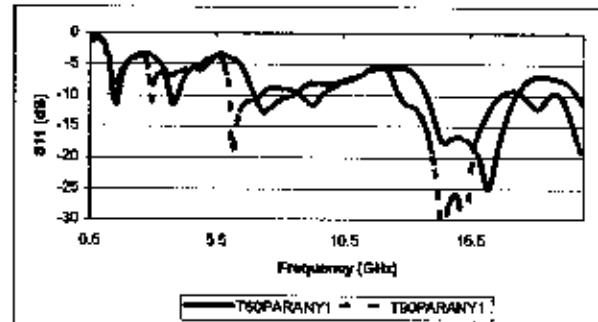


(c)

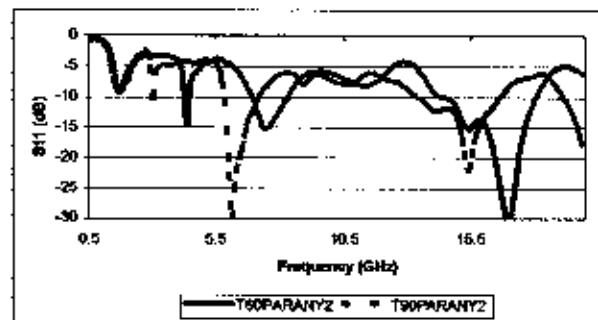
Figure 4. Modified parany gasket monopole and its truncated versions with 90° flare angle. (a) Modified parany gasket monopole (90MPARANY), (b) Truncated version of modified parany gasket monopole 1 (T90PARANY1), (c) Truncated version of modified parany gasket monopole 2 (T90PARANY2).



(a)



(b)



(c)

Figure 5. Comparison of the measured return losses of the antennas between 60° and 90° flare angles. (a) 60MPARANY vs. 90MPARANY, (b) T60PARANY1 vs. T90PARANY1, (c) T60PARANY2 vs. T90PARANY2.

IMPEDANCE AND GAIN BANDWIDTHS OF BROADBAND, ELECTRICALLY SMALL, STACKED CONICAL RESONATOR ANTENNAS

Paul E. Mayes and Paul W. Klock
Professors Emeritus, Electromagnetics Laboratory
Department of Electrical and Computer Engineering
University of Illinois, Urbana, IL 61801

Abstract: Electrically small antennas conventionally operate in the vicinity of a single tuned resonance. Either the Q is high or the efficiency is low. By using several resonators effectively connected in series, the input impedance can be made a periodic function of frequency. With the proper transformation of the input impedance, the impedance bandwidth can then be extended to a limit determined by allowable complexity and available space. However, the bandwidth determined by satisfactory power gain may not coincide. Since the antenna is small, the radiation pattern does not vary much with frequency. But, when the radiation and conduction losses from each pair of adjacent resonators are small, the phase between them approaches 180 degrees. As a result, the far fields of adjacent radiating resonators tend to cancel at the frequencies between the resonances of the individual resonators. In this band, the conductive loss may equal or exceed the radiation loss and the efficiency will be quite low. Although the match bandwidth may be large, the gain will vary widely within the match band and the antenna is rendered multiband. To minimize this effect, the antenna should retain sufficient size to produce significant radiation loss. Computer simulations are used to show examples of these phenomena.

1. Introduction

It has been recently demonstrated that the impedance bandwidth of an electrically small antenna can be extended by using a combination of small resonators as the radiating element [1]. However, the band of practical operation may not coincide with the band of good impedance match [2]. It is quite possible, indeed likely, that the efficiency of a very small antenna with large impedance bandwidth will vary with frequency. This paper shows how such a phenomenon originates in the case of nested-cone resonators and how the resulting gain variation can be controlled.

2. Efficiency and bandwidth

Concern about the relationship between gain bandwidth and impedance bandwidth is not of primary importance for those electrically small antennas that operate near a single resonance. Since the radiation pattern of a small antenna is dominated by the lowest-order spherical mode (dipole pattern), the directive gain does not change perceptibly over a wide range of frequency. Nor is the efficiency rapidly varying with frequency. Hence, the gain changes very little in the vicinity of resonance and the operating bandwidth is determined by the variation in impedance. This situation may change when multiple resonances are introduced in an effort to increase the match bandwidth. While the impedance bandwidth can be enhanced in this way, it does not necessarily follow that the gain bandwidth will be unaffected.

The problem becomes apparent when a complete analysis is performed on a double-resonator system like the two nested conical resonators shown in Figure 1. The radiating system is formed by placing three cones with a common axis in close proximity, having apices as nearly coincident as physically possible. In the system of Figure 1 the lower cone has a polar angle of 90 degrees, becoming thereby, a plane. In a physical embodiment, the system is fed by a coaxial cable, the shield of which is connected around a hole centered at the apex of the lower cone. The center conductor passes through a hole at the apex of the middle cone and attaches to the upper cone at its apex. For the computations done here, the feed system is modeled by a conducting cylinder that extends between the bottom and top cones, passing within a hole at the apex of the center cone. The antenna is excited by a ring of voltage sources that gird the feed cylinder. With this feed model there are no currents on the shield of the coax. In practice, the shield of the coax should be isolated from the antenna fields to improve the agreement between the computed and measured results.

Each cone extends from the feed region to specific radial distance, at which the cone is truncated at a constant distance from its apex. Although these truncation distances may be equal, there is no requirement that it be so. The lower and middle cones form one resonator. The middle and upper cones form another. When the polar angles that define each cone are within ten or so degrees of each other, each resonator has a rather high value of Q . This contrasts with the conventional biconical antenna where the angles are much larger and the impedance behavior for antennas having greater than a minimum length is essentially non-resonant.

The system can be made electrically small by loading each resonator in

such a manner that the resonant frequency is reduced. In Figure 1, each resonator is loaded with inductance placed on the rim. Actually, there are four such loads connected across the aperture of each resonator. When appropriate values of inductive reactance are achieved at the loads, each resonator individually would display a resonance when the cone lengths are less than one-quarter wavelength. The software used here permits the user to specify an arbitrary surface impedance for each patch. The frequencies of resonance are therefore adjusted by specifying inductive surface reactances of appropriate values for the patches that reside on the vertical conducting strips that are attached between the rims of adjacent cones. The surface resistance of these same patches is set by specifying the Q . In the first analyses the resistance of all other patches was set to zero (perfect conductor). In the last case, the surface resistance was taken to be characteristic of copper at 100MHz.

Since the resonators are open at the truncation, radiation will occur. Power is lost from the resonators by both radiation and dissipation. Of course, the amount of radiation depends upon the size of the system in wavelengths. When the inductive reactance of the combined loads on an individual resonator is large, the size reduction at resonance can be large, but the radiation from the resonator will be small and the resulting resonator will have a low efficiency. The input impedance of such a lossy resonator is similar to that of a parallel RLC (tank) circuit.

The method of feeding described above is equivalent to placing two tanks in series. When the two resonances are slightly displaced, the input impedance will cross the real axis of the Smith Chart at two closely spaced frequencies. Between the resonant frequencies, the impedance will form a loop on the chart, the size of which depends partly upon the separation of the resonant frequencies. By changing the values of the terminating inductors on one resonator, the size of the loop can be changed; smaller as the resonances move together, larger as they move apart. When a sufficiently small loop has been obtained, addition of a transformer at the input will center the loop on the chart so that the magnitude of the reflection coefficient will remain almost constant for all frequencies between the resonances. This conforms to Fano's criterion for maximum impedance bandwidth [3].

In Figure 1 the inductive loads are modeled as reactive strips that are connected from the rim of one cone to the rim of the adjacent cone. Four strips are placed on each cone, equally spaced in azimuth in an effort to maintain a radiation pattern that is nearly omnidirectional. The triangular patches shown on Figure 1 were used in a moment-method analysis. The first results were obtained by using the Finite Element Radiation Model (FERM). The FERM package is a

method of moments technique using the Rao, Wilton, Glisson (RWG) basis function [4]. It was not possible to analyze extremely small patches using this procedure. As a result, it was impossible to accurately model the feed. A new code, low-frequency method of moments (LFMOM) [5], was written recently to extend the basis functions to loop-tree [6] in addition to RWG.

Some results for input impedance of a double resonator computed using LFMOM are shown in Figure 2. The loop on the Smith Chart was obtained by using different inductors on each of the two conical resonators and adjusting these inductive terminations to move the resonances until the loop was the desired size. In Figure 2, the radius of the loop approximately corresponds to $| \Gamma^2 | = 0.5$ (SWR = 5.85). Half-power points are conventionally used to define the limits of the match bandwidth, even though more stringent requirements are often used, particularly for larger antennas.

In addition to the input impedance, the LFMOM code produces values of the far field. These values are integrated by the code to also produce values of the directive gain. The efficiency can then be obtained by comparing the radiation resistance to the input resistance [5]. Figure 3 shows that the efficiency varies with frequency; lower values coinciding with the band of best match.

3. Analysis of system of two tanks in series

The basic phenomenon that causes the dip in efficiency can be illustrated by some analysis of a series connection of the two tank circuits shown in Figure 4. The admittances of each tank are given by

$$\begin{aligned}
 Y_k &= G_k + (j\omega C_k + \frac{1}{R_k + j\omega L_k}) \\
 &= G_k + (1 - (\frac{\omega}{\omega_k})^2 + j \frac{\omega}{\omega_k} \left(\frac{C_k}{L_k} \right)^{\frac{1}{2}} R_k) / R_k (1 + jQ_k)
 \end{aligned}$$

where $\omega_k = (L_k C_k)^{-\frac{1}{2}}$ and $Q_k = \omega L_k / R_k$.

Figure 5 shows the variation in phase difference of the voltages across the two tanks in the vicinity of the resonances ω_1 and ω_2 for various values of G_k .

The important points to note about these results are:

(1) when the losses are low (high values of G_k), the phase difference between the voltages is approximately 180 degrees in the frequency span between the two resonances, and

(2) as the losses increase (lower values of G_k), the phase difference decreases.

From the above analysis it is to be expected that, when losses in the resonators are small, the voltages across the apertures of the stack of two conical resonators would be almost opposite in phase across the band between the two resonant frequencies. It follows that the radiation from the two resonators would approximately cancel at those frequencies and the net radiation would be small. When the radiated power is small, the power consumed in conduction losses in the antenna structure may dominate. This would account for the low values of efficiency for frequencies between the two resonances.

In order to counter the canceling effect of the resonator voltages, it is therefore imperative that the net radiated power be maintained at a high value, especially for those frequencies between resonances.

4. Computational analysis of a two-resonator system

The above analysis suggests that the efficiency could be increased by making the antenna larger with respect to the wavelength. This hypothesis has been tested by performing the LFMOM analysis on an antenna with the values of the terminal inductors reduced so that the resonances will occur at higher frequencies. The parameters of the antenna and the computed impedances are shown in Figure 6. The results of transforming the computed impedance by ratios of 0.5:1 and 0.15:1 are also shown. Since both the mismatch and efficiency are recognized to be functions of frequency, shifting the impedance loop to the center of the chart is not the best choice to maximize the (actual) gain bandwidth. A better choice would be to minimize the mismatch loss in the range of frequencies at which the efficiency is lowest. The efficiency was computed for an antenna having conductor loss as well as dissipation in the inductors. The results are shown in Figure 7. The difference in the efficiency caused by lossy conductive surfaces rather than perfect conductive surfaces in the antenna is small. A transformer with an impedance ratio of 0.14:1 provides a good approximation to best match at 163 MHz.

Figure 8 presents several computed gains as a function of frequency in the neighborhood of the resonances. As expected, the directive gain (DGDB1) is

very nearly constant. However, because of the reduced efficiency between resonances, the power gain (PGDB1) is nearly 10 dB below the directive gain at about 163 MHz. This shows a marked improvement over the case shown in Figure 3, where the efficiency varies from less than 1% to about 10%. An increase in the operating frequency from near 100 MHz to about 160 MHz causes an increase in the efficiency to a range between 10% and 26%, even though the value of Q for the load inductances has been decreased by a factor of 10. By using a transformer with impedance ratio of 0.14:1, the minimum mid-band actual gain (AGDB1) (includes the effect of both efficiency and mismatch loss) is realized near 163 MHz and does not vary much more than 3 dB from that value over the band from 154 to 177 MHz, a fractional bandwidth of 0.14 ($Q=7.1$). This result is obtained from an antenna structure that will fit within a sphere with radius of 19.95 cm. At 163 MHz, the corresponding value of ka is equal to 0.68. When this value is plotted along with the minimum values of Q computed from the Collin/Rothschild/McLean formula [2] as shown in Figure 9, it corresponds to an efficiency of about 78%. Even though the antenna of Figure 8 does not have a FBW that exceeds the theoretical maximum for a single resonator, the design concept utilizing multiple resonators holds the promise of achieving that result since the antenna in question occupies only 15% of the volume of a sphere of radius $ka = 0.68$. The match bandwidth can be readily extended by adding conical resonators to the stack without exceeding the previously established radius for the enclosing sphere.

5. Conclusions and plans for the future

It has been demonstrated that the resonator voltages of systems of series connected anti-resonant devices have phase differences which may vary widely across the band between adjacent resonant frequencies. When antenna systems are composed of such components, a difference in voltage phases can cause diminution of the radiated field, producing thereby a decrease in the efficiency. Since the phase difference is reduced by the presence of loss in the system, it is advantageous for a radiating system to maintain sufficient electrical size in the resonators to produce significant radiation. In this way, the variation in the efficiency can be minimized. As the electrical size of the radiator is decreased by means of loading that is predominantly reactive, it may be necessary to add dissipative loss to the antenna in order to reduce the variation in the efficiency at the expense of overall decrease in the efficiency.

An optimum design for reduced-size, multi-resonator antennas has not been found. A parametric study is needed. Since basing such a study on experimental data is impractical, given the number of parameters, computational modeling is in order. Up to this point, quasi-network modeling, combined with computer analysis based upon approximate models, have been used for both

design and evaluation. As a result, the agreement between measurements and computations is only qualitative. Although progress has been made in the analysis of fine features of the antenna, further improvements in the source model should be attempted. Also needed are techniques for more accurately representing the reactive loads. Finally, the computer predictions must be validated with careful measurements. A research program encompassing these advances is currently underway.

6. Acknowledgements

The work reported here was supported, in part, by a grant from the Communities Foundation of Texas, Inc.

7. References

- [1] P. E. Mayes and W. Gee, "Using Multiple Resonant Radiators for Increasing the Impedance Bandwidth of Electrically Small Antennas", *Proc. 24th Annual Antenna Applications Symposium*, Allerton Park, Illinois, September 2000.
- [2] P. E. Mayes and P. W. Klock, "Bandwidth and Efficiency of Some Electrically Small Antennas," *Proc. 26th Annual Antenna Applications Symposium*, Allerton Park, Illinois, September 2002.
- [3] R. M. Fano, "Theoretical Limitations on the Broadband Matching of Arbitrary Impedances," Ph.D. Thesis, MIT, 1947.
- [4] S. M. Rao, D. R. Wilton and A. W. Glisson, "Electromagnetic Scattering by Surfaces of Arbitrary Shape", *IEEE Trans. Ant. Propagat.*, vol. AP30, pp. 409-418, May 1982.
- [5] J.-S. Zhao, W. C. Chew and P. E. Mayes, "Accurate Analysis of Electrically Small Conical Antennas by Using the Low-Frequency Method", *Proc. Antenna Applications Symposium*, Allerton Park, Illinois, October 2001.
- [6] W. Wu, A. W. Glisson and D. Kajfez, "A comparison of two low-frequency formulations for the electric field integral equation," *Proc. 10th Annual Review of Progress in Applied Computational Electromagnetics*, vol. II, pp. 484-491, Monterey, California, March 1994.

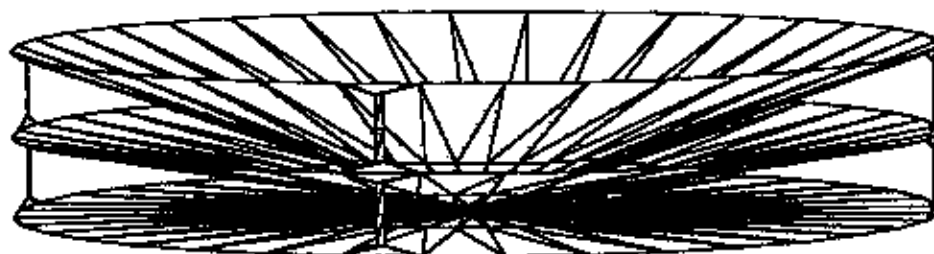
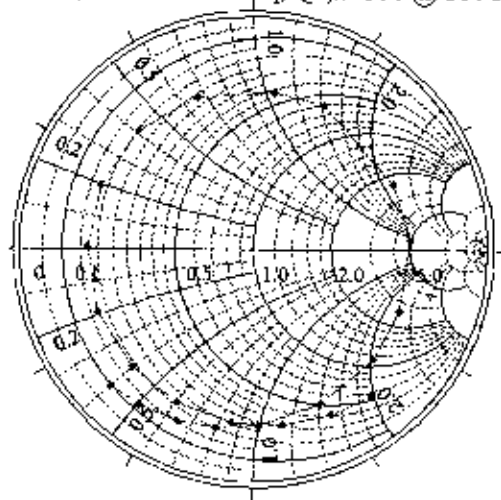


Figure 1. Nested set of two conical radiating resonators with feed region arranged for series connection, four (three visible) inductive strips arranged symmetrically around the periphery of each resonator.

Theta1=90, Theta2=80, Theta3=70 deg
 Radii: Outer=18.75, Inner1,3=0.2, Inner2=0.3 cm
 $X_{s1}=12.6$, $X_{s2}=9.0$ ohms/sq, $Q_{1,2}=100$ @ 100 MHz



Frequency, 89 - 100 MHz in 0.5 MHz steps
 Series Reactance = $0.035 \text{ Frequency (MHz)}$
 Transformer Ratio = 0.236:1

Figure 2. Computed impedance locus for a double resonator (DR) antenna plus a 5.57 nH inductor and a 0.236:1 transformer.

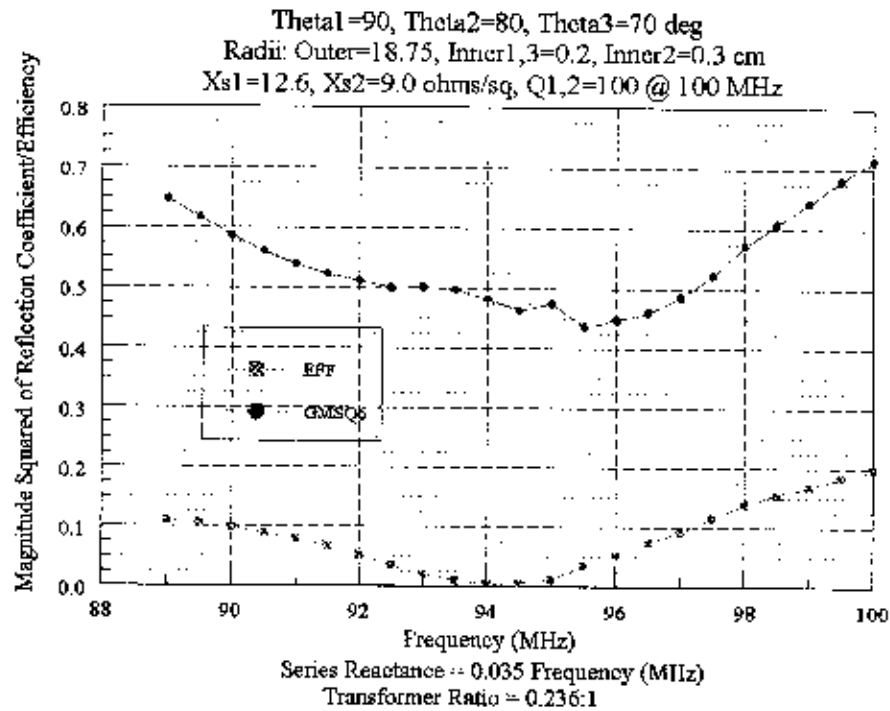


Fig 3. Magnitude squared of reflection coefficient for double resonator antenna with a 5.57 nH inductor and an ideal 0.236:1 transformer. Efficiency values are for antenna only, no losses have been included for the inductor and transformer. When determined on the basis of impedance match alone, the FBW for this antenna is 0.0425 ($Q=23.5$). At 100 MHz, $ka=0.42$.

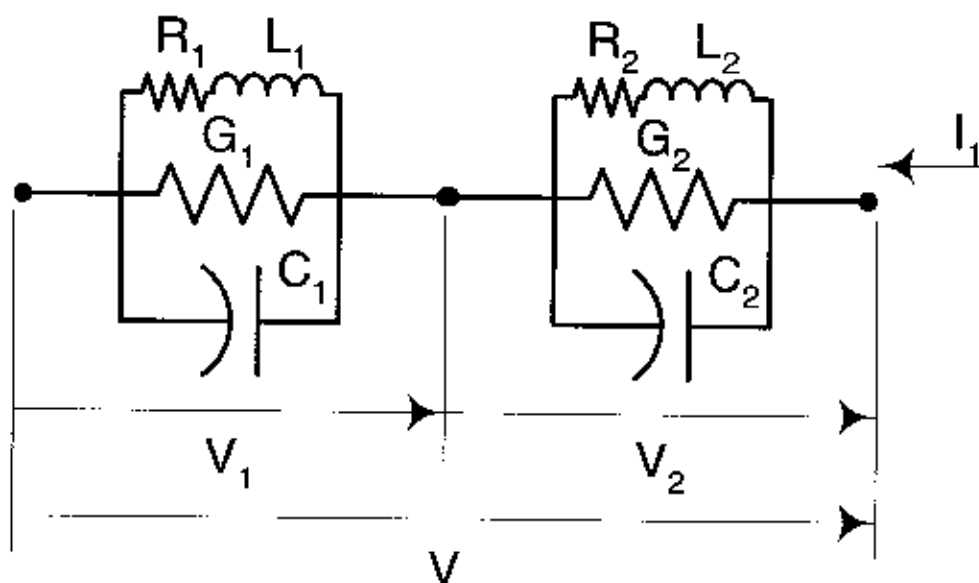


Figure 4. Schematic diagram of two series-connected tank circuits.

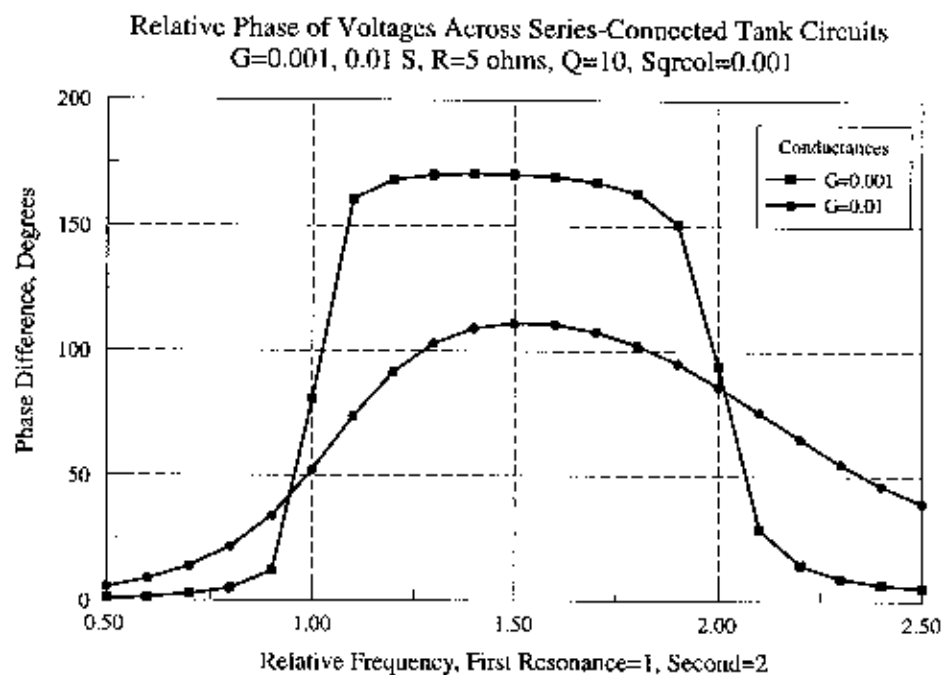
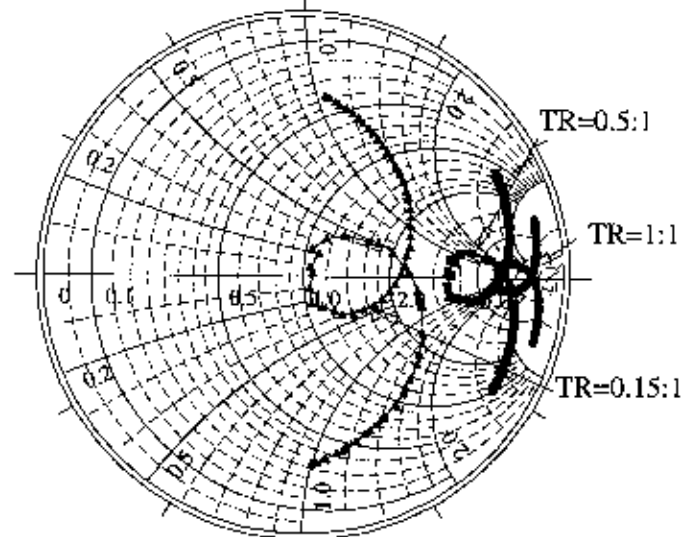


Figure 5. Relative phase of voltages across the series-connected tank circuit with two different values of the shunt conductance.

$\Theta_1=90$, $\Theta_2=80$, $\Theta_3=70$ deg
 Radii: Outer=18.75, Inner1,3=0.2, Inner2=0.3 cm
 $X_{s1}=3.0$, $X_{s2}=1.8$ ohms/sq, $Q_{1,2}=10$ @ 100 MHz



Frequency, 155.0 - 170.0 MHz in 0.2 MHz steps
 Strip angle = 2 deg, $R_1=1.14$, $R_2=0.728$ ohms, $L_1=18.2$, $L_2=11.6$ nH

Figure 6. Computed input impedance for a double-resonator antenna of the type shown in Figure 1, as seen through transformers with impedance ratios of 1:1, 0.5:1 and 0.15:1.

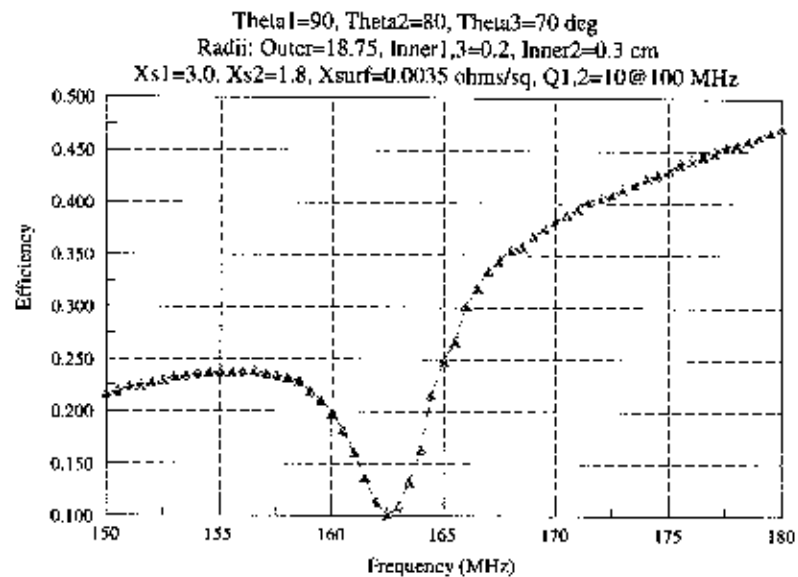


Figure 7. Computed efficiency versus frequency for an antenna similar to that shown in Figure 1, but with the parameters given above.

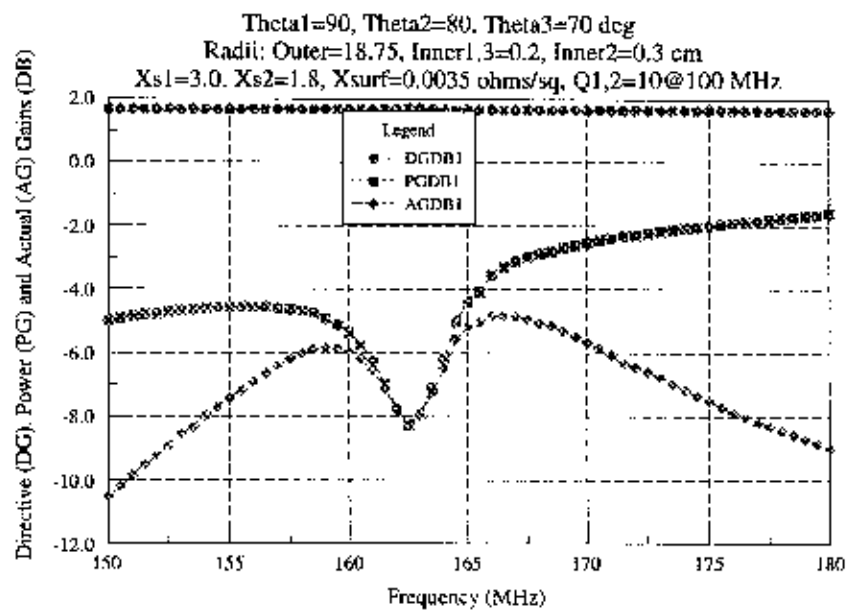


Figure 8. Gains calculated for stacked conical resonator antenna of Figure 7.

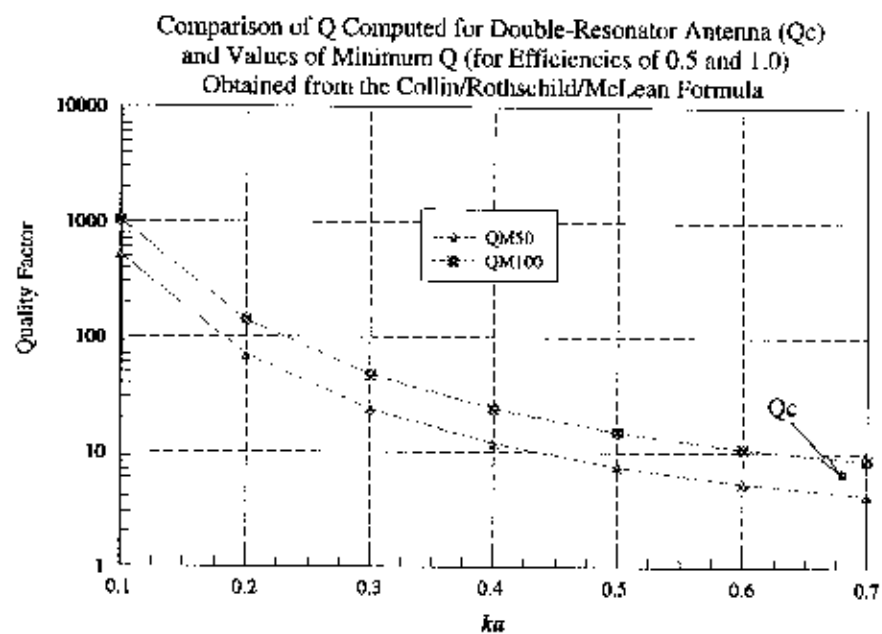


Figure 9. Value of Q computed for double-resonator antenna with average efficiency of about 0.2 and the minimum Q predicted for antennas with efficiencies of 0.5 and 1.0.

Bandwidth Enhancement and Comparison between Square Micro strip Patch Antenna

S. V. Khobragade¹, Dr. S. N. Talbar²,

1. Lecturer, Dept. of Electronics and Tele.

khobragadesanju@indiatimes.com

2. Prof. and head, Dept. of Electronics and Telecomm.

sntalbar@yahoo.com

Dr. Babasaheb Ambedkar Technological University, Lonere, Raigad-402103

Abstract:

Progress in Microstrip antenna surrounded to bandwidth enhancement. Paper demonstrates the comparison of patch parallel to substrate and 45 degree inclined to the substrate edge. Similar comparison will be based on bandwidth enhancement for the same type of antenna by loading technique. Experimentation result conform that the bandwidth is enhanced to the loading methods. Results also compare the parallel and inclined Microstrip antenna to the substrate materials.

1. Micro strip Antenna:

Micro strip antenna consists of a patch of metallization on a grounded substrate. These are low profile, light-weight antennas most suitable for aerospace, manpack and mobile applications. Because of their low power handling capability, these antennas could be used with transmitter and receiver applications. Micro strip antenna has matured considerably over the last 30 years and many of their limitation have been overcome. These antennas relates to the progress in bandwidth enhancement, combating surface wave effects, development of compact antennas, active antennas and reflect array, and progress in the analysis tools[7].

Major operational disadvantages of the microstrip antenna are their low efficiency, low power, high Q, poor polarization purity, spurious feed radiation and very narrow frequency bandwidth. Bandwidth is typically ranging from 5 to 50 percent [6]. Various techniques have been suggested for bandwidth enhancement. These are include: use of thick substrate with low relative dielectric constant ϵ_r , choice of suitable feeding technique, introduction of coupled modes, impedance matching and resistive loading [7].

The substrate in micro strip antenna is used to support the patch metallization. The dielectric constant of the substrate affects the confinement of fields and reduces radiation if a high value of ϵ_r for the substrate is used. Therefore, substrates with $\epsilon_r \leq 2$ are generally used for broadband micro strip antennas. It is to be noted that the bandwidth increases almost linearly with substrates thickness t , and a higher value of ϵ_r decreases the bandwidth. The confinement of fields can be expressed quantitatively in terms of quality factor Q of the antenna, which is defined as eq. (1) [1, 7].

$$Q = \frac{\omega W_T}{P_T} \quad (1)$$

where W_T is the total energy stored per cycle is the resonant frequency and P_T is the total power loss and ω is resonant frequency. The power loss is attributed to conductor loss (P_c), dielectric loss (P_d), surface wave loss (P_s) and radiation loss (P_r) which is expressed in eq. (2) [1, 4].

$$P_T = P_c + P_d + P_s + P_r \quad (2)$$

In general, radiation loss is dominant for antennas. A lower value ϵ_r and/or a thicker substrate will give rise to an increased fringing field and therefore larger value of a radiated power P_r . Similarly such a substrate will provide a low value of antenna capacitance resulting in a smaller value of energy stored W_T . The combination of higher value of P_r and a lower value of W_T will decrease Q of the antenna. For narrow band micro strip antennas Q is between 40 and 50. The relationship between, VSWR and the fractional bandwidth is given by eq. (3)[1, 5, 7]

$$BW = \frac{(VSWR - 1)}{Q\sqrt{VSWR}} \quad (3)$$

There are three types of substrates normally used for microstrip antennas. These are alumina or high ϵ_r substrates, composite material substrate, and honeycomb material is lightweight, sturdy and low ϵ_r near 1. Composite materials are obtained by adding fiberglass, quartz or ceramic in suitable proportion to the organic or synthetic materials to obtain the desired permittivity and the electrical and mechanical properties. The most commonly used combination is that of PTFE and glass. The resulting substrates have ϵ_r between 2.17 and 2.55. Combination of PTFE and ceramic is used to produce flexible substrates with ϵ_r near 10. These high ϵ_r substrates or alumina are used for miniaturization of micro strip antennas often at the cost of bandwidth. In general bandwidth is inversely proportional to the square root of the dielectric constant of the substrate [7].

2. Use of Chip Resistor Loading Technique:

Recently it has been proposed that [2], by replacing the shorting pin with a chip resistor of low resistance, the required antenna size can be significantly reduced for operating at fixed frequency; moreover, the antenna bandwidth can be greatly enhanced.

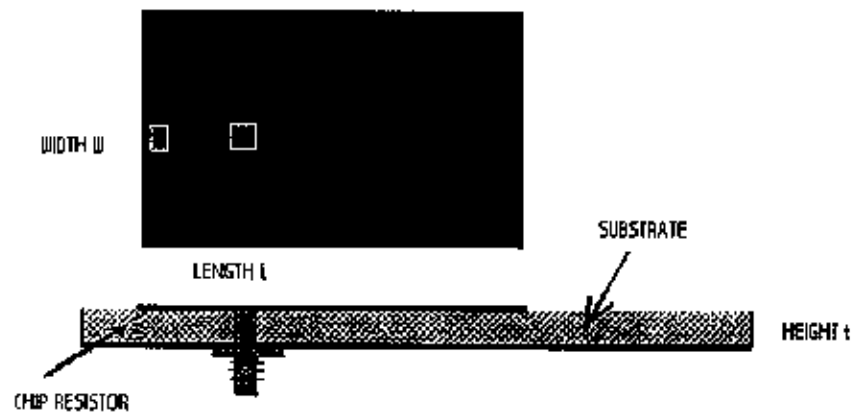


Figure - 1.0 Micro strip antenna with chip resistor

The geometry of a probe fed rectangular microstrip antenna with chip resistor loading is shown in figure 1. The rectangular patch had dimension = length $L \times$ width W and the substrate had a relative permittivity ϵ_r and thickness t . A 1.0 Ohm resistor was selected and placed at about the edge of the patch for maximum resonant frequency reduction. The patch can be exited with a 50 Ohm resistance. The resonant frequency is 710 MHz, which is much lower than that with the shorting pin loading; moreover the 10dB return loss impedance bandwidth is 9.3%, about 4.9 times that of a conventional patch and 6.6 times that

of the short circuited patch. Good matching condition provides a wide impedance bandwidth. For two different spacing say $g = 1\text{mm}$, the patch resonant at 739 MHz and has a bandwidth of 9.3%, while for $g = 2\text{mm}$, the resonant frequency is 742 MHz and the bandwidth is 9.8% [2].

The case shown in Table 1 is for $R=10\Omega$ and $C= 10\text{pF}$. For the maximum frequency reduction, loads are placed around the edge of the circular patch. The corresponding resonant frequency and impedance bandwidth for different spacing angles are listed in Table 1. Table 2 represent by combining chip-resistor and chip-capacitor loading, a significant effect in lowering the resonant frequency of the microstrip antenna with broadband characteristic can be obtained with only a very slight effect on the optimal feed position, which makes the present compact broadband microstrip antenna design very easy to implement. The corresponding fundamental component of the resonant frequency and the impedance bandwidth for circular patch with 32.5mm diameter is given in Table 3 [2]

Table 1: Measured resonant frequency and impedance bandwidth as a function of angle Φ , between the loading chip resistor and chip capacitor for $\epsilon_r = 4.4$, $t = 1.6\text{mm}$, $d = 21.97\text{mm}$, $R = 10\Omega$, $c = 10\text{pF}$ [2].

Φ degree	180	150	120	90	60	30
BW	10.9	10.9	10.6	10.4	10.6	10.9

Table 2: Dependence of the feed position, Resonant frequency, and Impedance Bandwidth on Loading Resistance for the case $\epsilon_r = 4.4$, $t = 1.6\text{mm}$, $d = 6.0\text{mm}$, $c = 1\text{Pf}$ [2].

$R(\Omega)$	100	200	300	400
BW%	5.7	8.5	8.8	3.5
Feed(r_0),mm	0.35	0.30	0.33	0.33

Table 3: Comparison of the antennas for $\epsilon_r = 4.4$, $t = 1.6\text{mm}$, $d = 32.5\text{mm}$, $d = 1\text{mm}$, $c = 0\text{pF}$ [2]

Regular Patch	14.2×3.1	43.8	818	1.7
Shorting-pin-Loaded Patch	23.2×1.8	43.8	818	1.7
$R = 1.0 \text{ Ohm}$	33.6×3.1	45.0	718	6.8

For the Impedance Bandwidth, a significant increase with increasing loading resistance is seen (Table 2 & 3). This behavior is reasonable because the quality factor of the microstrip patch is further decreases with the introduction of larger loading resistance (eq. 1). The enhancement of the bandwidth is seen to be more effective for circular patch with the larger radius as compare to rectangular patch.

3. Square Micro strip Patch Antenna:

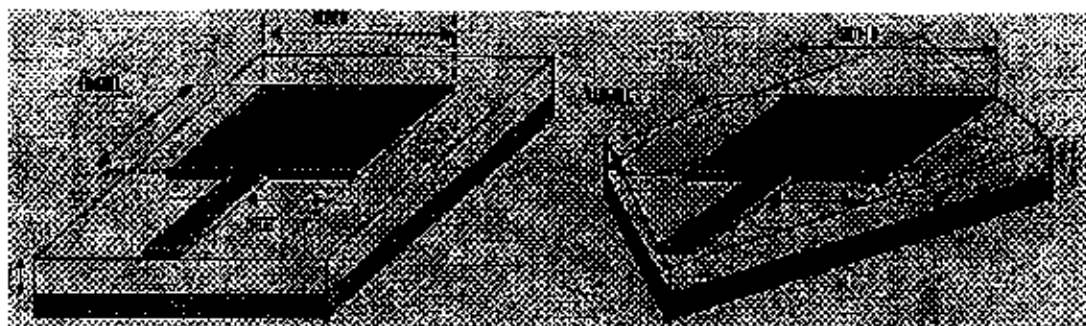


Figure - 2.0 Microstrip patch parallel to substrate edge and inclined to the substrate edge.

3.1 Antenna Dimension:

Because of the fringing effects, electrically the patch of the microstrip antenna looks greater than its physical dimensions. The dimension of the patch along its length have been extended on each end be a distance ΔL , which is a function of the effective dielectric constant ϵ_{eff} and width to height ratio ($\frac{W}{h}$). A very popular and practical approximate relation for the normalized extension of the length of the rectangular patch is given by eq. (4) [1].

$$\frac{\Delta L}{h} = 0.412 \frac{(\epsilon_{\text{reff}} + 0.3) \left(\frac{W}{h} + 0.264 \right)}{(\epsilon_{\text{reff}} - 0.258) \left(\frac{W}{h} + 0.8 \right)} \quad (4)$$

Where effective dielectric constant are referred to as the static values and they are given by equation (5) [1].

$$\epsilon_{\text{reff}} = \frac{\epsilon_r + 1}{2} + \frac{\epsilon_r - 1}{2} \left[1 + 12 \frac{h}{W} \right]^{-1} \quad \text{Where, } \frac{W}{h} > 1 \quad (5)$$

ϵ_r is relative dielectric constant. Similarly conductance is defined as equation (6) [1].

$$G_I = \frac{2P_{\text{rad}}}{|V_o|^2} \quad \text{Also } G_I = \frac{I_1}{120\pi^2} \quad (6)$$

Where, radiation power is $P_{\text{rad}} = \frac{|V_o|^2}{2\pi\eta_o} \int_0^\pi \left[\frac{\sin(\frac{k_o W}{2} \cos \theta)}{\cos \theta} \right]^2 \sin^3 \theta d\theta$

(7)

And $I_1 = \int_0^\pi \left[\frac{\sin(\frac{k_o W}{2} \cos \theta)}{\cos \theta} \right]^2 \sin^3 \theta d\theta$

(8)

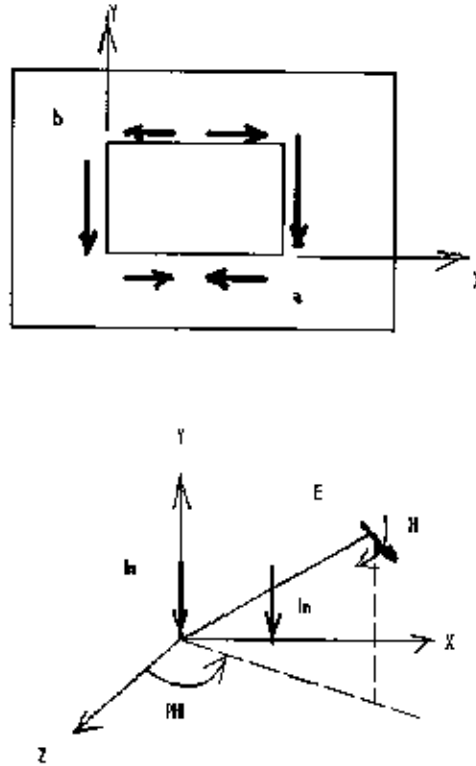


Figure – 3.0 the equivalent free space radiating magnetic-current line of the microstrip antenna.

$$E_z = C_{mn} \cos \frac{n\pi x}{a} \cos \frac{m\pi y}{b} \quad (11)$$

When the substrate thickness h is very small, then the dielectrics layer has only a minor effect on the radiation pattern. If we neglect its effect and use the expression given for E_z (eq. 11) under ideal open circuit boundary condition, then the equivalent magnetic current in the aperture is given by eq.(12)

$$J_{my} = a_z \times n E_z \quad (12)$$

With respect to the figure 3.0 the equivalent free space radiating magnetic – current line sources are [3],

$$\begin{aligned}
& -2hC_{10}, \text{ Along } x = 0, a \\
\text{Im} = & 2hC_{10} \cos \frac{\pi x}{a}, \text{ Along } y = 0 \\
& -2hC_{10} \cos \frac{\pi x}{a}, \text{ Along } y = b
\end{aligned} \tag{13}$$

The two line sources along $y = 0, b$ are oppositely and vary according to $\cos \frac{\pi x}{a}$ and hence produce no radiation in the z direction and relatively little radiation in the other directions.

4. Result and Conclusion:

The experiment is done with the help of rectangular patch parallel to the substrate edge. Chip resistor of 10 Ohm is used for this experiment. The transmitter manually rotates in different angles. The receiver detects antenna current and voltage. Similar experiment is done with the help of rectangular patch 45 degree inclined to the substrate edge. Once again transmitter rotates in same angles and same stages. Final result analyzed for the receiver current. The result compares the patches with and without chip resistor loading technique for parallel and 45 degree inclined to the substrate edge. The detail results are shown in figure 4.0 to figure 13.0.

By observing all the figures (figure 4.0 to 13.0), we come to following conclusions:

- Receiver current is more linear for patches with chip resistor than the patches without chip resistor.
- A characteristic with chip resistor is improved for all the level of the signals at any point.
- Characteristics for 45 degree inclined, is slightly improved as compared to the parallel patch.

With the help of Table 1, 2 and 3, bandwidth enhancement can be observed.

5. Reference:

- [1] Constantine A. Balanis, Antenna Theory Analysis and Design, pp 723-783
second edition, John Wiley and sons, Inc.

- [2] Kin-Lu Wong, Compact and Broadband Micro strip Antenna, pp 55-75
Wiley Series in Microwave and Optical Engineering Kai Chang,
Series Editor, 2002.
- [3] R.E.Collin, Antenna and Radio wave propagation, pp 273-285,
McGraw-Hill International Edition, 1985,
- [4] Annapurna Das & Sisir Das, Microwave Engineering, pp 261-271,
Tata McGraw Hill.
- [5] Richard C. Johnson, Antenna Engineering Handbook, pp 7-6 to 7-16
Third edition, McGraw Hill, 1993.
- [6] D.M. Pozar, "Micro strip Antenna", IEEE Proc., Vol. 80, pp 79-91,
January 1992.
- [7] Ramesh Garg, "Progress in Micro strip Antenna", IETE Technical
Review, Vol.18, Nos. 2 & 3 March – June 2001, pp 85-98.

Analysis of Modified Diamond Dipole for Ultra-Wideband Communication using FDTD Method

Srinivas Desamsetty^{*1}, Edward Lule^{*2}, Tadeusz Babij^{*3} and Kazimierz Siwiak^{§4}

^{*}Dept. of ECE, Florida International University,
University Park, Miami, FL 33199.

[§]TimeDerivative, Inc.,

P.O. Box 772088 Coral Springs, FL 33077

Email: sri_vas27@ieee.org¹, elule001@fiu.edu², babijt@fiu.edu³,
k.siwia@ieee.org⁴

Abstract: Ultra-wideband technology is a technology which uses short pulses rather than semi-continuous sinusoidal waveforms for communication, thereby transmitting the signal energy over a wide frequency band. This paper presents a novel ultra-wideband microstrip antenna: a modified diamond dipole. A diamond dipole consists of two triangular arms and was invented in 1947 [11]. In the modified diamond dipole the straight-line base of the two triangular arms (near the feed) is replaced with an arc. The behavior of the antenna is studied using Finite Difference Time Domain (FDTD) method. Performance is observed by varying radius of curvature of base of triangular arms (for constant flare angle) and by varying flare angle (for constant radius of curvature of base of triangular arms). We observed that by decreasing the radius of curvature (for constant flare angle), more energy is radiated. By increasing the flare angle, it has been observed that the number of resonant frequencies increased, return loss is decreased and performance bandwidth is increased. The impedance bandwidth has reached a maximum for a flare angle of 90 degrees (1.5 GHz to 8 GHz). We present a comparison of diamond dipole and modified diamond dipole. Finally, we show that the modified diamond dipole offers better performance in terms of impedance bandwidth and return loss, than the diamond dipole with zero flare angle.

1. Introduction

Ultra-wideband is a new technology with a lot of potential. This technology uses short pulses whose duration typically ranges from a few picoseconds to nanoseconds as opposed to the traditional sinusoidal signaling technique [1]. The signal occupies a very wide spectrum of bandwidth. Percentage bandwidth (% BW) is an important antenna performance parameter and is defined as

$$\%BW = \frac{2(f_H - f_L)}{(f_H + f_L)} \times 100 \quad (1)$$

where f_H and f_L is the upper and lower frequency limit between which the standing wave ratio of the antenna is less than a pre-selected value. FCC has defined Ultra-wideband as systems, which have a signal bandwidth of 20% or 500 MHz, which ever is smaller, measured at points 10 dB down from the peak in the signal power spectrum [2]. One of the most difficult parts in designing the UWB communication system is the design of the antenna. Lot of work is done in this area and many antennas have been designed both for radar and personal communication purposes [3]-[6], [11]. Because of their broadband characteristics, biconical antennas have been employed for many years in the VHF and UHF frequency ranges [7]. But, because of their massive structure on one side and attractive radiation characteristics on the other, geometrical approximations were made resulting in triangular sheet and bow tie antenna. Diamond dipole antenna and its counterpart, the bow-tie antenna were investigated in [1] and in this paper, the shape of diamond dipole antenna has been modified to obtain a better performance in terms of reflection coefficient and percentage bandwidth. When the straight line base of the triangular arms (touching the feed) of diamond dipole is replaced with a circular arc, a percentage bandwidth of above 100% is achieved. Flare angle and the radius of curvature are selected as the parameters, which can be varied and adjusted to obtain a very wide bandwidth. FDTD method is used to analyze the antenna. XFDTD from Remcom Inc. is used as a simulation tool because of its versatility in obtaining the performance of a structure for a very wide bandwidth with a single simulation run.

2. Geometry

Diamond dipole and modified diamond dipole are shown in Fig. 1. and Fig. 2. respectively. A dielectric substrate $79 \times 54 \times 1.5 \text{ mm}^3$ is selected and the antenna is centered on the substrate. The length of each arm is 38mm. Initially diamond dipole as in [1] is analyzed using XFDTD software. The shape of modified diamond dipole is derived from diamond dipole. The modified diamond dipole is constructed as follows: Initially diamond dipole with selected dimensions (flare angle, length and width of arms) is drawn. Next, the straight line base of triangular arms of diamond dipole is replaced with a circular arc (with selected radius of curvature) in such a way that the straight line base of diamond dipole (if present) forms a tangent to the circular arc. Thus the width becomes a function of flare angle and radius of curvature of the base arc and is generated automatically.

The alteration of radius of curvature of base and the flare angle are shown in Fig. 3. and Fig. 4.

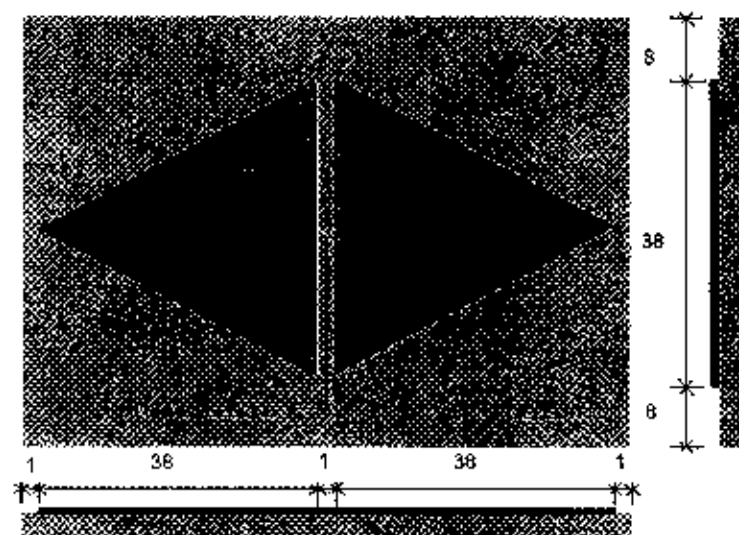


Fig. 1. Diamond Dipole

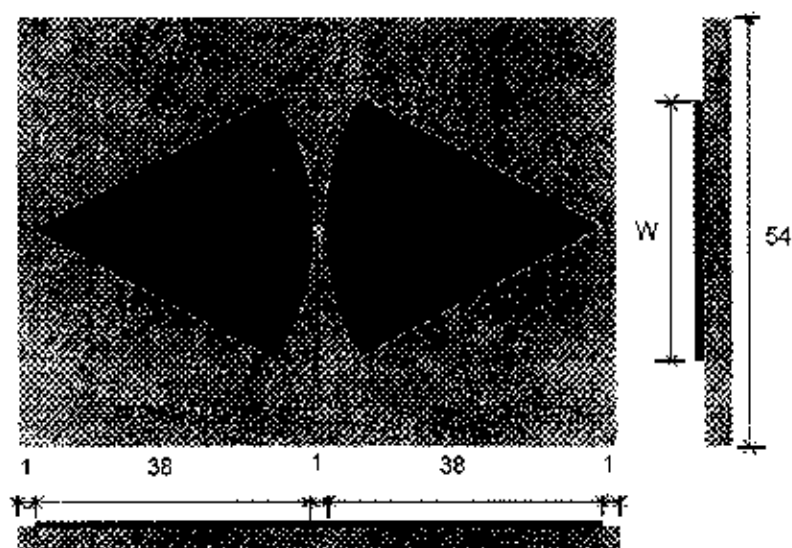


Fig. 2. Modified Diamond Dipole

(all dimensions are in mm)

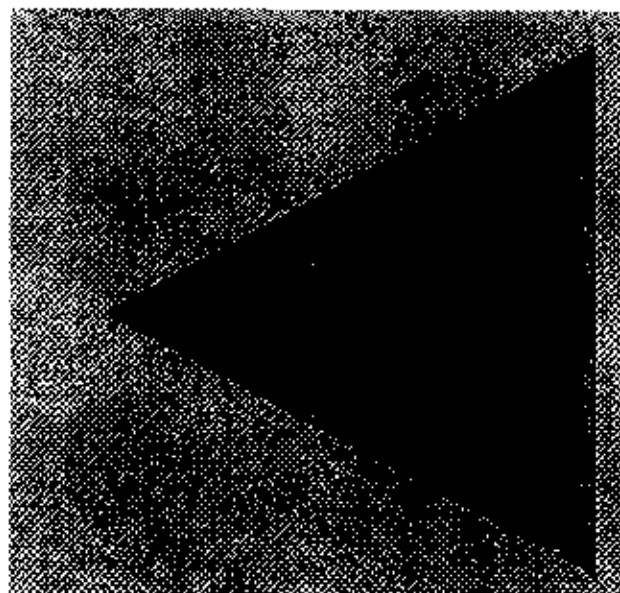


Fig. 3. Radius of curvature alteration of modified diamond dipole

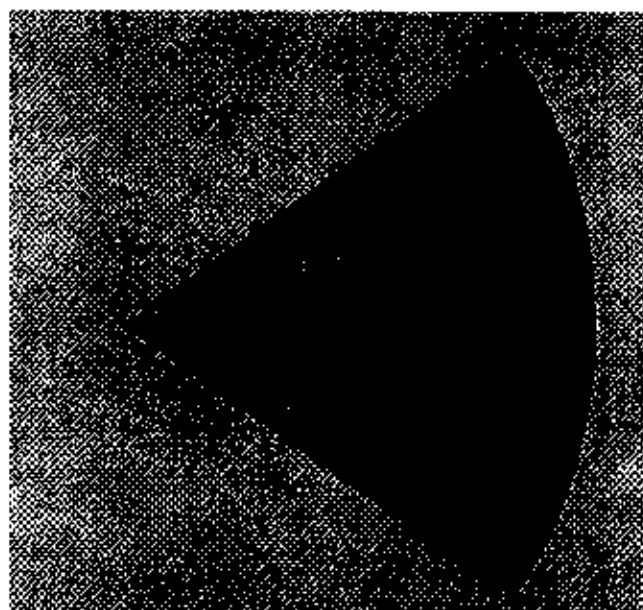


Fig. 4. Flare angle alteration of modified diamond dipole

A cell having dimensions of $\Delta x = \Delta y = 1\text{mm}$, $\Delta z = 0.5\text{mm}$ is chosen following the guidelines outlined in [8][9]. A problem space of $140 \times 100 \times 65$ is chosen and the antenna is centered allowing 15 cells for Liao boundary on all sides of the antenna. A dielectric substrate having a relative permittivity of 4.7 is chosen as dielectric material. A modulated Gaussian pulse having a pulse width of 512 time steps is chosen and the simulation is run for 10000 time steps. The Gaussian pulse used for excitation is shown in time domain in Fig. 5.

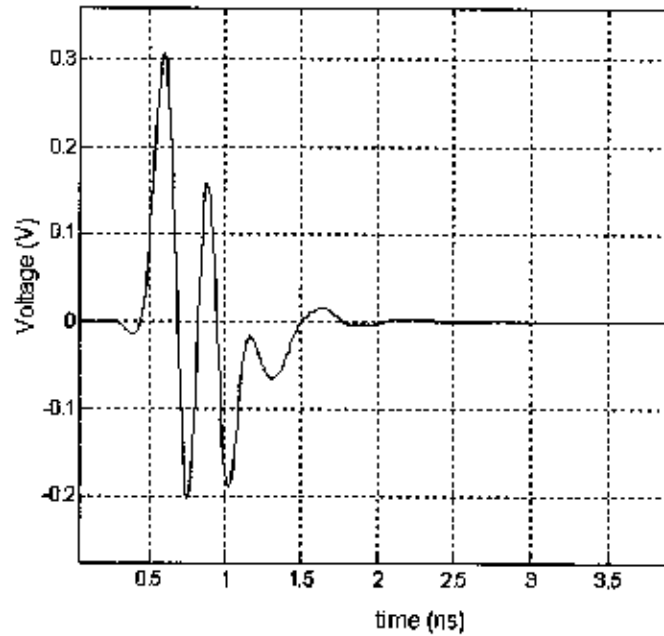


Fig. 5. Time Domain representation of modulated Gaussian pulse used as a source

Table 1
Information about the antenna models

Antenna Model	Semi-flare angle ($\alpha/2$) in degrees	Radius of curvature of base (R) in mm
MDIDO-A1	27	20
MDIDO-A2	27	30
MDIDO-A3	27	40
MDIDO-B1	35	20
MDIDO-B2	35	30
MDIDO-B3	35	40
MDIDO-C1	45	20
MDIDO-C2	45	30
MDIDO-C3	45	40

3. Behavior of modified diamond dipole

Semi-flare angle ($\alpha/2$) and radius of curvature (R) are varied to get nine antenna designs, using which the behavior of modified diamond dipole is analyzed. Semi-flare angles of 27° , 35° , 45° and radius of curvatures of base (of triangular arm) of 20mm, 30mm, 40mm are selected and nine antenna designs are formed and tabulated in Table 1. All parameters like the cell size, source details are kept unchanged for all the antenna models.

Initially, flare angle is kept constant and antennas are analyzed for different radius of curvatures of the base of triangular arms of modified diamond dipole. Hence MDIDO-A1, MDIDO-A2, MDIDO-A3 (Fig. 6.) and MDIDO-B1, MDIDO-B2, MDIDO-B3 (Fig. 7.) and MDIDO-C1, MDIDO-C2, MDIDO-C3 (Fig. 8.) are compared individually for return loss (S11). Next, radius of curvature of the base of triangular arms of modified diamond dipole is kept constant and the flare angle is modified. Hence MDIDO-A1, MDIDO-B1, MDIDO-C1 (Fig. 9.) and MDIDO-A2, MDIDO-B2, MDIDO-C2 (Fig. 10.) and MDIDO-A3, MDIDO-B3, MDIDO-C3 (Fig. 11.) are compared for return loss (S11).

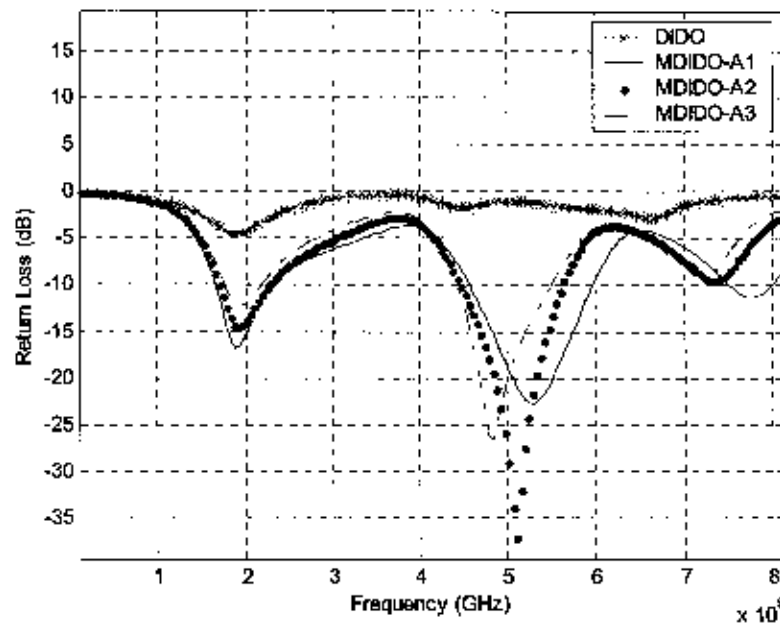


Fig. 6. Return Loss vs. Frequency for antenna models MDIDO-A1, MDIDO-A2, MDIDO-A3

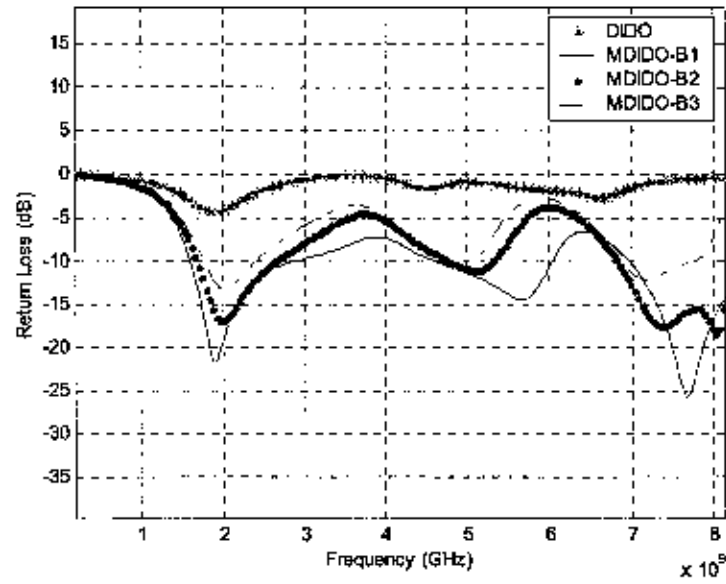


Fig. 7. Return Loss vs. Frequency for antenna models MDIDO-B1, MDIDO-B2, MDIDO-B3

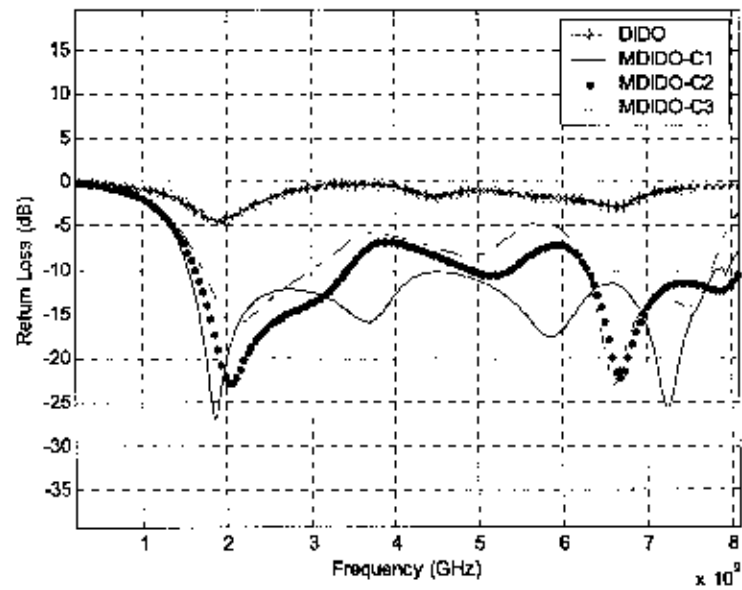


Fig. 8. Return Loss vs. Frequency for antenna models MDIDO-C1, MDIDO-C2, MDIDO-C3

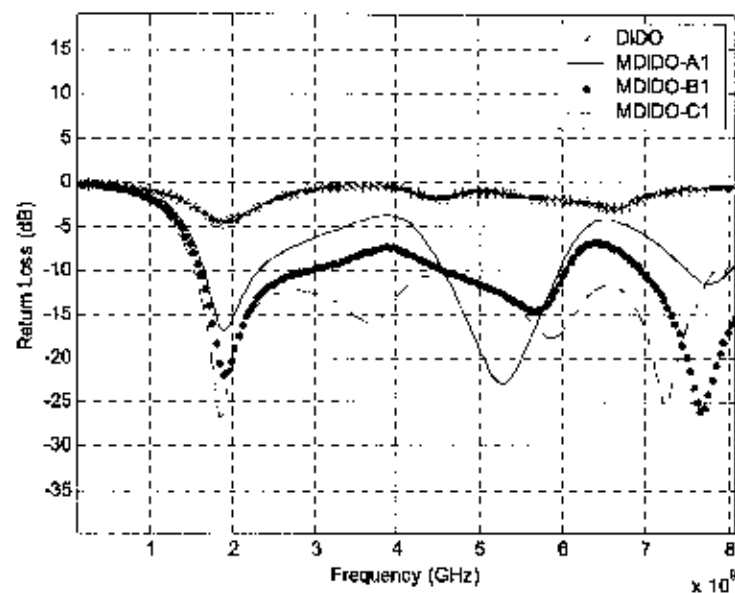


Fig. 9. Return Loss vs. Frequency for antenna models MDIDO-A1, MDIDO-B1, MDIDO-C1

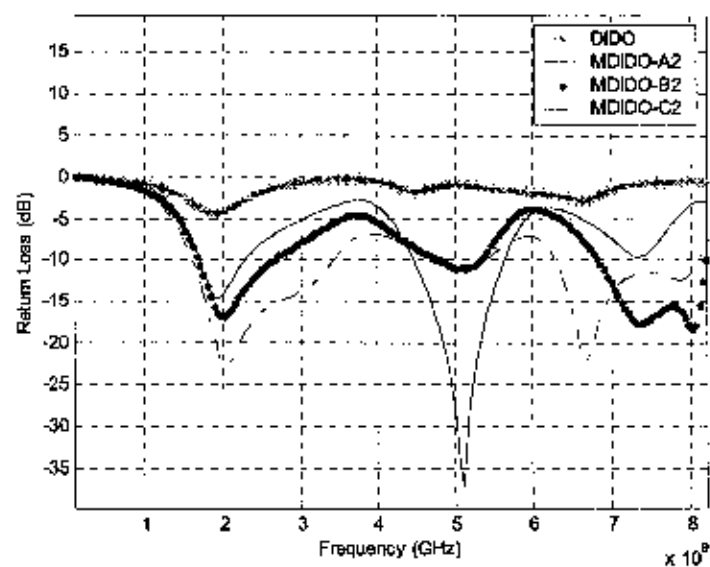


Fig. 10. Return Loss vs. Frequency for antenna models MDIDO-A2, MDIDO-B2, MDIDO-C2

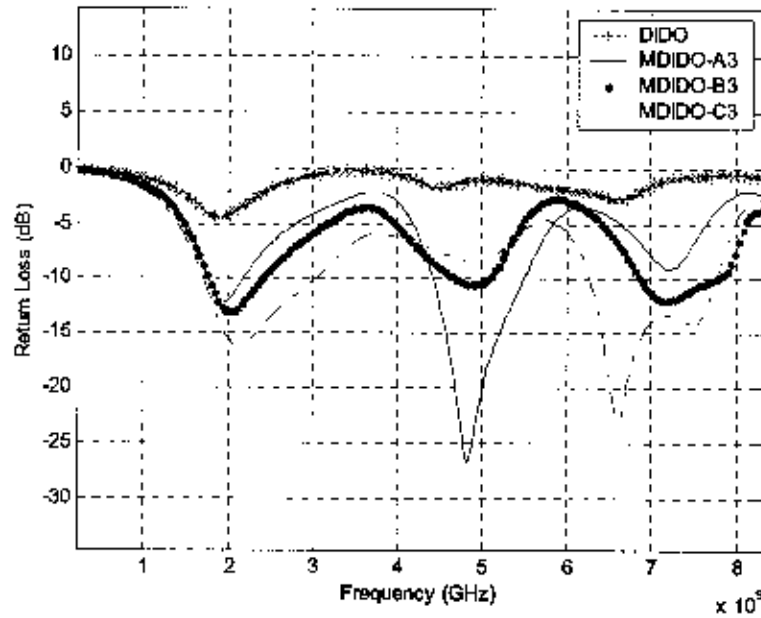


Fig. 11. Return Loss vs. Frequency for antenna models MDIDO-A3, MDIDO-B3, MDIDO-C3

4. Inference from the plots

From Fig. 6., Fig. 7., and Fig. 8. we have seen that for constant flare angle, if the radius of curvature of the base of the triangular arms is increased, there is a slight shift in resonant frequencies towards the left. From Fig. 9., Fig. 10., and Fig. 11. it is seen that for constant radius of curvature of the base of the triangular arm, if the flare angle is increased the number of resonant frequencies increased. Also there is a decrease in return loss with increase in flare angle.

5. Justification

In order to justify the shape modification of diamond dipole, Fig. 12., which is a blend of diamond dipole and modified diamond dipole is considered. This can be explained by taking the current density into account. Consider the portions A and B. In diamond dipole the current density exists on both A and B portions, shown in Fig. 12. In case of modified diamond dipole, portion A is absent (removed). Portion B has to accommodate the entire current present.

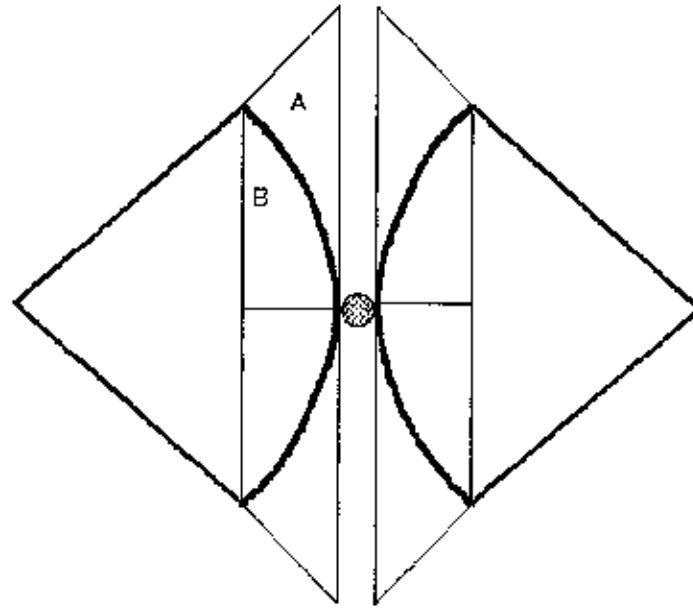


Fig. 12. Justification model-I

Any patch antenna can be modeled as a simple LC resonant circuit [10]. There will be different current densities at different portions of the antenna structure and these L and C values of the resonant circuit depends on the strength of these current densities, and the path and distance they travel on the antenna structure. The introduction of a circular arc base has a varied inductive effect. The modified diamond dipole can be divided into 5 regions as shown in Fig. 13. In region R1, diamond dipole and modified diamond dipole have almost the same size, and hence the current path is same for both the antennas in R1. In regions R2 and R4, modified diamond dipole has smaller area than diamond dipole and hence the current path is reduced (current density is increased). This can be modeled as a reduction in the inductance (shown in Fig. 14.). In regions R3 and R4 modified diamond dipole has a much smaller area than diamond dipole which accounts for much smaller current paths and a still reduced inductance. The equivalent circuits are shown in Fig. 14 . Hence the antenna acts a triple resonant circuit. This is the case for smaller flare angles. But if either the flare angle or the radius of curvature increases to a larger extent, it has the effect of increasing the arc length. In such case the antenna can be modeled as a resonant circuit of more than three resonant frequencies, since with the increase of the flare angle, the arc region increases (Fig. 13.) and hence the antenna can be divided into more number of regions and

hence modeled as an equivalent resonant circuit consisting of more resonant frequencies.

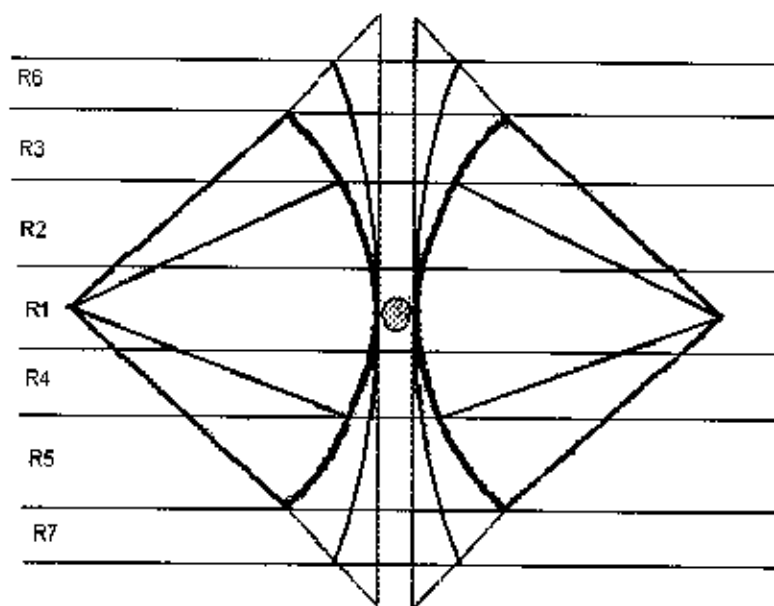
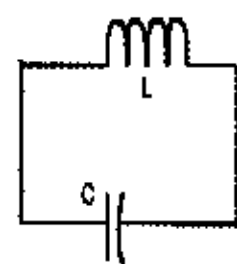
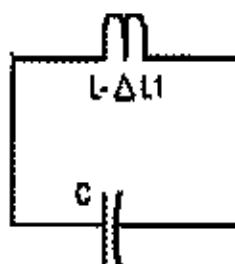


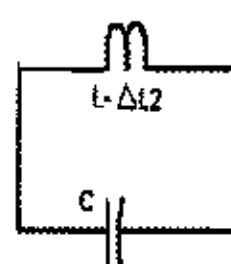
Fig. 13. Justification model-II



Equivalent circuit
of region R1



Equivalent circuit
of regions R2, R4



Equivalent circuit
of regions R3, R5

Fig. 14. Resonant circuits for justification model-II

For constant flare angle, if the radius of curvature of the base of the triangular arm is increased, the effect can be modeled as an increased inductance and decrease in resonant frequency. Hence there is a slight shift in resonant frequencies towards the right. For constant radius of curvature of the base of the triangular arm, if the flare angle is increased, there would be more sections of the antenna structure with different inductive effect. Hence the number of resonant frequencies increases with increase in flare angle.

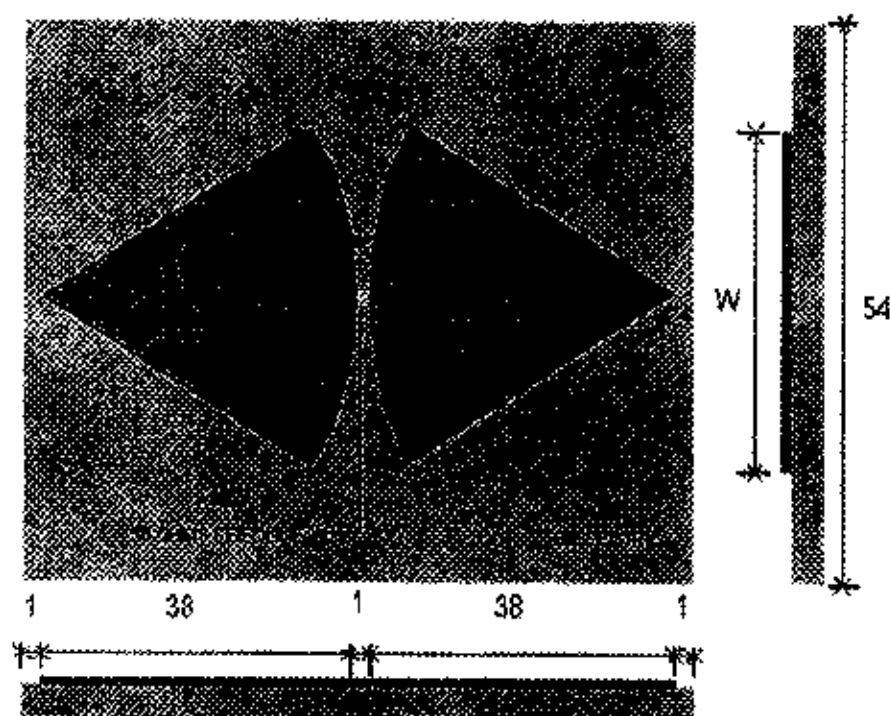


Fig. 15. Coordinate where current density (J_x is measured)

Fig. 16. shows a comparison of current densities measured at a point (60, 60, 33) of DIDO (diamond dipole) and MDIDO-A1. We observe that the current density at the point (60, 60, 33) is higher for modified diamond dipole than for modified diamond dipole. Now, to compare current densities of models having the same flare angle and different radius of curvatures of the base (of arms of modified diamond dipole) we have selected all the antenna models from MDIDO-A1, through MDIDO-C3. Fig. 17., Fig. 18. and Fig.19. shows a comparison of current densities of respective modified diamond dipoles measured at the same point. We observe that current density decreases as the radius of curvature of base increases.

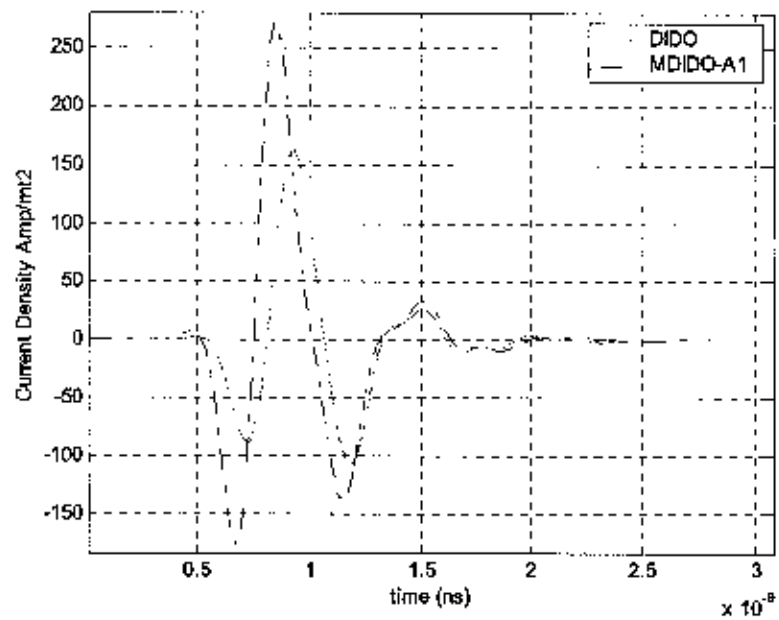


Fig. 16. Current density for DIDO and MDIDO-A1

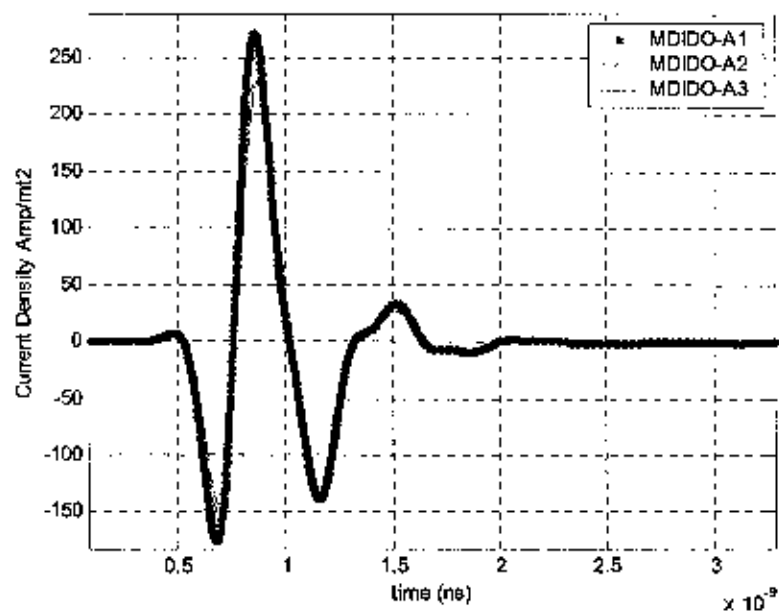


Fig. 17. Current density for MDIDO-A1, MDIDO-A2, MDIDO-A3

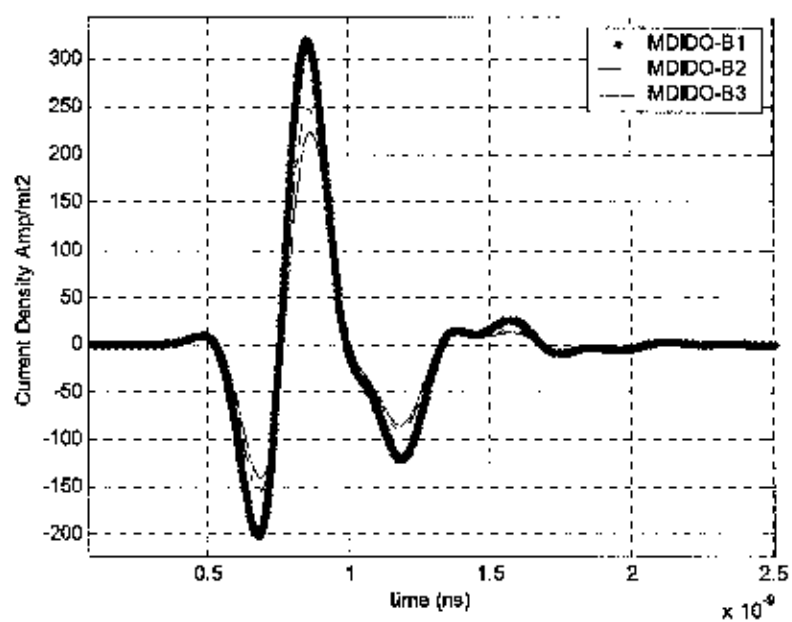


Fig. 18. Current density for MDIDO-B1, MDIDO-B2, MDIDO-B3

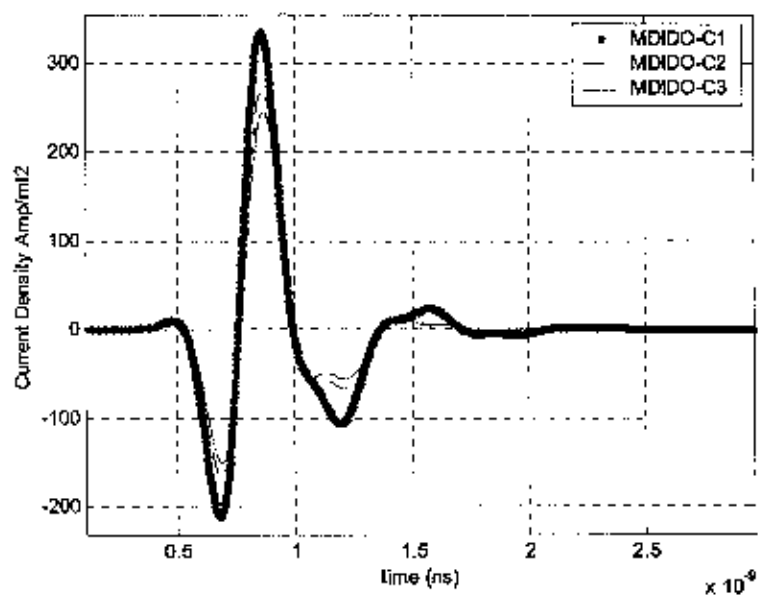


Fig. 19. Current density for MDIDO-C1, MDIDO-C2, MDIDO-C3

Hence the current density agrees well with the explanation given above. It can be said that number of resonant frequencies is a function of Flare angle (or the length of circular arc base) and return loss is a function of radius of curvature of base and Flare angle and lastly the value of resonant frequencies and bandwidth, a function of radius of curvature of base, Flare angle.

Hence radius of curvature of the base of triangular arm of modified diamond dipole has control over the return loss to a great extent (though the flare angle to some extent has control) and flare angle has control over the number of resonant frequencies. Radius of curvature of base also has control over the placement of the frequency band (S_{11} less than -10 dB) to a great extent, though the flare angle also has control over the frequency band, but to a lesser extent.

6. Design

From Fig. 6 through Fig. 8, we see that the return loss decreases as the radius of curvature decreases. The reason behind that is that for small radius of curvatures there is a smoother transition from the arc shaped base to the sides of the triangular arms of modified diamond dipole. Hence for a given flare angle, the smallest radius of curvature of the base gives the lowest return loss. The smallest radius of curvature for a given flare angle is nothing but the radius of In-circle of the triangular arm as shown in Fig. 20.

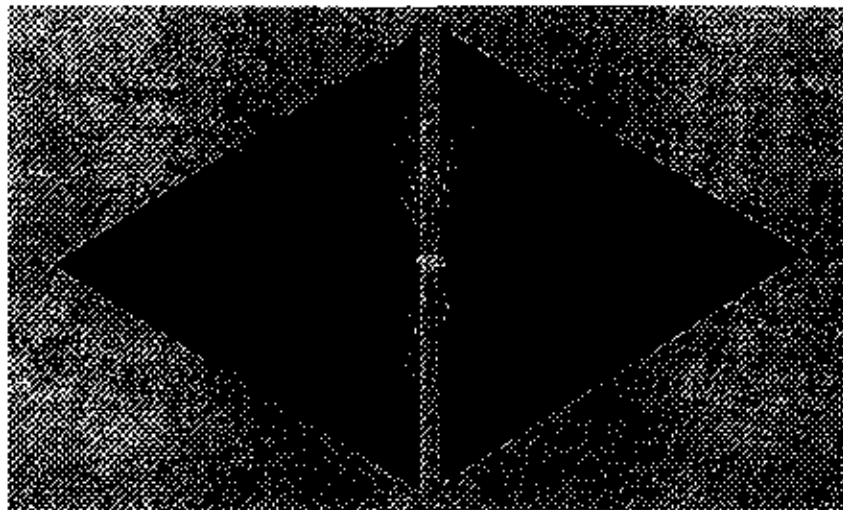


Fig. 20. Modified diamond dipole with base having radius of curvature equal to the radius of the incircle of triangular arm of diamond dipole

Three antenna models with the radius of curvatures of base equal to the radius of in-circles of triangular arms of respective antennas have been developed.

Table 2
Information about the most efficient antenna models in terms of return loss

Antenna Model	Semi-flare angle ($\alpha/2$) in degrees	Radius of curvature (R) in mm
MDIDO-EFF1	27	12
MDIDO-EFF2	35	13
MDIDO-EFF3	45	15

Fig. 21. shows a comparison of return loss of the antenna models shown in table 2. From Fig. 20, the return loss for modified diamond dipole with flare angle 27° has crossed the -20 dB mark (for all the frequencies of resonance) and that for modified diamond dipole with flare angle 35° , return loss has crossed the -15 dB mark (for all the frequencies of resonance) and that for modified diamond dipole with flare angle 45° , the return loss has crossed the -25 dB mark (for almost all the frequencies of resonance). The reason for obtain four resonant frequencies for all the flare angles can be attributed to the length of the base arc. Though the return loss at the frequencies of resonance is large the percentage bandwidth is small.

As the flare angle $\alpha \rightarrow 180$, $R \rightarrow 18\text{mm}$ (twice the length of the arm of modified diamond dipole) and in such case the modified diamond dipole would transform into circular dipole with each arm having a radius of 18mm. This is shown in Fig. 22. a1, b1, a2, b2, c1, c2 are the sides of triangular arms of modified diamond dipole. Fig. 23. shows the return loss of circular dipole. We have selected 90° to be a flare angle of the modified diamond dipole to study. The reason is that, as we have studied that as the radius of curvature increases (or with an increase in the arc length) the return loss increases which happens if we increase the flare angle. Also for very large flare angles ($\alpha \gg 90$) the shape of modified diamond dipole approaches the circular dipole (from Fig. 22.) Hence 90° (which is the angle in a semi circle) is chosen as the angle of interest. Hence the antenna with flare angle 90° , is tested for various radius of curvatures of the base of triangular arms. A value of 20mm as radius of curvature yielded the largest percentage bandwidth of 136.84%. Fig. 24. shows a plot of return loss vs. frequency of modified diamond dipole with 90° flare angle and 20mm radius of curvature of base of the arms.

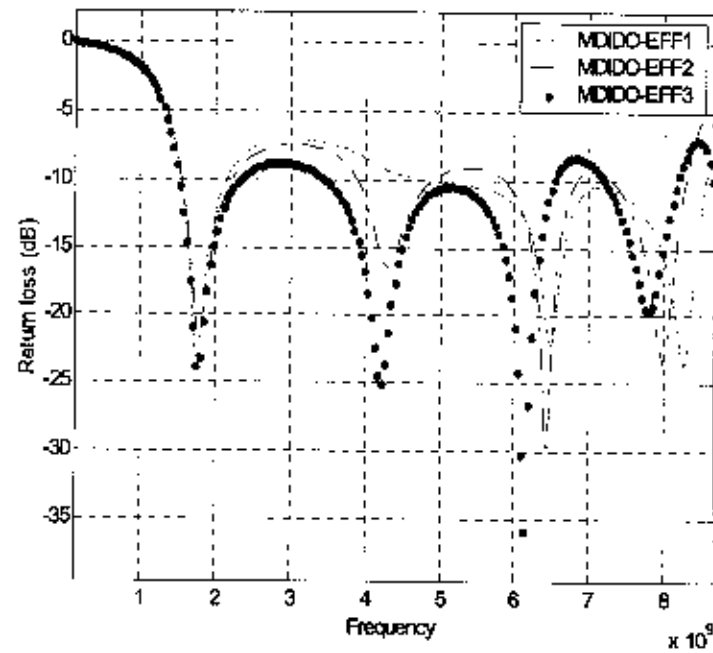


Fig. 21. Comparison of Return Loss vs. Frequency for various antenna models

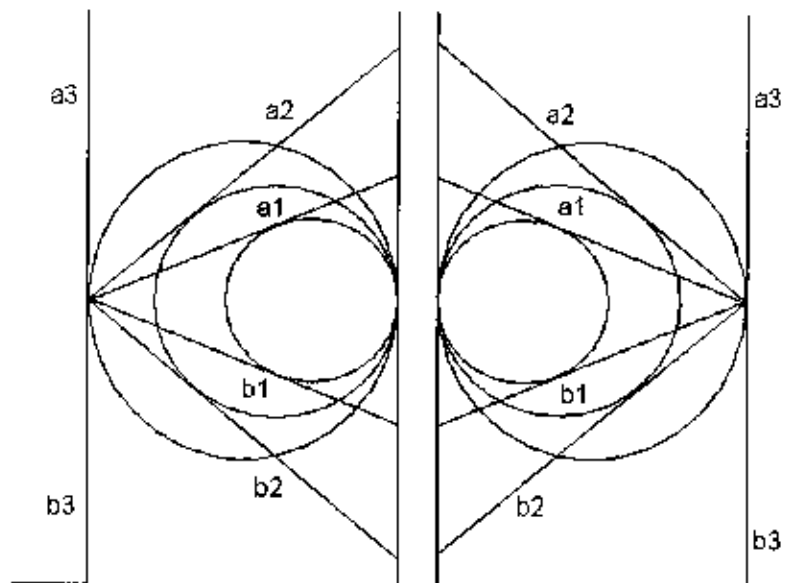


Fig. 22. Modified diamond dipole to circular dipole transformation

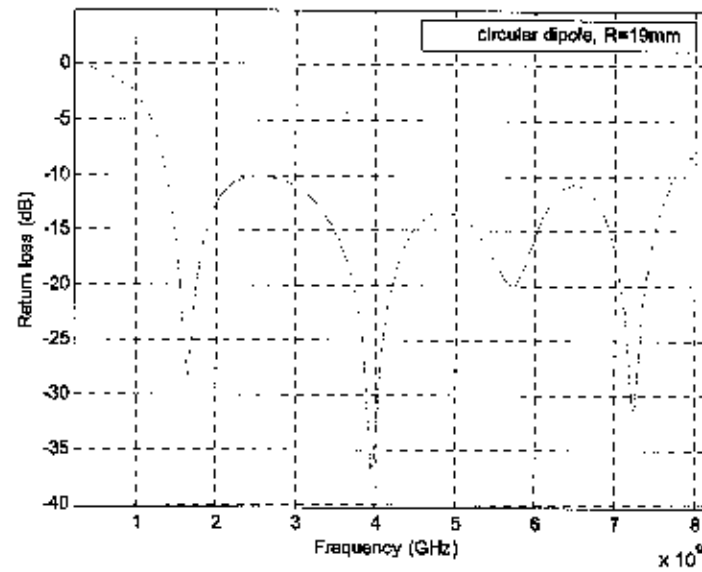


Fig. 23. Return Loss vs. Frequency of a circular dipole of radius $R=19\text{mm}$.

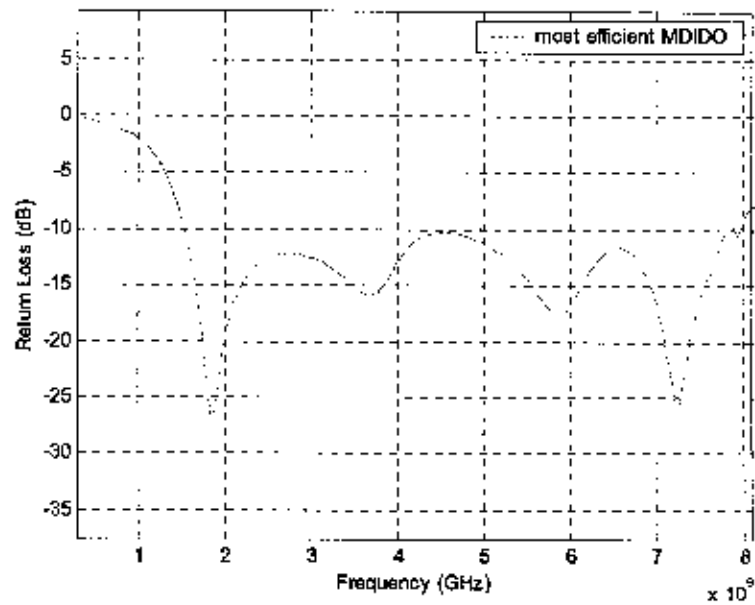


Fig. 24. Return Loss vs. Frequency for most Efficient modified diamond dipole

7. Conclusions

The shape of diamond dipole is altered in such a way that the straight line base of the triangular arms is replaced with a circular arc and the resulted antenna is named the modified diamond dipole. Flare angle and radius of curvature of base of triangular arms of modified diamond dipole are selected as design parameters and a design to obtain a percentage bandwidth of 137% (on a -10dB scale) has been proposed. This percentage bandwidth is very much larger than that obtained for diamond dipole. Hence modified diamond dipole is a better design than diamond dipole for use in a 50 ohm system.

7. References

- [1] K. Garg, "Ultra-wideband Antennas for Personal Communication Devices," M.S.Thesis, Dept. Electrical and Computer Eng., Florida Intl. University, Miami, 2001.
- [2] US 47 CFR Part 15 Ultra-Wideband Operations FCC Report and Order, 22April2002,http://www.fcc.gov/Bureaus/Engineering_Technology/Orders/2002/fcc02048.pdf.
- [3] D.S. Filipovic, M. Nurnberger, and J.L. Volakis, "Ultra-wideband Slot Spiral with Dielectric Loading: Measurements and Simulations", IEEE Antennas and Propagation Society International Symposium, vol. 3, pp. 1536-1539, July 2000.
- [4] W.H. Darden and W.D. Burnside, "An Ultra-Wideband Antenna for Pulsed Applications", Microwave Journal, Vol. 36, pp. 136-143, Sep 1993.
- [5] N. Yuan, J. He, and J. Mao, "A New Type of Ultra-Wideband Conical Antenna Ridged with a Novel Finline Radiator", International Journal of Infrared and Millimeter Waves, Vol. 19, No. 2, pp. 343-347, 1998.
- [6] J.D.S. Langley, P.S. Hall, and P. Newham, "Novel Ultra wide-bandwidth Vivaldi antenna with low crosspolarisation", Electronic Letters, Vol. 29, No. 23, pp. 2004-2005, Nov 1993.
- [7] C. A. Balanis, "Antenna Theory and Design", 3rd Edition, John Wiley & Sons, Inc., 2001.
- [8] K. Kunz and R. J. Lucbbers, "The Finite Difference Time Domain Method for Electromagnetics", CRC Press Inc., 1993.
- [9] Remcom Inc., "User's manual for XFDTD,"Version 5.0.4.7 Remcom Inc., July 1999.
- [10] F. Yang, X. Zhang, X. Ye and Y. R. Samii, "Wide-Band E-Shaped Patch Antennas for Wireless Communications", IEEE Trans. Ant. Propagat., Vol. 49, pp. 1094-1100, July 1993.
- [11] R. W. Masters, "Antenna," U. S. Patent, 2,430,353, November 4, 1947.

The Coaxial Cavity Antenna Implementation in the N-Port (Four and Eight) Feed Configuration

Dr. Tim Holzheimer, P.E.
Raytheon
Tactical Systems
Garland, Texas 75042

Abstract:

A coaxial cavity antenna, developed and patented by Raytheon, exhibits low dispersion over wide field-of-view (FOV) and multiple octaves or Ultra Wideband. This antenna is typically fabricated as a four point feed design, but an N-port, and specifically an eight-port, design is described. Both Finite Element modeled data and test data is presented on 1 to 2 GHz and 2 to 4 GHz versions of the four- and eight-port coaxial cavity antenna, as shown in figure 1. This antenna has essentially a flat phase and amplitude response over a ± 60 degree FOV. The antenna design is scalable over multiple frequency ranges, and antennas have been built covering frequency ranges from 20 MHz to as high as 44 GHz, with bandwidths on the order of four and one-half octaves. Multiple polarizations are still possible, but different mode responses are exhibited for each four-port versus eight-port feed design. The eight-port design is compared to the four-port with respect to the natural polarizations radiated in each case. Natural base polarizations are still dual linear, but coincident modal polarizations can be made the same or different depending on the application. The case of a monopulse tracking feed is illustrated with the presented data. Performance differences are noted for the four- versus eight-port feed designs.

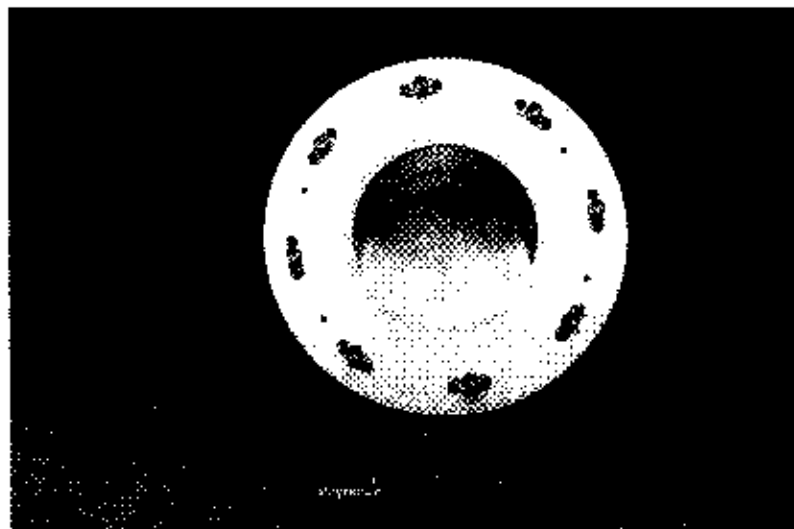


Figure 1. An Eight-Port Fed Raytheon patented, Coaxial Cavity Antenna.

1.0 Introduction:

The Coaxial Cavity antenna is one of numerous antennas that attain multi-octave bandwidth. Other examples include spirals, sinuous, TEM type structures and other variations such as Zig-Zags and Interlogs.[1-3] Extensive work with regard to wide band or wide bandwidth antennas operating over multiple octaves has been performed by numerous researchers such as Mayes, and others. The designs have accomplished multi-octave frequency coverage, typically in the 2 to 18 GHz or 6 to 18 GHz frequency bands. Unlike the Coaxial Cavity antenna these structures are generally traveling wave type structures.[4] However, they are complimentary just like the Coaxial Cavity antenna.

The sub-system perspective desires an antenna covering multiple octaves and having multiple polarization capability, flat amplitude and phase response over field of view and among similar elements, low cross-polarization and high efficiency. The coupling among arrayed elements should be small, and when installed should have high isolation.

The Coaxial Cavity Antenna was initially presented at the Antenna Applications Symposium 2000.[5] This was the first time a published paper had been presented describing the Raytheon patented Coaxial Cavity Antenna, which is shown in figure 2. This antenna is fully scalable over any octave or multi-octave frequency range and has been demonstrated over the 400 MHz to 40 GHz frequency range. This antenna design is a balanced complimentary structure that has N discrete feed points, is light weight, and generally is unloaded, i.e. no dielectrics are introduced into the cavity structure.

The differences are illustrated when these various elements are introduced into systems such as interferometers, direction finding arrays, tracking systems and various types of phased array antennas.[6-7]

The N-port Coaxial cavity antenna is a multiple mode device and this opens up additional applications. These include omni-directional sensing for communications and a potential tracking feed for a large reflector. This complements the apparent out of band operation of the Coaxial Cavity antenna.[8] Additionally, the Coaxial Cavity antenna exhibits low dispersion characteristics that can be used in polarimeters and interferometers.[9]

There are several different types of tracking feeds, which include azimuth and elevation monopulse and sum and delta. These tracking feeds have been previously described.[10] The application of the Coaxial Cavity antenna using an N-port configuration as a tracking feed is described in the following sections of this paper.

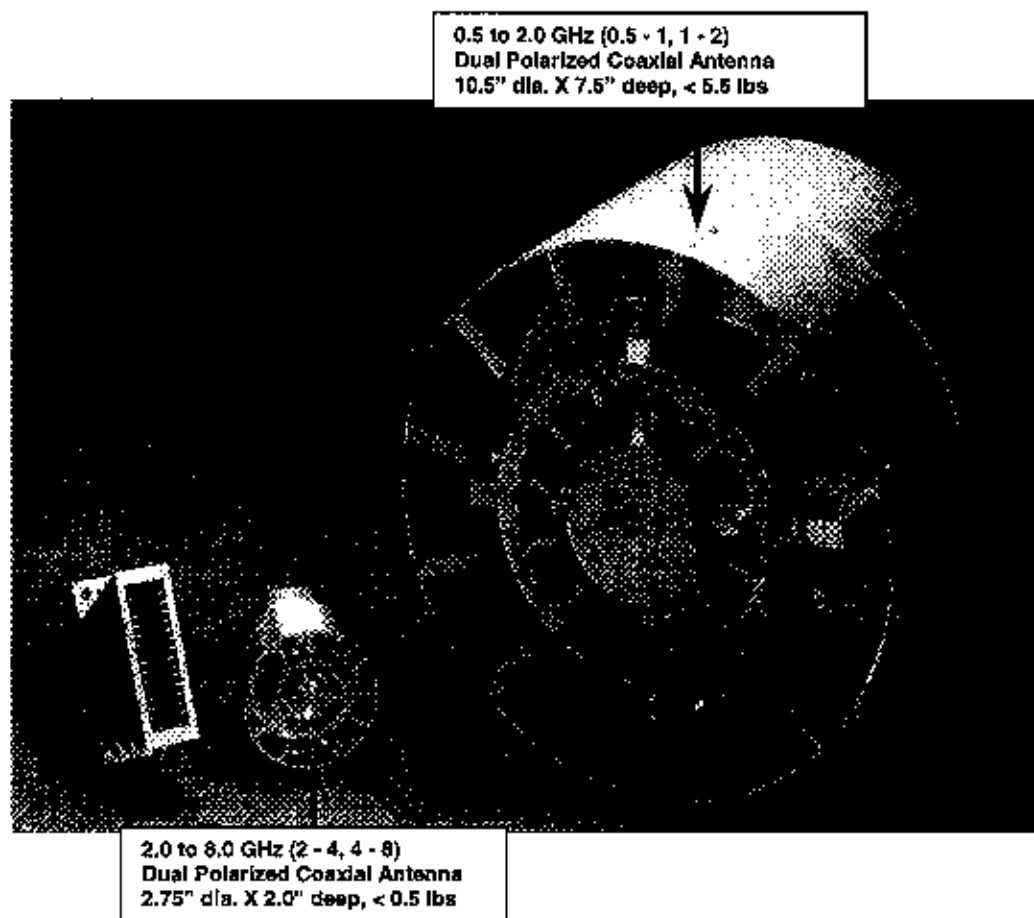


Figure 2. Raytheon patented coaxial cavity antennas illustrating scaling.

2.0 4-Port Fed Coaxial Cavity Antenna:

The Coaxial Cavity antenna is built in four-port configuration for normal use. The use of symmetric feed ports allows for the application of different phasing relationships that result in the formation of different radiation modes. The Modes for the four-port that were investigated are the mode 1 or sum mode and the mode 2 or difference mode. The modes were first verified using an HFSS model of the coaxial cavity antenna.[11] Two different models were generated in order to take advantage of field symmetry and to minimize computation time. These models are illustrated in figures 3 and 4. Figure 3 is the model for the mode 1 where the symmetry of the model is around one feed point, Figure 4 is the model for mode 2 where the symmetry is around two feed points. These simplifications did not impact calculation accuracy but did speed up the computational time.

The resultant model that has all four feeds included is illustrated in figure 5. Theoretical data was then calculated for the frequencies of 2, 3, and 4 GHz. Radiation patterns were calculated for the two principal plane cuts for both mode 1 and mode 2. These happen to coincide with the octave band of operation for the basic 2 to 4 GHz Coaxial Cavity antenna. These results showed excellent mode 1 and mode 2 radiation patterns.

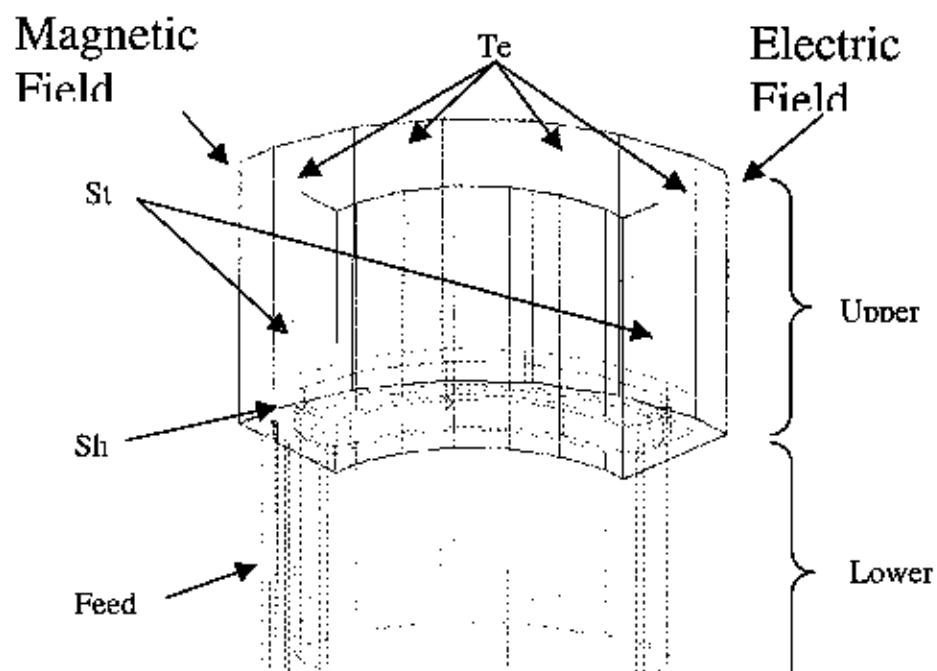


Figure 3: Schematic of base Coax Antenna structure used to compute the mode 1 sum pattern.

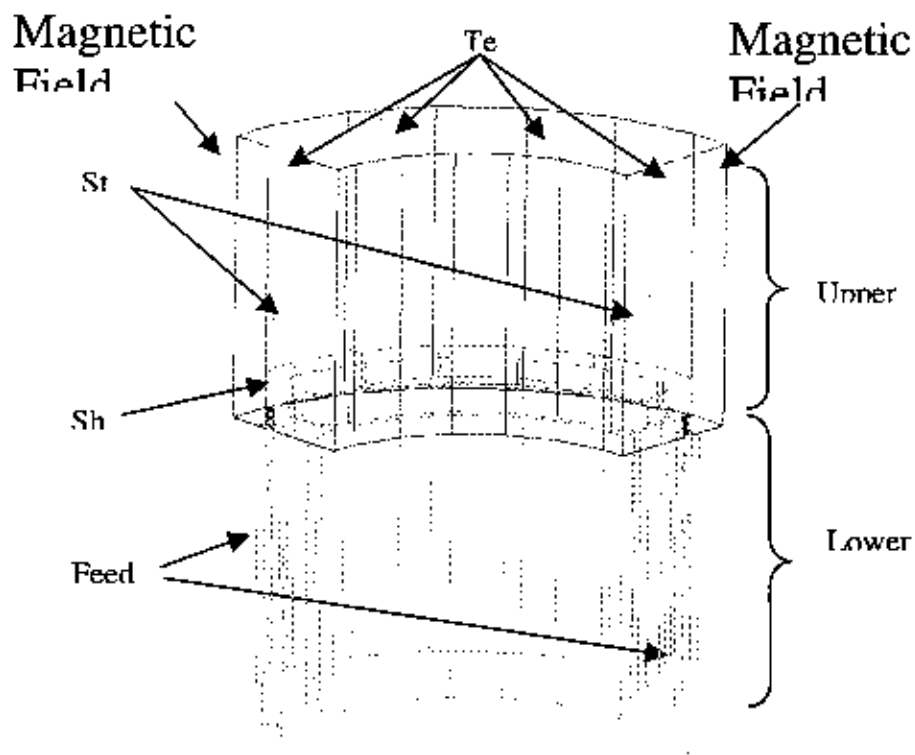


Figure 4: Schematic of base Coax Antenna structure used to compute the mode 2 difference pattern.

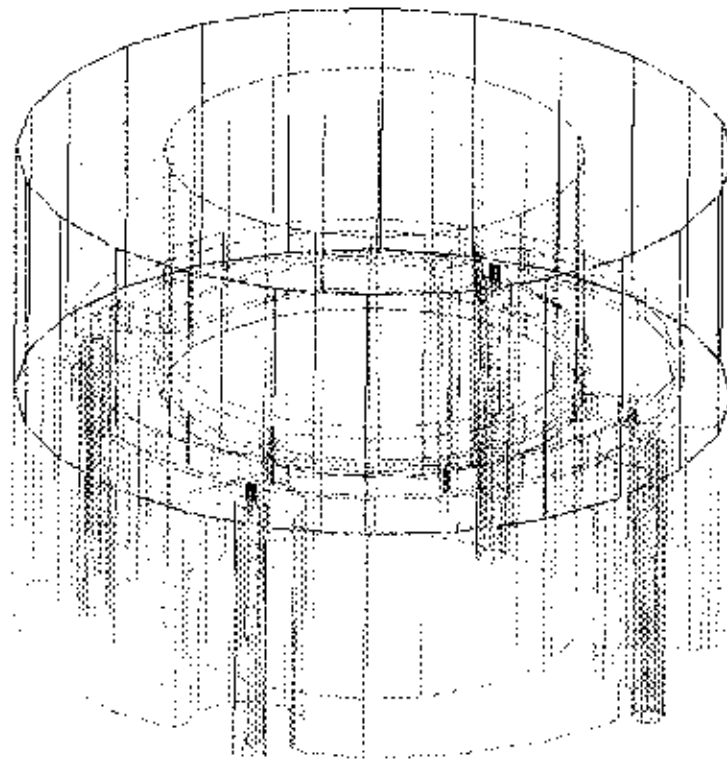


Figure 5: The complete Model of the 4-Port Fed Coaxial Cavity Antenna.

The Port phasing follows the outputs of the 4-port Butler matrix shown in figure 6. This Matrix was also built and used for performing antenna range measurements of the mode 1 and mode 2 radiation patterns. Figure 7 shows the theoretical radiation patterns calculated with HFSS at 2, 3, and 4 GHz for both principal planes. Figure 8 and 9 show the measured radiation patterns for mode 1 and mode 2 for the modeled 2 to 4 GHz coaxial cavity antenna.

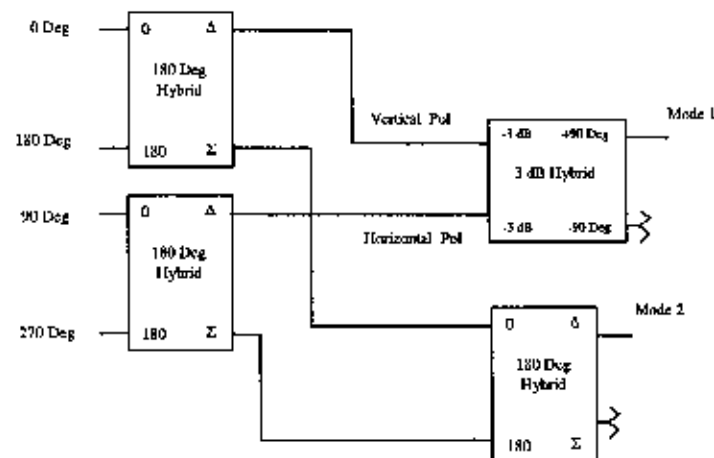


Figure 6. The 4-Port Butler Matrix providing correct phasing for Modeling and Measurements.

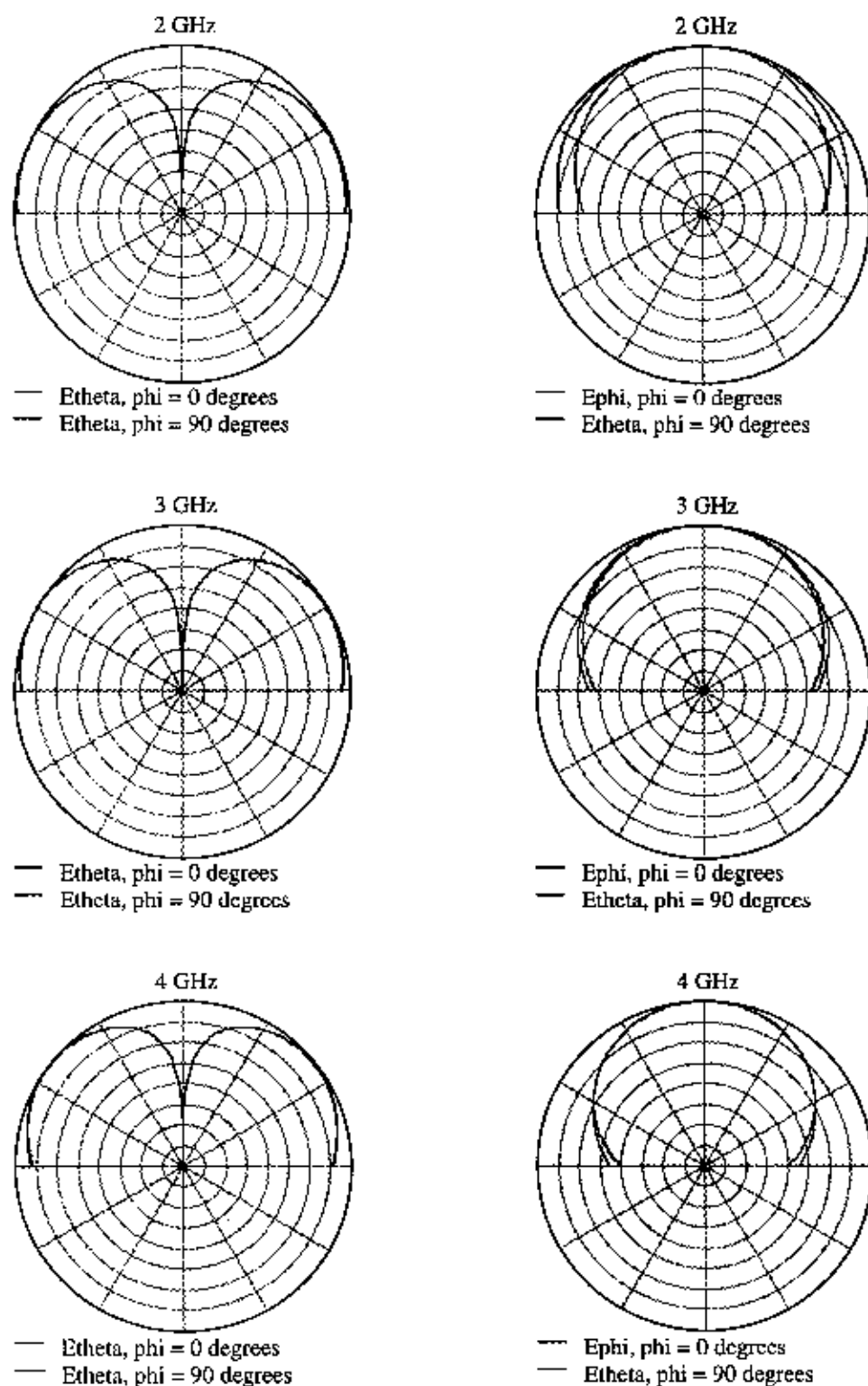
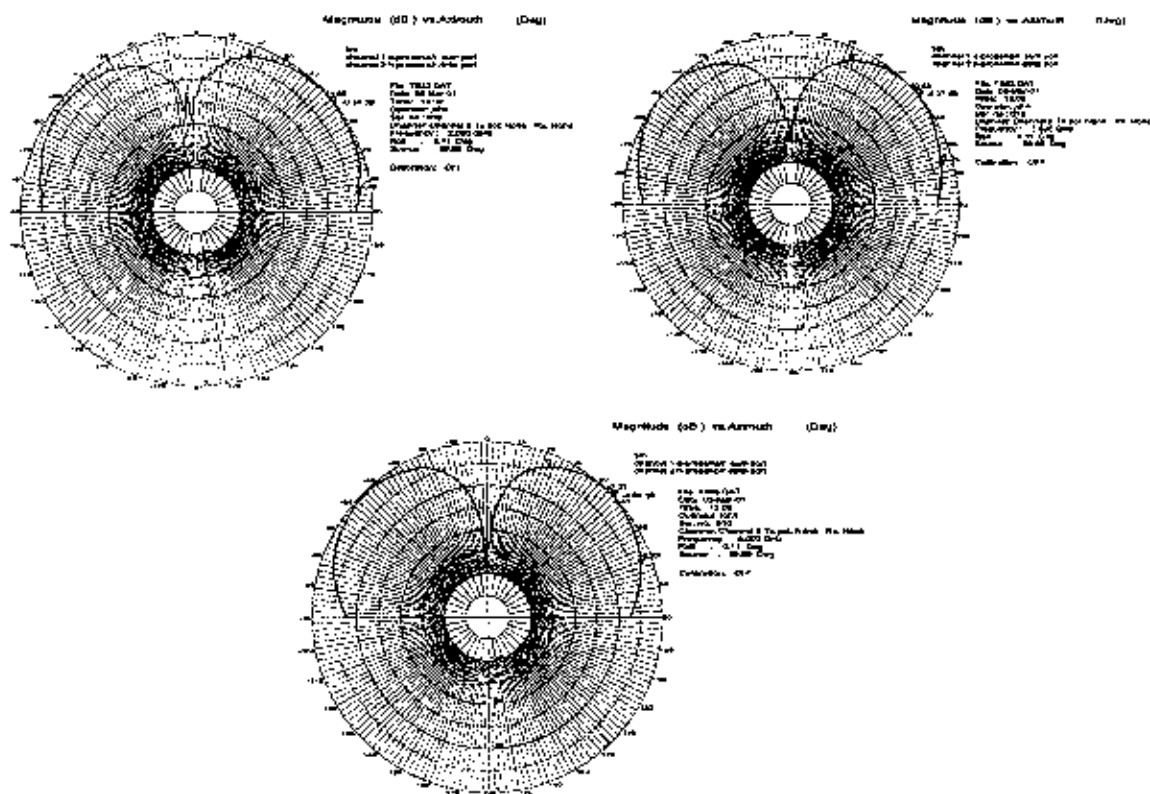
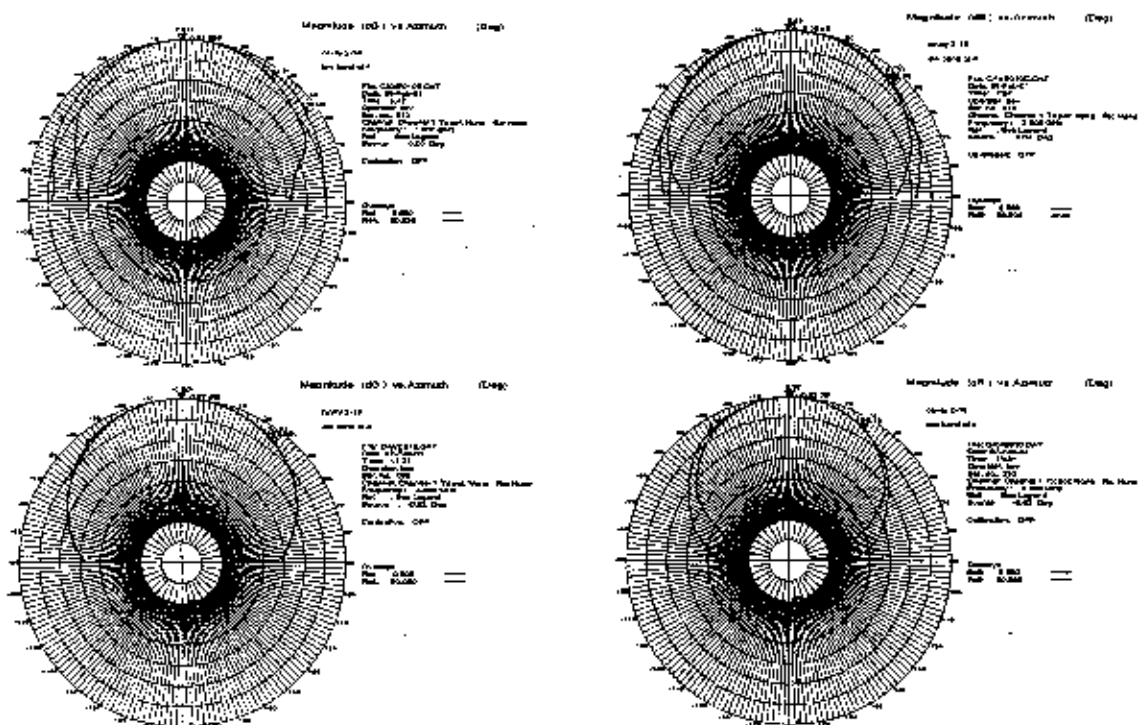


Figure 7: Mode 2 difference patterns (left column) and mode 1 sum patterns (right column) computed with the base Coax Antenna at 2 GHz (top row), 3 GHz (middle row) and 4 GHz (bottom row).



The Polarization is then checked for each mode that was measured. Mode 1 is circularly polarized in this case while mode 2 is linearly polarized. This is illustrated in figure 10 at the frequency of 2 GHz as measured on the antenna range. Measurements were taken with respect to a spinning linear source. Figure 11 shows the same radiation pattern of figure 10, but over the full octave of the 2 to 4 GHz antenna and illustrated in rectangular plot format. The nulls that show up in the mode 1 pattern illustrate the fact that mode 2 is linearly polarized with respect to mode 1 that is circularly polarized. This information can become extremely important for implementation in tracking.

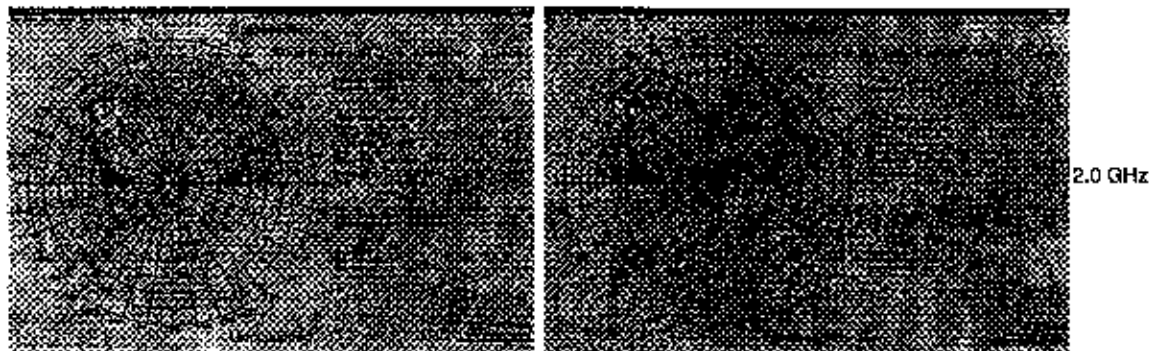


Figure 10. Spinning linear radiation patterns for the principal planes of the 2 to 4 GHz Coaxial Cavity antenna at 2 GHz.

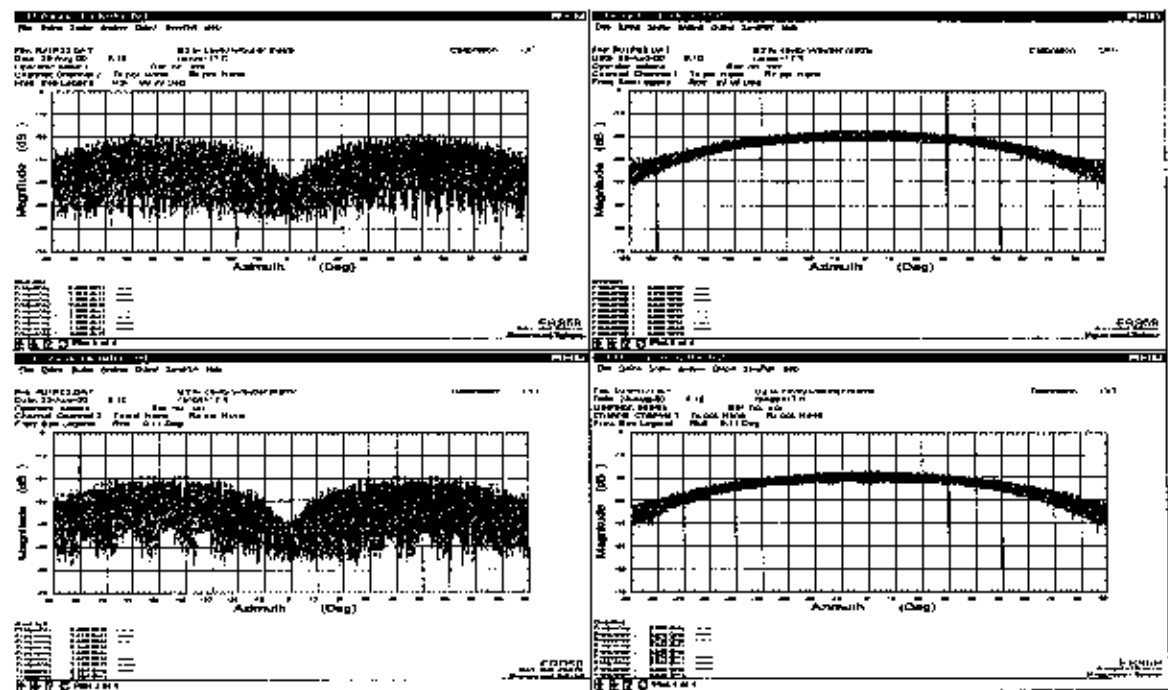


Figure 11. Spinning linear radiation patterns over the 2 to 4 GHz frequency range for the 2 to 4 GHz Coaxial Cavity antenna. The different colors are for different frequencies over the 2 to 4 GHz frequency range.

3.0 8-Port Fed Coaxial Cavity Antenna:

The Coaxial Cavity antenna is then built in the eight-port configuration. The use of symmetric feed ports allows for the application of different phasing relationships that result in formation of different radiation modes. The Modes for the eight-port that were investigated are the mode 1 or sum mode and the mode 2 difference mode. Again, the modes were first verified using an HFSS model of the coaxial cavity antenna. In this case one model was generated. Symmetry was taken advantage of where appropriate to minimize computation time. The model is illustrated in figures 12 and 13. Figure 12 is a three dimensional tilted side view showing the symmetry around the feed points. Figure 13 is a view of the model from the top showing the symmetry in the eight feed ports. These simplifications did not impact calculation accuracy, but did slightly improve the computational time.

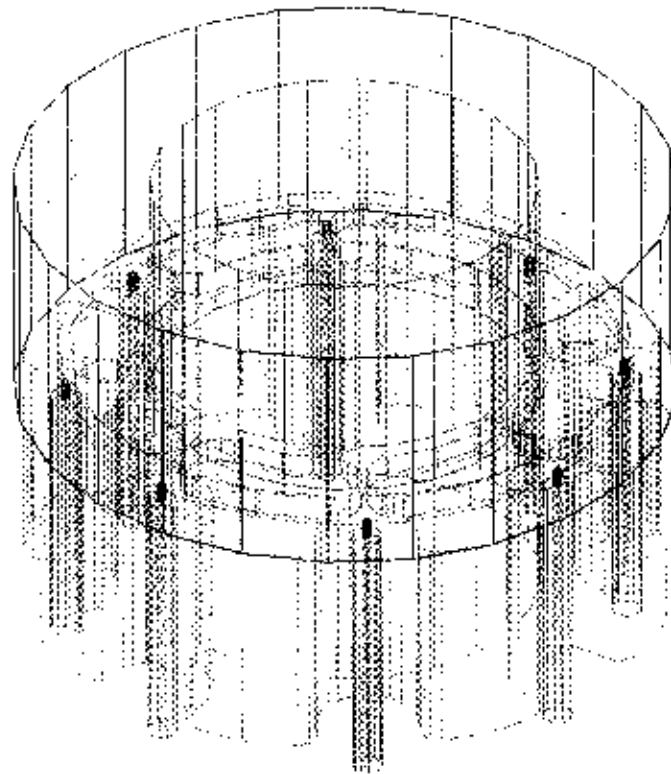


Figure 12. A Three Dimensional tilted side view of the 8-port fed Coaxial Cavity antenna showing the symmetry in the HFSS model.

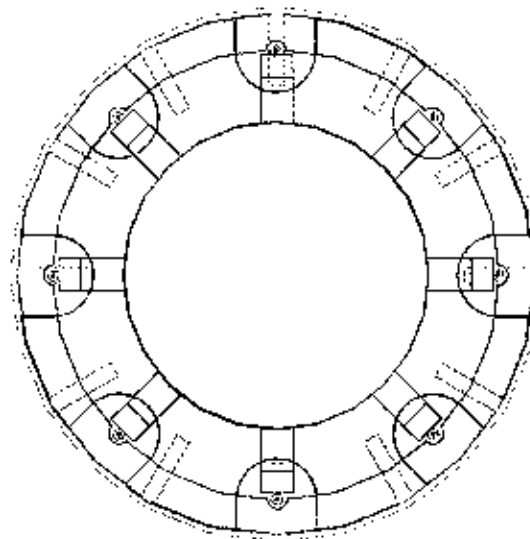


Figure 13. The Top view of the 8-port fed Coaxial Cavity antenna showing the feed port symmetry in the HFSS model.

The Port phasing follows the outputs of the 8-port Butler matrix shown in figure 14. This Matrix was also built and used for performing the antenna range measurements of the mode 1 and mode 2 radiation patterns. Figure 15 shows the theoretical phasing applied to the eight feed ports of the HFSS model.

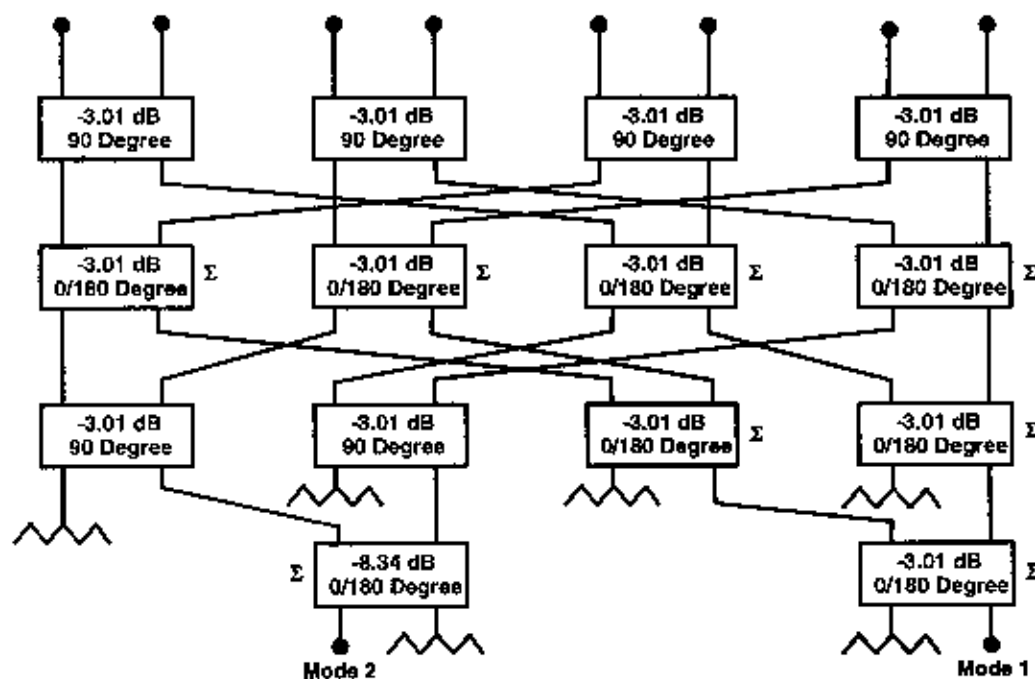


Figure 14. The Eight Port Butler matrix used for the radiation pattern measurements and phasing used for the HFSS model.

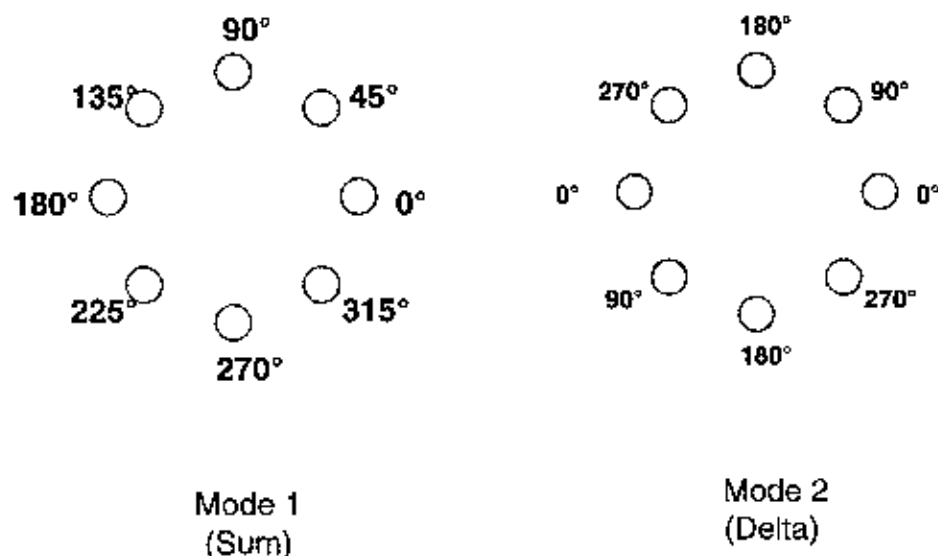


Figure 15. The Phasing applied to the eight feed ports in the HFSS model resulting in the mode 1 and mode 2 radiation patterns.

A Proprietary Finite Element modeling code was used to verify modeling using HFSS. The results are shown in figures 16 and 17 for modes 1 and 2. Co-polarization is the solid line and cross-polarization is the dashed line. This model had a perfect structure that was approximately close to the real antenna and had perfect phasing on the antenna feed ports. The results show excellent mode 1 and mode 2 antenna radiation patterns and very good axial ratio. The axial ratio shows that the mode 1 and mode 2 for the eight-port Coaxial Cavity antenna should have matched polarization responses.

The HFSS results showing mode 1 and mode 2 for the model of the eight port fed Coaxial Cavity antenna is shown in figure 18 at the frequencies of 1.5 and 2 GHz. The theoretical data showed a slight narrowing of the mode 1 radiation pattern at 2 GHz, however, both mode 1 and mode 2 did show the same polarization. Measured data is shown in figures 19 and 20 that verifies the model data at 1.4, 1.5 and 2 GHz. Figure 19 shows the mode 1 and 2 response to linear polarization while figure 20 shows the response to circular polarization.

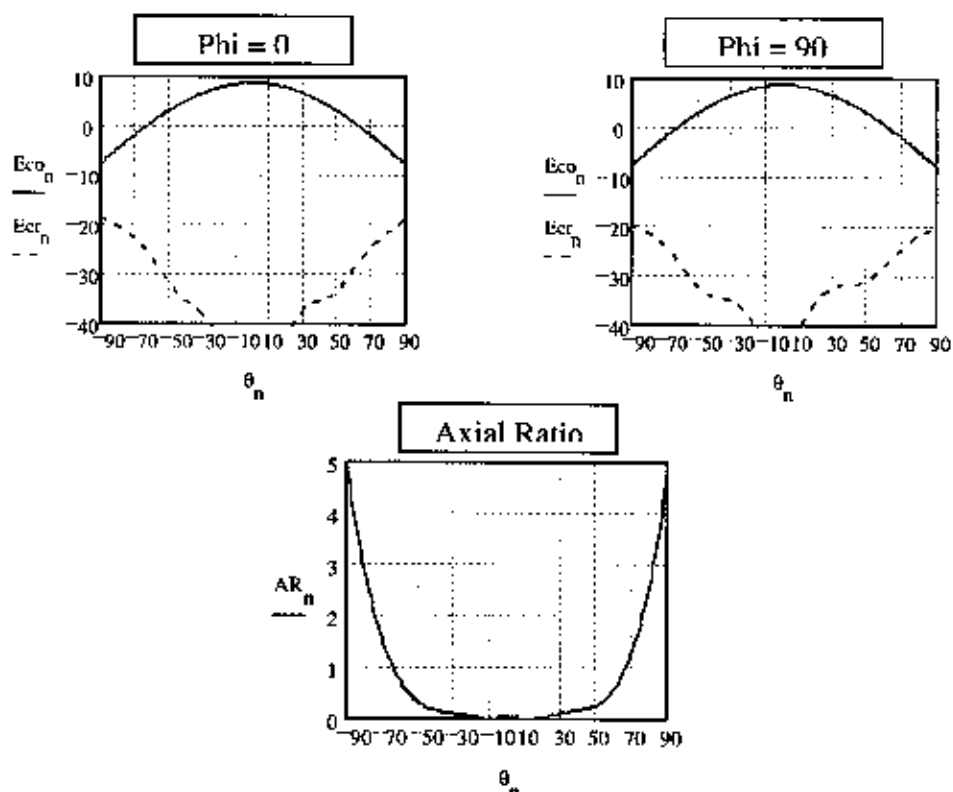


Figure 16. Proprietary Finite Element Code Modeled results for Mode 1 with perfect phasing and perfect structure at 3.5 GHz.

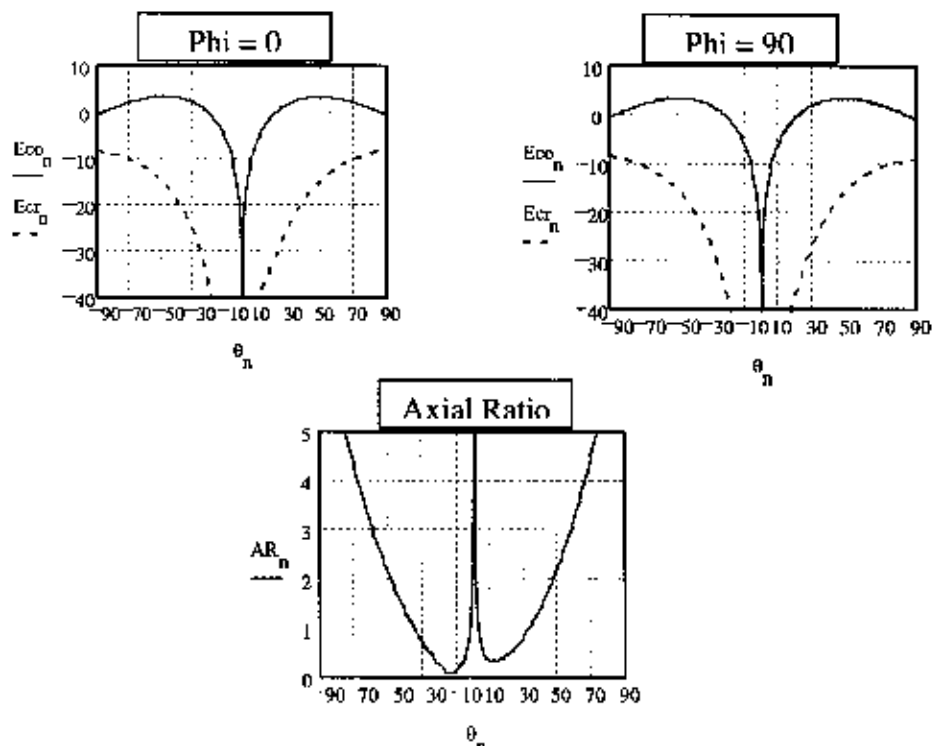


Figure 17. Proprietary Finite Element Code Modeled results for Mode 2 with perfect phasing and perfect structure at 3.5 GHz.

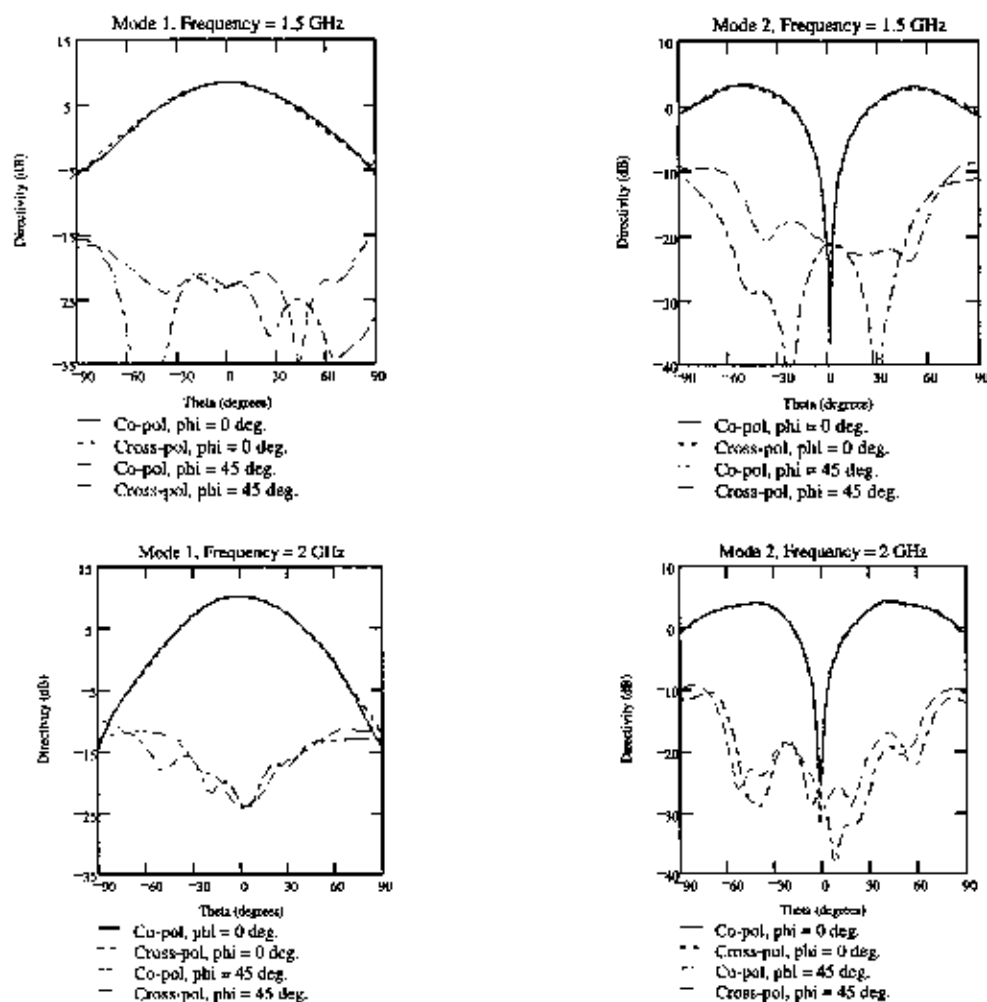


Figure 18. The HFSS Model results for Mode 1 and Mode 2 for the eight-port fed Coaxial Cavity antenna at 1.5 and 2 GHz.

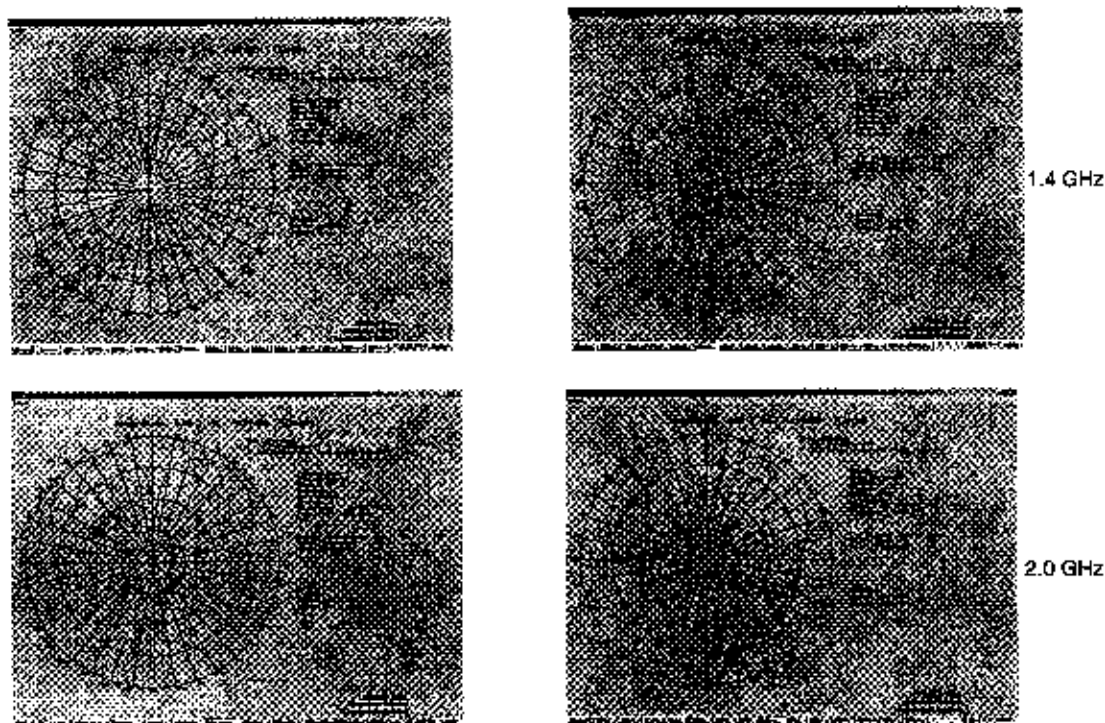


Figure 19. Measured eight-port Coaxial Cavity antenna Linear polarization response for modes 1 and 2.

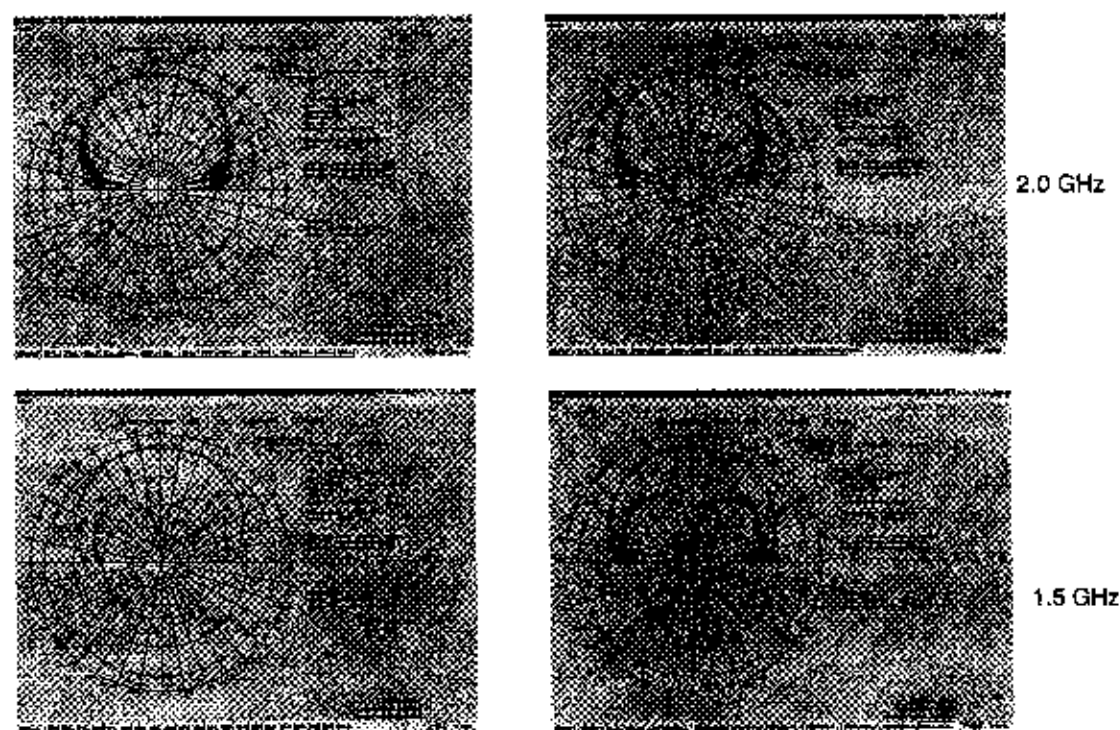


Figure 20. Measured eight-port Coaxial Cavity antenna Circular polarization response for modes 1 and 2.

4.0 8-Port Fed Coaxial Cavity Antenna Measurements Discussion:

Some discrepancies did appear in the measured radiation patterns for the eight-port fed Coaxial cavity antenna. It was discovered that there was an additional 6 to 7 dB of insertion loss in the mode 1 channel over that of the mode 2 channel. In addition, the mode 1 channel of the eight-port butler matrix did not show a 45 degree phase progression. This is shown in figure 21 for the mode 1 or sum channel. The Mode 2 channel was correct in phasing and the measured phasing is shown in figure 22.

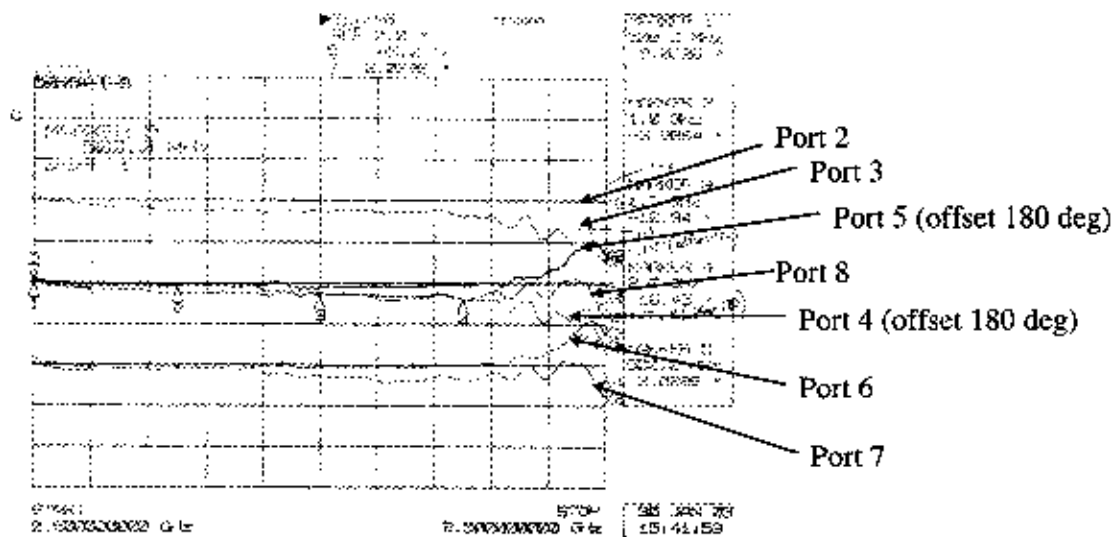


Figure 21. The Mode 1 channel of the eight-port butler matrix showing the problem in the required 45 degree phase progression.

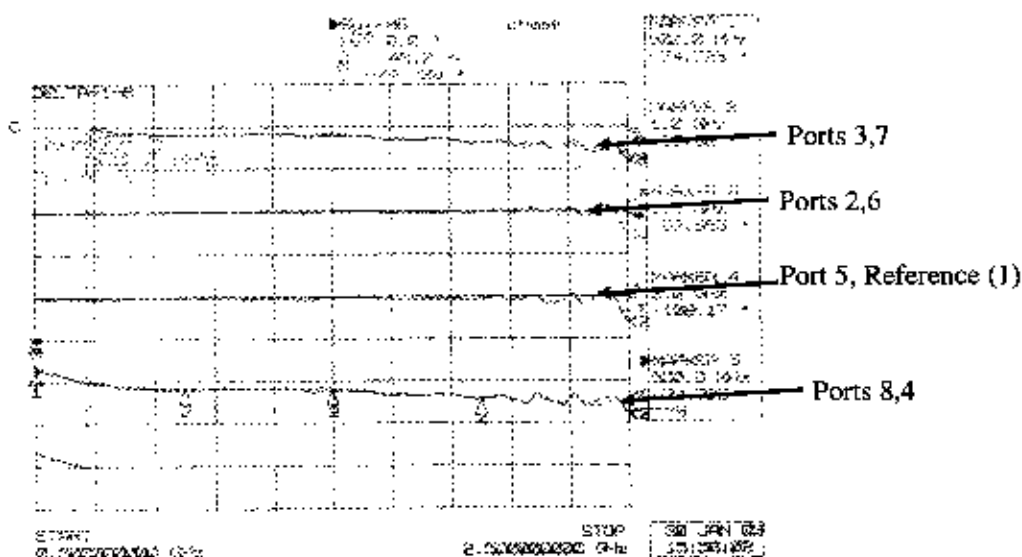


Figure 22. The Mode 2 channel of the eight-port butler matrix showing the correct phase progression.

The incorrect phasing shows up in the measured radiation patterns as skewing of the pattern from radiation normal and lack of symmetry in the radiation patterns. The added insertion loss of the mode 1 channel of the Butler matrix shows up in the difference between the radiation peaks of mode 1 versus mode 2. Mode 1 should be higher than mode 2. In some cases this is reversed and can be attributed to the difference in the insertion loss of the mode 1 channel over frequency.

5.0 Additional Applications:

Typical applications for these types of antennas, regardless of whether they are spirals, horns or coaxial cavity antennas, are in use as interferometer elements, direction finders, radar warning receiver (RWR) antennas, phased array elements, polarimeters and others. The interferometer and the polarimeter place the most stringent requirements on the antennas of the applications listed above. They require flat amplitude and phase over both field of view and frequency of operation. Stated another way, if the antenna can radiate an exact duplicate of an impulse then it will have the desired properties for use as an interferometer and polarimeter antenna element.

The elements used in these systems must be balanced against desired polarizations (usually all-polarization capable), operational frequency range, useful field of view and detection range, which translates into the amount of gain required of the antenna element. Mechanical considerations also exist, such as weight, complexity, and reliability of the design to survive operational vibration, shock, altitude, and/or other environmental factors.

The Capability to feed the Coaxial Cavity antenna in the N-port configuration provides the potential to use this element as a tracking feed. The particular tracking feed requirements will determine whether a 4-port or 8-port fed antenna will suffice for tracking. Losses due to the 4-port versus 8-port must be taken into account as discussed in section 4. Polarization requirements on mode 1 and 2 can dictate the 8-port over the 4-port Coaxial Cavity antenna.

6.0 Conclusions:

The coaxial cavity antenna has been described and data illustrating its low dispersion performance has been presented previously. The coaxial cavity antenna is scaleable over octave, multi-octave and any other desired frequency band. Numerous aperture sizes can be determined based on desired operating frequency bands and desired gain. The self-complimentary structure of the coaxial cavity antenna has been verified by using a four- and eight-element modeformer resulting in very acceptable sum (mode 1) and difference (mode 2) radiation patterns. The most surprising result is that the coaxial cavity antenna appears to have excellent mode 1 and 2 radiation patterns across the octave frequency band for which the Coaxial Cavity antenna was scaled.

The Four-port fed Coaxial Cavity antenna shows excellent mode 1 and mode 2 radiation patterns across its octave frequency band of operation. However, it is shown that although mode 1 is principally circularly polarized, mode 2 is linearly polarized. This would have to be considered in any tracking implementation. The loss in the four port feed network providing the correct port phasing is lower than the loss in the next natural step of eight ports.

The Eight-port fed Coaxial Cavity antenna shows excellent mode 1 and mode 2 radiation patterns across its octave frequency band of operation. Additionally, it is shown that mode 1 and 2 are principally circularly polarized. This was modeled using a proprietary Finite Element modeling code and HFSS. This can provide an easier tracking implementation. However, the loss in the eight-port feed network is greater than the four port. The phase requirements on the eight-port are more stringent, in that phase variation that is acceptable for the four port is not acceptable on the eight port for either mode 1 or 2. This was shown in the phase problem that was discovered in the eight-port butler matrix used for the antenna radiation pattern measurements.

The N-port fed coaxial cavity antenna does exhibit excellent mode 1 and 2 radiation patterns. This was shown with Proprietary Finite Element and HFSS modeling versus measured antenna radiation patterns. The results show that mode 1 and 2 can be supported on any version of the scaled Coaxial Cavity antenna. The only limitation is the size of the structure versus the size of the feeds implemented. Theoretically, any Coaxial Cavity antenna that is N-port fed can be phased to provide the desired mode 1 and 2 and in the desired polarization.

8.0 References:

1. R. G. Corzine and J. A. Mosko, Four-Arm Spirals, Artech House, Norwood, MA, 1990.
2. C. H. Walter, Traveling Wave Antennas, Dover Publications, Inc., New York, 1965.
3. Y. Mushiake, Self-Complimentary Antennas: Principle of Self-Complementary for Constant Impedance, Springer-Verlag, New York, 1996.
4. R. Jaeger, T. Holzheimer, R. Rudd and R. Ackerman, "Coaxial Cavity Antenna," Patent No. 6,356,241, 12 March, 2002.
5. T. R. Holzheimer "A Coaxial Cavity Antenna Exhibiting Low Dispersion Over a Wide Field of View," 2000 Antenna Applications Symposium, Allerton Park, Monticello, Illinois, 20-22 September, 1995, pp. 281-310.
6. T. R. Holzheimer, "An Implementation of a 0.5 to 2.0 GHz Circular 360 Degree Direction Finding Antenna," 1999 Antenna Applications Symposium, Allerton Park, Monticello, Illinois, 17-19 September, 1999, pp. 374-404.
7. T. R. Holzheimer, "High Accuracy DF Antenna Using COTS Hardware," 1995 Antenna Applications Symposium, Allerton Park, Monticello, Illinois, 20-22 September, 1995, pp. 12-1-12-30.
8. T. R. Holzheimer and S. Schneider, "Performance Enhancements with Applications of the Coaxial Cavity Antenna," 2001 Antenna Applications Symposium, Allerton Park, Monticello, Illinois, 19-21, September, 2001, pp. 171-193.
9. T. R. Holzheimer, "The Low Dispersion Coaxial Cavity as an Ultra Wideband Antenna," 2002 IEEE Conference on Ultra Wideband Systems and Technologies, Baltimore, Maryland, 21-23 May, 2002, pp. 333-336.
10. D. R. Rhodes, Introduction to Monopulse, McGraw-Hill Book Company, New York, 1959.
11. High Frequency System Simulator (HFSS), Version 8.2, Ansoft Corporation, Pittsburgh, Pennsylvania, 2002.

INVESTIGATION OF WIDEBAND LOW-PROFILE CANTED ANTENNAS FOR BROADSIDE RADIATION IN APERIODIC ARRAYS

J. T. Bernhard, B. Herting, J. Fladie, D. Chen, and P. E. Mayes
Electromagnetics Laboratory, ECE Department,
University of Illinois at Urbana-Champaign, Urbana, IL 61801
jbernhar@uiuc.edu
<http://antennas.ece.uiuc.edu>

Abstract: In this paper we describe experimental and simulation results for ongoing research on a family of low-profile antennas. These non-resonant canted sectors are intended to be elements for wideband array applications where traditional patch elements cannot meet the bandwidth requirements. To achieve stable impedance over a wide band, the proposed sectors operate in a non-resonant mode wherein the size is greater than one-half wavelength. Since the elements are too large to operate in a periodic array without suffering grating lobe losses, the intention is to employ them in aperiodic (random) arrays. The results presented here illustrate some of the design compromises among the total height of the antenna above the ground plane, achievable impedance bandwidth, and desired radiation characteristics. Current designs show promise with over 40% instantaneous bandwidths that maintain useful broadside radiation performance. The development of related structures that ameliorate the poor broadside radiation characteristics as frequency increases are also discussed.

1. Introduction

Planar microstrip antennas revolutionized phased array technology decades ago. To enable the next levels of array functionality, however, new array elements with expanded capabilities and appropriate array strategies are required to operate over wide frequency bands. While patch antennas have many desirable characteristics, their narrow impedance bandwidths make them unsuitable for wideband applications. Common wideband antennas, on the other hand, promise increased bandwidth, but at the expense of greater physical size and/or reduced gain. This situation captures a fundamental physical limitation analogous to the gain-bandwidth tradeoff in electrical networks. In the case of antennas, this limitation is defined by gain-bandwidth and size. Therefore, in order to increase significantly the bandwidth of low-profile antennas, the effective volume

occupied by the antenna structure must be increased. There are two alternatives: (a) increase the height, or (b) increase the lateral dimensions. These choices have implications not only for antenna design but also attainable array performance.

In this paper, we describe preliminary experimental and simulation results on a family of low-profile antennas intended for wideband applications where traditional periodic patch antenna arrays severely limit performance. The following section briefly discusses the current state of the art in wideband antennas. Section 3 presents the basic geometry of the canted sector antenna and its operational modes. Section 4 provides measurement and simulation data to illustrate some of the tradeoffs between impedance bandwidth and broadside radiation characteristics. Conclusions and directions for future work are included in Section 5.

2. State Of The Art In Wideband Antennas

A number of groups are pursuing wideband and ultra-wideband antenna arrays. The motivation for this research is the ability to use one antenna aperture for a number of applications across a large frequency spectrum, reducing the number of antennas on platforms such as satellites, vehicles, and ships. Most often, variants of TEM horns [1-3] or Vivaldi tapered slot antennas [4-6] are implemented and do provide very wide band operation. However, these antennas are not applicable in many scenarios due to their large thickness, complicated and labor-intensive feed networks, and considerable weight.

An alternative to the bulk of these radiators is a thin, planar design. However, thin profiles usually result in extremely small bandwidths. Several researchers have proposed angled feed lines [7] or sloped substrates [8-10] to achieve wider impedance bandwidths with simple microstrip antennas. However, all of these approaches require complicated and labor-intensive fabrication techniques to achieve the desired out-of-plane structure. Additionally, these microstrip elements are resonant structures, so while their bandwidth is increased with these methods, they can hardly be considered to be "wideband." The goal for this project is to achieve wideband array operation in a low-profile package. The non-resonant canted sector antennas selected to meet this goal are described in the following section.

3. Low-Profile Radiators – Geometry and Operating Modes

A basic canted triangular sector antenna is shown in Figure 1. The antenna is a planar sheet conductor in the shape of an isosceles triangle. Along the base line direction, the conducting sheet is parallel to the nearby ground plane. Along the

orthogonal direction (with the dimension L shown in Figure 1) the element is canted so that the centerline makes a small angle (labeled as α in Figure 1) with the ground plane. The apex containing the centerline is ideally coincident with the ground plane. It is this tip that is connected to the excitation means, so that strict adherence to the triangular geometry is not possible near the feed. In practice, the excitation comes from a coaxial cable with the center conductor of the cable connected to the tip of the element and the shield of the cable connected to the ground plane.

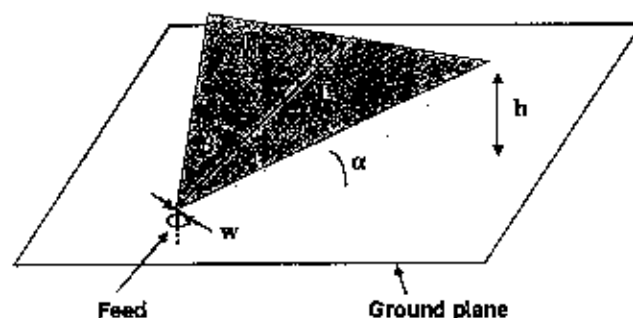


Figure 1. Simple wideband canted sector antenna.

Antenna impedance variation with frequency can often be associated with the mode of operation, which, in turn, is related to the size of the antenna in wavelengths. The performance of antennas that are about one-half wavelength or smaller in dimension is generally governed by resonance. Wider bandwidths are sometimes obtained by utilizing multiple closely spaced resonances. Antennas that are greater than one wavelength in size may be non-resonant. In these cases, operating bandwidth may be determined by pattern and/or gain performance rather than impedance. Antennas of intermediate size may display damped resonances that can be used to enhance the bandwidth. The subject antenna has a low profile and operates in a semi- or non-resonant mode when its length, L , exceeds about two-thirds of a wavelength. Table 1 summarizes the operational modes of the canted sector antennas.

Table 1: Modes of operation of canted sector antennas and their respective impedance bandwidths as a function of size (length) in wavelengths.

Operation Mode	Impedance Bandwidth (%)	Size
Resonant	$\sim 10\%$	$< \lambda/2$
Multi-resonant	$\sim 50\%$	$< \lambda/2$
Semi-resonant	$\sim 2:1$ (71%)	$\sim \lambda$
Non-resonant	$> 2:1^*$	$> \lambda$

*Note that the operating bandwidth may be determined by pattern/directive gain requirements.

4. Measurement and Simulation Results

Several prototype antennas have been fabricated; one of these is pictured in Figure 2. To facilitate measurements, the sizes were chosen so that the low frequency band limit would coincide with the low frequency capability of the test range, 2 GHz.



Figure 2: Photograph of a prototype canted sector antenna. For this particular design, the antenna has the following dimensions: $L = 9.7$ cm, and $\beta = 80^\circ$, with α taking one of three values: 5° , 10° , or 15° .

Simulations of the prototypes use low frequency moment method techniques [11] developed at the Center for Computational Electromagnetics at the University of Illinois. At this time a new geometry generator has been written that provide for variable size patches. The new generator uses smaller patches near the feed, where needed, and increasingly larger patches as distance increases away from the feed. In this way, the number of patches is reduced sufficiently to allow the analysis of antennas with small features near the feed. While this is important for accurate determination of the input impedance, it is less important for the calculations of patterns. However, the reduction in number of patches also

accelerates the computation of radiation patterns. We are also developing a computational code using time domain integral equations [12] that not only handles the small feed region around the antenna tip but also enables large array simulations using the elements.

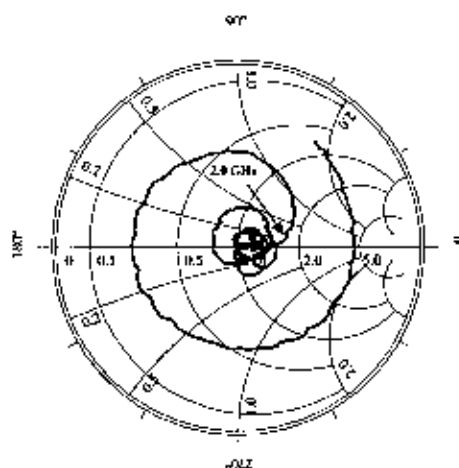


Figure 3: Measured input impedance from 0.9 GHz - 6.0 GHz for the antenna shown in Figure 2, with $L = 9.7$ cm, $\alpha = 15^\circ$, and $\beta = 80^\circ$.

In a first set of experiments, the antenna depicted in Figure 2 was measured for variable cant angles, α . In general, the match to 50 ohms improves and the 2:1 VSWR impedance bandwidth increases with increasing values of α . Figure 4 shows the measured input impedance of this antenna with $\alpha = 15^\circ$. Therefore, a compromise exists between the total height of the antenna above the ground plane and the achievable impedance bandwidth. It is apparent that, if there is no restriction on the size in wavelengths, the impedance bandwidth of the simple sector antenna is very large. However, the radiation pattern is likely to behave in the opposite way.

For a small sector the pattern is expected to be well-formed and stable with changes in frequency. As the frequency increases, and the sector becomes large compared to the wavelength, the pattern is likely to develop multiple lobes. Measurements of radiation patterns between 2 GHz and 3.5 GHz are presented for $\alpha = 15^\circ$ (which provides the worst possible broadside radiation characteristics from the range of α considered) in Figure 4. As these measurements demonstrate, the broadside characteristics of the antenna degrade as the operating frequency increases. The nature of the radiation patterns is well explained by the similarity between the canted sector and an electromagnetic horn with a long narrow

aperture. Radiation from the aperture is naturally directed along the perpendicular axis ($\theta = -90^\circ$ in Figure 4). Only the finite ground plane prevents the pattern maximum from occurring on the axis. However the E-plane pattern is broad since the vertical aperture is quite small. Hence, the zenith radiation is maintained until the vertical aperture becomes appreciable compared to the wavelength. The pattern is almost constant throughout the upper left quadrant, capable of supporting the scanning of a vertically polarized beam through the entire 90 degrees. Assuming that broadside operation is desirable, the radiation characteristics reduce the operational bandwidth of this antenna to approximately 40% centered at 2.5 GHz.

Another issue is the cross-polarization characteristics of the element in the H-plane. As shown in Figure 4, the cross-polarization components can be substantial off boresight. For large, fixed beam arrays, the effect may be minimal, although the power radiated in the off-boresight directions will affect the directive gain of the element. Of greater consequence would be the presence of the cross-polarization in the element pattern in a scanning array based on this antenna. Depending on the application, it may be necessary to reduce the cross-polarization to achieve wider scan angles.

To investigate this issue further, we conducted experimental and simulation studies on the variation of cross-polarization with both sector angle and elevation. Some of the results of this study are shown in Figure 5. In general, the smaller the sector angle, the lower the cross-polarization level. However, there is another cost involved. To achieve the same kind of impedance bandwidth at the lower end of the operating band, the length of the sectors must increase as the sector angle decreases.

5. Conclusions and Directions for Future Work

In this canted antenna design, several design tradeoffs exist between elevation angle, sector angle, impedance bandwidth, and broadside radiation characteristics. In general, impedance bandwidth increases with increasing cant angle, α . As the cant angle increases the bandwidth over which the sector displays acceptable broadside radiation decreases. As expected, cross-polar radiation performance of canted sectors is related to the sector angle, β . Prototypes with smaller sector angles had slightly lower levels of cross-polar radiation, but we found that the lengths and sometimes the cant angles of these sectors had to be increased in order to deliver the same kinds of impedance bandwidth provided by sectors with larger sector angles with smaller cant angles.

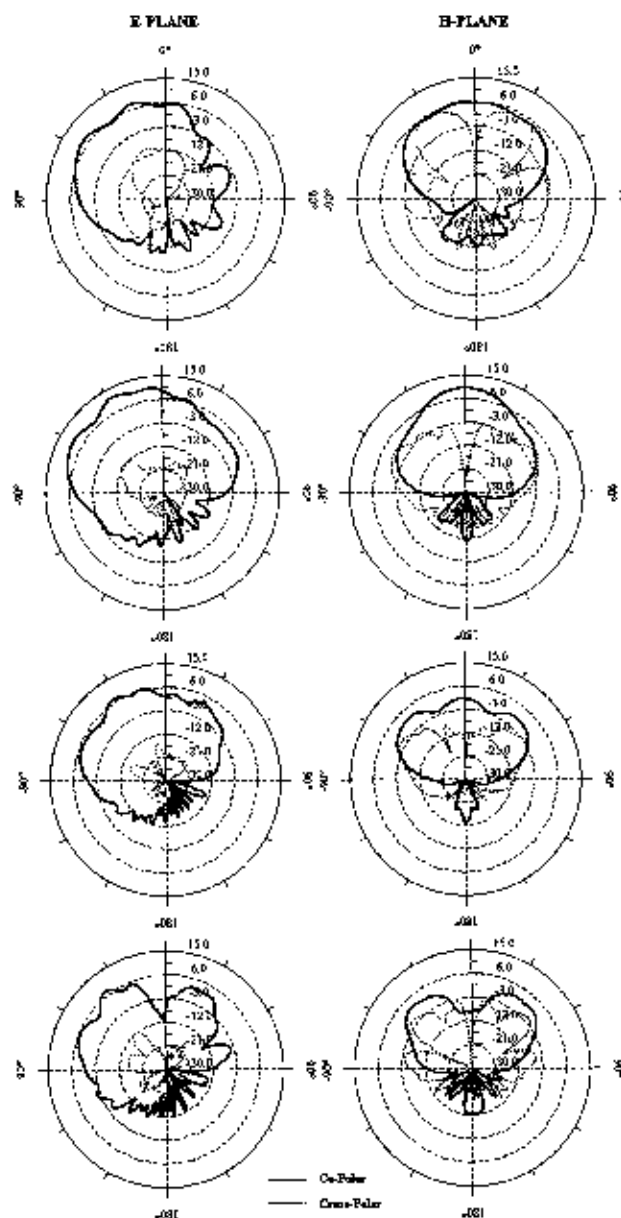


Figure 4: Measured co- and cross-polar E-plane and H-plane gain patterns [dB] for the antenna shown in Figure 2 at 2.0 GHz, 2.5 GHz, 3.0 GHz, and 3.5 GHz. All measurements were taken with a square ground plane with a dimension of 60 cm.

Future work in this project includes the development of a design-oriented model for the antenna element that takes both the impedance and radiation properties of the sector into account. Geometric changes to the antenna are also being considered to help mitigate the endfire characteristics of the structure as

frequency increases. Finally, work is ongoing to develop fast computational tools [12] that will be used to simulate these antenna elements in large aperiodic arrays.

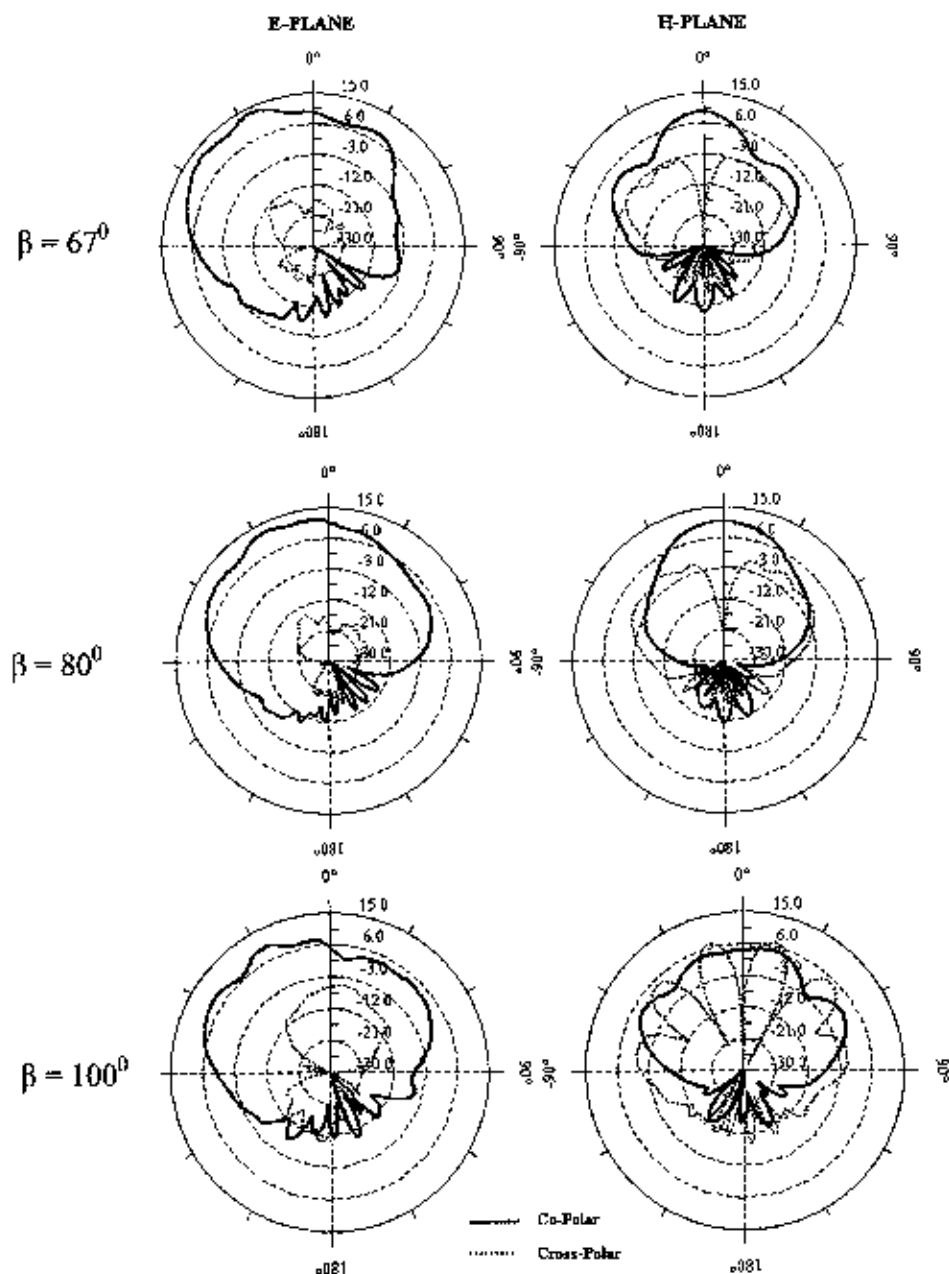


Figure 5: Measured E-plane and H-plane gain patterns [dB] over a range of sector angles for a cant angle of 10° at 2.5 GHz (the 100° sector measurement was taken at 2.58 GHz where the VSWR was less than 2). The length of the 67° sector was 12.5 cm, that of the 80° sector was 9.7 cm, and that of the 100° sector was 10 cm.

6. Acknowledgments

This work is sponsored by the United States Army Research Office through Research Agreement DAAD19-02-1-0398.

7. References

- [1] E. L. Holzman, "A wide band TEM horn array radiator with a novel microstrip feed," *Proc. 2000 IEEE Int. Conf. on Phased Array Systems and Technology*, 2000, pp. 441-444.
- [2] L. Li-Chung, T. Chang, and W. D. Burnside, "An ultrawide-bandwidth tapered resistive TEM horn antenna," *IEEE Trans. on Antennas and Propagat.*, vol. 48, pp. 1848-1857, Dec. 2000.
- [3] D. T. McGrath, "Blindness effects in ground plane-backed TEM horn arrays," *Proc. 1998 AP-S IEEE Int. Symp. on Antennas and Propagation*, vol. 2, 1998, pp. 1024-1027.
- [4] A. O. Boryssenko and D. H. Schaubert, "Single-polarized, dielectric-free, Vivaldi tapered slot phased array: performance prediction," *Proc. 2001 AP-S IEEE Int. Symp. on Antennas and Propagation*, vol. 2, 2001, pp. 436-439.
- [5] D. H. Schaubert, "Wide-band phased arrays of Vivaldi notch antennas," in *Proc. Tenth Int. Conf. on Antennas and Propagation*, vol. 1, 1997, pp. 6-12.
- [6] N. Schuneman, J. Irion, and R. Hodges, "Decade bandwidth tapered notch antenna array element," in *Proc. of the 2001 Antenna Applications Symposium*, Allerton Park, Monticello, Illinois, 2001, pp. 280-294.
- [7] N. Herscovici, "A wide-band single-layer patch antenna," *IEEE Trans. on Antennas and Propagat.*, vol. 46, pp. 471-474, Apr. 1998.
- [8] Y.-M. Jo, "Broad band patch antennas using a wedge-shaped air dielectric substrate," *Proc. IEEE Int. Symp. on Antennas and Propagation*, vol. 2, 932-935 (1999).
- [9] R. K. Mishra and S. S. Pattnaik, "Resonant frequency of wedge shaped microstrip antenna," *Electron. Lett.*, vol. 26, pp. 912-913, June 1990.
- [10] D. R. Poddar, J. S. Chatterjee, and S. K. Chowdhury, "On some broad-band microstrip resonators," *IEEE Trans. on Antennas Propagat.*, 31, pp. 193-194, Jan. 1983.
- [11] J. S. Zhao, W. C. Chew and P. E. Mayes, "Accurate analysis of electrically small conical antennas by using the low-frequency method," in *Proc. 2001 Antenna Applications Symposium*, Allerton Park, Monticello, Illinois, 2001, pp. 135-151.
- [12] N.-W. Chen, K. Aygun, and E. Michielssen, "Transient analysis of a canted sector antenna with the modeling of fine feed features," in *Proc. IEEE Int. Symp. on Antennas and Propagation*, vol. 2, 2001, pp. 384-387.

Some Lessons Learned About Truncation Effects in Wideband Vivaldi Arrays

Anatoliy O. Boryssenko & Daniel H. Schaubert

Antenna Laboratory, Electrical and Computer Engineering,
University of Massachusetts, Amherst, MA, 01003, USA
E-mail: boryssen@ecs.umass.edu schaubert@ecs.umass.edu

ABSTRACT

Input impedances, mutual coupling and radiation patterns of Vivaldi antenna elements in small phased arrays are presented. The data provide insights into truncation effects in these arrays. It appears that the resonances of the isolated element play a significant role in the performance finite arrays. Splitting and shifting of element resonances, similar to that in coupled resonant circuits, are observed. A better understanding of these phenomena may lead to effective design methods for finite arrays of Vivaldi antennas, a problem that is extremely difficult with existing computer simulations.

1. INTRODUCTION

The results of experiments and full-wave simulation of wide bandwidth Vivaldi tapered slot antenna arrays have been presented at the Antenna Applications Symposium and elsewhere [1]-[5]. Experimental results were reported for some relatively large arrays; for example, Pozgay reported results for a 1799-element array [6]. Many applications, however, would benefit from the use of wide bandwidth arrays, or subarrays, comprised of only a few hundred elements. The individual antennas in such small arrays do not behave as they do in infinite arrays or as the central elements of a large array, e.g., [7], [8]. So far, published data showing the effects of various parameters on the performance of wide bandwidth Vivaldi antenna arrays is limited to infinite arrays, in which all elements behave the same. Our results obtained by using full-wave simulations of infinite and finite arrays of Vivaldi antennas suggest that the behavior a particular element design in an infinite array often is not a good indicator of that particular design's suitability for use in a finite array.

In this paper, we present some of the insights gained by extensive full-wave analysis of finite and infinite arrays of dielectric-free Vivaldi antennas. A single geometry of a Vivaldi element is considered, Fig. 1a, and results are presented for

this element in arrays of various sizes, e.g., Fig. 1b and 1c. For the arrays, the E-plane direction corresponds to the YZ-plane and H-plane direction to the XZ plane in accordance with the Cartesian coordinates in Fig. 1. The broadside direction coincides with the Z-axis.

The results presented here illustrate active and passive input impedances, mutual coupling, and radiation patterns for the selected element design. These results provide some insights into the phenomena that contribute to element performance in small, wide bandwidth arrays. Eventually, we hope to understand and quantify the physical phenomenology underlying truncation effects and performance in small wide bandwidth arrays. Furthermore, we hope to provide guidance for the design of Vivaldi elements that operate well in small to moderate size arrays. For example, we have observed that an element's performance in small arrays often can be better predicted by its *isolated* impedance than by its impedance in an infinite array. This has led to a design procedure for elements in small arrays [9].

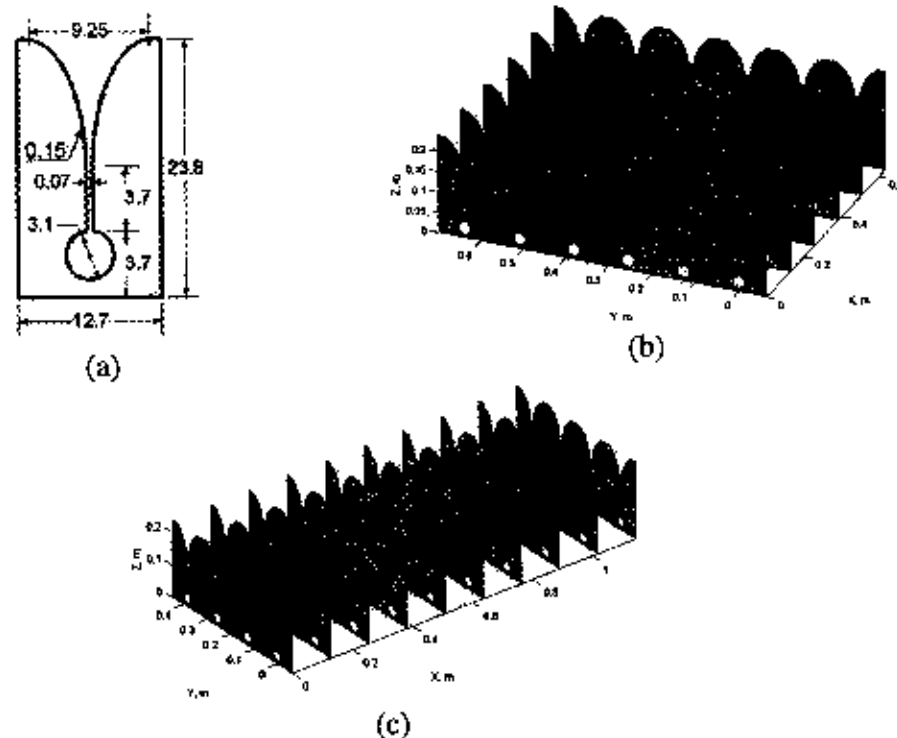


Fig. 1. (a) Geometry of dielectric-free Vivaldi element with opening rate $R_a=0.15$ for exponential profile. (b) 6x6 array. (c) 4x12 array.

An interesting perspective on the performance of wide bandwidth arrays is provided in Fig. 2a, which shows the input impedances of a single, isolated element and the same element (Fig. 1a) in an infinite array. The element spacing in the array is one-half wavelength at 1.18 GHz. Near this frequency, the element impedances, isolated and infinite array, are nearly the same. However, at lower frequencies, which typically are part of the operating regime for wide bandwidth arrays but not for narrow bandwidth arrays, these impedances differ considerably. It appears that the good behavior of the infinite array is achieved by reducing the Q of the single-element resonances and by lowering the frequency at which the first resonance provides reasonably good radiation resistance. In other words, when properly designed, mutual coupling in the infinite array improves wide bandwidth operation because (1) sharp resonances of the single element are suppressed and (2) the low-frequency portion of the band, where the single element is not an efficient radiator, becomes useful.

The impedances of the elements when placed in an 8×8 array are quite different from the relatively simple behavior observed in Fig. 2a. The element impedances vary considerably from element to element and the low-frequency regime, below 0.2 GHz, is not usable. When compared to the infinite array, the element-to-element variations of the 8×8 array can be interpreted by two phenomenological models, which give slightly different but useful insights: (1) the absence of mutual coupling from "missing" elements, those outside the array boundaries, affects elements differently depending on their locations with respect to the array edges, and (2) scattering of radiated or guided waves from the truncation of the periodic array structure alters the performance from that observed in the infinite array. The mutual coupling model assumes an element-by-element view of the array and helps to explain local phenomena. The wave-based model views the entire array as a structure and is useful to explain global phenomena. The wave-based model also is promising as a means to speed computations for moderately large arrays that are comprised of too many elements to efficiently simulate by brute force element-by-element methods [10].

In this paper, only dielectric-free Vivaldi elements are considered. The numerical results are obtained by using the UMass time-domain integral-equation (TDIE) MoM solver [11], [12]. The TDIE code efficiently analyzes finite arrays in active and passive modes, Fig. 3. In the active mode, all elements are driven. In the passive mode, the source is applied to one particular port while others are passively terminated. Short-circuit terminations are shown here and the terminal

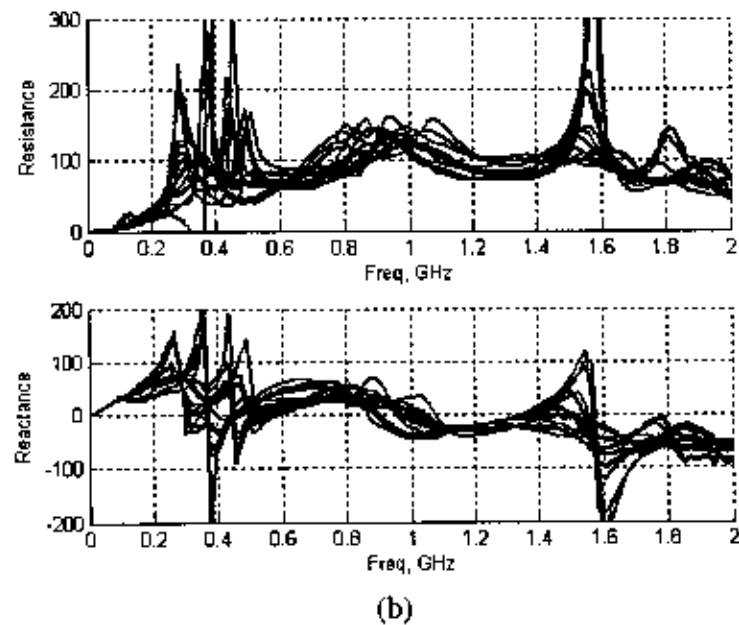
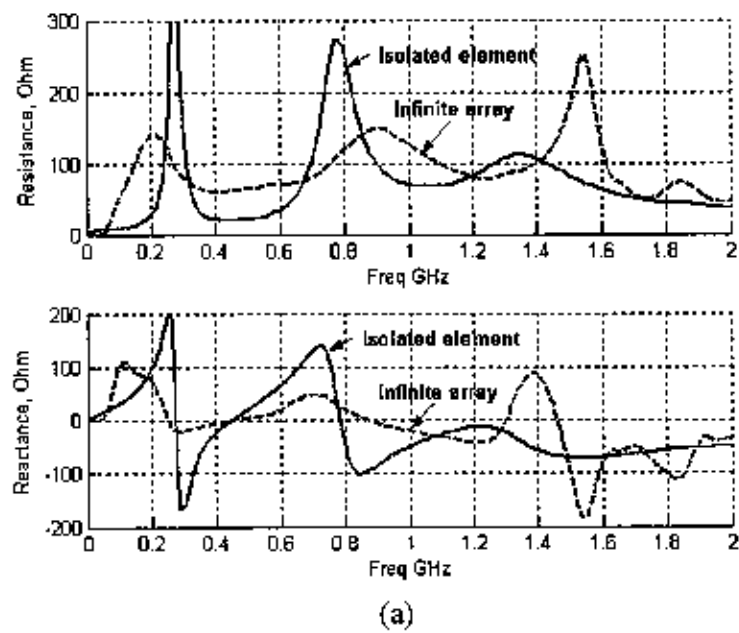
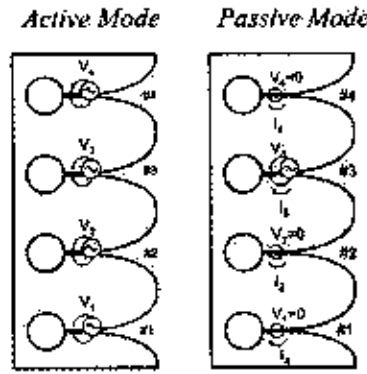


Fig. 2. (a) Input impedance of isolated element and infinite array (broadside beam), (b) Broadside active input impedances for 8x8 array.

current is computed for all antenna ports. From these currents, the port admittance matrix is calculated by repeating the computations with the generator applied successively to each of the array elements. From the port admittance matrix, the passive and active input impedances and the scattering matrix can be computed, Fig. 3b.



(a)

$$Y_{k,3} = I_k/V_3, \quad k=1, \dots, 4, \quad V_{1,2,4} = 0, \quad V_3 \neq 0$$

$$\Rightarrow [Y]_{4 \times 4}^{\text{pass}} \Rightarrow [Z]_{4 \times 4}^{\text{pass}} = ([Y]_{4 \times 4}^{\text{pass}})^{-1}$$

$$\Rightarrow [S]_{4 \times 4} = ([E] + [Y]_{4 \times 4}^{\text{pass}})^{-1} \cdot ([E] - [Y]_{4 \times 4}^{\text{pass}})$$

$$Z_{\text{imp},k}^{\text{active}} = \sum_{n=1}^4 Z_{n,k} \cdot I_n/I_k = \sum_{n=1}^4 Z_{n,k} \cdot \frac{\sum_{p=1}^4 Y_{p,n} \cdot \exp(-jp\phi)}{\sum_{q=1}^4 Y_{q,k} \cdot \exp(-jq\phi)}$$

$$k=1, \dots, 4$$

ϕ - progressive phase shift to scan beam

(b)

Fig. 3. Analysis approaches: (a) schematic sketch of linear Vivaldi arrays driven in active and passive modes, (b) basic definition and transformations to formulate port matrices of active and passive arrays.

2. E-PLANE AND H-PLANE COUPLING IN FINITE VIVALDI ARRAYS

Single-polarized Vivaldi antenna arrays exhibit different coupling characteristics in the E-plane and H-plane. This is not surprising since the elements are in electrical contact along the E-plane (on the same metallic sheet) whereas they are linked only by the electromagnetic fields in the H-plane. To observe the differences in E-plane and H-plane coupling while preserving some of the physics associated with planar apertures, we have studied arrays of various sizes, $1 \times N$, $2 \times N$, $3 \times N$, etc. Fig. 4a shows active element impedances (broadside beam) for arrays comprised of N elements on a metallic sheet and 2 metallic sheets, i.e., $N \times 2$ (E-plane) arrays. Fig. 4b shows impedances for arrays comprised of 2 elements per metallic sheet and N sheets, i.e., $2 \times N$ (H-plane) arrays. All unique values of input impedances for these arrays (broadside beam) are shown in the figure, as well as the impedance of the isolated element.

The following salient trends are observed:

- Element-to-element variations are much greater for E-plane arrays than for H-plane arrays.
- The low-frequency boundary for both the E-plane and the H-plane arrays is limited by very high Q resonances and a rapid decrease of the input resistance.
- The strong first resonance of the isolated element has a dominant effect on low-frequency operation of E-plane and H-plane arrays.
- The useful operating band of H-plane arrays is relatively independent of the number of elements, probably because H-plane coupling is weaker than E-plane coupling.
- Mutual coupling causes the resonances of the isolated element (0.4 and 0.8 GHz) to split, move and change in strength. As the number of elements in the arrays increases, the resistance and reactance near the resonance change more rapidly with frequency, but the strength of the resonances tends to diminish.
- Strong modification and splitting of the resonances take place for the E-plane arrays and the same effect is weaker for the H-plane arrays.
- Based on observations in Fig. 2b for an 8×8 array, Fig. 4, and other cases that have been simulated, E-plane coupling is strong, particularly at low frequencies, and it has a significant impact on element impedances and on variations from element to element.

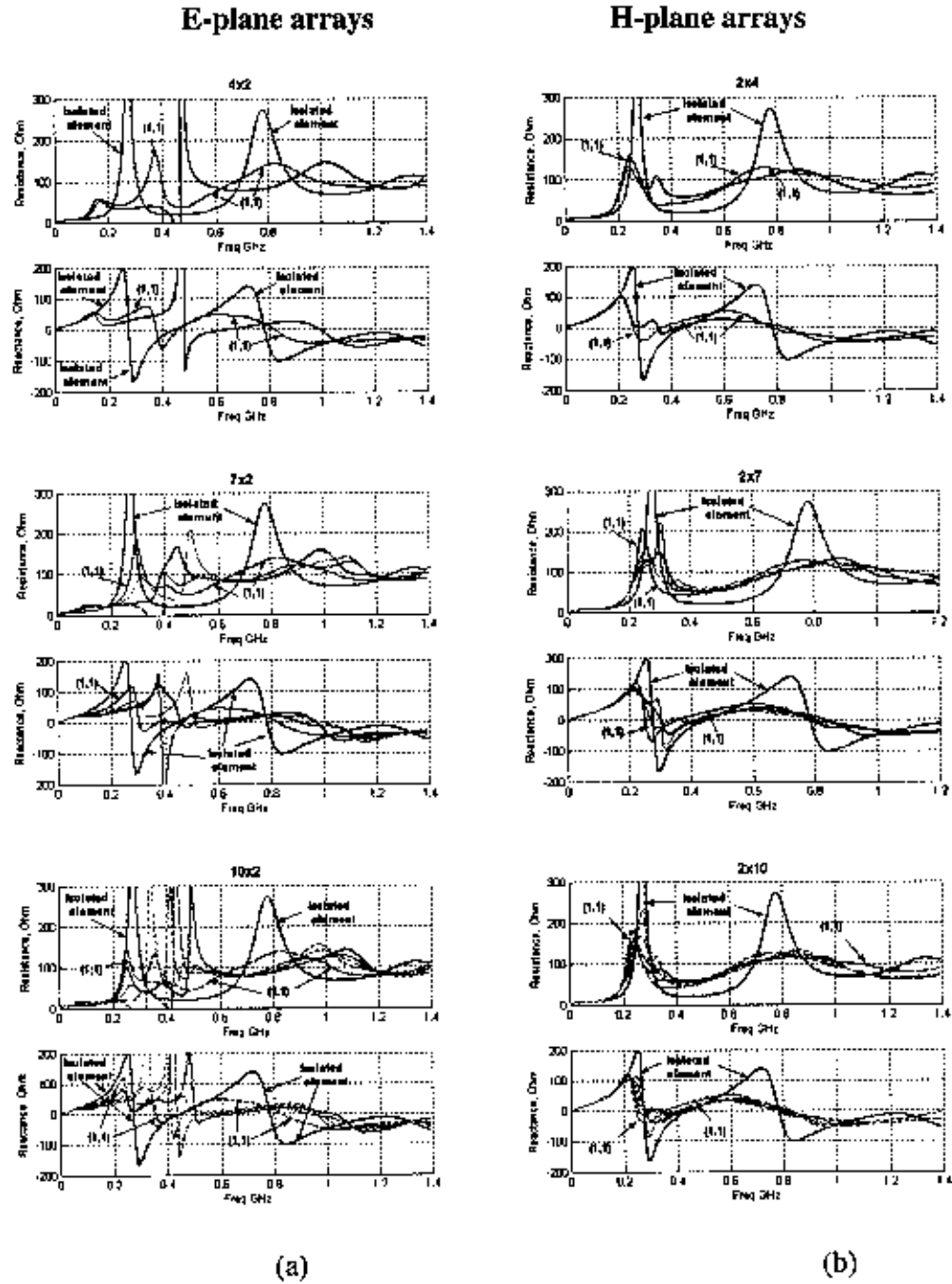


Fig. 4. Simulated active input impedances for isolated element and unique elements of Vivaldi phased arrays: (a) $N \times 2$, E-plane array, (b) $2 \times N$, H-plane array; $N=4, 7, 10$. Isolated element and (1,1) edge element are marked.

3. COUPLING IN FINITE VIVALDI ARRAYS

Figures 5 - 8 show the magnitude of the coupling coefficient, $20 \log_{10}|S_{ij}|$, for 5x5 and 3x9 arrays, respectively. At low frequencies, the E-plane coupling (along y direction) is stronger, Fig. 5. At 1.2 GHz, the coupling is less affected by the metallic contact of elements in the E-plane and the coupling decreases more symmetrically, Fig. 7. At 0.8 GHz, H-plane coupling along the center row decreases more rapidly than along the upper and lower rows, Fig. 6. This may be due to a wave-based resonance across the array at this frequency since the contours of constant coupling display the expected convex shape at 0.6 and 1.0 GHz, not shown.

Comparison of the data in Fig. 5 - 8 with the measured coupling reported in [7] suggests that the magnitude of coupling in single-polarized arrays is similar (within about 5 dB) to that in dual-polarized arrays. However, coupling in the single-polarized array has not been studied as thoroughly as the measured results in [7] so it is not known if the coupling in single-polarized arrays varies as rapidly with frequency and location in the array as that observed in the dual-polarized array.

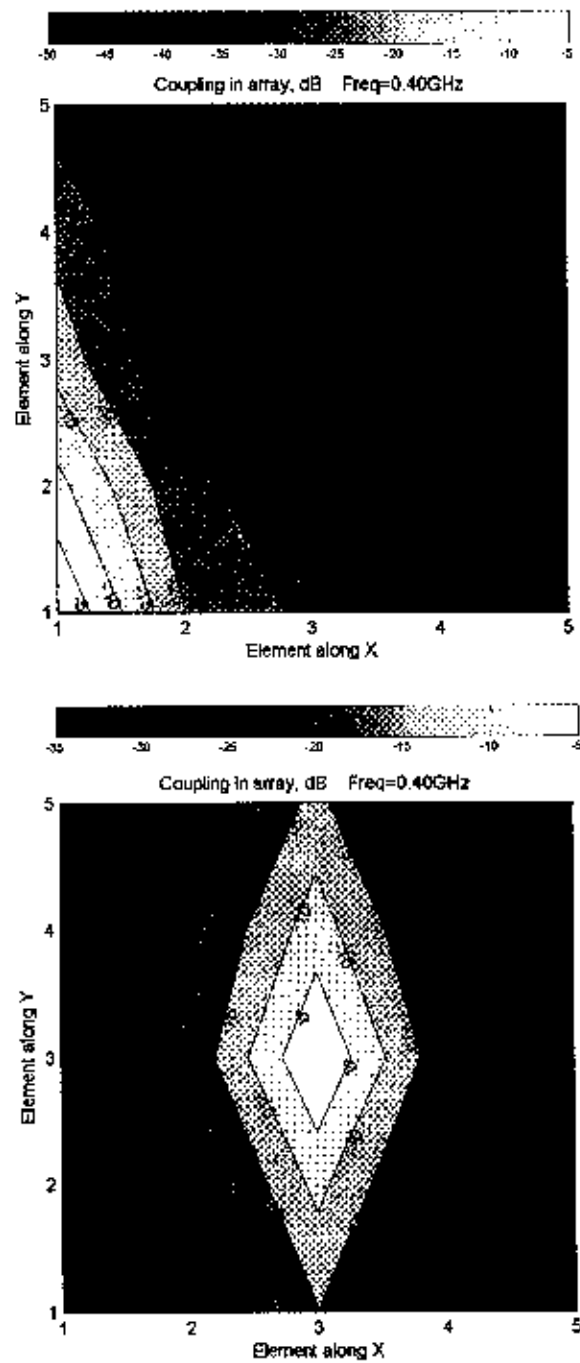


Fig. 5. Coupling to {1,1} corner element (at the top right) and center {3,3} element (at the bottom) of 5x5 Vivaldi at 0.4 GHz frequency.

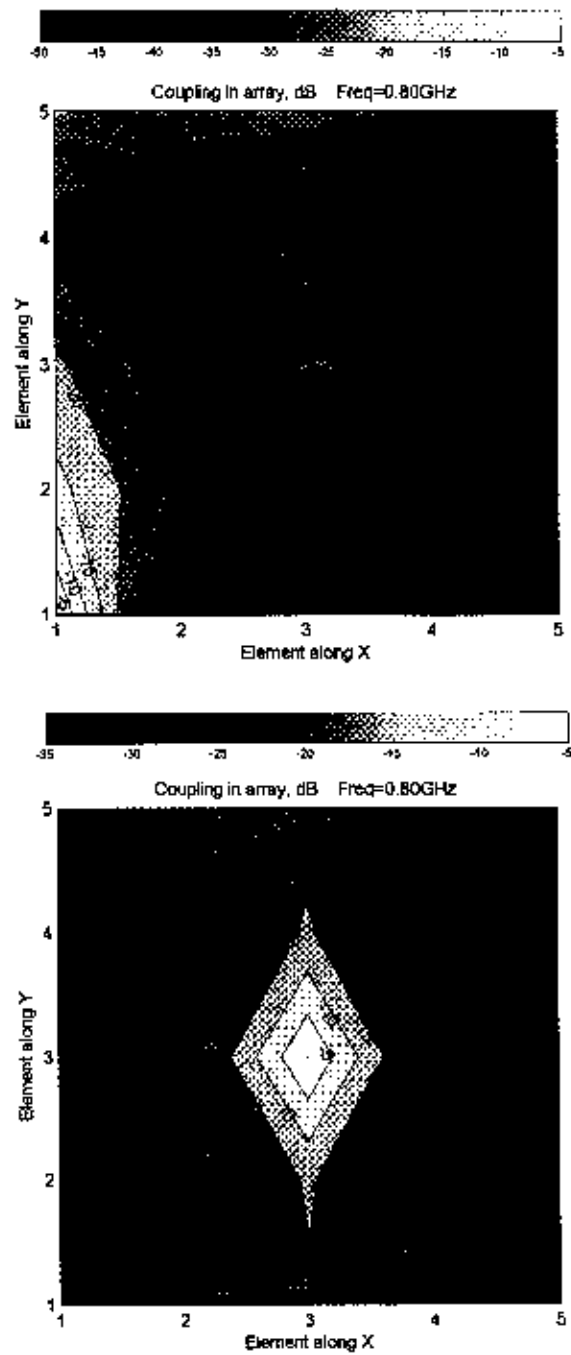


Fig. 6. Coupling to {1,1} corner element (at the top right) and center {3,3} element (at the bottom) of 5x5 Vivaldi at 0.8 GHz frequency.

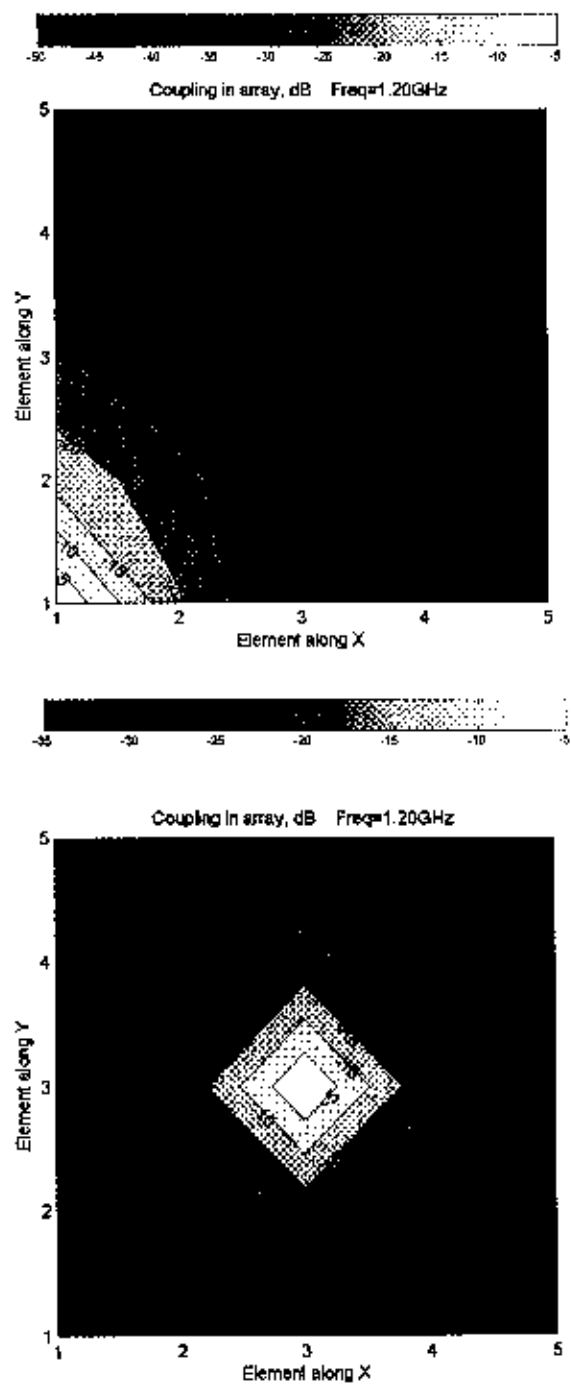


Fig. 7. Coupling to {1,1} corner element (at the top right) and center {3,3} element (at the bottom) of 5x5 Vivaldi at 1.2 GHz frequency.

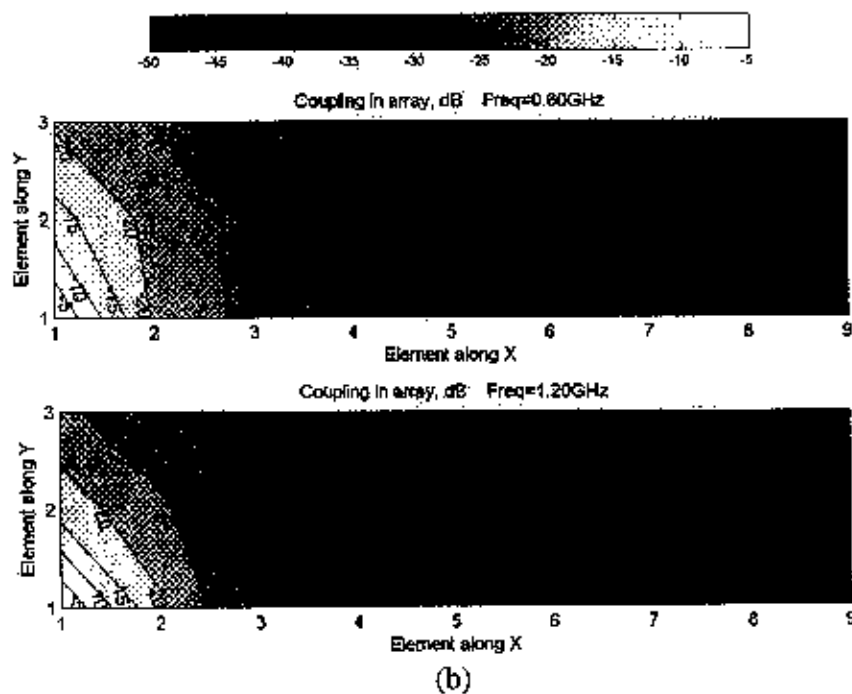
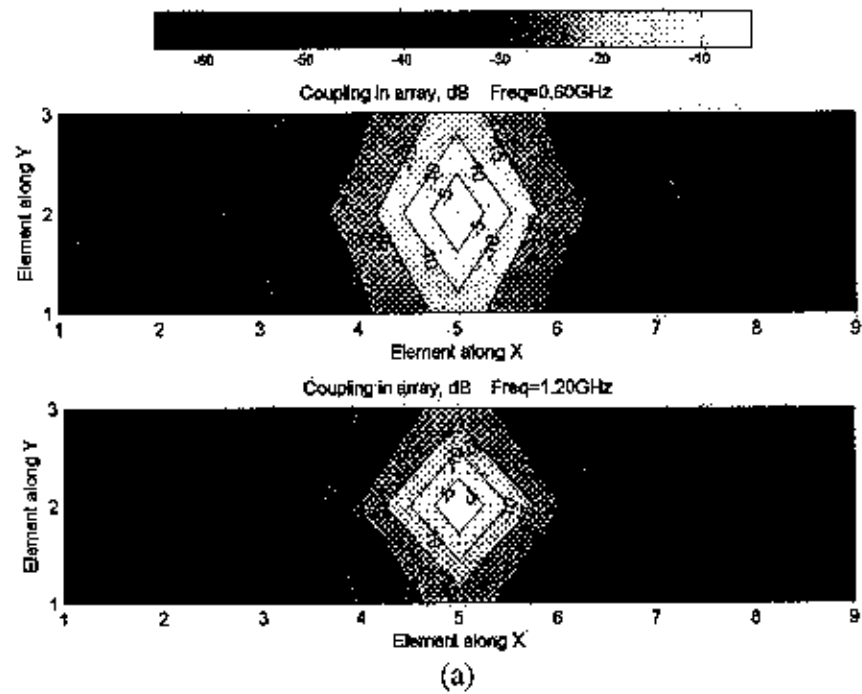


Fig. 8. Coupling for 3x9 array at frequencies 0.6 and 1.2 GHz. (a) {2,5} center element. (b) {1,1} corner element.

4. PASSIVE AND ACTIVE INPUT IMPEDANCES

Input active (at the top) and passive (at the bottom) impedances of elements in a 6x6 single-polarized array are shown in Figs. 9 - 11. The active mode for the array means that all elements are driven with 1 volt, 0° phase (broadside beam) while in the passive mode just one element is driven and others are terminated with 100-Ohm loads. The plots show the impedances of three adjacent elements starting from one corner of the array (element 01-01) and moving along the edge on separate sheets, Fig. 9, on the same metallic sheet, Fig. 10, and along the diagonal, Fig. 11.

The active impedances (at the top) are similar to the data for an 8x8 array in Fig. 1, but it is easier to see the individual element impedances in Figs. 9 - 11. One of the prominent features of the data in Fig. 9 is the similarity of the plots, which show elements that are located on the ends of different metallic sheets. These elements are coupled to each other in the H-plane direction. The impedances are relatively insensitive to the location of the metallic sheet within the array. Even the corner element's impedance, active and passive, is essentially the same as that of the edge element on the central metallic sheet. For edge elements on the same metallic sheet (Fig. 10), the element-to-element variation is significant in the vicinity of 0.4 GHz, where the isolated element has its first resonance (see Fig. 1a). Similarly, the active and passive impedances vary considerably along the array diagonal, Fig. 11.

A second prominent feature of the data in Figs. 9 - 11 can be observed most easily in the passive impedances of Fig. 9. Comparing these plots to the isolated element, it appears that the resonances at 0.4 and 0.8 GHz in Fig. 1a each has split into two closely spaced resonances. This splitting can be observed in all of the passive impedances of Fig. 9 - 11, and in the first resonance of the active impedances of elements 02-02 and 02-01. The first resonances of the active impedances of elements 03-03 and 03-01 are not split, but they are shifted upward about 100 MHz from the isolated element resonance. This phenomenon of resonance splitting and shifting is common when two or more resonant circuits are coupled. Hence, the resonance splitting and its variation from element to element in the array is a natural consequence of the mutual coupling model for the array.

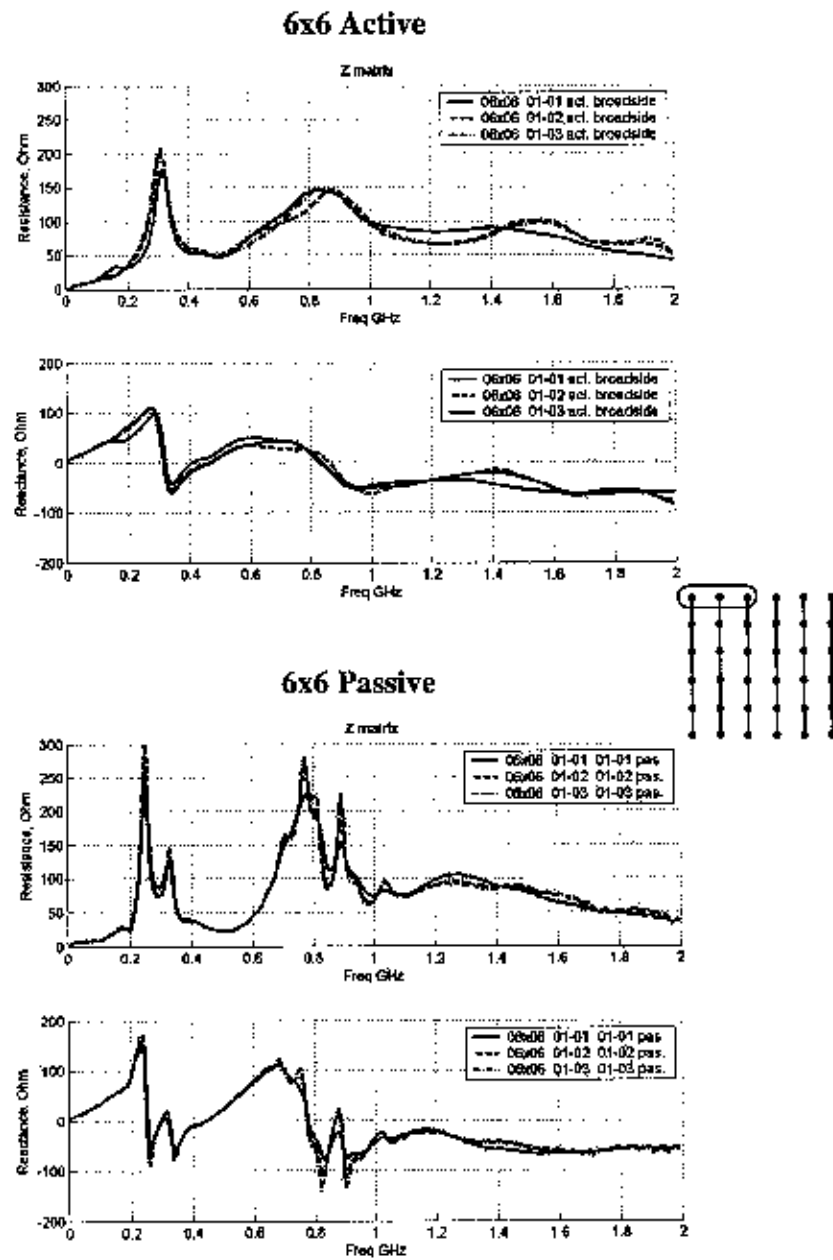


Fig. 9. Input active broadside (at the top) and passive (at the bottom) impedances of elements in 6x6 single-polarized array: elements on adjacent sheets, H-plane coupled.

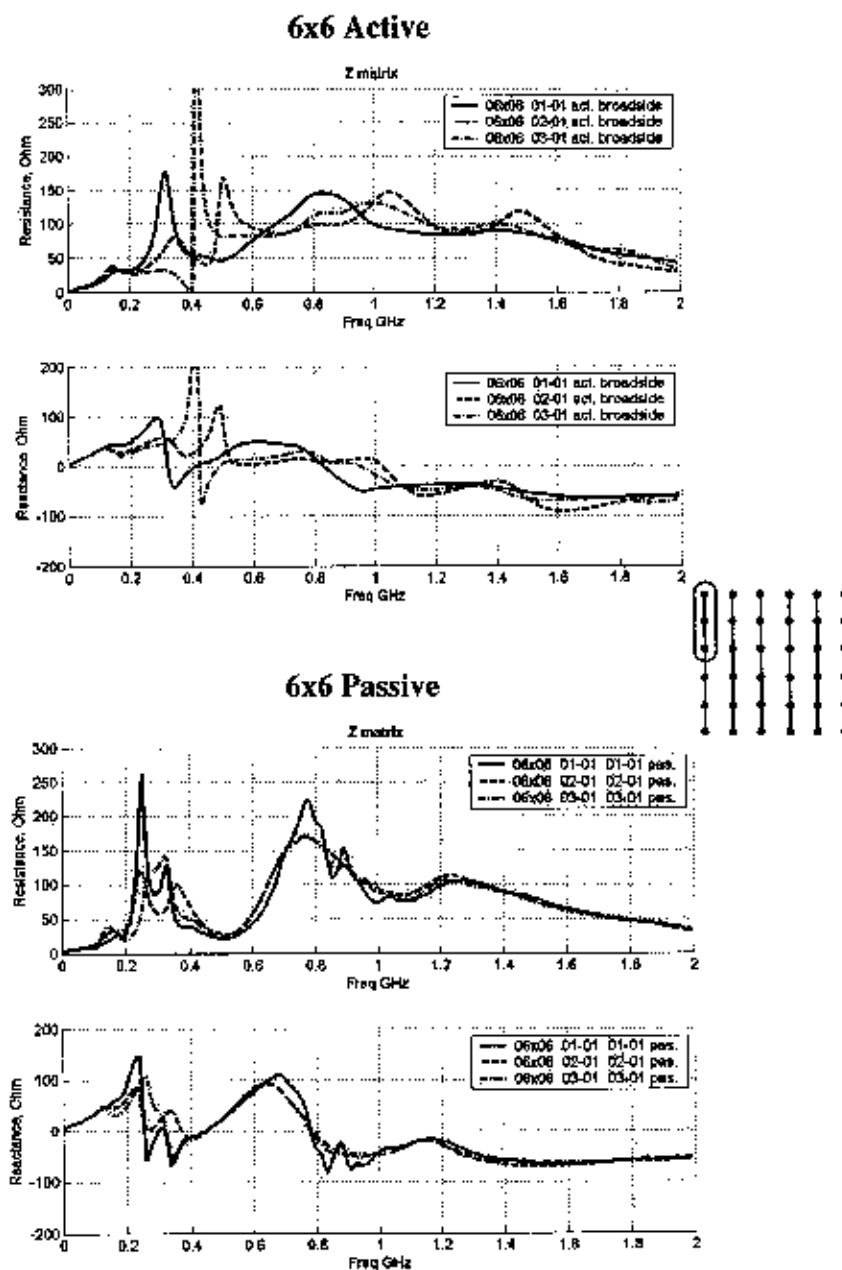


Fig. 10. Input active broadside (at the top) and passive (at the bottom) impedances of elements in 6x6 single-polarized array: elements on same sheet, E-plane coupled.

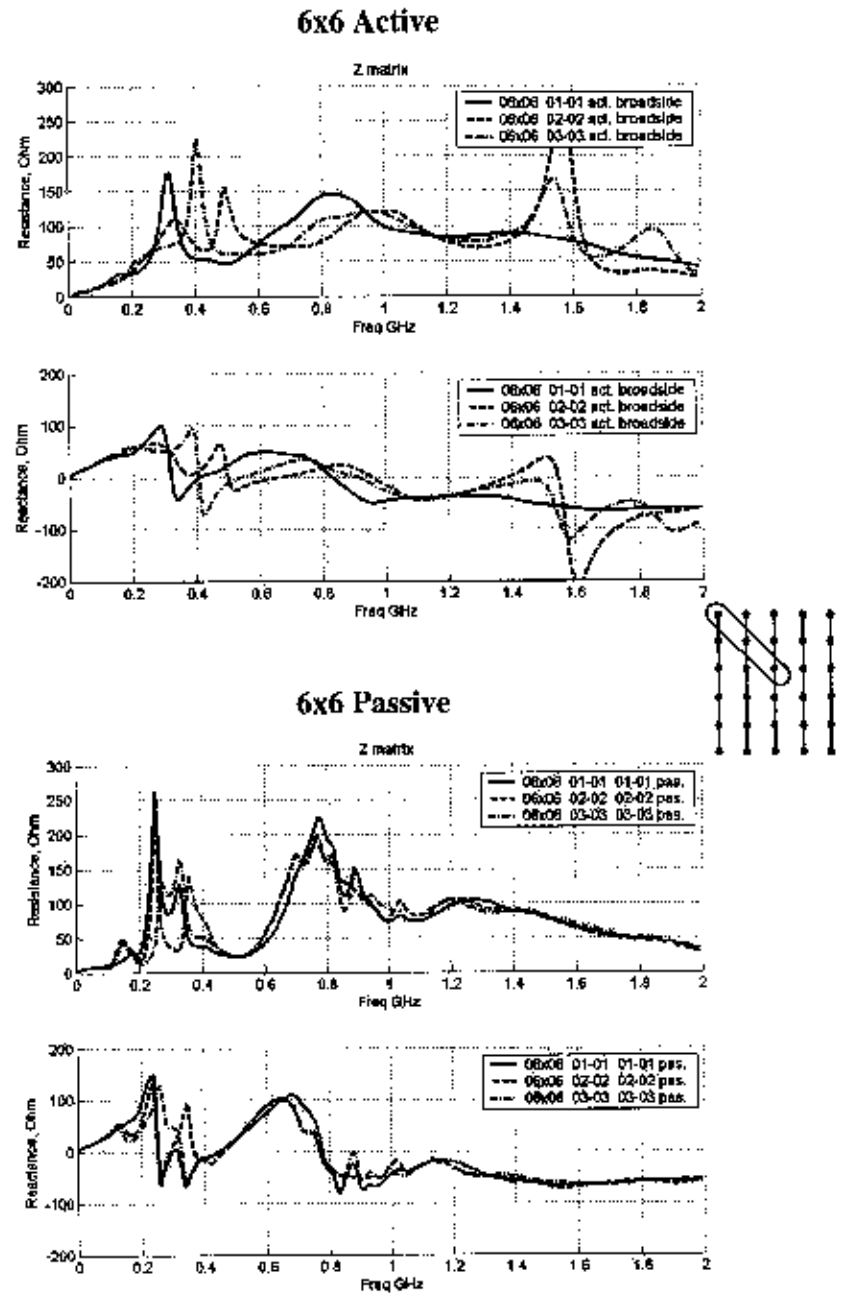


Fig. 11. Input active broadside (at the top) and passive (at the bottom) impedances of elements in 6x6 single-polarized array: elements along diagonal.

5. RADIATION PROPERTIES OF FINITE VIVALDI ARRAYS

The full-wave EM analysis enables computation of the radiation patterns of Vivaldi elements and finite arrays. Several such cases are illustrated in three series of data in Fig. 12 - 16. All radiation patterns are normalized to the antenna broadside gain factor. The normalization is accomplished by numerical integration over the surface of a sphere that encloses the antennas/arrays. Patterns are computed with 1-degree resolution. E-plane and H-plane patterns are shown on each plot.

Computed radiation patterns of a single Vivaldi element and an active broadside 5x5 phased array are plotted in Fig. 12 at frequencies 0.4, 0.8 and 1.2 GHz. At 0.4 GHz the isolated element has a nearly omnidirectional pattern in both the E-plane and H-plane. At the higher frequencies, the pattern has lobes and minima that will further develop into an endfire radiation pattern at much higher frequencies. The 3-dB beamwidth of the 5x5 array changes from about 60° at 0.4 GHz to about 20° at 1.2 GHz. The sidelobe level is about -12 dB at 0.8 and 1.2 GHz. The front-to-back ratio is less than 5 dB at 1.2 GHz. The directive gain of the isolated element is 0.5 dB at 0.4 GHz and about 3 dB at 0.8 and 1.2 GHz. The gain of the 5x5 array at these frequencies is 9, 14 and 17 dB, respectively.

Radiation patterns of an entire 3x3 array and just the center driven element are shown in Fig. 13 at 0.4, 0.8 and 1.2 GHz. At 1.2 GHz, the central element E-plane pattern exhibits ripple due to truncation of the array. Chio, et al, observed similar effects in an 8x8 dual-polarized array [7]. The central element patterns show some significant differences in the E-plane and H-plane pattern shapes, but the entire array has good beam symmetry throughout its 3-dB beamwidth because (1) the array factor selects only the central portion of the element pattern, and (2) the nine individual element patterns vary in such a way that the superposition of radiation from all elements is more symmetric than any single element.

Figures 14-16 illustrate the element-to-element variations of active element patterns in a 5x5 single-polarized array. Figure 14 shows the patterns for edge elements on adjacent metallic sheets (H-plane coupled), while Figure 15 shows patterns of edge elements on the same sheet (E-plane coupled) and Figure 16 shows patterns of elements along the diagonal. The central element (3,3) radiation pattern is symmetrical whereas the patterns of other elements are asymmetrical. The active element directivity is about 2 - 5 dB within the frequency band considered here.

The active element patterns have wide beamwidths in both the E-plane and H-plane directions, which is required for wide-scan applications. The angular spacing of the ripples caused by array truncation is less than for the 3x3 array, as expected.

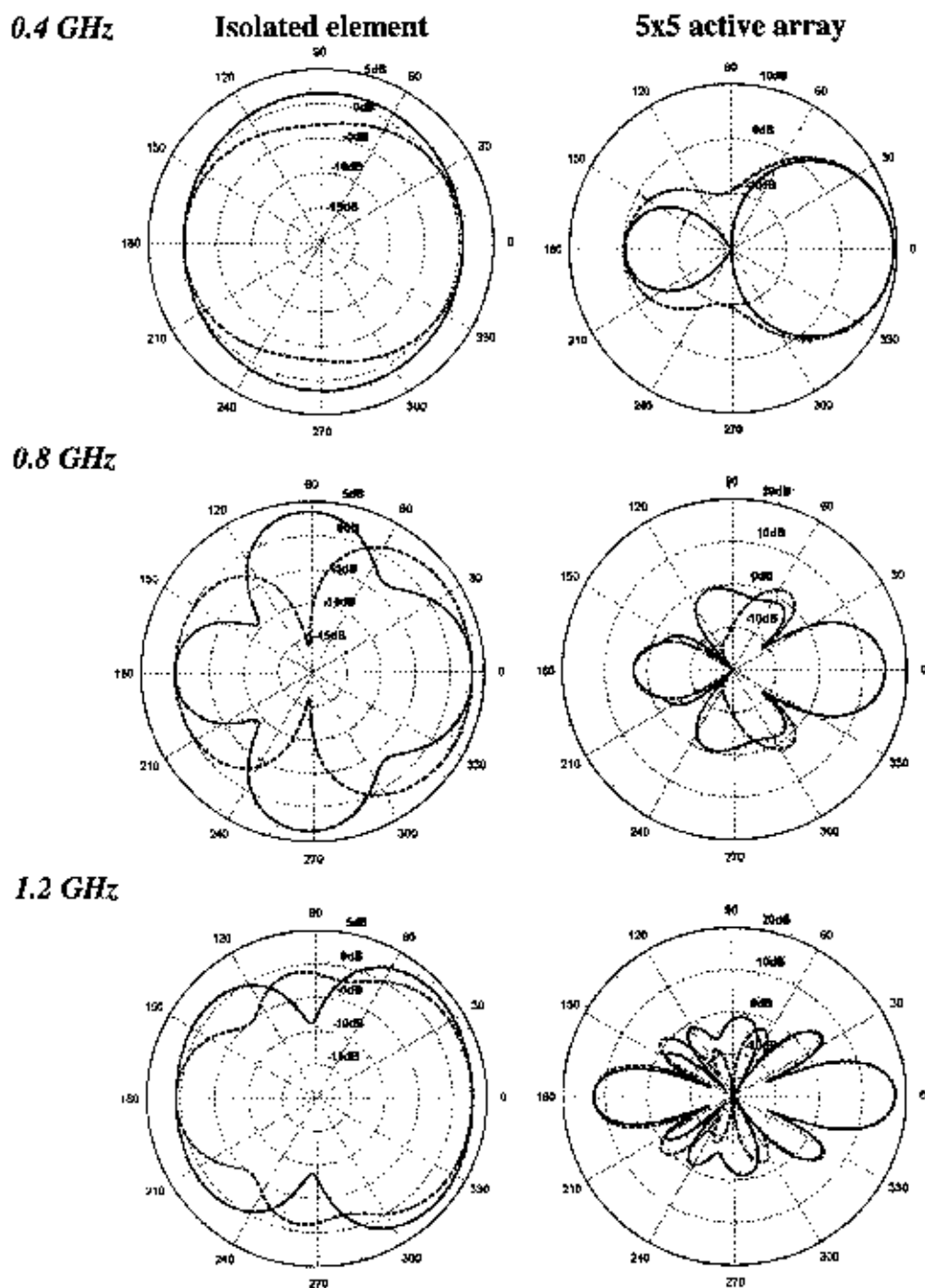


Fig. 12. Radiation patterns of isolated element (at the left) and active broadside 5x5 phased array (at the right) at 0.4, 0.8 and 1.2 GHz frequencies. E-plane pattern in solid line and H-plane in dashed line.

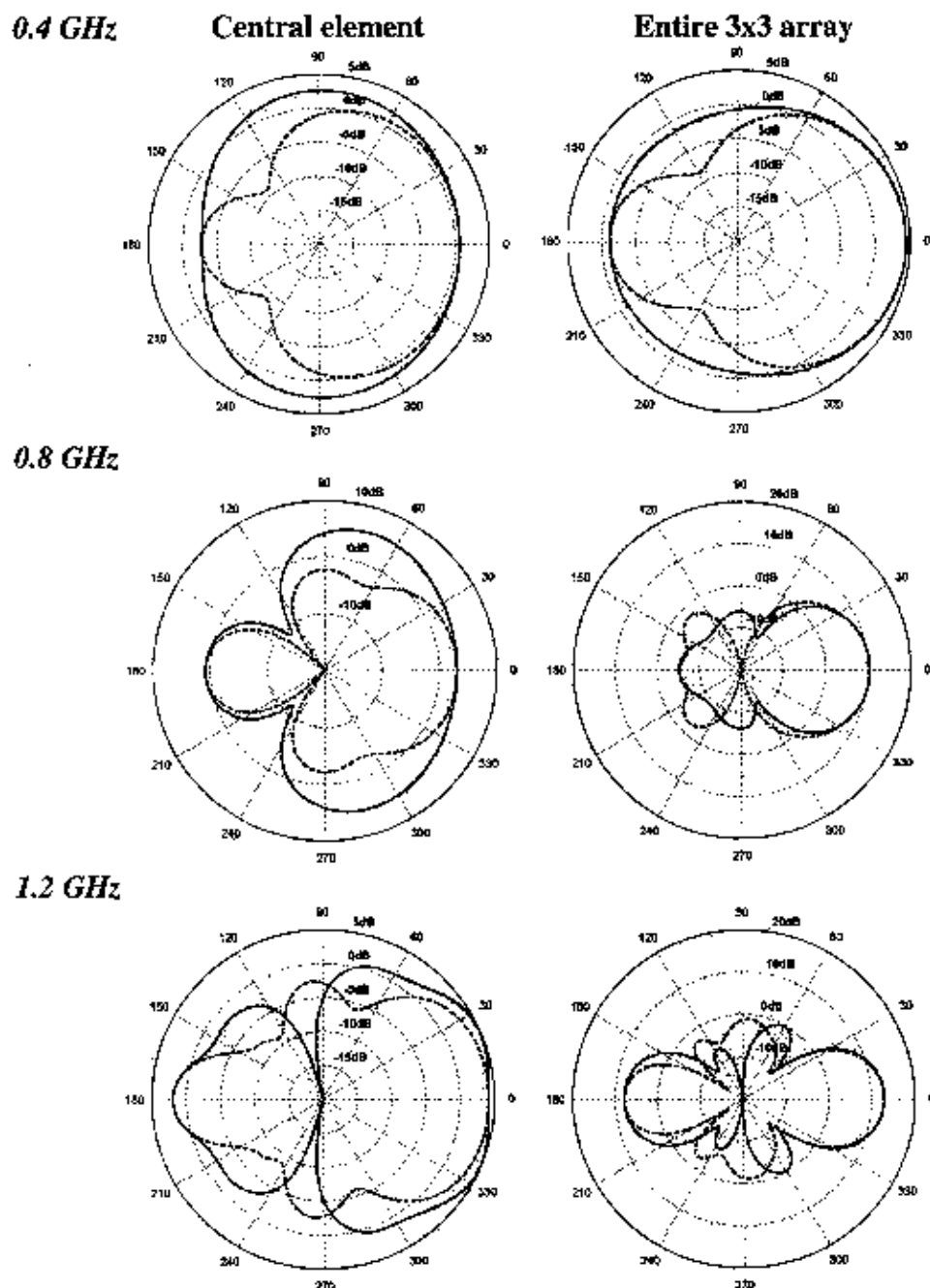


Fig. 13. Radiation patterns of central element in 3x3 array (at the left) and entire 3x3 array (at the right) at 0.4, 0.8 and 1.2 GHz frequencies. E-plane pattern in solid line and H-plane in dashed line.

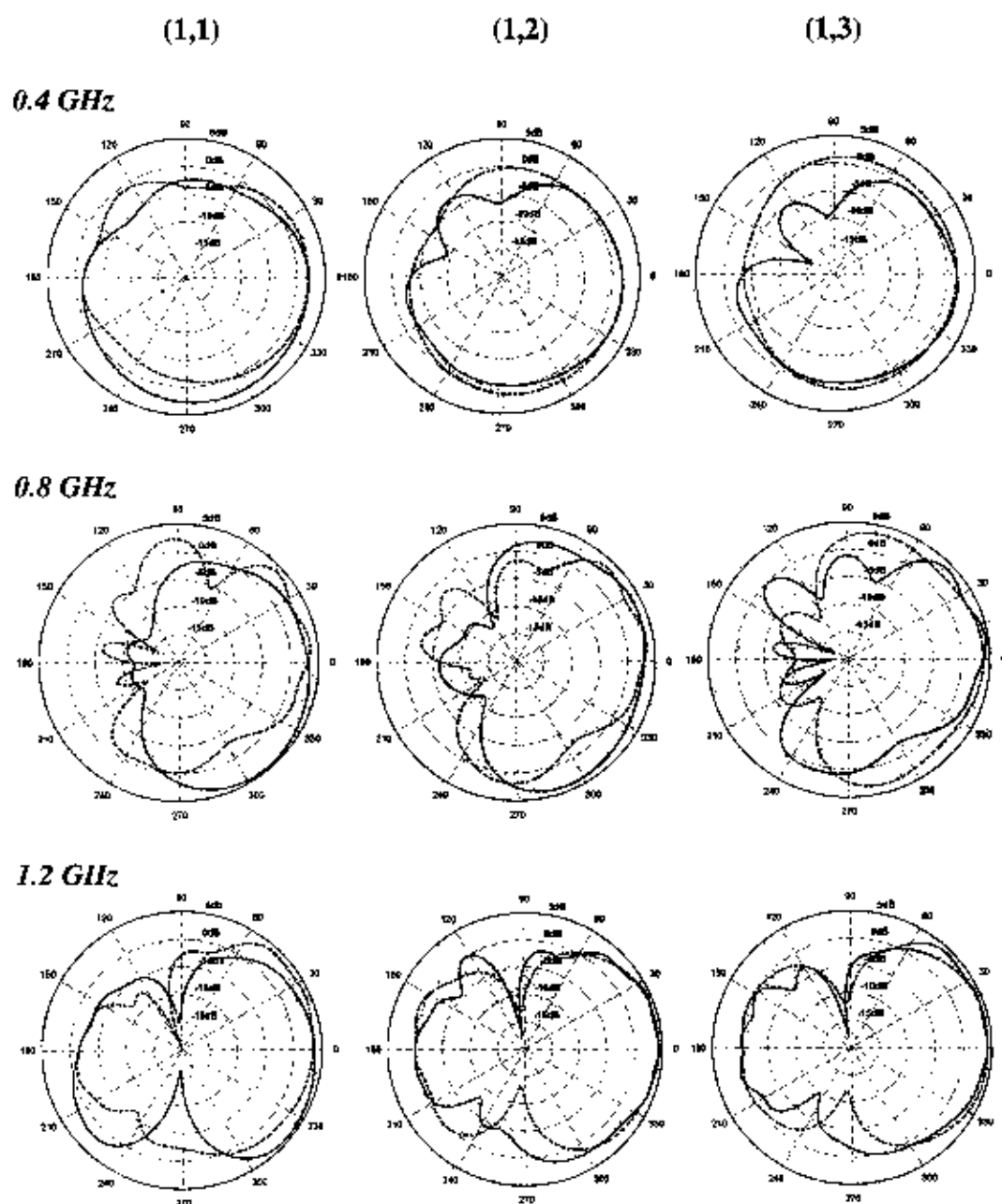


Fig. 14. Active element patterns in 5x5 single-polarized array: elements on adjacent sheets, H-plane coupled at 0.4, 0.8 and 1.2 GHz. E-plane pattern in solid line and H-plane in dashed line.

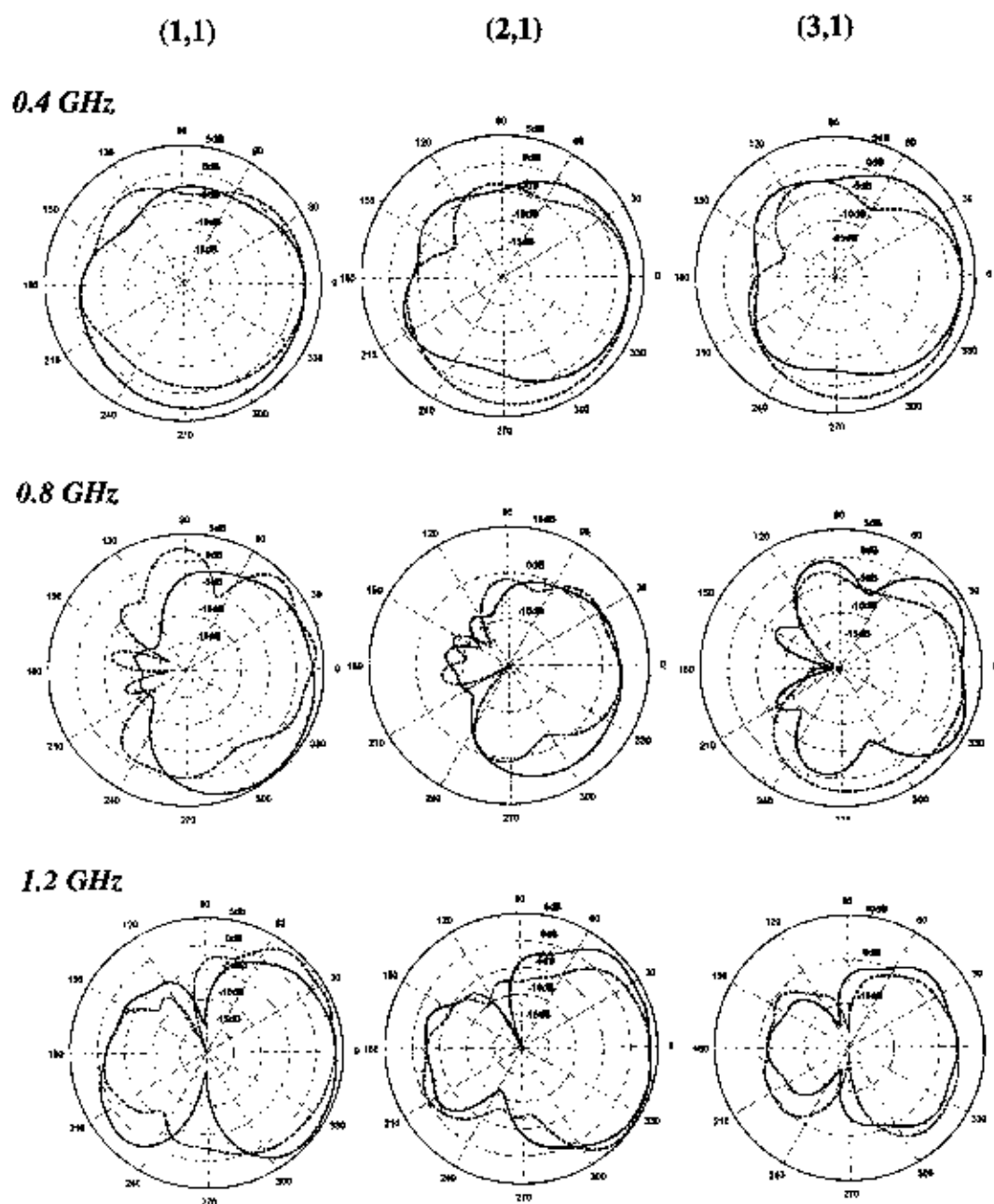


Fig. 15. Active element patterns in 5x5 single-polarized array: elements on same sheet, E-plane coupled at 0.4, 0.8 and 1.2 GHz. E-plane pattern in solid line and H-plane in dashed line.

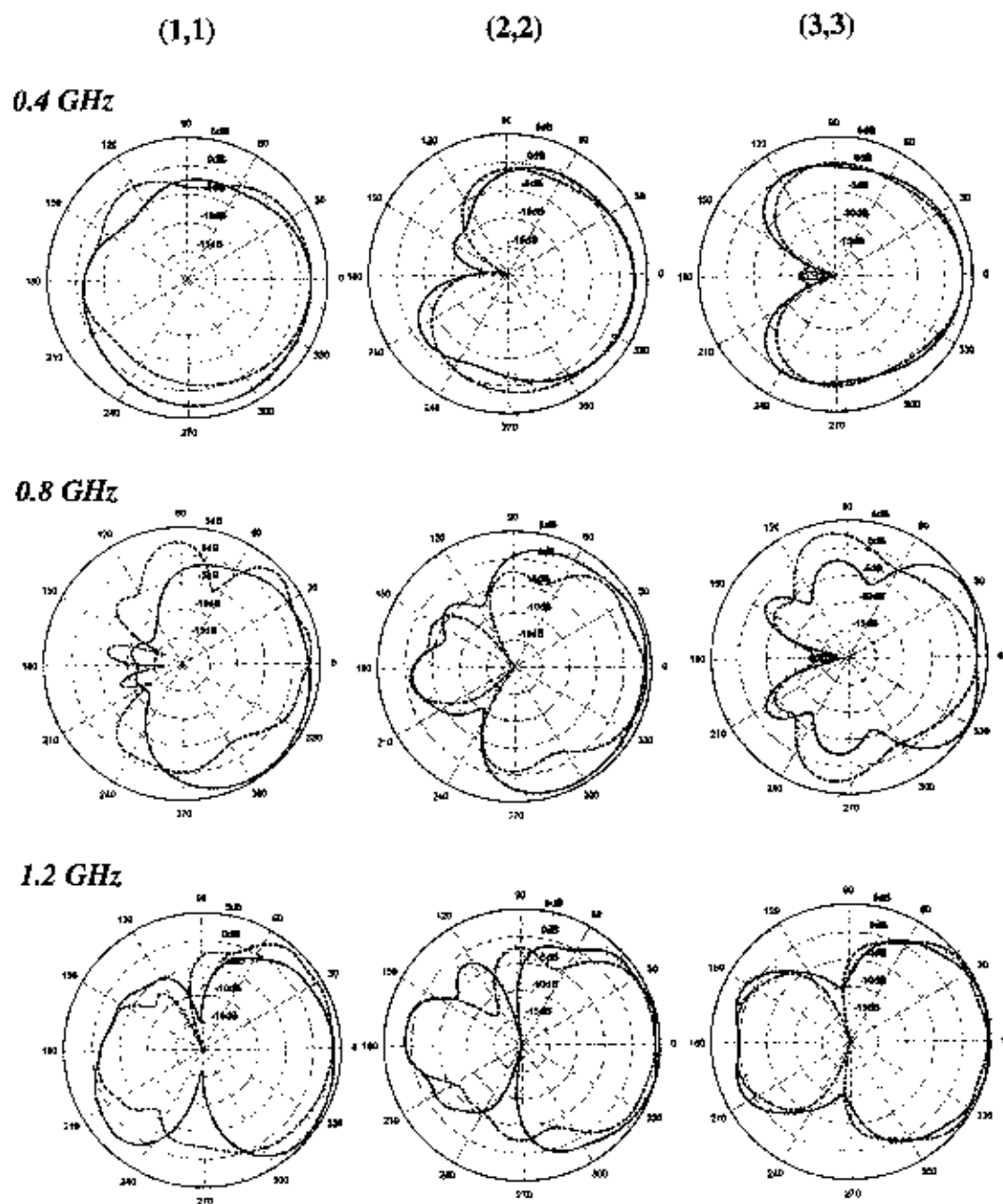


Fig. 16. Active element patterns in 5x5 single-polarized array: elements along diagonal at 0.4, 0.8 and 1.2 GHz. E-plane pattern in solid line and H-plane in dashed line.

6. PHASE CENTER LOCATION IN SMALL VIVALDI ARRAYS

In many applications, the location of the phase center of the antenna is important. For small arrays of Vivaldi antennas, the phase center locations of individual elements and of entire arrays have been investigated.

The phase center of single Vivaldi antennas is located along the centerline of the slot. Considering a conical region around boresight with total cone angle of approximately 20° , the z coordinate of the phase center (distance from the base of the antenna in Fig. 1) has been computed. For most cases studied to date, the phase center location for a particular plane of observation is reasonably constant over this cone. However, the phase center for the E-plane tends to be near the aperture of the antenna whereas the phase center for the H-plane is nearer the base of the antenna.

The phase centers in the principal planes are displayed in Fig. 17 for an isolated element, for the center element of a 3×3 array and for the fully active 3×3 array. In the latter case, the phase center is along the center axis of the array. The apparent phase center sometimes lies outside of the antenna, which extends from $z = 0$ to $z = 23.8$ cm. The E-plane and H-plane phase centers seldom coincide for this antenna design, but for most frequencies they are within one-half wavelength.

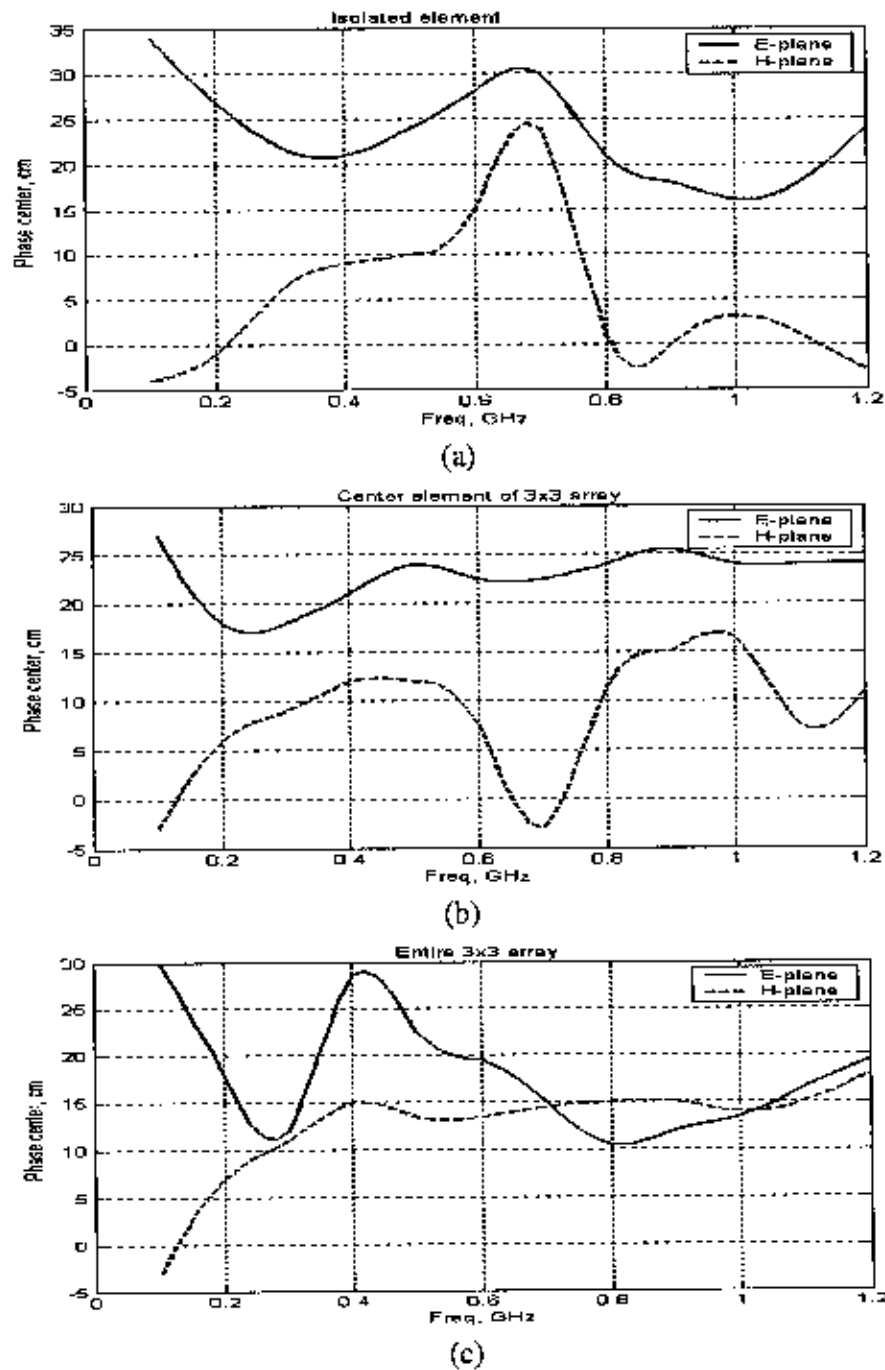


Fig. 17. Phase center location with respect to the element origin. (a) Isolated Vivaldi element. (b) Center element of 3x3 array when just that element is driven. (c) Entire 3x3 array.

SUMMARY

Mutual coupling and truncation effects in small arrays of Vivaldi tapered slot antenna arrays have been investigated. A particular dielectric-free Vivaldi antenna element was selected for study and its impedance and radiation patterns were studied over the frequency range 0.1 – 1.2 GHz, where an infinite array of the elements operates well. Infinite and finite arrays (2x10, 3x9, 5x5, 8x8, etc) of this element were analyzed by using a full-wave simulation code to determine active and passive input impedances, mutual coupling and radiation patterns. The behavior of the arrays and of the individual antennas within the arrays sometimes can be explained, at least heuristically, by considering a mutual coupling model or a wave-based model.

Although previous simulations of infinite arrays showed that mutual coupling plays a major role in wide-bandwidth performance, the studies reported here indicate that the resonances of the isolated element dictate the frequency bands where problems are likely to occur in small arrays. Calculated values of mutual coupling in the single-polarized arrays of dielectric-free antennas are similar to the values measured for a dual-polarized array of stripline-fed Vivaldi antennas.

Radiation patterns of elements in small arrays display asymmetries and truncation ripple as expected. The E-plane and H-plane phase centers of the antennas are not coincident, but they are within about one-half wavelength over most of the operating frequency range.

It is hoped that this and other studies of this type will lead to a better understanding of finite wide-bandwidth Vivaldi arrays, and that design procedures will evolve to mitigate the extensive computations required to design finite arrays.

ACKNOWLEDGEMENT

This work was supported in part by DSO National Labs. ASTRON provided partial support for development of the TDIE code used in this work.

REFERENCES

- [1] N. Schuneman, J. Irion and R. Hodges, Decade Bandwidth Tapered Notch Antenna Element, *Proceedings of the 2001 Antenna Applications Symposium*, 2001, Monticello, IL, pp. 280-294.
- [2] M. Kragalott, W.R. Pickles and M.S. Kluskens, "Design of a 5:1 Bandwidth Stripline Notch Array from FDTD Analysis," *IEEE Trans. Antennas Propagat.*, Vol. 48, November 2000, pp. 1733 – 1741.
- [3] D.H. Schaubert, "Scanning Characteristics of Stripline-Fed Tapered Slot Antennas on Dielectric Substrates," *Proceedings of the 1993 Antenna Applications Symposium*, Monticello, IL, September 1993.
- [4] T-H. Chio and D. H. Schaubert, "Parameter Study and Design of Wideband, Widescan Dual-Polarized Tapered Slot Antenna Arrays," *IEEE Trans. Antennas Propagat.*, Vol. 48, No. 6, pp. 879-886, June 2000.
- [5] W.R. Pickles and M. Kragalott, "Ultra-Broadband Phased-Array Antenna," *Proceedings of the 1999 Antenna Applications Symposium*, September, 1999, Monticello, IL, pp. 310-330.
- [6] J.H. Pozgay, "A Wideband Sub-Array Radiator for Advanced Avionics Applications," presented at the 1992 Antenna Applications Symposium, September 1992, Monticello, IL, (not printed in Proceedings).
- [7] T-H Chio, D. H. Schaubert and H. Holter, "Experimental Radiation and Mutual Coupling Characteristics of Dual-Polarized Tapered Slot Antenna (TSA) Arrays," *Proceedings of the 1999 Antenna Applications Symposium*, September, 1999, Monticello, IL, pp. 280-309. See also, H. Holter, T-H. Chio and D.H. Schaubert, "Experimental Results of 144-Element Dual-Polarized Endfire Tapered-Slot Phased Arrays," *IEEE Trans. Antennas Propagat.*, Vol. 48, November 2000, pp. 1701-1718.
- [8] H. Holter and H. Steyskal, "On the size requirement for finite phased-array models", *IEEE Trans. Antennas Propagat.*, Vol. AP-50, June 2002, pp. 836-840.
- [9] A.O. Boryssenko and D.H. Schaubert, "A Design Approach for Small Array of Dielectric-Free Vivaldi Antennas to Minimize Truncation Effects", accepted to *2003 Phased Array Symposium*, Boston, October 14-17.

- [10] A.O. Boryssenko, D.H. Schaubert and C. Craeye, "A Wave-Based Model for Mutual Coupling and Truncation in Finite Tapered-Slot Phased Arrays," *2003 IEEE Antennas and Propagation Society International Symposium Digest*, Vol. 4, pp. 11-14, Columbus, OH.
- [11] A.O. Boryssenko and D.H. Schaubert, "Time-Domain Integral-Equation-Based Solver for Transient and Broadband Problems in Electromagnetics", *AMEREM Symposium*, Annapolis, MD, June 2-7, 2002, pp. 1-11.
- [12] *Time-Domain Integral Equation Code: Description and Manual*, A.O. Boryssenko and D.H. Schaubert, Antenna Laboratory, University of Massachusetts, Amherst, MA, 2002.

ELECTRONICALLY CONTROLLED BEAM-STEERING ANTENNA (DEMO)

V.A. Manasson, L. Sadovnik, M. Aretskin, A. Brailovsky, P. Grabiec,
D. Eliyahu, M. Felman, V. Khodos, V. Litvinov, J. Marczewski, R. Mino
WaveBand Corporation
17152 Armstrong Ave.
Irvine, CA 92614

Abstract: A new type of electronically controlled beam-steering antenna has been experimentally demonstrated. The antenna architecture is different from that of conventional phased array antennas. The key element of the antenna is a semiconductor chip carrying an array of pixels that constitute a reconfigurable hologram. This W-band antenna is capable of continuously steering a beam or creating multiple beams in arbitrary directions. Samples of beam patterns are presented. We also provide a movie clip demonstrating antenna operation.

Electronically controlled phase delays (phase shifters) are key elements of any conventional phased array antenna (PAA). Phase shifters are used as solo devices and are also integrated into transmit/receive modules. The major disadvantage of using conventional phase-shifters is their high cost. When the cost of the necessary quantity (up to several thousands) is considered, the phased array becomes prohibitively expensive for most potential applications.

The antenna we describe here is based on a different architecture. There are no traditional phase shifters. The key element of the antenna is a semiconductor chip that carries a set of individually controlled PIN structures. Electromagnetic waves propagate through the chip, which also serves as a planar dielectric waveguide. The PIN structures (PINs) locally affect the wave propagation velocity and thus cause the semiconductor chip to function as a hologram. The monolithic design entails an enormous cost reduction. Antenna fabrication cost with this new architecture will even satisfy the automobile market with its very strict cost containment requirements.

The antenna fabricated for this demo contains a single silicon chip. Each of 216 PINs has an individual binary current control. The total power required to control

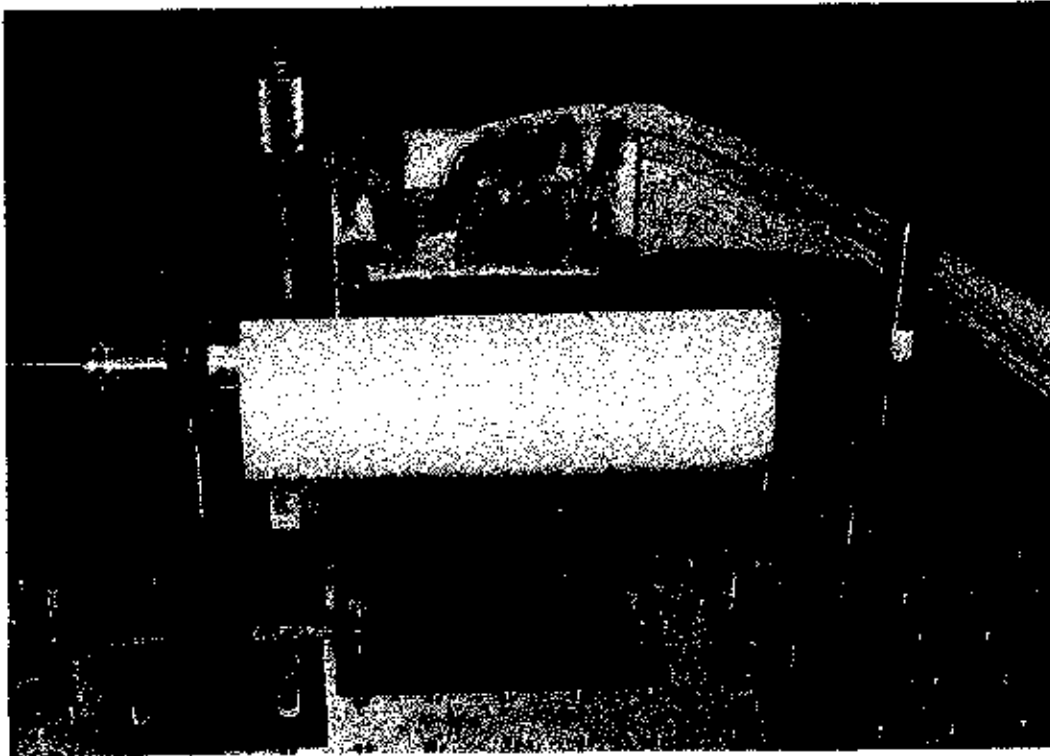


Fig. 1 Electronically controlled single chip antenna.

the entire aperture is less than one Watt. The aperture is fed through a single-mode dielectric waveguide with evanescent coupling between the waveguide and the silicon chip. We used a cylindrical lens to form the beam in the elevation plane (see Fig. 1). In the azimuth plane, the antenna can form a beam in practically any direction within a wide steering angle. Some examples of beam patterns are shown in Fig. 2. They were obtained at a frequency of 76 GHz in the transmitting mode using a near-field measurement technique (NSI near-field measurement system). The antenna is a reciprocal device that is capable of operating in the receiving mode as well. In the demo setup it was operating as a receiving millimeter-wave sensor.

Since the semiconductor chip behaves as a hologram, the antenna is capable of forming beam patterns of various shapes. Several examples of beam patterns comprising two independently controlled beams are shown in Fig. 3. This feature may be useful for simultaneous communication with two moving objects.

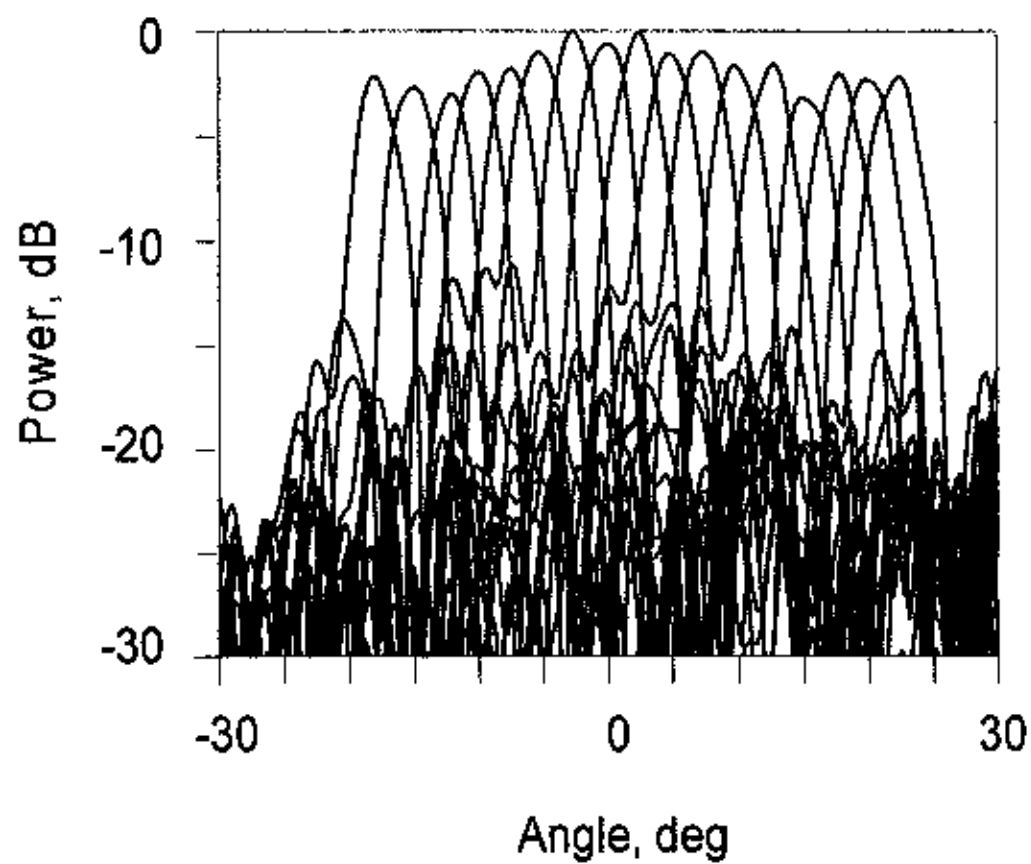


Fig. 2. Antenna possesses practically continuous beam-steering capability.

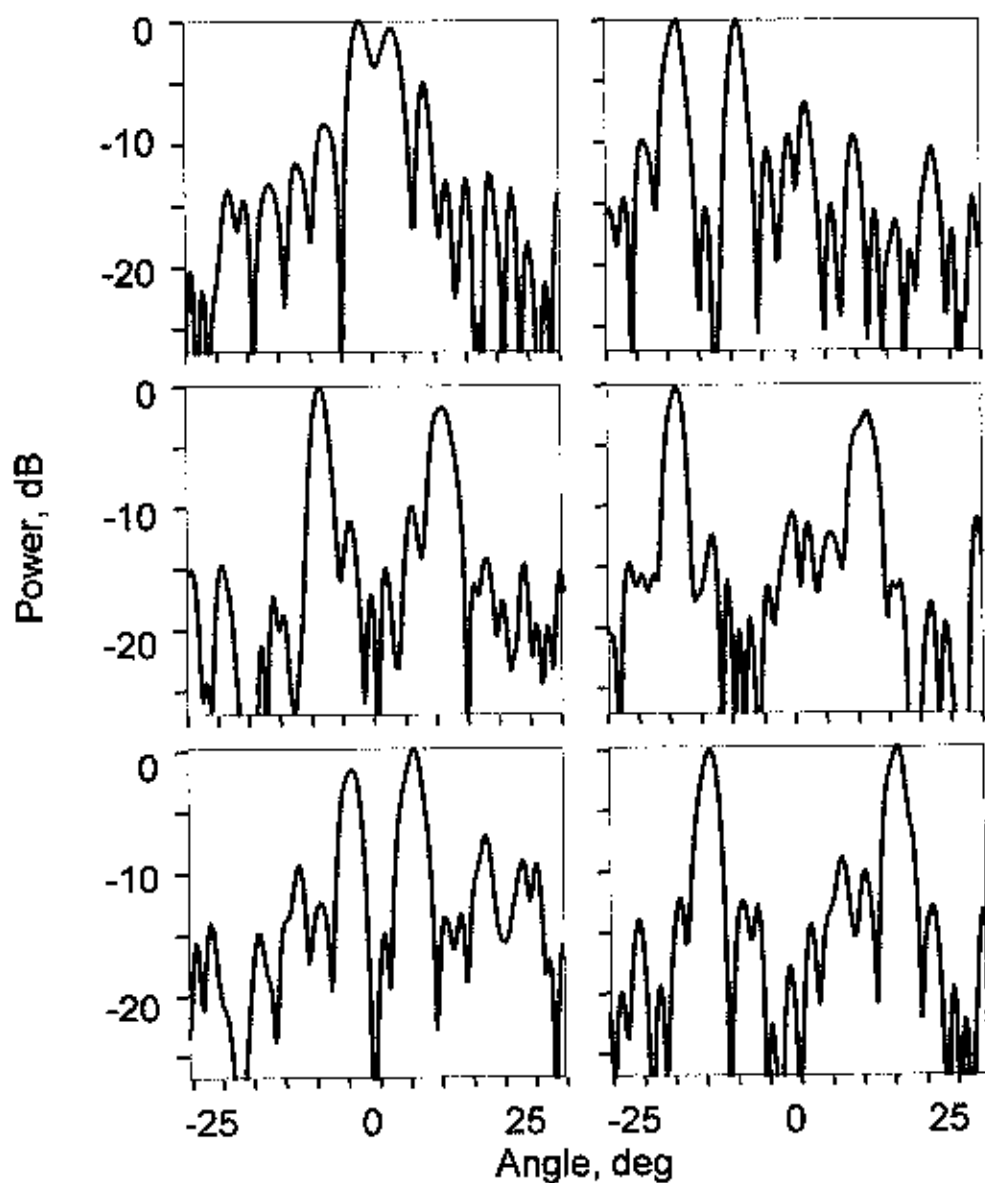


Fig.3. Examples of beam patterns comprising two simultaneous beams. Each beam direction was selected independently.

The operation of the single-chip electronically controlled beam steering antenna can be demonstrated using the setup shown in Fig.4.

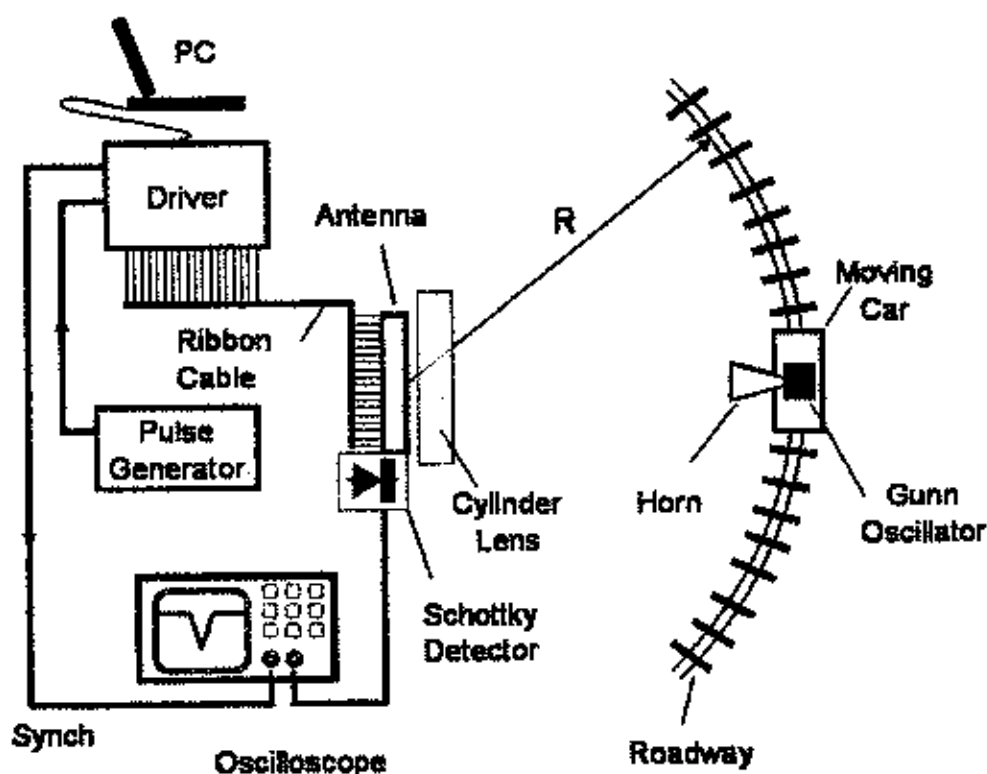


Fig. 4. Antenna demo setup. Railroad tracks

The antenna chip is connected to the driver. The driver, operating as a shift register, is controlled via a PC. The signal received by the antenna is detected by the Schottky diode and displayed on the oscilloscope screen. To synchronize the oscilloscope scan and antenna scan, we use a pulsed generator, which also serves as a clock that synchronizes the hologram recording. The driver converts a series pulse sequence from the PC into parallel current pulses feeding the chip PINs. To record a single antenna pattern, 216 pulses are required to be sent from the PC to the driver. Less than 10 μ s is needed to switch from one antenna pattern to another. The scanning cycle consists of 80 sequential antenna patterns with a main lobe step of 0.5 deg. The full scan time is ~ 1 ms.

In summary, we have experimentally demonstrated, for the first time, the feasibility of single-chip beam steering at W-band. The antenna showed excellent beam-control over a steering range of 45 degrees with a beam-switching time as short as 10 μ sec. Potential applications of this technology include missile seekers, airborne and space radar, aircraft landing guidance systems, and automotive collision warning sensors.

A K_a -BAND ELECTRONICALLY SCANNED ANTENNA FOR MULTI-FUNCTION RF APPLICATIONS

R. Dahlstrom, S. Weiss, E. Viveiros, A. Bayba, and E. Adler
U.S. Army Research Laboratory
2800 Powder Mill Road
Adelphi, MD 20783
dahlstrom@arl.army.mil

Abstract: An electronic scanning antenna (ESA) that uses a beamformer such as a Rotman lens has the ability to form multiple beams for shared-aperture applications. This characteristic makes the antenna suitable for integration into systems exploiting the Multi-Function Radio Frequency (RF) concept, meeting the needs for a Future Combat System (FCS) RF sensor. Such an antenna has been built and successfully tested at ARL to be used in a system to demonstrate this multiple-beam, shared-aperture capability at K_a band. Each antenna, one for transmit and one for receive, consists of the Rotman lens for azimuthal beamforming, with 19 beam ports and 34 array ports, a 2 channel by 16 port PIN-diode switch for beam selection for each of two channels, 32 MMIC amplifiers at the active array ports, and an eight by 32 aperture-fed microstrip patch array, which provides focusing in elevation. We will discuss the development of the antenna including future efforts and present the results of measurements of its performance.

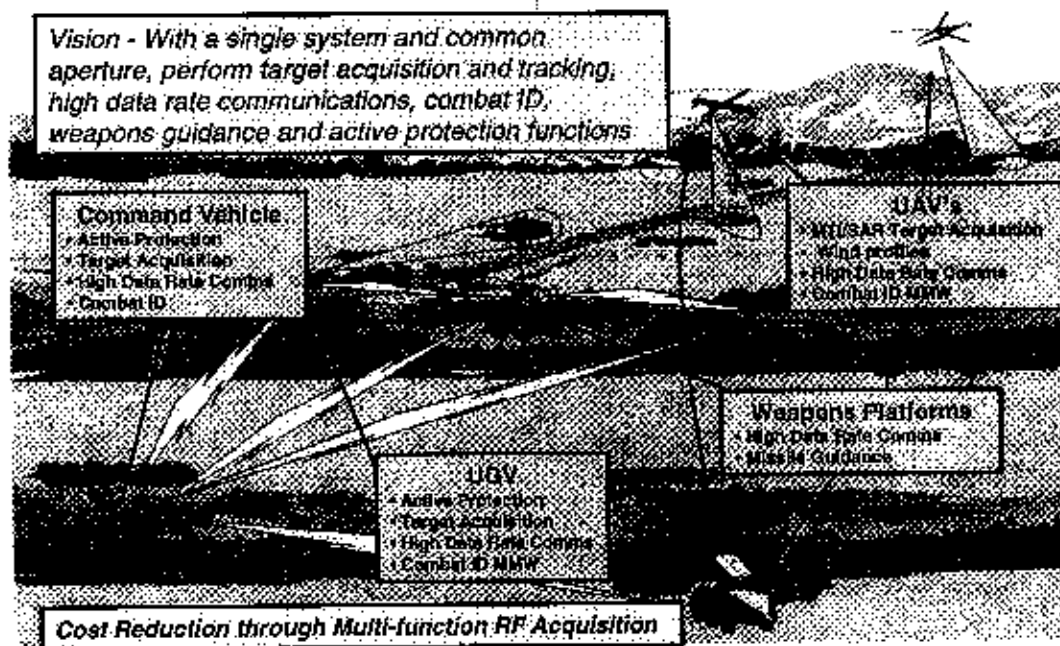


Figure 1. Multi-function RF concept

1. INTRODUCTION

The U.S. Army Research Laboratory (ARL) is currently pursuing key technologies for low-cost, advanced battlefield sensors for multimode radar and communication platforms as shown in figure 1. These radar and communication functions include active/passive target acquisition, combat identification, weapons guidance, secure point-to-point communications, active protection, networks for situational awareness, and signal intercept. Typically, each of these functions is performed by a separate piece of equipment specifically designed for that purpose, with its own electronics package and antenna. As more of these functions are added to a vehicle, the available space suitable for antennas is quickly depleted, and costs and weight increase rapidly. Incorporating multiple-function components into these systems can considerably reduce total system size, weight, and cost. By sharing a single antenna aperture, one can time- and/or frequency-multiplex both radar and communications functions, or, in the case of multiple-beam antennas, perform them simultaneously. One such approach, described herein, uses one K_a -band, multipurpose, electronic scanning antenna (ESA) to perform the functions required by several systems [1].

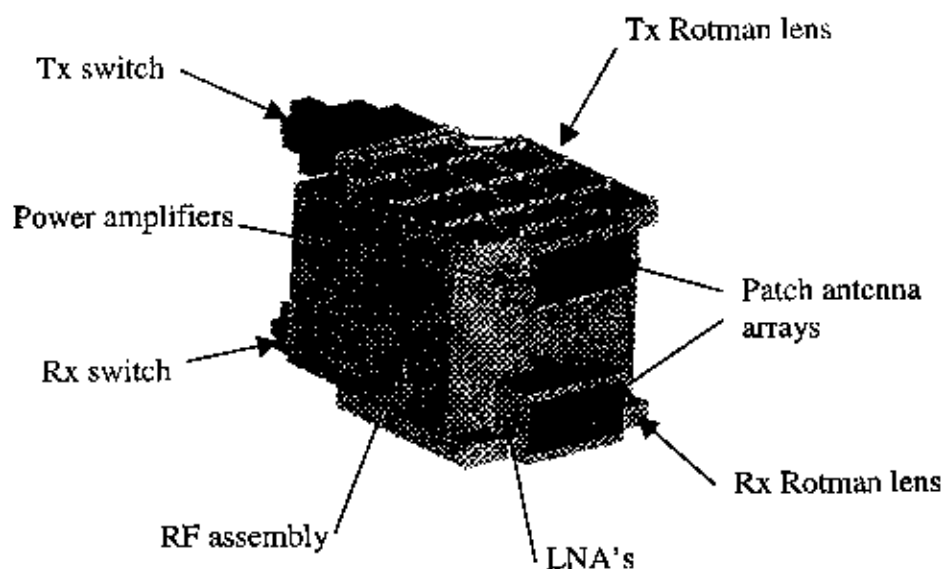


Figure 2. MFRF antenna configuration

2. SYSTEM DESCRIPTION

In the K_a -band ESA we have developed, shown in figure 2, we achieve the simultaneous performance of multiple functions by combining a multiple-beam antenna array with a PIN-diode switching network while maintaining a broad overall system bandwidth of better than 36 to 40 GHz. The complete antenna system consists of a 16 (vertical) x 32 (horizontal) array of slot-fed microstrip patch radiators fed by the Rotman lens horizontally, and by microstrip corporate

feeds vertically. The lens has 19 input ports, with the port on each end intended to be terminated to provide a symmetric environment for the remaining ports. The center 17 ports correspond to azimuth beam-scanning positions covering ± 22.5 degrees from broadside. A dual-channel beam-switching network (BSN) is used to select one of the beams for each channel. For transmit, 32 power amplifiers are inserted between the output ports of the lens and the patch array to increase the power radiated. A single amplifier could have been placed at the input to the switch, but a higher power amplifier would have been needed to make up for the losses in the switch and the lens and a much higher power switch would have been needed to avoid exceeding its power handling capability. For receive, low noise amplifiers are used between the lens and the patch array to minimize degradation of receiver noise figure by losses in the Rotman lens and the switch.



Figure 3. Demonstration multi-function RF system

The transmit and receive lens assemblies are used as the top and bottom of the MFRF system package with the patch arrays mounted in between as shown in figure 3.

3. ESA OPERATION

Operation in an electronically scanned mode involves remotely controlling the BSN to switch either of the signal source inputs to any of the 17 beam ports of the Rotman lens, in a sequential or random scan, as desired. Adding time-multiplexed functions requires only that the appropriate beam selection be made at the same time as the input signal is switched. A fixed-beam communication channel can be added by coupling to the appropriate beam port. In a similar

manner, incorporating additional functions merely adds to the complexity of the BSN, not of the antenna itself.

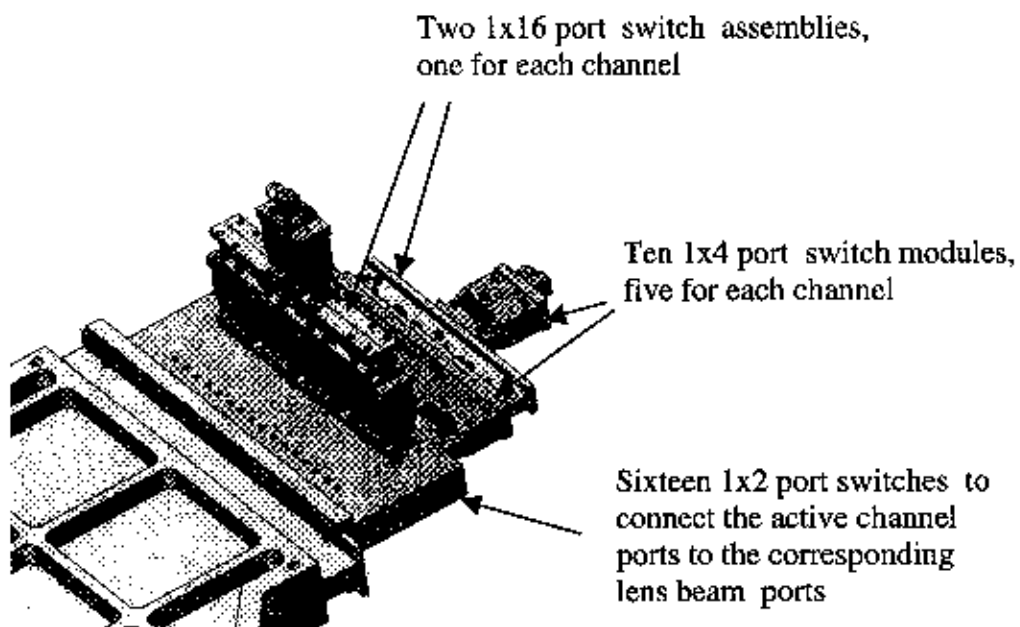


Figure 4. Trex Enterprises 2x16 PIN diode switch

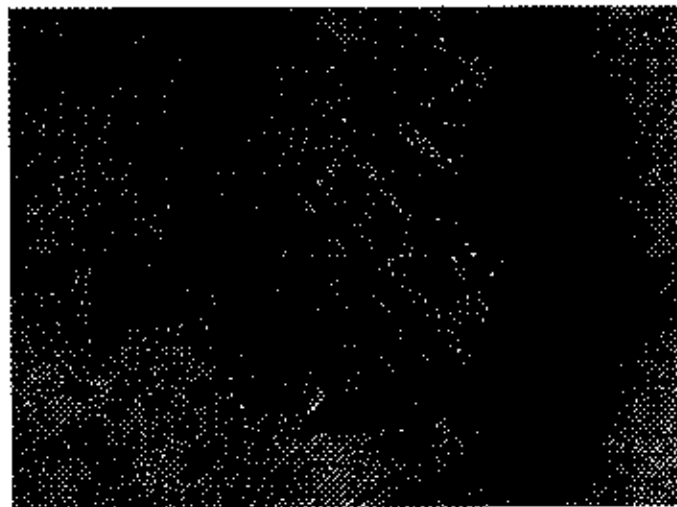


Figure 5. Photo of Trex PIN-diode switch

4. BEAM-SWITCHING NETWORK

The 2x16 BSN is an array of PIN-diode switches that operates from 36 to 40 GHz. The PIN-diode switch configuration is shown in figure 4. It uses SPDT switch elements in four successive stages to achieve 1x16 switching. To achieve 2x16 switching, each of these 1x16 switches is followed by an array of sixteen

SPDT switches to connect the selected output of each to the corresponding lens beam port. In addition, switching is provided to terminate unused ports. Since the signal passes through six stages of switching in the 2x16 configuration, it is important that the loss of each stage be minimized. Even with a loss of only 1 dB

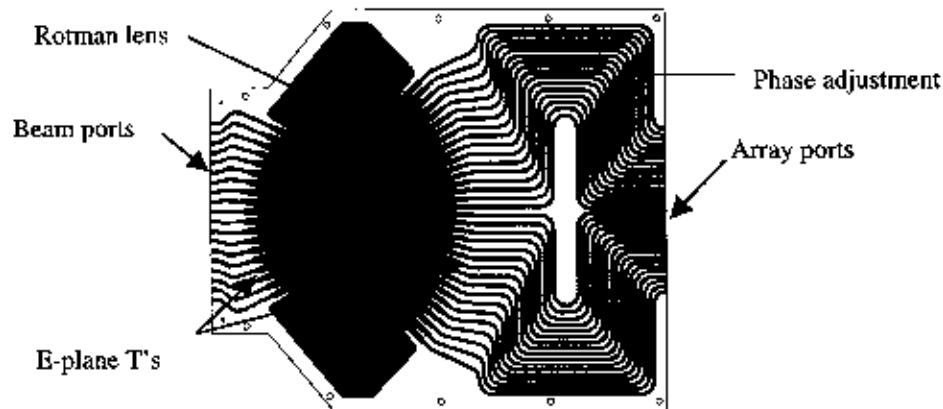


Figure 6. Rotman lens - Shaded areas show signal paths

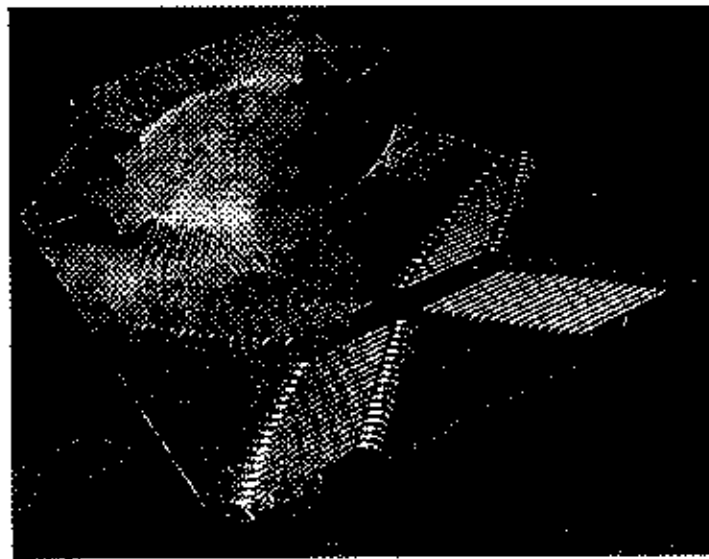


Figure 7. Rotman lens – one half shown, with absorber

per stage, additional losses due to transitions and interconnects in a microstrip package could bring the total insertion loss up to nearly 10 dB. By using switch elements optimized in the 36 to 40 GHz frequency range and interconnecting them with low-loss wave guide, the measured insertion loss was brought down to 3 to 6 dB over the band for all ports. The switch assembly is shown in figure 5.

5. ROTMAN LENS

The key to achieving a low-cost, compact, multibeam antenna is the use of a Rotman lens to provide the appropriate phasing to each element of the array. The lens has 19 beam ports (shown on the left in figure 6) that couple the signal into the broad parallel-plate region of the lens. The lens' geometry is chosen so that each beam port, by virtue of its position, produces the desired array phasing for its associated beam angle at the output ports. The direction of the beam radiating from the antenna can therefore be controlled by selection of an appropriate beam port. In addition, the amplitudes at the outputs are somewhat greater in the center, potentially reducing the first sidelobes below the 13 dB which would otherwise be expected for uniform excitation. The Rotman lens design differs from that of other lenses in that it has three perfect focal points on the beam feed, with the other sources approximated on a circular focal arc. In other words, when a source is turned on at one of these foci, a linear phase taper appears across the linear

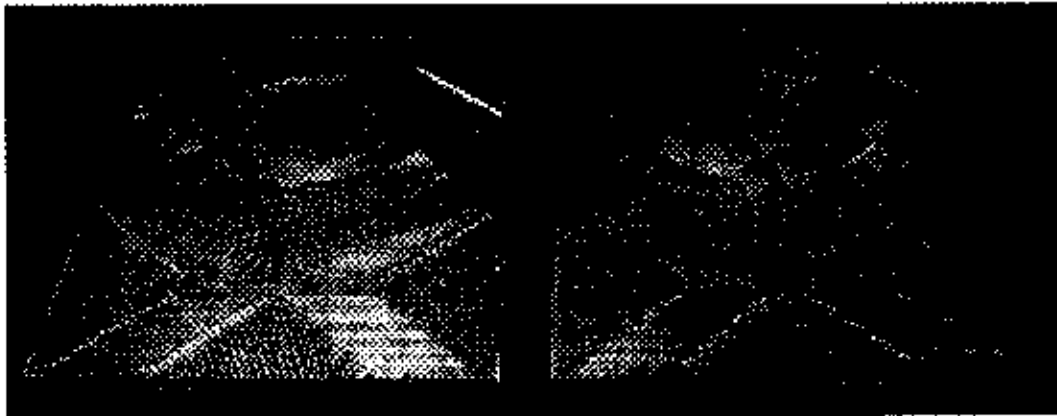


Figure 8. Rotman lens – mating halves shown

array of output ports. The small phase errors at the intermediate positions do not significantly degrade antenna performance. The Rotman lens is an inherently wide-bandwidth device, because the path lengths to the output ports correspond to a true time delay, rather than just providing the desired phase. Therefore, the correct phasing is achieved independently of frequency. The medium used for this lens is waveguide, with the E field oriented parallel to the broad walls of the lens to reduce reflections at the input and output ports. In this orientation, the wavelength of the signal traveling through the lens is a function of the wall spacing. The corresponding variation of the velocity of propagation of the signal in the lens causes a shift in beam angle with frequency for angles off broadside. Using an E field oriented perpendicular to the broad walls of the lens could eliminate this effect, but over the limited frequency range used here, the beam shift is small, about $\pm 4\%$. The Rotman lens design is based on one provided to ARL by the Georgia Tech Research Institute [2, 3].

The lens was fabricated from rectangular blocks in symmetric halves as shown in figures 7 and 8 with absorber installed. This splits the waveguides in the center of the broad wall, where the current is at a minimum, and also reduces vertical cutting depth for the dimensionally sensitive features. The thickness of the lens was made substantially greater than the waveguide height (7X) for structural rigidity (bending stiffness is increased by nearly 300X). The penalty is increased mass. However, pocketing the non-lens side of the blocks reduced the weight. For fabrication tolerances, it was determined that critical side-to-side dimensions should be held to $\pm .003''$, but that the tolerance for the depth should be limited to $\pm .0005''$. Of particular concern was flatness and alignment of the mating surfaces of the two halves. To address the alignment, pins were incorporated; and to ensure contact of mating surfaces, fourteen $\frac{1}{4}$ -20 bolts were used – together producing a nominal contact pressure of 250 psi. The material chosen was aluminum (alloy 6061-T6).

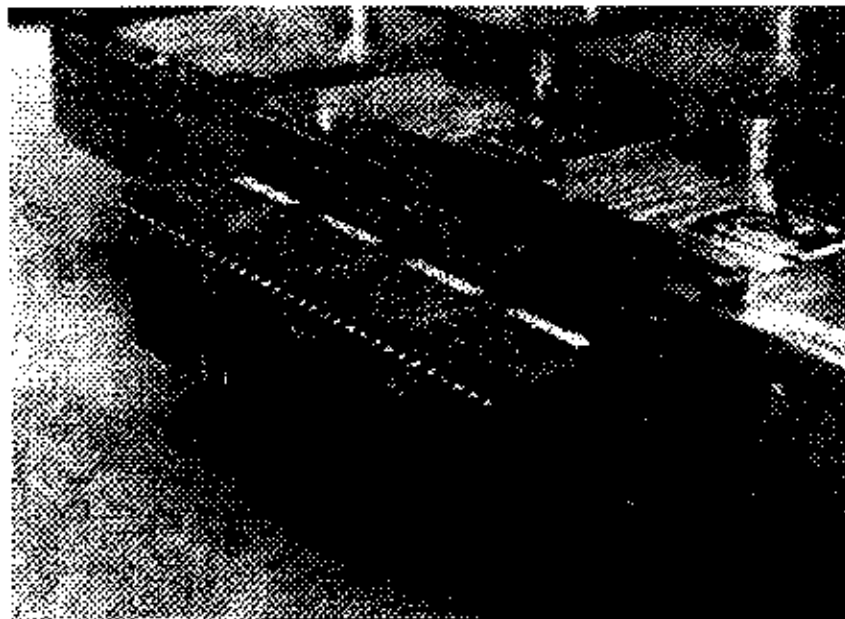


Figure 9. Amplifier assemblies mounted on Rotman lens

6. AMPLIFIERS

MMIC amplifiers, 1-watt power amps for transmit and 2.1 dB noise figure low-noise amps for receive, are packaged eight to a module and mounted to the array ports of the lens as shown in figure 9. A Quasi-Yagi waveguide-to-microstrip transition is at the lens interface and Corning Gilbert GPPO connectors are used to connect to the patch array. Figure 10 shows the amplifiers mounted on the microstrip substrate and figure 11 shows the completed antenna assembly.



Figure 10. MMIC amplifiers on microstrip

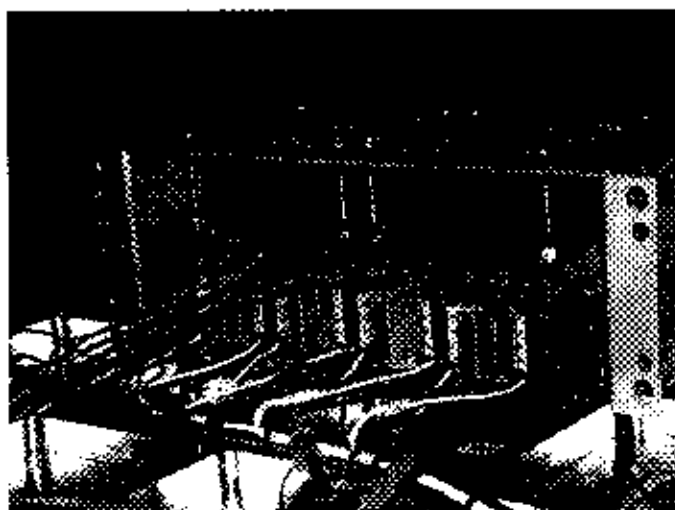


Figure 11. MMIC amplifiers mounted to lens and patch array

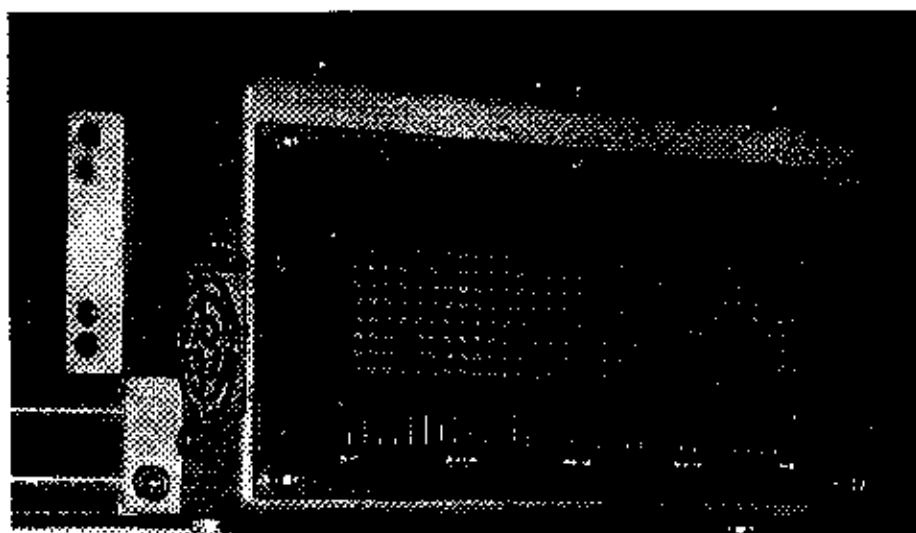


Figure 12. Patch array mounted to antenna/amplifier assembly

7. PATCH ARRAY

A slot-fed patch array, shown in figure 12, was used for the radiating element because it is broadband, compact, and can provide scanning in elevation in the

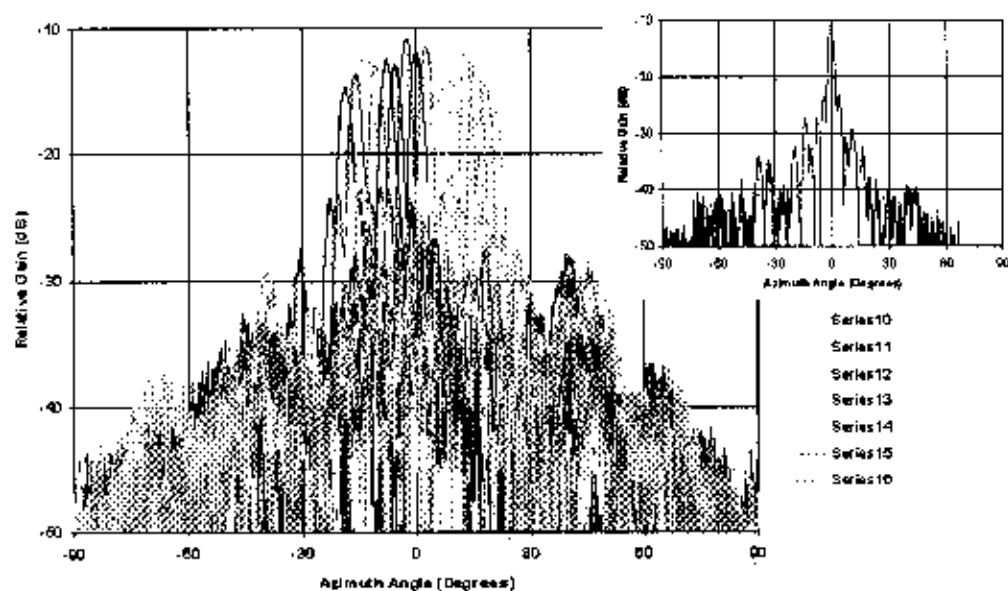


Figure 13. Measured receive patterns at 36.8 GHz

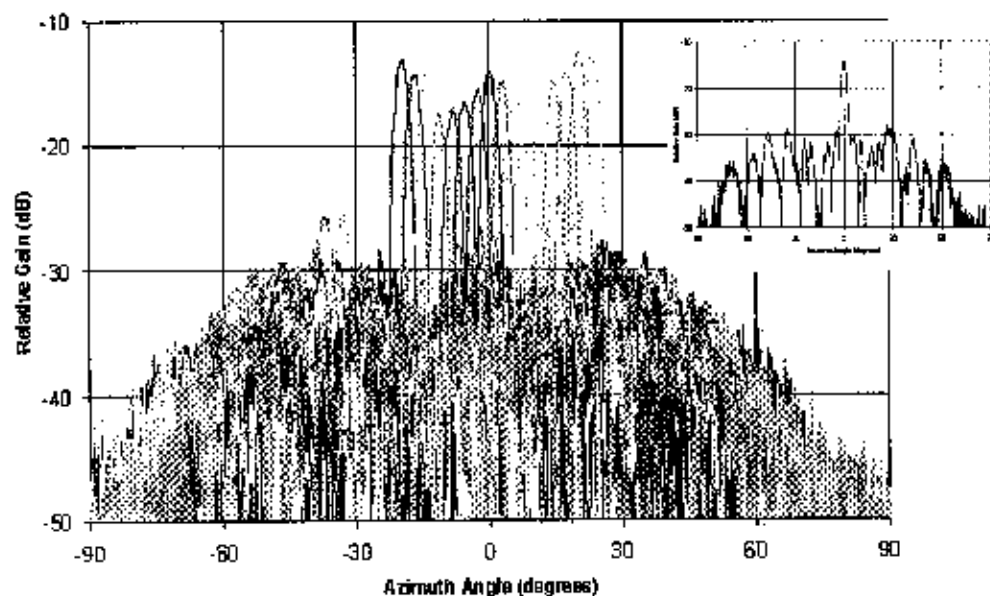


Figure 14. Measured receive patterns at 38.6 GHz

future, although a fixed beam antenna is currently used, providing a 10-degree broadside beam.

8. ANECHOIC CHAMBER MEASUREMENTS

The antennas were tested in an anechoic chamber at ARL. Beam scanning in azimuth was measured to be greater than 22 degrees. The radiation pattern of the receive antenna for the center (broadside) beam and all beams superimposed is

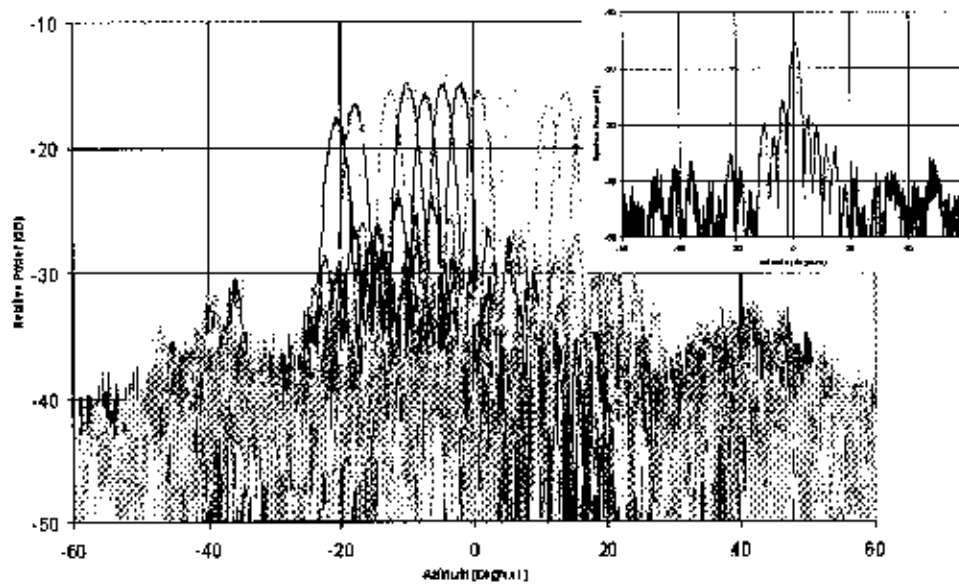


Figure 15. Measured transmit patterns at 36.8 GHz

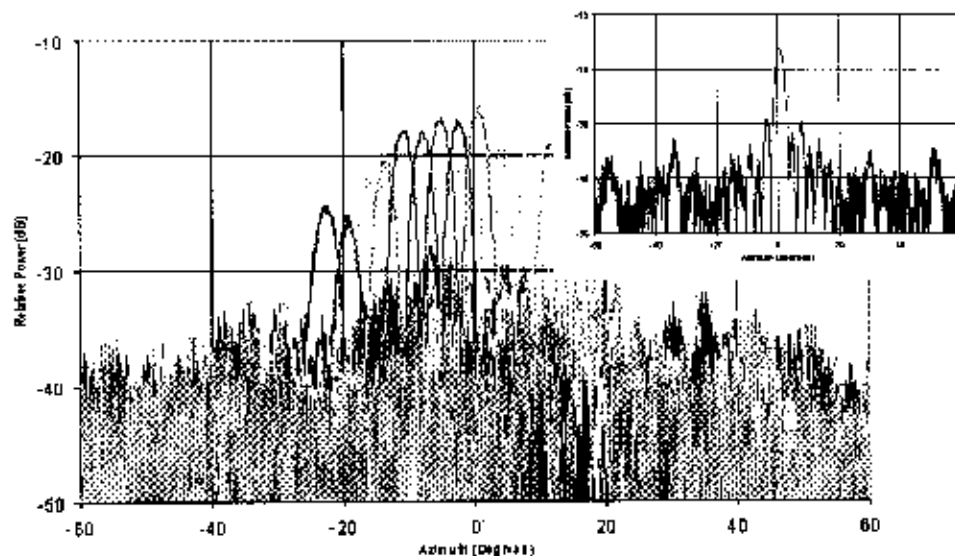


Figure 16. Measured transmit patterns at 38.6 GHz

shown in figure 13 at 36.8 GHz and in figure 14 at 38.6 GHz. Similar patterns are shown for transmit in figures 15 and 16. Receive and transmit gains are given in

figures 17 and 18, respectively. The measured performance is summarized in table 1.

9. FUTURE PLANS

Ongoing efforts related to this work include reducing the size, weight, and loss of the Rotman lens while increasing the scan range, adding the ability to electronically scan in elevation, and creating switch technologies that continue to be reliable, compact, and low loss with increased numbers of channels and ports.

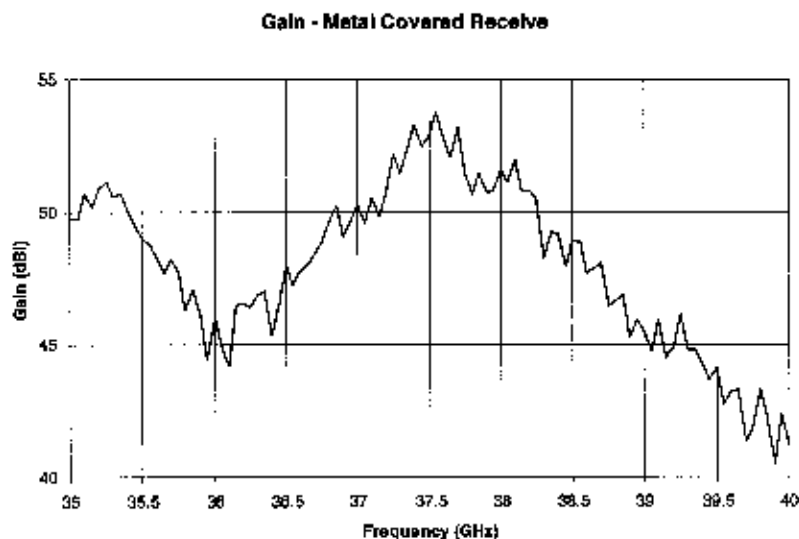


Figure 17. Measured receive gain

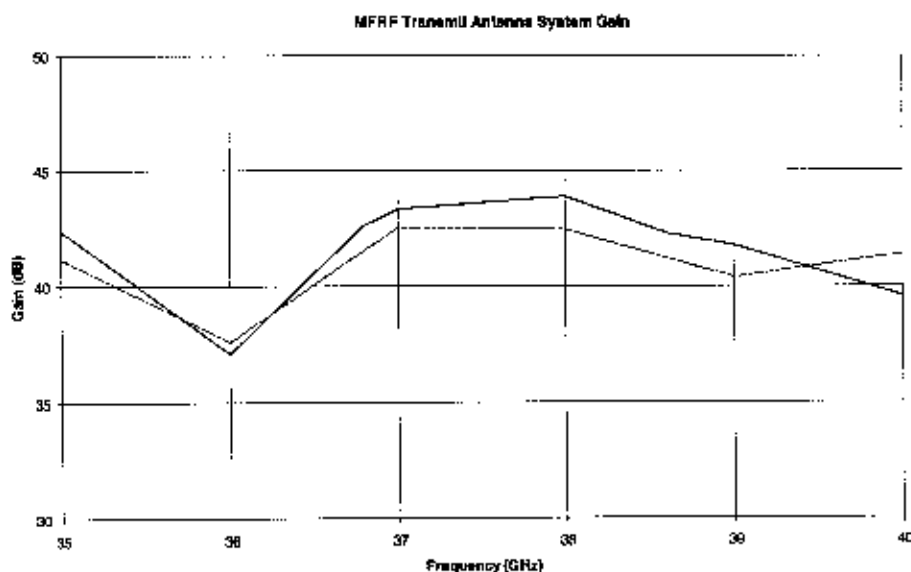


Figure 18. Measured transmit gain

Architectures under evaluation include cavity-based designs and stripline configurations using various dielectrics. In the area of BSN development, we are pursuing crossbar or tapped-line designs and exploring other technologies.

10. CONCLUSION

An electronically scanned antenna system has been described that has the potential to meet the needs of one or more radar and/or communications systems residing on a single platform. Sharing the antenna aperture in this way makes it unnecessary to have separate antennas for each system. The advantages of this technique include smaller total size, less weight, and lower cost. With further enhancements in Rotman lens architectures, BSNs, and wideband apertures; multimode and multibeam affordable ESA's will surely have a great impact on future combat systems.

Parameter	Specification
Antenna gain, Receive	41-53 dBi (with low-noise amplifiers)
Antenna gain, Transmit	36-44 dBi (with power amplifiers)
Azimuth beamwidth	2.6° nominal at 38 GHz
Azimuth sidelobes	11 dB peak at center, 9 dB with scan
Polarization	Vertical
Beam scan	±22.5° azimuth (17 beams)

Table 1. Multi-function RF antenna performance

REFERENCES

1. S. Weiss, R. Dahlstrom, O. Kilic, E. Viveiros, S. Tidrow, F. Crowne, E. Adler, "Overview of the Multifunction RF Effort – An Army Architecture for an Electronically Scanned Antenna," *Proceedings of the 2002 Antenna Applications Symposium*, pp. 119-129.
2. E. O. Rausch, A. F. Peterson, and W. Wiebach, "A Low Cost, High Performance, Electronically Scanned MMW Antenna," *Microwave J.*, vol. 40, no. 1, pp. 20-32, January 1997.
3. E. O. Rausch, A. F. Peterson, and W. Wiebach, "Millimeter Wave Rotman Lens," *Proceedings of the 1997 IEEE National Radar Conference*, pp. 78-81, May 1997.
4. R. Dahlstrom, A. Bayba, "A Rotman Lens Implementation for Multi-Function RF Antenna Applications," *Proceedings of the 2002 Antenna Applications Symposium*.

5. T. Katago, S. Mano, and S. Sato, "An Improved Design Method of Rotman Lens Antennas," *IEEE Trans. Antennas and Propagation*, vol. AP-32, no. 5, pp. 524–527, May 1984.
6. H.-H. Fuchs, D. Nüßler, "Design of Rotman lens for beamsteering of 94 GHz antenna array," *Electronic Letters*, vol. 35, no. 11, pp. 854-855, 27 May 1999.

Impedance, Bandwidth and Q of the General One-Port Antenna

Steven R. Best and Arthur D. Yaghjian¹
Air Force Research Laboratory
Sensors Directorate, Antenna Technology Branch
80 Scott Drive
Hanscom AFB, MA 01731

1. INTRODUCTION

In this paper, an approximate expression is presented for the bandwidth of a single-feed (one-port), lossy (or lossless) antenna in terms of its input impedance. This expression for bandwidth is valid for all ranges of frequency, that is, throughout the entire antiresonant as well as resonant frequency regions of the antenna. Both conductance and matched VSWR (voltage-standing-wave-ratio) bandwidth are considered. It is shown that the inverse of the matched VSWR bandwidth is a more reliable quantity for approximating the antenna Q over a wider range of frequencies. The approximate expression for the matched VSWR bandwidth of a tuned antenna differs from previous expressions in that it is inversely proportional to the magnitude of the frequency derivative of the antenna's input impedance, Z , at every frequency.

The antenna quality factor, Q , is defined independently of bandwidth as 2 times the ratio of average "reactive energy" in the fields of the antenna to the energy dissipated in a period by the antenna in the form of radiated power and power loss. An exact expression for the Q of a general, one-port, lossy or lossless antenna is then presented in terms of two dispersion energies and the frequency derivative of the input reactance of the antenna. The values of these dispersion energies are determined from both the radiation fields and the fields within the antenna material. The far-field dispersion energy, W_R , is determined from subtracting the radiation-field energy of the antenna from its total-field energy to get a finite "reactive energy". The material-loss dispersion energy, W_L , is determined from the fields within the antenna material.

It is also shown that the defined Q of the antenna is approximately proportional to the magnitude of the frequency derivative of the antenna's input impedance and thus, the Q is inversely proportional to the matched VSWR bandwidth of the antenna at all frequencies. The approximate expression for the antenna bandwidth and its relationship to Q are both more generally applicable and more accurate than previous formulas.

¹ Visiting Scientist

Numerical solutions to thin, straight-wire and wire-loop, lossy and lossless antennas confirm the accuracy of the approximate expressions and the inverse relationship between matched VSWR bandwidth and the defined Q over frequency ranges that cover several resonant and antiresonant frequency bands.

2. ANTENNA IMPEDANCE AND ITS FREQUENCY DERIVATIVE

Consider the general one-port antenna as depicted in Figure 1. The feed point impedance of this general antenna is a complex quantity $Z(\omega)$, defined as

$$Z(\omega) = R(\omega) + jX(\omega) \quad (1)$$

where $R(\omega)$ is the frequency dependent feed point resistance and $X(\omega)$ is the frequency dependent feed point reactance. (Note that radian frequency ω , being equal to 2π times the frequency in Hz, is used to define the frequency dependent properties of the antenna.) The bandwidth and Q of this general antenna are defined under the condition where the antenna is tuned at a frequency ω_0 with a series reactance $X_s(\omega)$ (comprised of a series inductance L_s or a series capacitance C_s), where the tuned antenna feed point impedance is written as

$$Z_o(\omega) = R_o(\omega) + jX_o(\omega) \quad (2)$$

where,

$$X_o(\omega) = X(\omega) + X_s(\omega) \quad (3)$$

and where

$$X_s(\omega) = \begin{cases} \omega L_s, & X(\omega_0) < 0 \\ \frac{1}{\omega C_s}, & X(\omega_0) > 0 \end{cases} \quad (4)$$

At the tuned frequency ω_0 ,

$$X_o(\omega_0) = X(\omega_0) + X_s(\omega_0) = 0 \quad (5)$$

The frequency derivative of $X_o(\omega)$ with respect to ω can be written at the tuned frequency ω_0 as

$$\frac{dX_o}{d\omega}(\omega_0) = \frac{dX}{d\omega}(\omega_0) + \frac{|X(\omega_0)|}{\omega_0} \quad (6)$$

and the magnitude of the frequency derivative of $Z_O(\omega)$ with respect to ω can be written at the tuned frequency ω_O as

$$\left| \frac{dZ_O}{d\omega}(\omega_O) \right| = \sqrt{\left[\frac{dR_O}{d\omega}(\omega_O) \right]^2 + \left[\frac{dX_O}{d\omega}(\omega_O) \right]^2} \quad (7)$$

If the tuning reactances, L_S and C_S , are assumed to be lossless, the tuned antenna's resistance and its frequency derivative are equal to those of the untuned antenna. Assuming lossless reactances and substituting (6), equation (7) becomes

$$\left| \frac{dZ_O}{d\omega}(\omega_O) \right| = \sqrt{\left[\frac{dR}{d\omega}(\omega_O) \right]^2 + \left[\frac{dX}{d\omega}(\omega_O) + \frac{X(\omega_O)}{\omega_O} \right]^2} \quad (8)$$

3. ANTENNA BANDWIDTH AND QUALITY FACTOR

In this section of the paper, expressions for antenna bandwidth and quality factor are presented. The detailed derivations for these expressions are not presented here as this is not intended to be the main focus of this work. Rather, the focus of this work is to demonstrate the usefulness and validity of these expressions through a complete set of numerical solutions to several lossless and lossy antennas, which include a straight-wire (dipole) antenna; a circular-loop antenna; a very lossy, low Q antenna; and a lossy, electrically small antenna. Detailed derivations of the expressions for bandwidth and Q can be found in [1] and [2].

3.1 Conductance Bandwidth

The conductance bandwidth for an antenna tuned at a frequency ω_O is defined as the difference between the two frequencies at which the power accepted by the antenna (including both radiated power and power loss), excited by a constant voltage, is a given fraction of the power accepted at the frequency ω_O . The conductance at a frequency ω of an antenna tuned at the frequency ω_O can be written as

$$G_O(\omega) = \frac{R_O(\omega)}{R_O^2(\omega) + X_O^2(\omega)} \quad (9)$$

From (9), it can be seen that there is a problem with using conductance bandwidth, namely, that the frequency derivative of $G_O(\omega)$ evaluated at ω_O equals

$$\frac{dG_o}{d\omega}(\omega_o) = \frac{-\frac{dR_o}{d\omega}(\omega_o)}{R_o^2(\omega_o)} \quad (10)$$

and thus it is not zero at ω_o unless $\frac{dR_o}{d\omega}(\omega_o) = 0$. This means that in general, the conductance bandwidth will not reach a maximum at the frequency ω_o . In antiresonant frequency ranges where both the resistance and the reactance of the antenna are changing rapidly with frequency, the conductance may not possess a maximum and consequently the conductance bandwidth may not exist in these antiresonant frequency regions.

At frequencies well away from the antiresonant frequency regions of most antennas, $\frac{dX_o}{d\omega}(\omega_o)$ is greater than zero and $\left| \frac{dR_o}{d\omega}(\omega_o) \right|$ is much smaller than $\left| \frac{dZ_o}{d\omega}(\omega_o) \right|$. Under these conditions the conductance will peak at a frequency much closer to ω_o than the bandwidth and a simple expression for the conductance bandwidth can be found. If it is assumed that the power accepted by the antenna at frequencies $\omega = \omega_o + \Delta\omega_{\pm}$ is equal to $(1 - \alpha)$ times its value at ω_o then the conductance bandwidth is given by

$$FBW_{cw} = \frac{\Delta\omega_+ - \Delta\omega_-}{\omega_o} \approx \frac{2\sqrt{\beta} R_o(\omega_o)}{\omega_o \left| \frac{dZ_o}{d\omega}(\omega_o) \right|} \quad (11)$$

$$\text{where } \sqrt{\beta} = \sqrt{\frac{\alpha}{1-\alpha}} \leq 1.$$

For most tuned antennas operating near resonant frequency regions, where $\frac{dX_o}{d\omega}(\omega_o) > 0$ and $\left| \frac{dR_o}{d\omega}(\omega_o) \right| \ll \left| \frac{dZ_o}{d\omega}(\omega_o) \right|$, the conductance bandwidth of the antenna has generally been written as follows [3]

$$FBW_{cw} \approx \frac{2\sqrt{\beta} R_o(\omega_o)}{\omega_o \frac{dX_o}{d\omega}(\omega_o)} \quad (12)$$

For the half-power conductance bandwidth, $\beta = 1$, and equations (11) and (12) simplify accordingly. It is important to note that in antiresonant regions of the antenna, where $\frac{dX_o}{d\omega}(\omega_o) < 0$, equation (12) will not approximate the bandwidth of the tuned antenna.

3.2 Matched VSWR Bandwidth

The matched VSWR bandwidth for an antenna tuned at a frequency ω_0 is defined as the difference between the two frequencies on either side of ω_0 at which the VSWR equals a constant s , or, equivalently, at which the magnitude squared of the reflection coefficient

$|\Gamma_o(\omega)|^2$ equals $\alpha = \frac{(s-1)^2}{(s+1)^2}$, provided the characteristic impedance Z_{CH} of the feed line equals $Z_o(\omega_0) = R_o(\omega_0)$. The magnitude squared of the reflection coefficient can be written as follows

$$|\Gamma_o(\omega)|^2 = \frac{X_o^2(\omega) + [R_o(\omega) - R_o(\omega_0)]^2}{X_o^2(\omega) + [R_o(\omega) + R_o(\omega_0)]^2} \quad (13)$$

Both $|\Gamma_o(\omega)|^2$ and its derivative with respect to ω are zero at ω_0 . Consequently, $|\Gamma_o(\omega)|^2$ has a minimum at ω_0 for all values of the frequency ω_0 at which the antenna is tuned and matched to the feed line. This means that the matched VSWR bandwidth determined by

$$\frac{X_o^2(\omega) + [R_o(\omega) - R_o(\omega_0)]^2}{X_o^2(\omega) + [R_o(\omega) + R_o(\omega_0)]^2} = \alpha \quad (14)$$

unlike the conductance bandwidth, exists at all frequencies, that is, throughout both the antiresonant ($\frac{dX_o}{d\omega}(\omega_0) < 0$) and resonant ($\frac{dX_o}{d\omega}(\omega_0) > 0$) frequency regions. Therefore, the matched VSWR bandwidth is a more fundamental, universally applicable definition of bandwidth for a general antenna than the conductance bandwidth.

Beginning with equation (14), a simple expression for the matched VSWR bandwidth for the tuned antenna can be found and is given as follows

$$FBW_v = \frac{\Delta\omega_+ - \Delta\omega_-}{\omega_0} \approx \frac{4\sqrt{\beta} R_o(\omega_0)}{\omega_0 \left| \frac{dZ_o}{d\omega}(\omega_0) \right|} \quad (15)$$

$$\text{where } \sqrt{\beta} = \sqrt{\frac{\alpha}{1-\alpha}} = \frac{s-1}{2\sqrt{s}}.$$

For the half-power matched VSWR bandwidth, $s = 5.828$ and $\sqrt{\beta} = 1$. A comparison of equations (15) and (11) reveals that

$$FBW_v(\omega_0) = 2 FBW_{co}(\omega_0) \quad (16)$$

wherever the conductance bandwidth $FBW_{CD}(\omega_0)$ exists, namely outside the antiresonant frequency regions. The matched VSWR bandwidth $FBW_V(\omega_0)$ has the distinct advantage over the conductance bandwidth of existing at every tuned frequency ω_0 , that is, within both resonant and antiresonant frequency regions.

3.3 Exact and Approximate Expressions for the Quality Factor (Q) of an Antenna

The quality factor $Q(\omega_0)$ for an antenna tuned to have zero reactance at the frequency ω_0 can be defined [3]-[10] analogously to the quality factor for resonant circuits, namely

$$Q(\omega_0) = \frac{\omega_0 W(\omega_0)}{P_A(\omega_0)} \quad (17)$$

where $W(\omega_0)$ is the reactive energy and $P_A(\omega_0)$ is the power accepted by the antenna that includes both radiated power and power loss.

An exact expression for $Q(\omega_0)$ in (17) is derived through relating the antenna's input impedance to the fields of the antenna and then expressing both $W(\omega_0)$ and $P_A(\omega_0)$ in terms of these quantities. Again, the details of these derivations are contained in [1] and [2] and only a brief summary and the resulting expressions are presented here.

The reactive energy $W(\omega_0)$ is expressed in terms of the frequency derivative of the tuned antenna's input reactance and the field quantities as follows:

$$W(\omega_0) = W_m(\omega_0) + W_e(\omega_0) = 2W_m(\omega_0) = 2W_e(\omega_0) \quad (18)$$

where $W_m(\omega_0)$ is the magnetic reactive energy and $W_e(\omega_0)$ is electric reactive energy. Additionally,

$$W(\omega_0) = \frac{|I_0|^2}{4} \frac{dX_{in}}{d\omega}(\omega_0) - [W_L(\omega_0) + W_R(\omega_0)] \quad (19)$$

where $W_L(\omega_0)$ and $W_R(\omega_0)$ are the dispersion energies associated with material loss and the antenna fields, respectively. These dispersion energies can be written as follows

$$\begin{aligned} W_L(\omega_0) = & \frac{\omega_0}{2} \operatorname{Im} \int_{V_a} \left(\mu_r \frac{d\mathbf{H}}{d\omega} \cdot \mathbf{H}^* + \varepsilon_r \frac{d\mathbf{E}}{d\omega} \cdot \mathbf{E}^* \right) dV \\ & + \frac{\omega_0}{4} \int_{V_a} \left(\frac{d\mu_r}{d\omega} |\mathbf{H}|^2 + \frac{d\varepsilon_r}{d\omega} |\mathbf{E}|^2 \right) dV \end{aligned} \quad (20)$$

where the frequency dependence of \mathbf{H} and \mathbf{E} are not explicitly written and where the complex permeability and permittivity of the material comprising the antenna are given as

$$\mu = \mu_r - j\mu_i, \quad \varepsilon = \varepsilon_r - j\varepsilon_i \quad (21)$$

For thin-wire lossy antennas with $\mu_i = 0$, $\varepsilon_i = \sigma/\omega$, $\frac{d\mu_r}{d\omega} \approx \frac{d\varepsilon_r}{d\omega} = 0$, where σ is the conductivity of the wire, the dispersion energy, W_L in (20) can be further simplified to

$$W_L = \text{Im} \int_{\text{wire length}} \mathcal{R}(l) \frac{dI}{d\omega}(l) \cdot I^*(l) dl, \quad \frac{\delta}{d} \ll 1 \quad (22)$$

where d is the wire diameter and δ is the “skin depth”. Additionally, $\mathcal{R}(l) = \frac{1}{\pi\sigma d\delta}$ is the resistance per unit length of wire and $I(l)$ is the total current flowing in the wire at the position l along the wire.

The dispersion energy $W_R(\omega_0)$ can be written as follows

$$W_R(\omega_0) = \frac{1}{2Z_f} \int_{4\pi} \text{Im} \left(\frac{d\mathbf{F}}{d\omega} \cdot \mathbf{F}^* \right) d\Omega \quad (23)$$

where Z_f is the characteristic impedance of free space and \mathbf{F} is the complex far electric field pattern $\mathbf{F}(\theta, \phi)$ defined by

$$\mathbf{F}(\theta, \phi) = \lim_{r \rightarrow \infty} r e^{ikr} \mathbf{E}(\mathbf{r}, \theta, \phi) \quad (24)$$

It is very significant to note that the frequency derivatives of the field quantities and current in (22) and (23) are determined with the antenna feed point (driving) current set to a constant value for all frequency (1 A in the case of the numerical results presented in Section 4).

The total power accepted by the antenna $P_A(\omega_0)$ can also be expressed as a function of the field quantities as follows

$$P_A(\omega_0) = \frac{1}{2Z_f} \int_{4\pi} |\mathbf{F}|^2 d\Omega + \frac{\omega_0}{2} \int_{V_a} (\mu_i |\mathbf{H}|^2 + \varepsilon_i |\mathbf{E}|^2) dV \quad (25)$$

However, it is more convenient to write $P_A(\omega_0)$ simply as a function of the antenna's feed point current and impedance as

$$P_s(\omega_o) = \frac{|I_o|^2 R_o(\omega_o)}{2} \quad (26)$$

Substituting equations (19) and (26) into equation (17) an **exact expression** for the quality factor of an antenna is found to be

$$Q(\omega_o) = \frac{\omega_o}{2 R_o(\omega_o)} \frac{dX_o}{d\omega}(\omega_o) - \frac{2\omega_o}{|I_o|^2 R_o(\omega_o)} [W_L(\omega_o) + W_R(\omega_o)] \quad (27)$$

Note that $Q(\omega_o)$ in (27) differs from the conventional formula for the quality factor [3]

$$Q_c(\omega_o) = \frac{\omega_o}{2 R_o(\omega_o)} \frac{dX_o}{d\omega}(\omega_o) \quad (28)$$

by the term $\frac{2\omega_o}{|I_o|^2 R_o(\omega_o)} [W_L(\omega_o) + W_R(\omega_o)]$. The formula in (28) is commonly used to determine the quality factor and bandwidth [$1/Q_c$ for half-power conductance bandwidth and $2/Q_c$ for half-power matched VSWR bandwidth] of tuned antennas. In general, neither $Q_c(\omega_o)$ in (28) nor $|Q_c(\omega_o)|$ accurately approximates the “exact” Q in (17) and (27) of tuned antennas in antiresonant regions.

The total dispersion energy, $W_L(\omega_o) + W_R(\omega_o)$, can be estimated to get an approximate expression for $Q(\omega_o)$ that can be related to the bandwidth of the tuned antenna. From [2], it can be shown that $Q(\omega_o)$ can be approximated as follows for all regions of frequency, that is, throughout both resonant and antiresonant regions

$$Q(\omega_o) \approx Q_z(\omega_o) = \frac{\omega_o}{2 R_o(\omega_o)} \left| \frac{dZ_o}{d\omega}(\omega_o) \right| \quad (29)$$

Comparing (29) with (15) one finds that $Q(\omega_o)$ can be directly related to the inverse of the matched VSWR bandwidth as follows.

$$Q(\omega_o) \approx \frac{2\sqrt{\beta}}{FBW_V(\omega_o)} \approx \frac{\omega_o}{2 R_o(\omega_o)} \left| \frac{dZ_o}{d\omega}(\omega_o) \right| \quad (30)$$

4. NUMERICAL SOLUTIONS

In this section of the paper, numerical solutions for several lossless and lossy antennas are used to validate the expressions presented for the bandwidth and quality factor of the tuned antenna. The antennas considered here include the straight-wire (dipole) antenna; the circular-loop antenna; a resistively loaded, low Q dipole antenna; and an electrically small folded spherical helix dipole antenna. The numerical analysis of these antennas is

performed using the Numerical Electromagnetics Code, version 4 (NEC) [11]. Using NEC, the impedance properties of these antennas are computed over a wide range of operating frequencies ω .

Using the computed impedance data, the exact matched VSWR bandwidth is determined for each operating frequency by tuning the antenna at the desired operating frequency with a lossless series reactance. The tuned frequency is designated ω_0 . A lossless inductor, L_S , is used to tune the antenna's reactance $X(\omega_0)$ to zero [$X_0(\omega_0) = X(\omega_0) + X_S(\omega_0) = 0$] if $X(\omega_0)$ is less than zero; and a lossless capacitor, C_S , is used to tune the antenna's reactance to zero if $X(\omega_0)$ is greater than zero. Once the antenna is tuned at the desired operating frequency, the VSWR of the tuned antenna is determined for all frequencies ω , under the condition that the feed line impedance Z_{CH} is equal to the antenna's tuned impedance at ω_0 , that is, $Z_{CH} = Z_0(\omega_0) + R_0(\omega_0)$. The exact matched VSWR bandwidth about the tuned frequency ω_0 is determined for a specific value of VSWR s , from the range of frequencies $(\omega_+ - \omega_-)$ where the VSWR is less than or equal to s .

$$FBW_{V\text{EXACT}} = \frac{\omega_+ - \omega_-}{\omega_0} \quad (31)$$

In addition to determining the exact matched VSWR bandwidth, the exact Q of the antenna is found using equation (27). The first term on the left hand side of (27),

$\frac{\omega_0}{2R_0(\omega_0)} \frac{dX_0(\omega_0)}{d\omega}$, is evaluated directly from the antenna's feed point impedance,

where $\frac{dX_0(\omega_0)}{d\omega}$ is evaluated using equation (6). The second term on the left hand side

of (27), $\frac{2\omega_0}{|I_0|^2 R_0(\omega_0)} [W_L(\omega_0) + W_R(\omega_0)]$, is evaluated numerically from the antenna's field and current distributions.

The dispersion energy, $W_R(\omega_0)$ is evaluated directly using equation (23). The complex far-field pattern is evaluated at each frequency over the entire sphere of radiation in angular increments of 0.5 degrees in both standard spherical angular sweep planes, θ and ϕ . This results in a total of 260,281 complex far-field values being determined at each frequency. If the antenna being evaluated is known to have an angular symmetric radiation pattern (amplitude), the number of far-field points evaluated and the integral in (23) can be simplified accordingly. The frequency derivative and integral in (23) are evaluated numerically for each observation angle and frequency as necessary. In frequency regions where the frequency derivative $\frac{dF}{d\omega}$ varies rapidly, the frequency

increment must be set to a value that will ensure numerical convergence. Generally, $\frac{dF}{d\omega}$

varies most rapidly in frequency regions near antiresonance. The frequency increment used to evaluate the expression in (23) is typically set to 0.5 or 1 MHz. However, in

regions very near antiresonance, frequency increments of less than 0.1 MHz may be necessary.

Another factor that must be considered in the evaluation of (23) is the polarization of the antenna's far-field radiation. If the antenna is purely linearly polarized, the total dispersion energy $W_R(\omega_0)$ is simply determined from the antenna's single polarization component. If the antenna radiates orthogonal polarization components, as is the case for the circular-loop antenna, the dispersion energy associated with each component must be determined. The total dispersion energy is then found from the summation of the individual component dispersion energies.

If the exact Q is determined for a lossy antenna, the material loss dispersion energy $W_L(\omega_0)$ must be evaluated using (22). To evaluate the frequency derivative and integral in (22), the current distribution along the wire is calculated using NEC at each operating frequency. The number of segments along the wire must be chosen to ensure that the current distribution is adequately determined as a function of wire length. Additionally, the frequency increment must be chosen to ensure that the frequency derivative $\frac{\partial I}{\partial \omega}$ is evaluated properly.

In addition to determining the exact matched VSWR bandwidth and exact Q of each antenna, the approximate expressions for quality factor, $Q_C(\omega_0)$ and $Q_Z(\omega_0)$, determined from (28) and (29) respectively, are both evaluated and compared to the exact values. To compare the exact matched VSWR bandwidth with the antenna's quality factor, the exact bandwidth value is converted to an equivalent value of quality factor using (30) as follows

$$Q_b(\omega_0) \approx \frac{2\sqrt{\beta}}{FBW_{V_EXACT}(\omega_0)} \quad (32)$$

4.1 Conductance and Matched VSWR Bandwidth

Consider a lossless center-fed, straight-wire (dipole) antenna having an overall length of 1 m and a wire diameter of 1 mm. Using NEC, the feed point (input) impedance of this antenna was computed and is presented in Figure 2 for a frequency range covering its first resonant and antiresonant frequency regions. At low frequencies, where the antenna is small with respect to the operating wavelength, the feed point resistance (and its frequency derivative) is small and the magnitude of the feed point reactance (and its frequency derivative) is relatively high. With increasing frequency, the antenna becomes self-resonant at a frequency where its length is approximately one-half of the operating wavelength and antiresonant at a frequency where its length is approximately equal to the operating wavelength. With further increase in frequency, the antenna's impedance will undergo successive regions of resonance and antiresonance. For this straight-wire antenna, the first resonant frequency occurs at approximately 144 MHz and the first

antiresonant frequency occurs at approximately 279 MHz. To illustrate the limitations of using exact conductance bandwidth versus exact matched VSWR bandwidth, both are computed at resonance and antiresonance and compared with the approximate expressions for bandwidth given in equations (11), (12) and (15).

The exact conductance bandwidth is determined by setting the feed voltage driving the tuned antenna to a constant value (1 Volt) and normalizing the power accepted by the antenna to that of the tuned frequency. The power accepted by the straight-wire antenna as a function of frequency, normalized to the values at the tuned frequencies of resonance and antiresonance, are presented in Figures 3 and 4, respectively.

Examining Figure 3, which presents the accepted power versus frequency normalized to the power accepted at its resonant frequency, it is seen that the maximum accepted power occurs near the resonant frequency and that the conductance bandwidth about the resonant frequency is reasonably well defined. The exact half-power conductance bandwidth about resonance is 7.16% while the approximate half-power conductance bandwidth determined from (11) and (12) is 12.09% and 12.36%, respectively. Both of these values are somewhat reasonable approximations to the exact conductance bandwidth and they are similar in magnitude since the frequency derivative of the antenna's resistance is relatively small compared to that of the antenna's reactance in regions near resonance.

Examining Figure 4, which presents the accepted power versus frequency normalized to the power accepted at the antiresonant frequency, it is seen that the maximum accepted power does not occur near the antiresonant frequency and that the conductance bandwidth about the antiresonant frequency is not defined. This illustrates the significant limitation in using conductance bandwidth to define the bandwidth and quality factor of the antenna in frequency regions near antiresonance.

As an alternative to using conductance to define the bandwidth properties of the antenna, matched VSWR bandwidth may be used. The matched VSWR bandwidth of the tuned antenna is determined directly from the antenna's VSWR properties where the VSWR is determined by assuming the transmission line feeding the antenna has a characteristic impedance equal to the antenna's feed point resistance at the tuned frequency. For the purposes of this work, the VSWR of the straight-wire antenna is not presented. Rather, $1 - |\Gamma_o(\omega)|^2$ is presented for the matched VSWR referenced to the resonant and antiresonant frequencies in Figures 5 and 6, respectively.

Examining Figures 5 and 6, it is evident that the matched VSWR bandwidth exists and is well defined in frequency regions of resonance and antiresonance, and is therefore a more reliable indication of the antenna's bandwidth properties than the conductance bandwidth, which does not exist in regions of antiresonance. The exact matched VSWR bandwidth, defined at the equivalent half-power points ($s = 5.828$, $1 - |\Gamma_o(\omega)|^2 = 0.5$), is found to be 25.2% and 37.5%, referenced to the resonance and antiresonance frequencies, respectively. The approximate half-power matched VSWR bandwidth, again defined at the equivalent half-power points, is found from (15) to be 24.2% and 38.9%, referenced

to the resonant and antiresonant frequencies, respectively. These approximate values are in excellent agreement with the exact values in regions of both resonance and antiresonance.

4.2 Bandwidth and Quality Factor of the Lossless Straight-Wire Antenna

In the previous section, the exact and approximate conductance and matched VSWR bandwidth of the lossless straight-wire antenna were calculated and compared. It was shown that the matched VSWR bandwidth provides a more reliable indication of the antenna's inherent bandwidth properties throughout resonant and antiresonant frequency regions. In the remaining sections of this paper, the exact and approximate quality factor (Q) of several lossless and lossy antennas are computed and compared with the antenna's exact matched VSWR bandwidth to illustrate several important points. First, the comparisons illustrate the significant relationship that exists between exact Q and exact matched VSWR bandwidth over all regions of operating frequency. Second, the comparisons illustrate the validity of using the approximate expressions for matched VSWR bandwidth and Q [specifically equation (30)] through all regions of frequency.

The first antenna considered is the lossless, straight-wire (dipole) antenna that was described in the previous section. This antenna has an overall length of 1 m and a wire diameter of 1 mm. The calculated (NEC) impedance properties of this antenna were previously presented in Figure 2 for a frequency range covering the first resonance and antiresonance.

Using the calculated feed point impedance, the exact matched VSWR bandwidth was calculated using equation (31) with a defined VSWR, $s = 1.5$. This exact matched VSWR bandwidth was then converted to an equivalent Q using equation (32). In this case, $\sqrt{\beta} \approx 0.2041$. This conversion to an equivalent Q allows the exact matched VSWR bandwidth to be compared directly with the exact Q [determined using equation (27)] and the approximate Q [determined using equations (28) and (29)]. For graphical presentation purposes, the equivalent Q determined from the exact matched VSWR bandwidth is designated Q_b .

The frequency derivative of the antenna's reactance was used to determine the approximate Q using equation (28). For graphical presentation purposes, this approximate Q is designated Q_c . Additionally, the frequency derivative of the antenna's impedance was used to determine the approximate Q using equation (29). For graphical presentation purposes, this approximate Q is designated Q_z . Finally, the exact Q of the antenna was calculated using the frequency derivative of the antenna's reactance and the frequency derivative of the antenna's radiated far-field properties using equation (27).

A comparison of the exact Q , Q_b , Q_c and Q_z for the lossless straight-wire antenna is presented in Figure 7. Examining Figure 7, it is significant to note the excellent agreement between the exact Q , the equivalent Q determined from the exact bandwidth, Q_b , and the approximate Q determined from the frequency derivative of the antenna's

impedance, Q_z . These three quantities are determined in significantly different manners yet; they remain in excellent agreement throughout all ranges of frequency including both resonant and antiresonant regions. It is also significant to note that the conventional approximation of Q , Q_c , determined from the frequency derivative of the antenna's reactance, does not provide a reasonable estimate of the exact Q or the antenna's matched VSWR bandwidth in frequency regions near antiresonance.

Beyond the antenna's first resonant and antiresonant frequency regions, the antenna's input impedance will undergo successive alternating regions of resonance and antiresonance. The input impedance of the lossless, straight-wire antenna as a function of increasing frequency is presented in Figure 8 for a frequency range of 450 MHz through 2000 MHz. In regions of resonance, the antenna's input resistance is of moderate value, while in regions of antiresonance it is high in value. A comparison of the exact Q , Q_b , Q_c and Q_z over this range of frequency is presented in Figure 9. It can be seen that the values of exact Q , Q_b and Q_z remain in excellent agreement throughout all ranges of frequency including all regions of resonance and antiresonance. It can also be seen again that the conventional approximation of Q , Q_c , does not provide a reasonable estimate of the exact Q or bandwidth in regions of antiresonance.

Considering the form of equation (27), the expression for exact Q , and the reasonable agreement that exists between exact Q and the conventional approximation (Q_c) at low frequencies and in frequency regions near resonance; and the disagreement between exact Q and Q_c in regions near antiresonance, we can conclude the following: At very low frequencies, where the antenna is small, and in frequency regions near resonance, the dominant factor in determining the quality factor of the antenna is the frequency derivative of its input impedance, $\frac{dX}{d\omega}$. This also implies that the dispersion energies W_L and W_R are close to zero in these frequency regions. It is also significant to note that in these frequency regions, the value of $\frac{dR}{d\omega}$ is relatively small. In frequency regions near antiresonance, the frequency derivative of the antenna's input reactance is less dominant and the dispersion energies W_L and W_R become significant in determining the quality factor of the antenna.

It has been suggested that the magnitude of the frequency derivative of the antenna's reactance provides a more reliable indication of the exact Q and bandwidth than the frequency derivative itself [12]. The approximate Q over the full range of frequencies was calculated using equation (28) where $\frac{dX}{d\omega}$ was replaced with $\left|\frac{dX}{d\omega}\right|$. This new approximate Q , designated $|Q_c|$, is compared with the exact Q in Figure 10. Other than very near the exact frequency of antiresonance, the approximate Q calculated using $\left|\frac{dX}{d\omega}\right|$ does not provide a reasonable estimate of exact Q or bandwidth in regions of antiresonance. Using $\left|\frac{dX}{d\omega}\right|$ does provide a reasonable estimate of exact Q and bandwidth

very near the exact frequency of antiresonance because very near this frequency, $\frac{dR}{d\omega} = 0$ and $\left| \frac{dX}{d\omega} \right| = \left| \frac{dZ}{d\omega} \right|$.

4.3 Bandwidth and Quality Factor of the Lossless and Lossy Circular-loop Antenna

In this section of the paper, the quality factor and matched VSWR bandwidth of the circular-loop antenna are considered. The circular-loop antenna considered here has a total wire length of approximately 2.18 m and a wire diameter of 1 mm. The total wire length, and hence loop circumference, was chosen such that the first resonant frequency of the circular-loop, that is where $X = 0$ and $\frac{dX}{d\omega} > 0$, identically matches the first

resonant frequency of the straight wire antenna, approximately 144 MHz. The lossless input impedance of the circular-loop was calculated using NEC and is presented in Figure 11. One of the significant differences to note in comparing the impedance properties of the circular-loop antenna to those of the straight-wire antenna is that at low frequencies, the circular-loop antenna undergoes an antiresonance prior to its first resonance. The frequency of the circular-loop's first antiresonance is approximately 66 MHz.

A comparison of the exact Q , Q_b , Q_c and Q_z for the lossless circular-loop antenna is presented in Figure 12. Examining Figure 12, it is again evident that the exact Q , the exact matched VSWR bandwidth, and the approximate expressions for Q (Q_z) are in excellent agreement over all ranges of frequency. The conventional approximate expression for Q is agreement with the exact Q at low frequencies and in regions of resonance however, it does not provide a reasonable approximation of the exact Q in regions of antiresonance.

To further illustrate the agreement between exact Q and the exact matched VSWR bandwidth in regions of antiresonance, an expanded view of the antiresonant frequency region (≈ 66 MHz) is presented in Figure 13. The agreement between exact Q , Q_b and Q_z , illustrates the dependence and significance of using the radiation dispersion energy term, W_R , in determining the exact Q of the lossless antenna. To illustrate the significance of the loss dispersion energy term, W_L , in determining the exact Q of the lossy antenna, the quality factor and bandwidth of the lossy circular-loop were determined. Loss was included in the NEC model of the circular-loop by specifying finite wire conductivity. In this case, the conductivity of copper was specified in the model.

The exact Q , exact matched VSWR bandwidth (Q_b) and approximate Q (Q_c and Q_z) were determined for the lossy circular-loop and are presented in Figure 14. In Figure 14, the terms comprising the expression for exact Q [equation (27)] are presented separately to illustrate the significance of using each term in calculating the exact Q . The curve for Q_c represents the conventional approximation for Q [equation (28)] and the first term of the

exact Q in equation (27). The curve representing $Q_C + Q_R$, is a calculation of exact Q using only Q_C and the radiation dispersion energy W_R terms. Note that the summation of these two terms does not provide an accurate calculation of the exact Q . Once the loss dispersion energy term is included in the calculation of exact Q , the results are consistent with matched VSWR bandwidth and the approximate Q (Q_A) determined using equation (29).

4.4 A Comment on the Quality Factor and Lower Bound on Q for the Lossless and Lossy Antenna

In the previous section, the quality factors of the lossless and lossy circular-loop antenna were determined using the exact expression for Q and the approximate expressions for Q (Q_A and Q_C). In examining Figures 13 and 14, it is evident that the Q of the lossy circular-loop is less than that of the lossless loop. This is an expected result since a lossy antenna has a lower Q and correspondingly larger bandwidth than its lossless counterpart.

An interesting point to examine is the relative behavior of the lossy straight-wire and circular-loop antennas as a function of decreasing frequency. It is well known that the fundamental limit, or lower bound of Q for the lossless antenna increases with decreasing frequency as follows [6]

$$Q_{LIMIT} = \frac{1}{(ka)^3} + \frac{1}{ka} \quad (33)$$

where k is the free space wave number $\frac{2\pi}{\lambda}$, and a is the radius of an imaginary sphere encompassing the maximum physical dimension of the antenna. For very low frequencies where ka is very small, the first term in (33) dominates and (33) can be simplified to

$$Q_{LIMIT} \approx \frac{1}{(ka)^3} \quad (34)$$

This implies that for any lossless antenna, having a fixed volume and far-field pattern, the Q increases without bound with decreasing frequency. It is interesting to now consider the behavior of the lossy straight-wire (electric dipole) and circular-loop (magnetic dipole) antennas.

The very small, lossy, electric dipole of length l has a radiation resistance that can be approximated as

$$R_R \approx 20 \left(\frac{kl}{2} \right)^2 \quad (35)$$

If the skin depth $\delta < d/2$, where d is the diameter of the wire, the lossy electric dipole has a loss resistance given by

$$R_L^e \approx \frac{l}{2\pi d} \sqrt{\frac{kc\mu_0\rho}{2}} \quad (36)$$

where ρ is the resistivity of the wire. The lower bound on the quality factor of the lossy electric dipole can be approximated as

$$Q^e \approx \frac{\eta_e}{\left(\frac{kl}{2}\right)^3} \approx \frac{20}{\left(\frac{kl}{2}\right)^3} \left[\frac{1}{20 \left(\frac{kl}{2}\right)^2 + R_L^e} \right] \quad (37)$$

where η_e is the radiation efficiency of the electric dipole. For small values of k , equation (37) can be simplified as follows:

$$Q^e \approx \frac{40}{kl R_L^e} \quad (38)$$

With decreasing frequency, k approaches 0 and therefore, Q^e approaches ∞ . For any small, lossy, electric dipole antenna (or any small lossy antenna operating in an electric dipole mode) the fundamental lower bound on radiation Q approaches infinity with decreasing frequency.

The very small, lossy, magnetic dipole of radius r has a radiation resistance that can be approximated as

$$R_R^m \approx 20 \pi^2 (kr)^4 \quad (39)$$

The lossy magnetic dipole has a loss resistance given by

$$R_L^m \approx \frac{2r}{d} \sqrt{\frac{kc\mu_0\rho}{2}} \quad (40)$$

The fundamental limit on the quality factor of the lossy magnetic dipole can be approximated as

$$Q^m \approx \frac{\eta_m}{(kr)^3} \approx 20 \pi^2 kr \left[\frac{1}{20 \pi^2 (kr)^4 + R_L^m} \right] \quad (41)$$

where η_m is the radiation efficiency of the magnetic dipole (loop). For very small values of k , equation (41) simplifies to

$$Q^m \approx \frac{20 \pi^2 k r}{R_L^m} \quad (42)$$

With decreasing frequency, k approaches 0 and therefore, Q^m approaches 0. For any small, lossy, magnetic dipole antenna (or any small lossy antenna operating in a magnetic dipole or loop mode) the fundamental lower bound on radiation Q approaches zero with decreasing frequency.

Evidence of the relative behavior of the quality factors of the small lossy dipole and loop antennas is given by first considering the relative behavior of their efficiencies as a function of decreasing frequency. The efficiency of the straight-wire (dipole) and circular-loop antennas discussed in the previous sections are compared in Figure 15 for frequencies below their first resonant frequency (144 MHz). It is significant to note the difference in their relative behavior with decreasing frequency when the antennas are very small electrically.

Comparisons of the approximate Q (Q_L) relative to the lower bound on Q for the lossless and lossy straight-wire and circular-loop antennas are presented in Figures 16 and 17, respectively. As discussed above, the lower bound on Q for both the lossless and lossy straight-wire antenna increases towards infinity with decreasing frequency. It is significant to note that the actual Q for the straight-wire antenna is significantly greater than the lower bound. The lower bound on Q for the lossless circular-loop antenna increases towards infinity with decreasing frequency. However, the lower bound on Q for the lossy loop approaches zero with decreasing frequency. It is again significant to note that the actual Q for the circular-loop is significantly greater than the lower bound. At no time is the actual quality factor less than the lower bound defined approximately by

$$\frac{\eta}{(ka)^3}.$$

4.5 Bandwidth and Quality Factor of a Lossy Electrically Small Antenna

In the previous sections, the bandwidth and quality factor of the straight-wire and circular-loop antennas were considered. The dimensions of these antennas were chosen such that they are self-resonant at the same frequency and at a frequency where their overall dimensions would not be considered electrically small. The straight-wire antenna is resonant at a frequency where its overall length is approximately one-half of the operating wavelength ($ka \approx 1.57$). The circular-loop antenna is resonant at a frequency where its overall length is approximately equal to the operating wavelength ($ka \approx 1$). In this section, the bandwidth and quality factor of an electrically small antenna are considered to illustrate the validity of the exact and approximate expressions for Q for antennas of small size and more complex geometry. In this case, the configuration of the antenna is chosen such that it is self-resonant at a frequency where it may be considered electrically small.

The electrically small antenna considered here is the folded spherical helix dipole antenna depicted in Figure 18. The monopole version of this antenna is described in [13] and [14]. This antenna has an overall height and diameter of approximately 11.8 cm and a wire diameter of 2.6 mm. It has a single feed point and operates in a folded dipole (loop or magnetic-dipole) mode. It is self-resonant at a frequency of approximately 209.5 MHz ($ka \approx 0.26$) with a resonant resistance of 49.5Ω and an efficiency of 92%. The feed point impedance properties of this antenna are depicted in Figure 19. Operating in a folded dipole or magnetic-dipole mode, its impedance properties undergo an antiresonance prior to its first resonance.

A comparison of the exact Q , Q_b , Q_C and Q_Z for the lossy electrically small folded spherical helix dipole antenna is presented in Figure 20. Examining Figure 20, it is again evident that the exact Q , the exact matched VSWR bandwidth, and the approximate expressions for Q (Q_Z) are in excellent agreement over all ranges of frequency. It is also significant to note two additional points. First, at its resonant frequency of 209.5 MHz, this antenna exhibits a quality factor that is within 1.5 times the fundamental lower bound on Q . Finally, as with any lossy antenna operating in a magnetic-dipole or loop mode, the radiation Q approaches zero with decreasing frequency.

4.6 Bandwidth and Quality Factor of a Lossy Very Low Q Antenna

In this section, the bandwidth and Q of a lossy, very low Q antenna are considered to validate the exact and approximate expressions for bandwidth and Q for antennas with a low Q , that is, a Q less than 2. The antenna considered here is a resistively loaded straight-wire antenna having a length of 1 m and a wire diameter of 1 mm. The antenna is uniformly loaded over 101 segments with a resistance of 10 ohms per segment.

The input impedance properties of this resistively loaded antenna are depicted in Figure 21. This antenna undergoes a resonance and antiresonance at frequencies of approximately 174 MHz and 219 MHz, respectively. A comparison of the exact Q , Q_b , Q_C and Q_Z for this antenna is presented in Figure 22. Over the range of frequencies presented here, the radiation Q is approximately less than 2. Examining Figure 22, it is again evident that the exact Q , the exact matched VSWR bandwidth, and the approximate expressions for Q (Q_Z) are in very good agreement over all ranges of frequency for these low values of Q . It is also significant to note that the equivalent Q determined from the exact matched VSWR bandwidth and the expression for Q_Z are in excellent agreement. It is also important to note that in determining the exact Q using equation (27), the resistance per unit length of the wire was assumed to be 10 ohms when determining the loss dispersion energy, W_L .

5. DISCUSSION

It was shown that the matched VSWR bandwidth is a more reliable quantity for defining the bandwidth properties of an antenna than the conductance bandwidth. An exact expression for the quality factor (Q) of a general one-port antenna was presented. It was shown that the exact Q of the general one-port antenna is a function of the frequency derivative of the antenna's input reactance and two dispersion energy terms associated with material loss and the radiation fields. Approximate expressions for the quality factor and matched VSWR bandwidth were presented. These expressions were shown to be more reliable than previous expressions in predicting the antenna's Q and bandwidth throughout all regions of frequency, that is, throughout regions of resonance and antiresonance. Numerical solutions for the straight-wire, circular-loop, electrically small antenna and a low Q antenna were presented validating these expressions.

6. REFERENCES

- [1] A. D. Yaghjian and S. R. Best, "Impedance, Bandwidth and Q of Antennas," *IEEE APS Symposium*, vol. 1, pp. 501-504, Columbus, OH, June 2003.
- [2] A. D. Yaghjian and S. R. Best, "Impedance, Bandwidth and Q of Antennas," Submitted to the *IEEE Trans. Antennas Propagat.*
- [3] R.L. Fante, "Quality factor of general ideal antennas," *IEEE Trans. Antennas Propagat.*, vol. AP-17, pp. 151-155, March 1969.
- [4] L.J. Chu, "Physical limitations of omni-directional antennas," *J. Appl. Phys.*, vol. 19, pp.1163-1175, December 1948.
- [5] R.E. Collin and S. Rothschild, "Evaluation of antenna Q ," *IEEE Trans. Antennas Propagat.*, vol. AP-12, pp. 23-27, January 1964.
- [6] J.S. McLean, "A re-examination of the fundamental limits on the radiation Q of electrically small antennas," *IEEE Trans. Antennas Propagat.*, vol. 44, pp. 672-676, May 1996.
- [7] W. Geyi, P. Jarnuszewski, and Y. Qi, "The Foster reactance theorem for antennas and radiation Q ," *IEEE Trans. Antennas Propagat.*, vol. 48, pp. 401-408, March 2000.
- [8] J.C.-E. Sten, A. Iljujanen, and P.K. Koivisto, "Quality factor of an electrically small antenna radiating close to a conducting plane," *IEEE Trans. Antennas Propagat.*, vol. 49, pp. 829-837, May 2001.
- [9] J.C.-E. Sten and A. Iljujanen, "Notes on the quality factor and bandwidth of radiating systems," *Electrical Engineering*, vol. 84, pp. 189-195, 2002.
- [10] R.F. Harrington, "Effect of antenna size on gain, bandwidth, and efficiency," *J. Res. Nat. Bureau Stand.*, vol. 64D, pp. 1-12, January 1960.
- [11] G. Burke, Numerical Electromagnetics Code (NEC), V4.1, Lawrence Livermore National Laboratory, Jan 1992.
- [11] D.R. Rhodes, "Observable stored energies of electromagnetic systems," *Journal of The Franklin Institute*, vol. 302, pp. 225-237, September 1976.
- [12] S. R. Best, "The Performance Properties of an Electrically Small Folded Spherical Helix Antenna," 2002 *IEEE APS Symposium*, Vol. 4, pp. 18-21, June 2002.
- [13] S. R. Best, "The Radiation Properties of Electrically Small Folded Spherical Helix Antennas," Accepted for publication, *IEEE Trans. Antennas Propagat.*

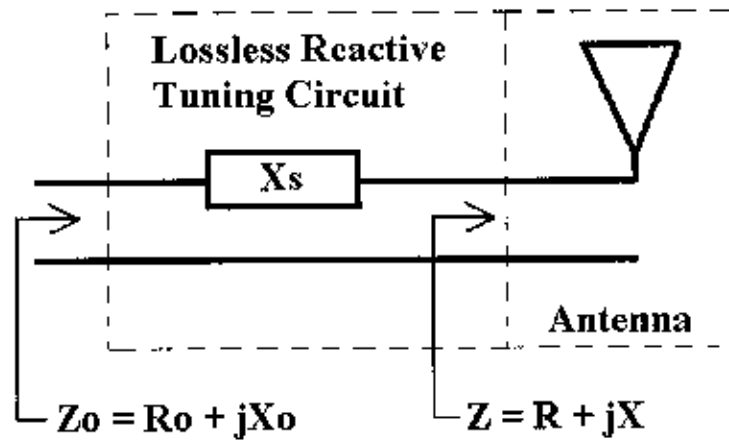


Figure 1. The general one-port antenna tuned with a lossless, series reactive circuit.

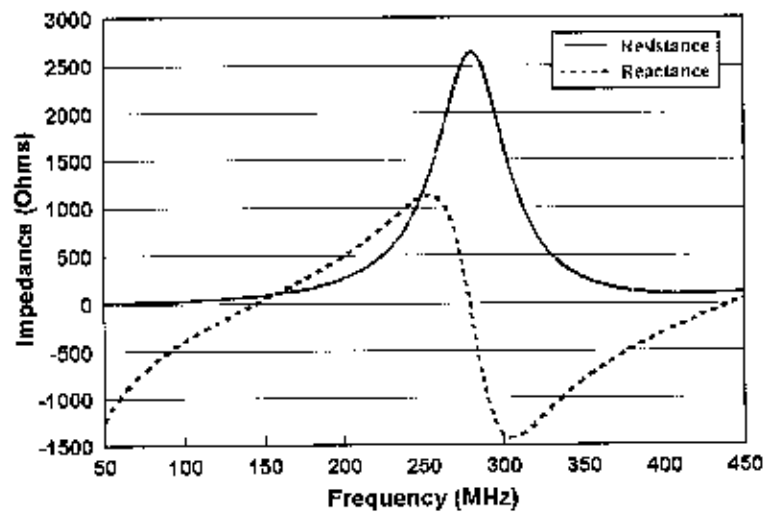


Figure 2. Input impedance of the lossless straight-wire (dipole) antenna having an overall length of 1 m and a wire diameter of 1 mm.

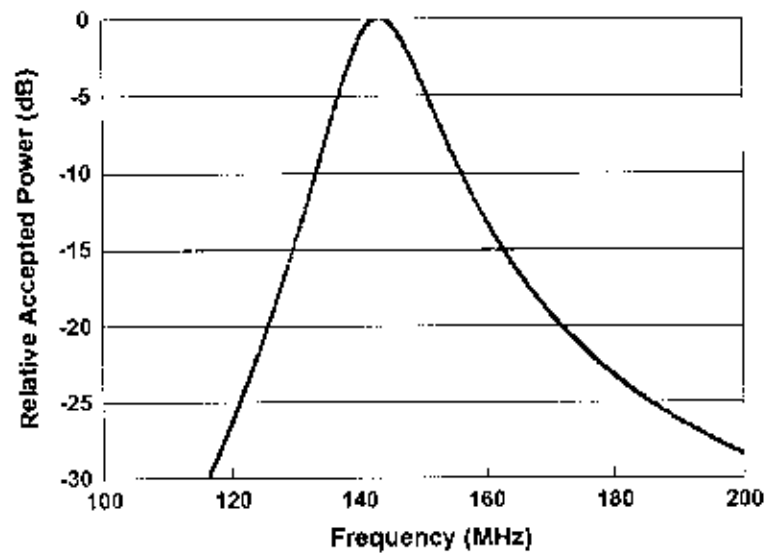


Figure 3. The power accepted by the lossless straight-wire (dipole) antenna normalized to the power accepted by the antenna at its resonant frequency (144 MHz) when the antenna is fed with a constant voltage. This provides an indication of conductance bandwidth.

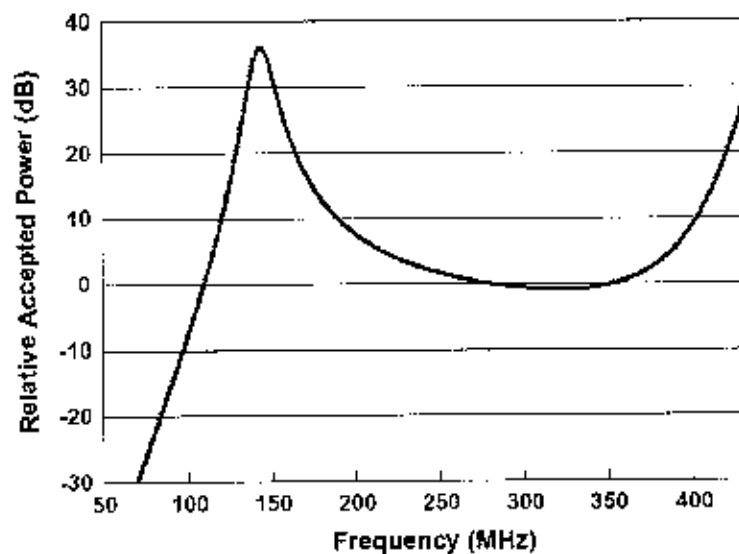


Figure 4. The power accepted by the lossless straight-wire (dipole) antenna normalized to the power accepted by the antenna at its antiresonant frequency (279 MHz) when the antenna is fed with a constant voltage. This provides an indication of conductance bandwidth.

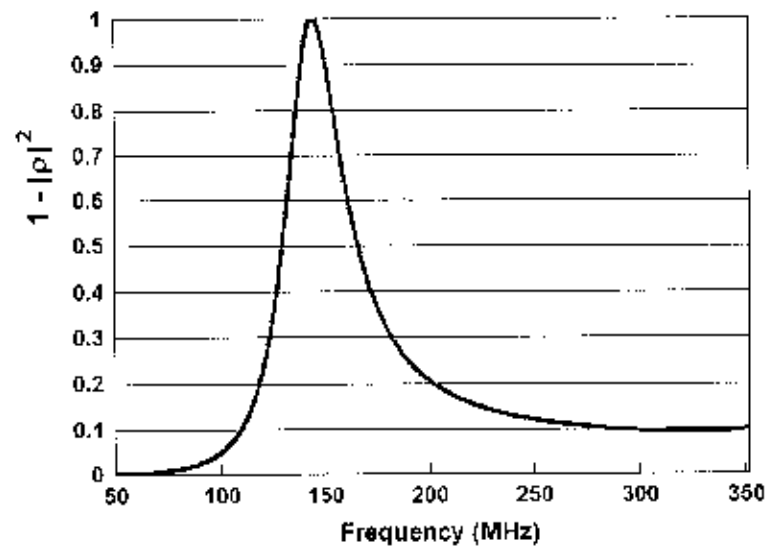


Figure 5. $1 - |\Gamma_a(\omega)|^2$ for the lossless straight-wire (dipole) antenna referenced to the resonant frequency (144 MHz). This provides an indication of the matched VSWR bandwidth.

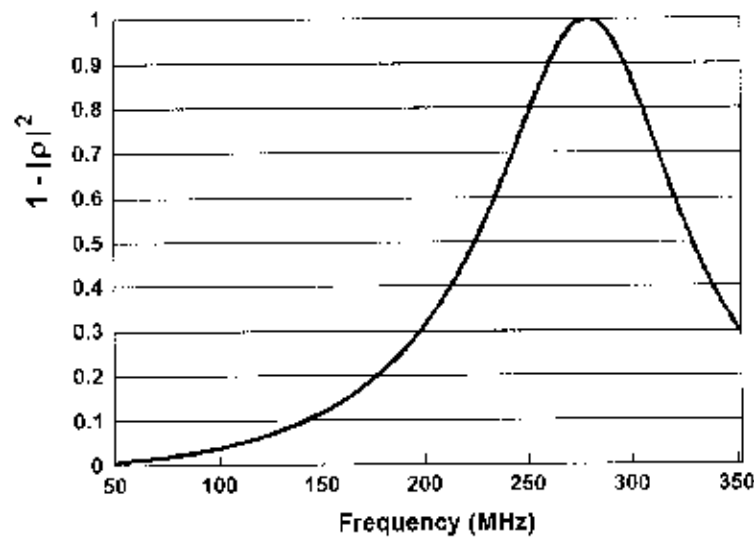


Figure 6. $1 - |\Gamma_a(\omega)|^2$ for the lossless straight-wire (dipole) antenna referenced to the antiresonant frequency (279 MHz). This provides an indication of matched VSWR bandwidth.

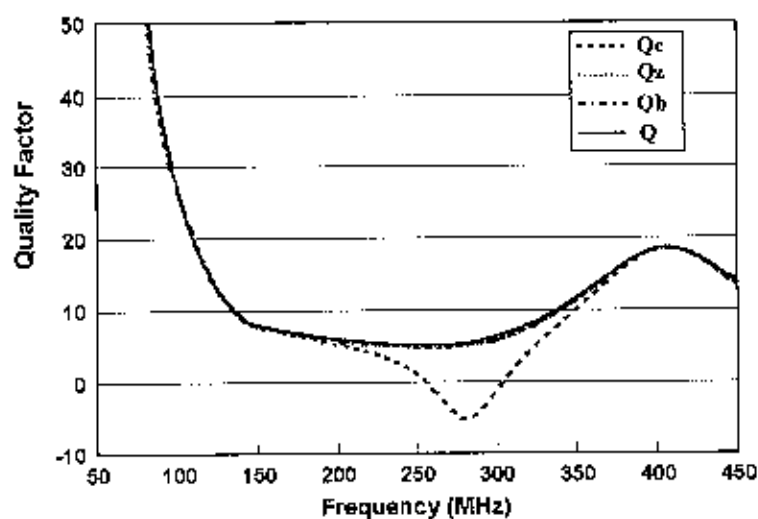


Figure 7. A comparison of the exact Q , the equivalent Q determined from the antenna's matched VSWR bandwidth Q_b , and the approximate Q determined from the frequency derivative of the antenna's impedance and reactance, Q_z and Q_c , respectively for the lossless straight-wire antenna.

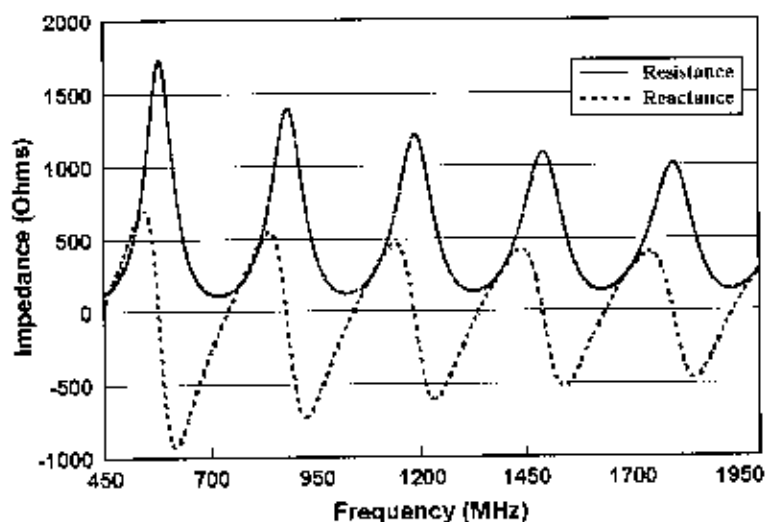


Figure 8. Input impedance properties of the lossless, straight-wire (dipole) antenna as a function of increasing frequency, covering a frequency range of 450 MHz through 2000 MHz.

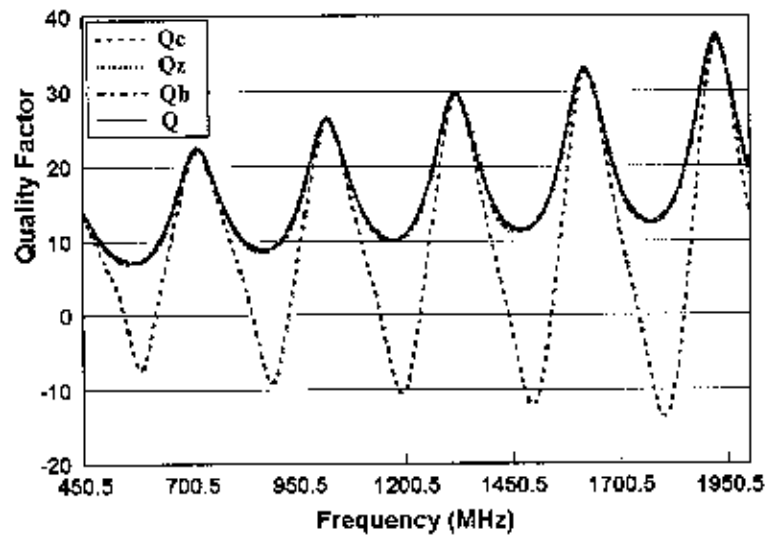


Figure 9. A comparison of the exact Q , the equivalent Q determined from the antenna's matched VSWR bandwidth Q_b , and the approximate Q determined from the frequency derivative of the antenna's impedance and reactance, Q_z and Q_c , respectively, for the lossless straight-wire antenna, covering a frequency range of 450 MHz through 2000 MHz.

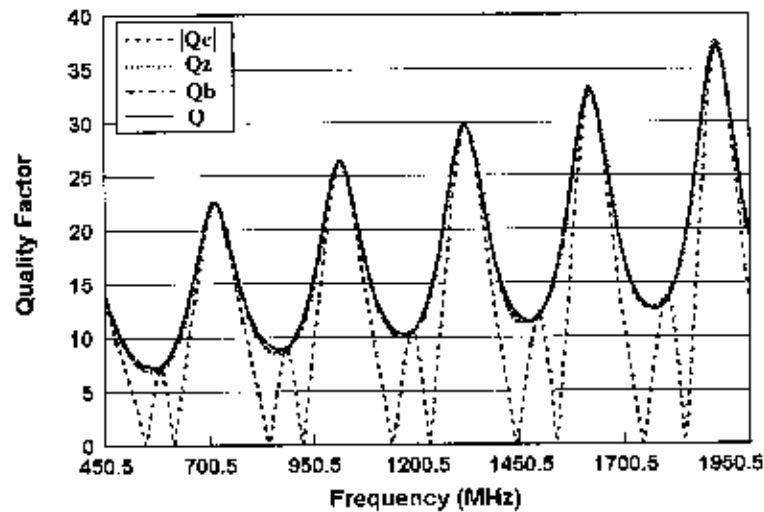


Figure 10. A comparison of the exact Q , the equivalent Q determined from the antenna's matched VSWR bandwidth Q_b , and the approximate Q determined from the frequency derivative of the antenna's impedance and the magnitude of the frequency derivative of the antenna's reactance, Q_z and $|Q_c|$, respectively, for the lossless straight-wire antenna, covering a frequency range of 450 MHz through 2000 MHz.

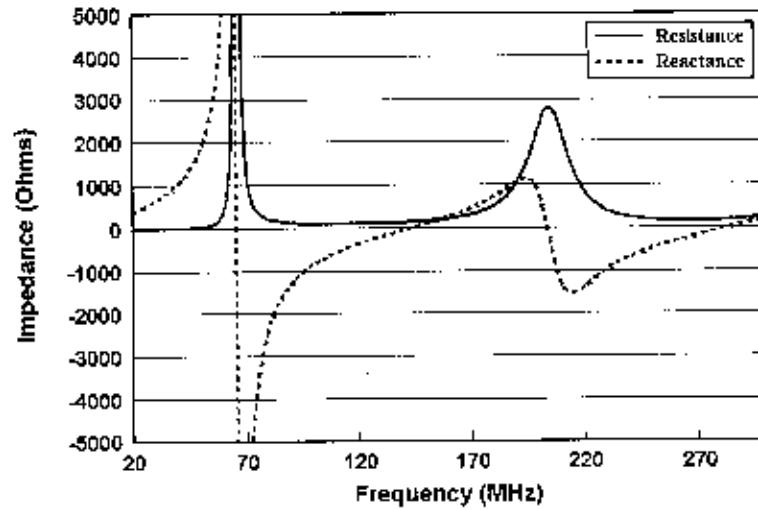


Figure 11. Input impedance of the lossless circular-loop antenna having an overall length of approximately 2.18 m and a wire diameter of 1 mm.

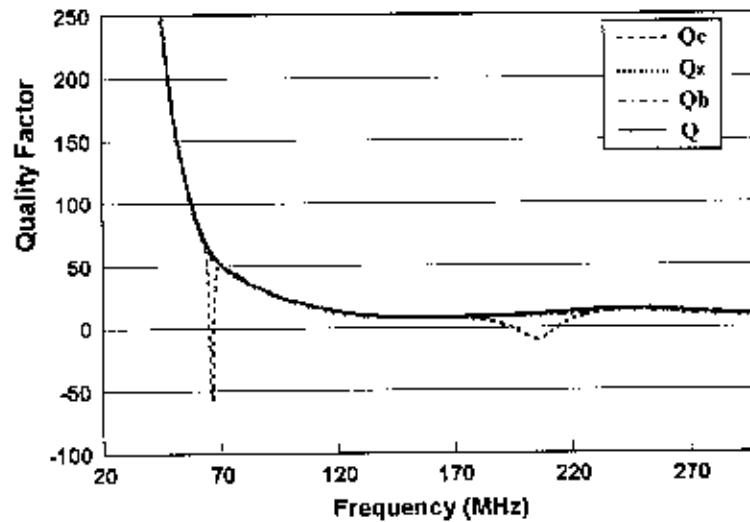


Figure 12. A comparison of the exact Q , the equivalent Q determined from the antenna's matched VSWR bandwidth Q_b , and the approximate Q determined from the frequency derivative of the antenna's impedance and reactance, Q_z and Q_c , respectively, for the lossless circular-loop antenna.

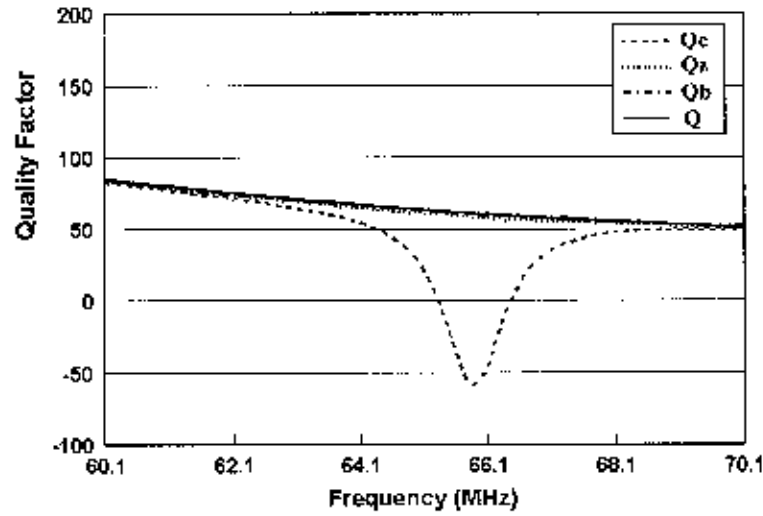


Figure 13. A comparison of the exact Q , the equivalent Q determined from the antenna's matched VSWR bandwidth Q_b , and the approximate Q determined from the frequency derivative of the antenna's impedance and reactance, Q_z and Q_c , respectively, for the lossless circular-loop antenna in the frequency region of antiresonance.

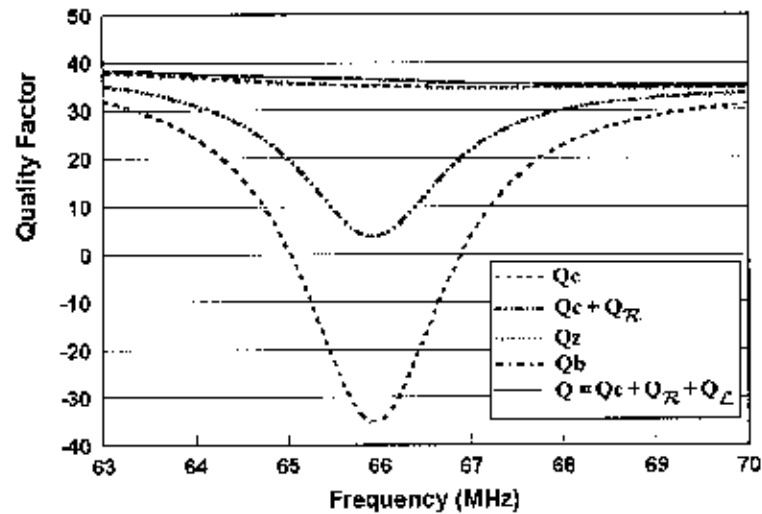


Figure 14. A comparison of the exact Q (and its component terms), the equivalent Q determined from the antenna's matched VSWR bandwidth Q_b , and the approximate Q determined from the frequency derivative of the antenna's impedance and reactance, Q_z and Q_c , respectively, for the lossy circular-loop antenna in the frequency region of antiresonance.

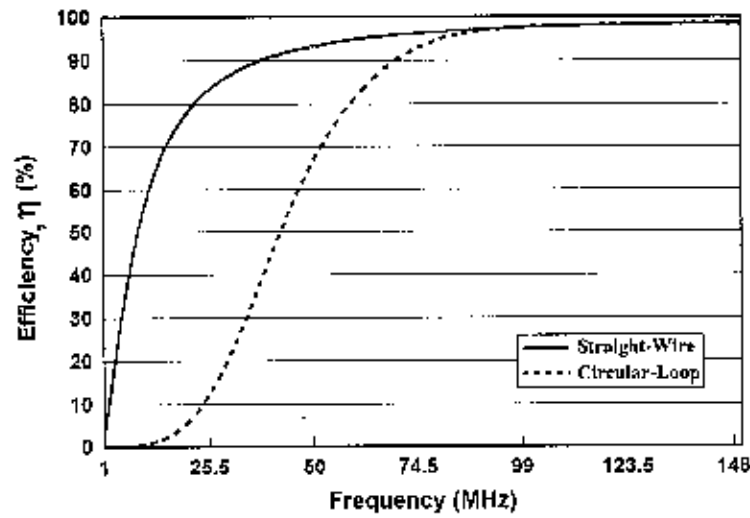


Figure 15. The radiation efficiencies for the lossy straight-wire (electric dipole) and circular-loop antenna (magnetic dipole) as a function of decreasing frequency.

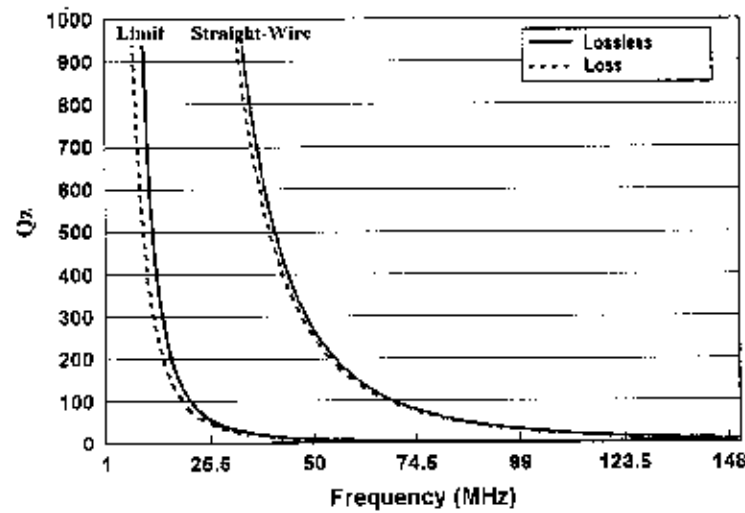


Figure 16. A comparison of the approximate Q (Q_z) and the lower bound on Q for the lossless and lossy straight-wire antennas.

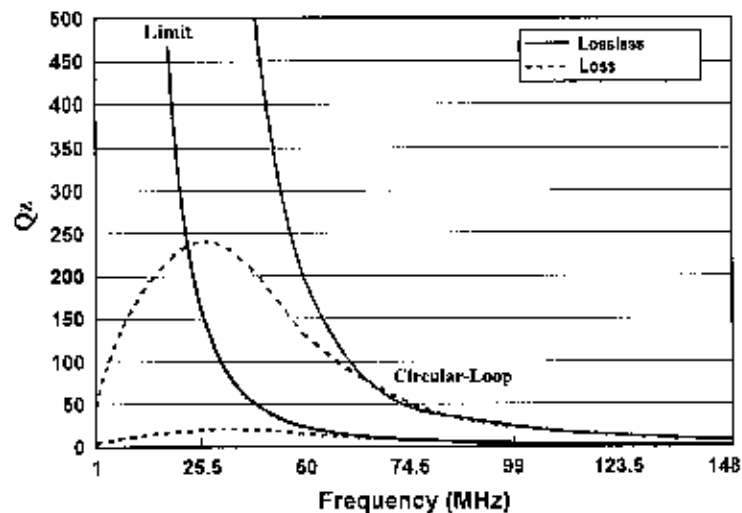


Figure 17. A comparison of the approximate Q (Q_z) and the lower bound on Q for the lossless and lossy circular-loop antennas.

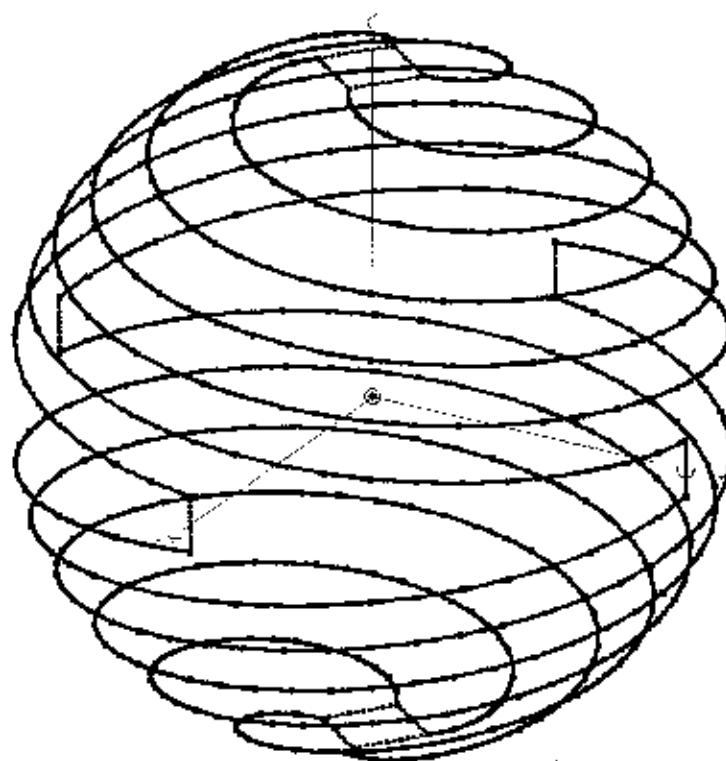


Figure 18. The electrically small folded spherical helix dipole antenna having an overall height and diameter of approximately 11.8 cm and a wire diameter of 2.6 mm.

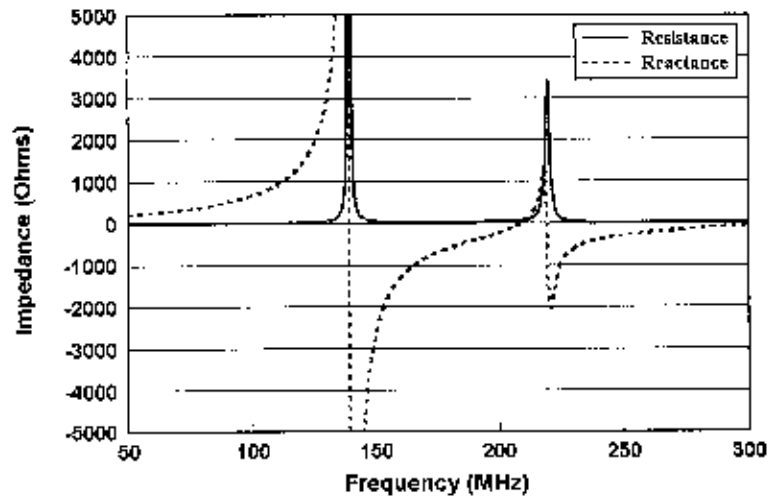


Figure 19. Input impedance of the lossy electrically small, folded spherical helix dipole antenna.

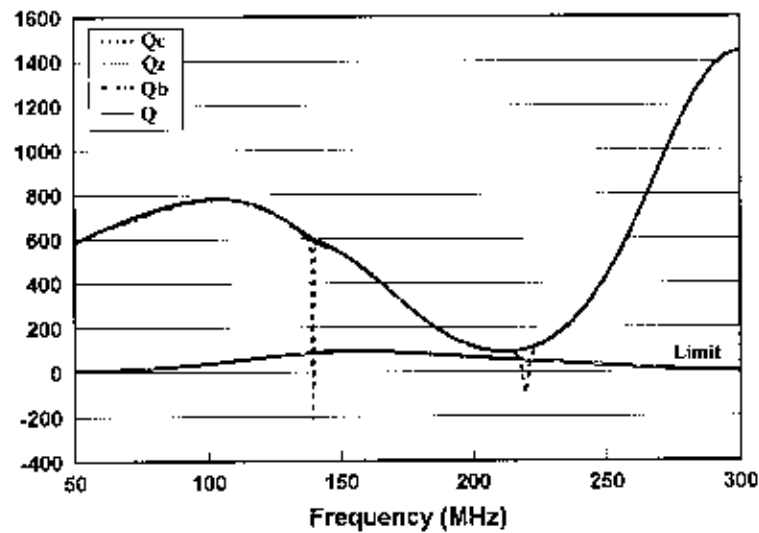


Figure 20. A comparison of the exact Q , the equivalent Q determined from the antenna's matched VSWR bandwidth Q_b , and the approximate Q determined from the frequency derivative of the antenna's impedance and reactance, Q_z and Q_c , respectively, for the lossy electrically small folded spherical helix dipole antenna.

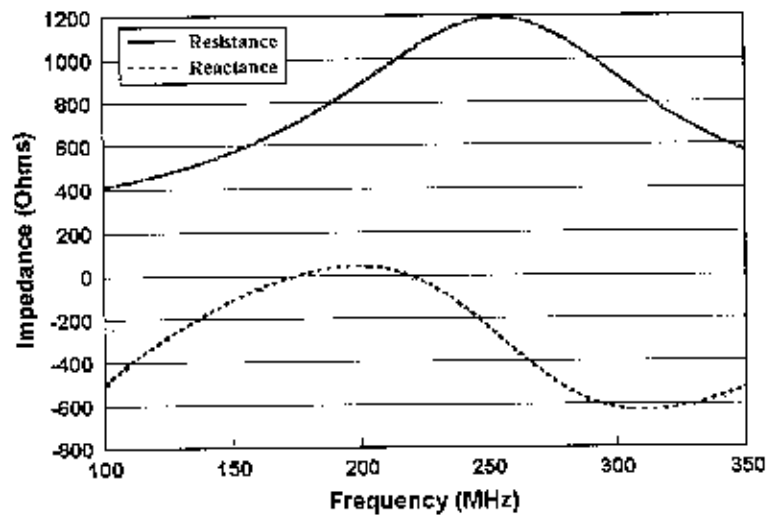


Figure 21. Input impedance of the lossy, resistively loaded, low Q antenna.

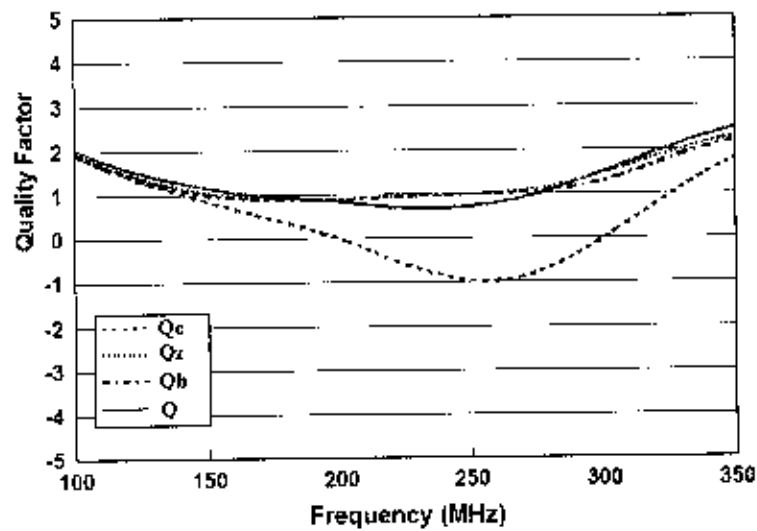


Figure 22. A comparison of the exact Q , the equivalent Q determined from the antenna's matched VSWR bandwidth Q_b , and the approximate Q determined from the frequency derivative of the antenna's impedance and reactance, Q_z and Q_c , respectively, for the lossy, resistively loaded, low Q antenna.

On the Radiation Properties of Electrically Small Multi-Arm Folded Wire Antennas

Steven R. Best
Air Force Research Laboratory
Sensors Directorate, Antenna Technology Branch
80 Scott Drive
Hanscom AFB, MA 01731

Abstract: The radiation properties of electrically small folded wire antennas are considered and compared as a function of height, occupied volume, geometry and the number of folded arms in the antenna structure. The radiation properties considered here include resonant resistance, efficiency and bandwidth, which is indicated by the antenna quality factor, Q . It is demonstrated that electrically small, multiple-arm, folded wire antenna designs offer significant performance improvement in terms of increasing resonant resistance, bandwidth and efficiency. However, when multiple-arm, folded wire antennas of the same height and occupied volume, but having significantly differing geometries, are made to be resonant at the same frequency, they exhibit similar resonant behavior. This illustrates that the resonant performance properties of these antennas are primarily a function of their height and occupied volume relative to the resonant wavelength. Additionally, various design options are considered and described for achieving self-resonance and a reasonable impedance match with any electrically small folded wire antenna design.

Keywords: Electrically small antennas; folded monopole antennas; folded dipole antennas.

1. INTRODUCTION

In a previous effort [1-2], the radiation properties of the multiple-arm, folded spherical helix antenna were described and it was shown that self-resonance, low Q and a reasonable impedance match (relative to a 50 Ω feed line) could be obtained in an electrically small volume by adjusting the number of folded arms and the individual arm length. In the previous work, the spherical helix geometry was chosen because it efficiently filled the spherical volume defined by an imaginary sphere having a radius equal to the maximum dimension of the antenna. *[Note: The radius of the imaginary sphere is defined by the maximum dimension of the antenna when the antenna operates in*

a "monopole configuration" where it is base fed and it is mounted over an infinite ground plane. The radius of the imaginary sphere is defined by one-half the maximum dimension of the antenna when the antenna operates in a "dipole configuration" where it is center-fed and no ground plane is used. An electrically small antenna is generally considered to be an antenna having a maximum spherical radius equal to $\frac{\lambda}{2\pi}$. Here, an electrically small antenna is one having a maximum spherical radius equal to $\frac{\lambda}{4\pi}$ [3].

Achieving self-resonance, low Q (relative to the fundamental lower bound on Q) and a reasonable impedance match in an electrically small volume is not unique to the folded spherical helix geometry. While the spherical helix geometry naturally fills a spherical volume, the design concepts associated with achieving self-resonance and an impedance match in an electrically small size can be used with any geometry.

Here, the concepts that were used in designing the folded spherical helix antenna are described in detail and they are applied to a variety of antenna geometries to illustrate that the antenna geometry, in and of itself, is not the significant factor in achieving the desired resonant performance properties. Additionally, it is shown that these design concepts can be implemented in a number of ways and the performance properties remain similar (within reasonable limits). This leads to the general conclusion that the resonant performance properties of these antennas are primarily a function of the antenna's height and occupied volume relative to the resonant (or tuned) wavelength.

2. ACHIEVING SELF-RESONANCE AT LOW FREQUENCIES

Consider the generic folded monopole antenna depicted in Figure 1, having a height of 6 cm, a diameter of 12 cm and a wire diameter of 1 mm. The radius of an imaginary sphere encompassing the maximum dimension of this antenna is approximately $a = 8.48$ cm.

Using a criteria of $a = \frac{\lambda}{4\pi}$, this antenna could be considered electrically at frequencies less than approximately 281 MHz. The folded monopole antenna shown in Figure 1 is modeled over an infinite PEC ground plane. This antenna is essentially a half-loop fed against a ground plane and operates in "magnetic-dipole" mode at very low frequencies. Additionally, it is important to note that the discussion and design concepts presented here apply equally to the folded dipole antenna, which is essentially a full loop. The impedance properties of the folded monopole shown in Figure 1 were calculated using the NEC 4 engine of EZNEC Pro [4] and are presented in Figure 2. In this case, the impedance of the antenna was calculated to include the effects of copper loss within the wire.

At very low frequencies, the folded monopole's impedance exhibits a very low resistance (R) and a reasonably low inductive (positive) reactance (X). With increasing frequency, the folded monopole's impedance eventually undergoes an antiresonance, which is characterized by a very rapid transition from a large $-X$ value to a very large $+X$ value

and where $\frac{dX}{d\omega}$, the frequency derivative of X , is less than zero. With further increase in frequency, the folded monopole's impedance exhibits a resonance, where $X = 0$, and $\frac{dX}{d\omega} > 0$.

For a folded monopole having the perimeter ratio described here, the resonant frequency is approximately 686.5 MHz and the feed point resistance is approximately 66 Ω . Operating in a folded dipole mode, where the ground plane is replaced by the image of the wire structure, the resonant resistance would be approximately 132 Ω . [Note: A typical folded dipole antenna, designed to have a resonant feed point resistance near 300 Ω , has a highly compressed perimeter ratio, where the depth of the folded structure is significantly less than its overall length (as defined in the E-plane).]

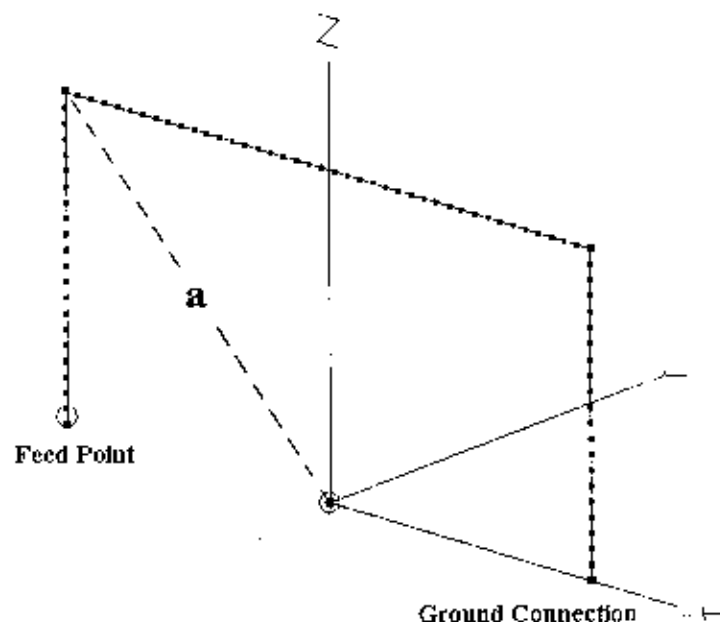


Figure 1. Geometry configuration of the single-wire folded monopole antenna operating against an infinite PEC ground plane.

2.1 Lowering the Self-Resonant Frequency

Achieving resonance ($\frac{dX}{d\omega} > 0$) at a frequency less than the inherent resonant frequency of the antenna is more than simply an exercise in tuning out the high capacitive reactance that exists in the frequency region between antiresonance and resonance. At its inherent

resonant frequency, the folded monopole antenna behaves as a series R, L, C circuit having a feed point impedance of the form $Z(\omega) = R(\omega) + jX(\omega)$, where $X(\omega) = \omega L - j\frac{1}{\omega C}$ and the effective values of L and C are such that $X(\omega) = 0$. To lower the resonant frequency, the effective values of L and/or C at feed point must be increased. As the effective values of L or C at the feed point increase, the resonant frequency decreases, and the total impedance curve of the folded monopole is essentially compressed towards lower frequencies.

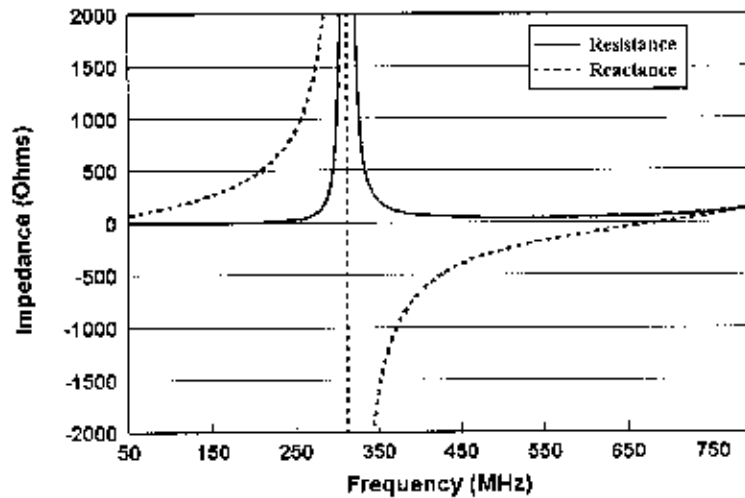


Figure 2. Input impedance properties of the single-wire folded monopole antenna through the first antiresonant and the first resonant frequencies.

When the resonant frequency decreases and resonance compression within the total impedance curve occurs, the value of the inherent resonant resistance does not track with the decreasing resonant frequency. As the resonant frequency of a fixed size or fixed volume antenna decreases with increasing values of effective L and C at the feed point, the resonant resistance and bandwidth decrease as well. This is a result of the fact that the antenna is much smaller relative to the longer resonant wavelength. An antenna's resonant performance properties are primarily a function of the antenna's size or occupied volume relative to the resonant wavelength. At the same time, it is recognized that antennas of different class or type, while occupying the same volume and having the same resonant frequency, may have different resonant performance properties. In the case of the folded monopole antenna, it is also interesting to note that the self-resonant frequency can be decreased to a frequency lower than the inherent antiresonant frequency.

To lower the resonant frequency of the folded monopole antenna, the effective values of L and C at the feed point can be increased in a number of ways. The self-inductance of the antenna can be increased by simply adding wire length to the structure or adding a fixed or tunable lumped inductive load as illustrated by the meander line and inductive

load antenna configurations depicted in Figure 3. The total wire length in the meander line configuration is approximately 40.4 cm. The impedance properties of these antennas, both designed to be resonant at the same frequency, are presented in Figure 4. The resonant frequency of these antennas is approximately 539 MHz, which is a 21.5% reduction relative to the initial folded monopole configuration of Figure 1. At the lower resonant frequency, the resonant resistance decreases from 66 Ω (at the inherent resonant frequency) to 40.8 Ω and to 48.5 Ω for the meander line and inductive load configurations, respectively. Some difference in resonant resistance is expected since the configurations are notably different and the loss within each antenna differs as a function of the wire loss and inductor loss. The inductor load was assumed to be lossless and has a value of inductance, $L_S = 0.0335 \mu\text{H}$. It is significant to note that the meander line and inductive load configurations exhibit very similar resonant resistance even though resonance is achieved with different techniques.

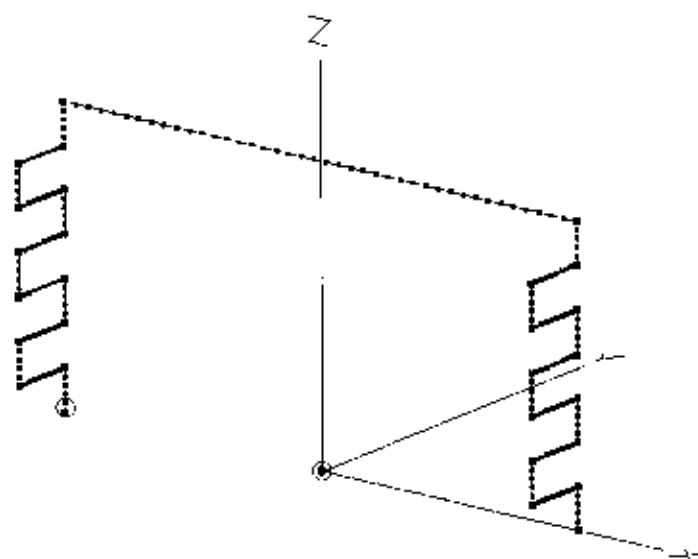
The approximate resonant Q of these configurations was calculated using the following expression [5]

$$Q \approx \frac{\omega}{2R} \sqrt{\left(\frac{dR}{d\omega}\right)^2 + \left(\frac{dX}{d\omega} + \frac{|X|}{\omega}\right)^2} \quad (1)$$

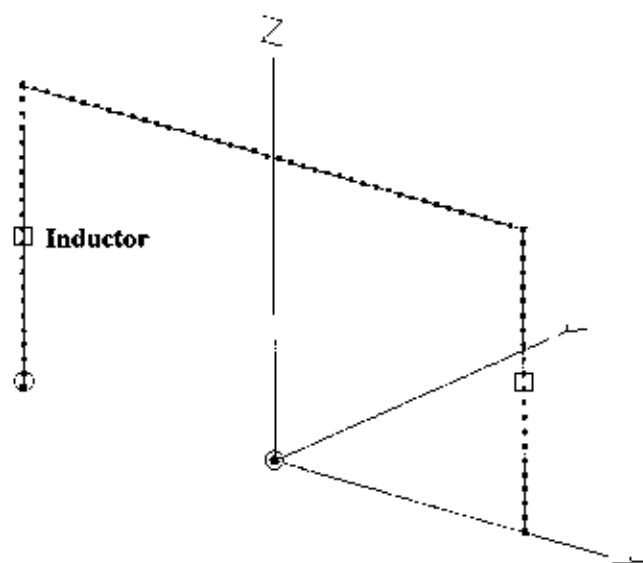
where R and X are the antenna's frequency dependent feed point resistance and reactance, respectively. The Q was found to be 10.3 and 11.6 for the meander line and inductive load configurations respectively. The inverse Q of the antenna provides a very accurate indication of the bandwidth properties of the antenna, indicating that the resonant bandwidths of these antennas are very similar. The resonant Q of the initial folded monopole configuration is 6.2 indicating its bandwidth is greater than that of the meander line and inductor loaded configurations. The resonant bandwidth decreases with decreasing resonant frequency because the volume of the antenna is much smaller relative to the longer resonant wavelength.

Another interesting point to consider is the change in impedance occurring at 539 MHz between the initial folded monopole configuration and both the meander line and inductive load configurations. The initial folded monopole configuration has an impedance of $43.2 - j188.1 \Omega$ at 539 MHz, while the meander line and inductive load configurations are resonant, having resistances of 40.8 Ω and 48.5 Ω , respectively. Increasing the self-inductance of the antenna structure to lower the resonant frequency will effectively tune the capacitive reactance to zero but will not, in general, significantly affect the resistance properties of the antenna at the new resonant frequency. *[Note: This will generally remain valid under the condition where the antenna's new resonant frequency is well above the antenna's inherent antiresonant frequency and the antenna's inherent resistance is decreasing with decreasing frequency. As the operating frequency approaches antiresonance, the inherent resistance begins to increase rapidly and will differ significantly from that of the antenna with the lower resonant frequency, when compared at the same frequency. With these simple configurations made to be resonant*

at a lower frequency, antenna's resonant resistance will be less than that of the antenna's resistance at its inherent resonant frequency.]



Meander Line Inductively Loaded Folded Monopole



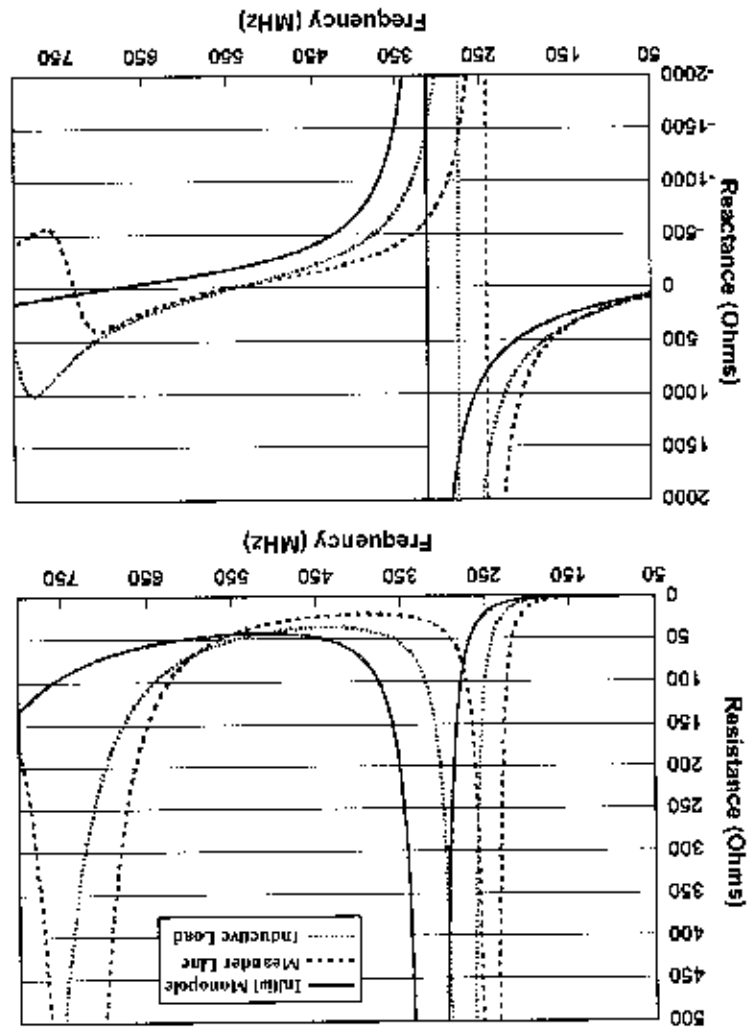
Fixed or Tunable Lumped Element Inductor Loaded Folded Monopole

Figure 3. Geometry configurations of the meander line and inductive load folded monopole antenna configurations.

The antenna configuration depicted in Figure 5 was used to lower the resonant frequency of the initial folded monopole from 686.5 to 337 MHz, which was simply a result of the

plate were a solid metal sheet.
current paths established by a finite number of discrete wires that would not exist if the adds additional self-inductance to the feed point impedance because of the additional Figure 5. The wire "plate" structure used to top load the folded monopole antenna also monopoles. An example of capacitive top-loading of the folded monopole is depicted in top-load the antenna with a wire or plate structure as is commonly done with top-loaded One of the common techniques used to increase the effective feed point capacitance is to inductance at the feed point, the effective capacitance at the feed point can be increased. As an alternative to lowering the resonant frequency with an increase in the effective

Figure 4. Input impedance properties of the meander line and inductive load folded monopole antenna configurations.



specific choice of the wire top plate dimensions (12 cm x 12 cm). At the lower resonant frequency of 337 MHz, the top-loaded configuration has a resistance of 25.8 Ω , which is again lower than that of the initial resonant resistance of 66 Ω . The resonant Q of this antenna increases to a value of 10.3. An interesting point to note is that when the inductive load configuration of Figure 3 is tuned to be resonant at 337 MHz ($I_s = 0.168$ μ H), its resonant resistance is 22.7 Ω . These resistance values do not compare to the resistance of the initial folded monopole at 337 MHz, which is 420.6 Ω . At this frequency, the initial folded monopole is operating very close to its primary antiresonant frequency. The resonant Q of this inductive load configuration is 44.1, a value significantly larger than that of the top-loaded configuration because the top-load configuration has a much larger occupied volume. Increasing the volume of a resonant antenna decreases its Q and increases its bandwidth. A comparison of the impedance properties of top-loaded and inductive loaded antennas, both resonant at 337 Ω , is presented in Figure 6.

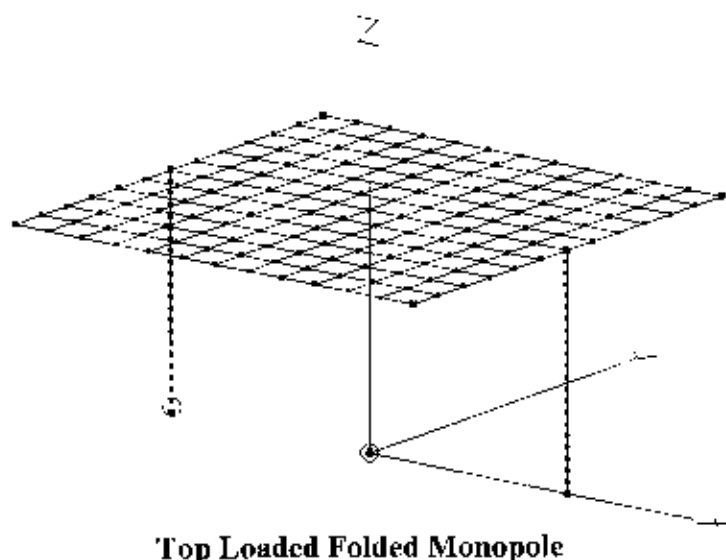


Figure 5. Geometry configuration of the capacitive top-plate folded monopole antenna.

2.2 Tuning the Antenna Below Antiresonance

In the previous section, several techniques that may be used to lower the inherent resonant frequency of the folded monopole configuration were illustrated. While differing in design approach, it is significant to note that when these antenna configurations are made to be resonant at the same frequency, they exhibit very similar resonant properties. The major performance issue to consider in lowering the resonant frequency of a fixed size or fixed volume antenna is that with decreasing resonant frequency, the resonant resistance and bandwidth decrease, primarily as a result of the

fact that the height and volume of the antenna decreases relative to the longer resonant wavelength.

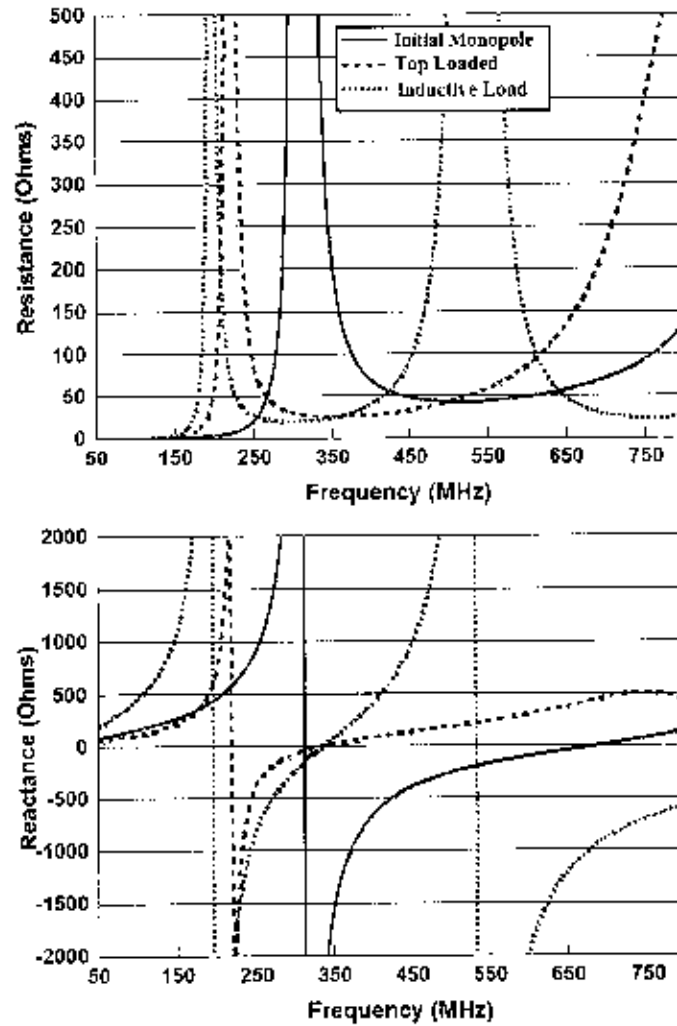
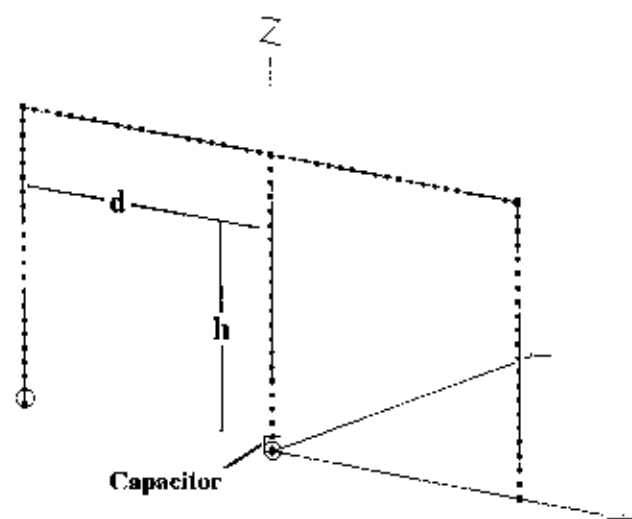


Figure 6. Input impedance properties of the initial folded monopole, the top-loaded folded monopole and the inductive load folded monopole antennas.

Here, an approach to achieving resonance at very low frequencies (where the antenna is very small electrically) is considered that mitigates the issue associated with the decreasing resonant resistance that occurs with the configurations described in the previous section. Considering the impedance properties of the initial folded monopole configuration depicted in Figure 2, it is seen that below the antiresonant frequency where the feed point reactance is positive, there is a frequency at which the feed point resistance is equal to $50\ \Omega$. If this positive inductive reactance is tuned to zero at the feed point with a series capacitance, the antenna will be resonant and it will be impedance matched to $50\ \Omega$.

For the folded monopole of Figure 1, the feed point resistance is $50\ \Omega$ at a frequency of 267 MHz. The reactance at this frequency is approximately $1250\ \Omega$, which is a significant value of reactance to tune with a series capacitor at the feed point. The practical concerns associated with this approach include the high antenna Q (narrow bandwidth) that exists at low frequencies (as a result of the antenna having a very small volume relative to the long wavelength) and the issues associated with the loss and reasonable capacitance value of the tuning capacitor. At 267 MHz, the Q of the initial folded monopole configuration is approximately 91.7.

The other issue that to consider is that the frequency at which the antenna exhibits a $50\ \Omega$ feed point resistance can be decreased to further lower the desired operating frequency of the antenna. For example, in addition to lowering the inherent resonant frequency of the antenna, all the antenna configurations described in the previous section decrease the frequency where the antenna exhibits a $50\ \Omega$ resistance. This behavior is illustrated in the impedance curves presented in Figures 4 and 6. The frequency at which the resistance is $50\ \Omega$ for the meander line and the inductive load configuration ($L_S = 0.168\ \mu\text{H}$), is 216 MHz and 179 MHz, respectively. At the same time, the value of inductance needed to be tuned at these lower frequencies increases. The inductive reactance increases to $1623\ \Omega$ and $2974\ \Omega$ for the meander line and inductive load configurations respectively. The Q at these frequencies increases relative to the Q of the initial configuration at 267 MHz, indicating that the bandwidth of these antennas will be narrower. The Q of the meander line and inductive load configurations is 154 and 321, respectively.



**Fixed or Tunable Capacitively Loaded
Folded Monopole**

Figure 7. Geometry configuration of the capacitive load folded monopole antenna.

Another technique that can be used to lower the frequency where the antenna exhibits a $50\ \Omega$ resistance is depicted in Figure 7. In this case, a fixed or tunable capacitor is added to the structure with the addition of another folded arm [6]. The capacitor can be placed at any location, d and height h and its value can be adjusted accordingly to adjust the frequency where the resistance is equal to $50\ \Omega$. In the configuration of Figure 7, the capacitance is adjusted to $3\ \text{pF}$ to set the frequency at which the resistance is $50\ \Omega$ to approximately $179\ \text{MHz}$, matching that of the inductive load configuration described above. The Q of this antenna is approximately 355 , which is not significantly different than that of the inductive load configuration. A comparison of the antennas' impedance properties is presented in Figure 8. The advantage of the capacitor load configuration is that less tuning capacitance required at the feed point because the feed point reactance is lower than that of the inductive load configuration, $1733\ \Omega$ compared to $2974\ \Omega$.

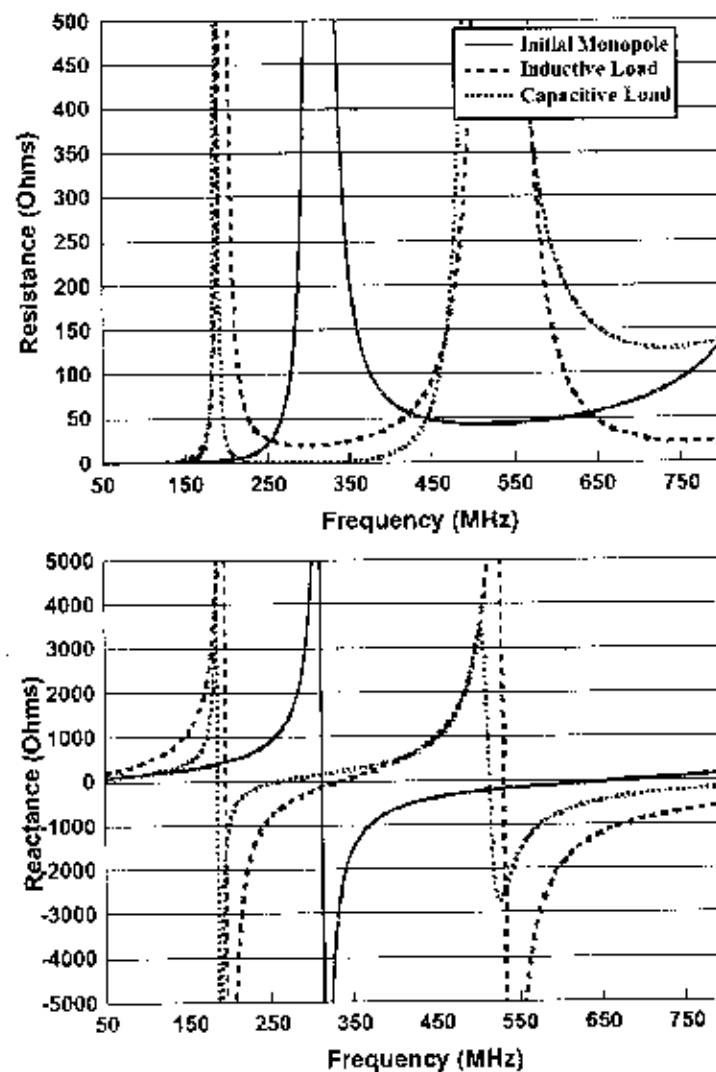


Figure 8. Input impedance properties of the initial folded monopole, the inductive load monopole and the capacitive load monopole.

3. INCREASING RADIATION RESISTANCE AT LOW FREQUENCIES

In the previous section, several techniques were described for lowering the frequency at which the folded monopole becomes resonant. While a lower resonant frequency can be easily achieved using a number of configurations, the performance trade-offs associated with doing so must be recognized. Specifically, the resonant resistance and bandwidth decrease significantly with decreasing resonant frequency. While not specifically discussed in the previous sections, the antenna efficiency generally decreases as well.

It was also shown that at frequencies below antiresonance, the antenna can be tuned to operate at a frequency where it inherently has a feed point resistance equal to $50\ \Omega$. Using a number of techniques, this frequency can be decreased so that the antenna can be made smaller relative to the tuned wavelength. Again, the performance trade-offs associated with tuning the antenna at lower frequencies must be recognized. Specifically, with decreasing frequency, the operating bandwidth decreases rapidly. Additionally, lowering the frequency where the antenna exhibits a $50\ \Omega$ resistance also increases the inductive reactance, resulting in a higher reactance to tune at the feed point.

In this section, the technique used to increase the radiation resistance at resonance, in designing the folded spherical helix, is briefly described. In the next section, it will be applied to a variety of folded wire antenna configurations so that their performance properties can be compared as a function of different physical configurations.

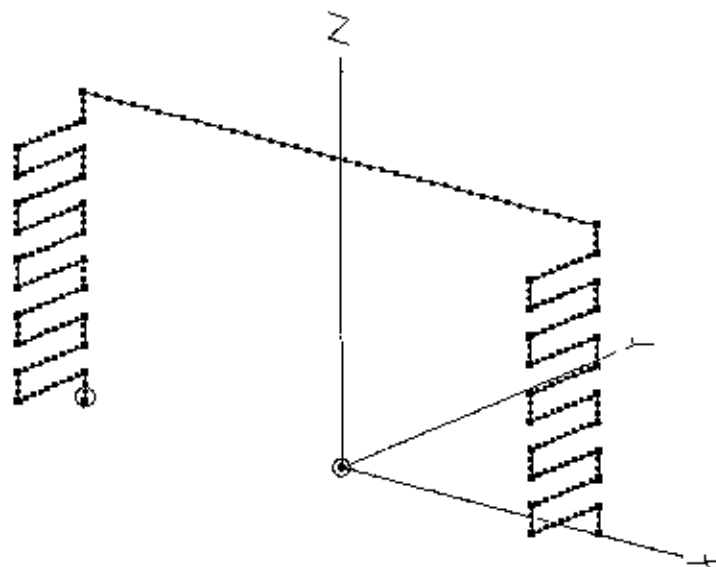


Figure 9. Geometry configuration of the meander line folded monopole antenna with increased total wire length.

Consider the 2-arm meander line folded monopole configuration shown in Figure 9, which is similar to the configuration shown in Figure 3, except that the total wire length in the antenna has been arbitrarily increased to approximately 62.6 cm. This configuration will have a lower resonant frequency, lower bandwidth (as indicated by increasing Q) and lower efficiency. The configuration of Figure 3 has a resonant frequency of 539 MHz and a resonant resistance and computed efficiency of 40.8 Ω and 98.8%, respectively. The 2-arm configuration of Figure 9 has a resonant frequency of 430 MHz and a resonant resistance and computed efficiency of 26.5 Ω and 97.3%, respectively. The Q of these antennas is 10.3 and 17.4 for the configurations of Figure 3 and Figure 9, respectively.

As the total wire length in the meander line configuration increases and the resonant frequency decreases, the resonant resistance continues to decrease. At some point, the antenna will be very small relative to the resonant wavelength and the resonant resistance will approach zero. To mitigate the diminishing resonant resistance, the number of folded arms within the structure can be increased as done with the folded spherical helix antenna, and the resonant resistance (specifically the radiation resistance) will increase significantly.

Several multiple folded arm configurations are depicted in Figure 10. These include a 3, 4, 5 and 6-arm configuration of the meander line folded monopole antenna of Figure 9. As the number of folded arms increases two things occur. First, the resonant frequency increases slightly and second, the resonant resistance increases significantly. The 3-arm configuration has a resonant frequency of 451 MHz and a resonant resistance of 62.7 Ω while the 4-arm configuration has a resonant frequency of 474 MHz and a resonant resistance of 121 Ω . It is very significant to note that the 5 and 6-arm configurations are not self-resonant. This is a result of the increasing self-capacitance within the structure (between the arms) which has the affect of diminishing the self-inductance of the meander sections. While this affect causes the resonant frequency of the 3 and 4-arm configurations to increase, it is so significant in the 5 and 6-arm configurations that self-resonance is not achieved.

Given that the 3 and 4-arm configurations of Figure 10 are resonant at a frequency higher than the 2-arm meander line configuration (of Figure 9), it is obvious that the total wire length in each meander line section can be increased to lower their resonant frequencies to match that of the 2-arm configuration, 430 MHz. Note that length of the meander section (6 cm height) in the 2-arm configuration of Figure 9 is approximately 25.3 cm. In the case of the 3-arm configuration, the wire length in the meander section is increased to approximately 27.4 cm. The resonant frequency is 430 MHz, the resonant resistance and Q are 57.4 Ω and 12.3, respectively. In the case of the 4-arm configuration, the wire length in the meander section is increased to approximately 29.5 cm. The resonant frequency is 430 MHz, the resonant resistance and Q are 98.8 Ω and 10, respectively. The impedance properties of the 2, 3 and 4-arm configurations are presented in Figure 11. With the increase in the number of folded arms, the resonant resistance increases and the resonant Q decreases (indicating that the bandwidth increases). The efficiency of these antennas is 97.3%, 97.9% and 98.1% for the 2, 3 and 4-arm configurations, respectively.

An alternate multi-arm folded monopole configuration is depicted in Figure 12. This antenna is a 4-arm configuration where the wires at the top of the antenna are connected about the perimeter of the antenna geometry rather than at the center. With this configuration, having the same meander section length as the 2-arm configuration of Figure 9, the resonant frequency decreases to 390 MHz where the resonant resistance is approximately $97\ \Omega$. The initial decrease in resonant frequency is expected since there is slightly more wire comprising the connection between the vertical meander sections and the wire around the perimeter of the antenna volume increases the effective capacitance to ground. Together, these factors contribute to the decrease in resonant frequency.

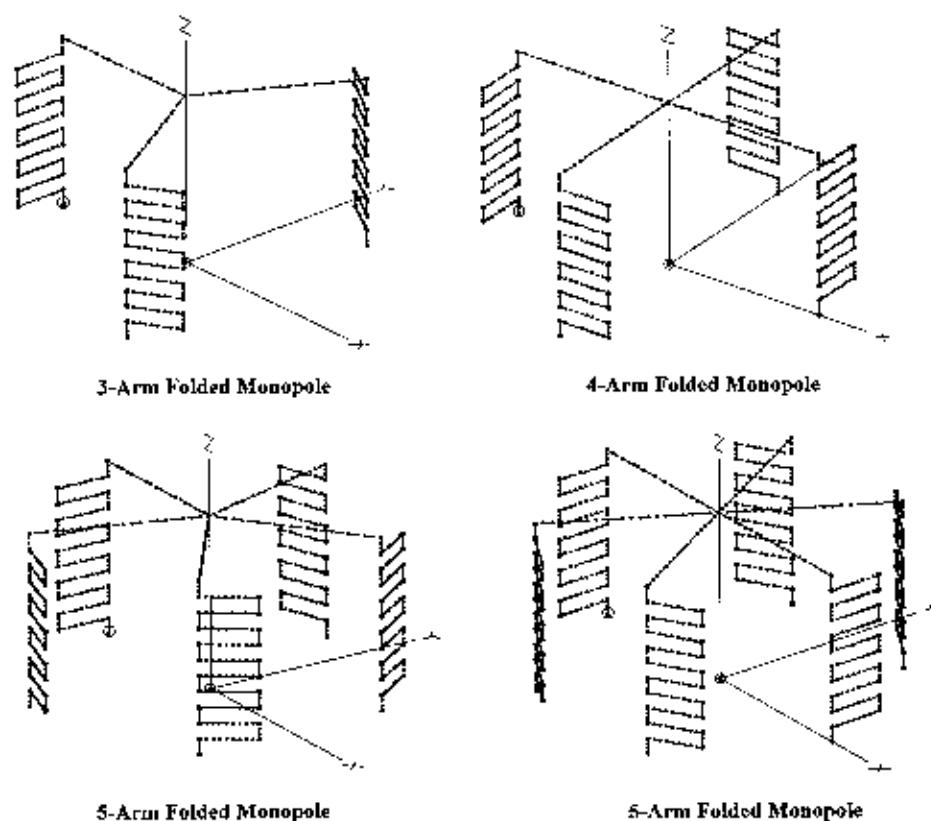


Figure 10. Geometry configuration of the multi-arm meander line folded monopole antennas.

Having a lower resonant frequency, it is obvious that the total wire length in each meander section can be decreased and the resonant frequency of the antenna can be increased to 430 MHz. In this case, the total wire length in each meander section is decreased to approximately 20.5 cm. At the resonant frequency of 430 MHz, this configuration has a resonant resistance of $118\ \Omega$ and a Q of 6.7. This configuration offers a substantial decrease in Q (increase in bandwidth) as a result of the increase in occupied volume. As evident from the resonant resistance, this configuration also offers

a larger effective height at its resonant frequency, which is consistent with top-loaded antennas [7].

Both of the 4-arm folded monopole configurations can be designed with an increase in wire length such that they are resonant at a lower frequency where the resonant resistance would be closer to $50\ \Omega$. With this further decrease in resonant frequency there would be a corresponding increase in Q . Increasing the wire length in the 4-arm configuration of Figure 10 to 50.2 cm, the resonant frequency decreases to 300.2 MHz, where the resonant resistance is approximately $50.8\ \Omega$ and the Q is 22.8. This configuration and value of resonant frequency are significant when considering the antennas to be discussed in the next section.

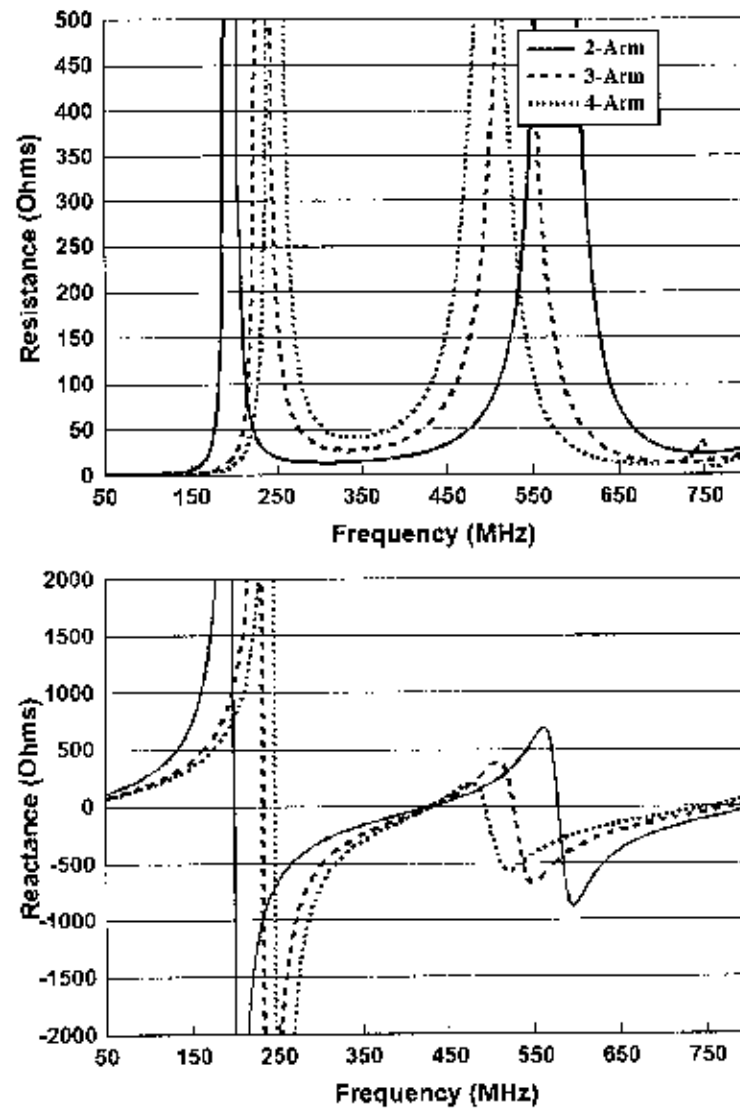


Figure 11. Input impedance properties of the multi-arm inductor line folded monopole antennas.

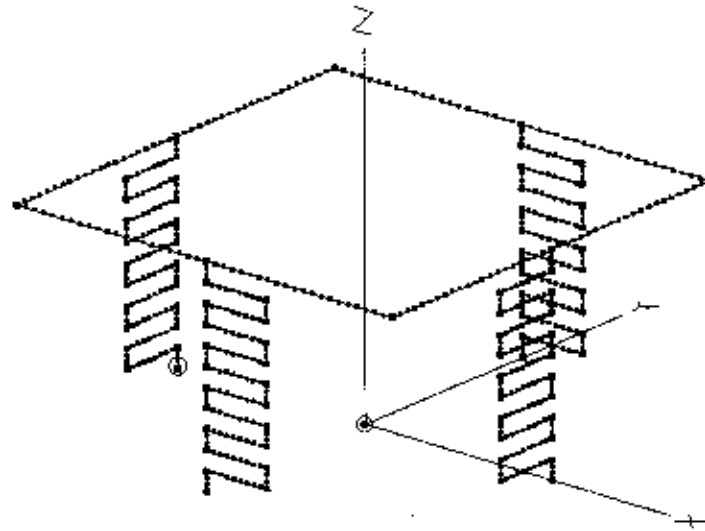


Figure 12. Geometry configuration of the alternate folded monopole antenna having the top wires connected about the perimeter of the antenna volume.

4. COMPARING MULTI-ARM FOLDED MONOPOLE ANTENNAS

In the previous section, several multi-arm folded monopole configurations were considered and their performance properties were briefly examined as a function increasing the number of folded arms and decreasing resonant frequency. It was demonstrated that with an increase in the number of folded arms, a significant increase in the resonant resistance can be realized. This can be significant in the design of small antennas where the resonant resistance is typically very low. In all cases however, with decreasing resonant frequency, there is a corresponding decrease in the resonant resistance, bandwidth and efficiency.

In this section, several very specific multiple-arm folded monopole antennas are considered as a function of differing geometry. Antennas of differing geometry are made to have the same overall height, the same physical volume and the same resonant frequency. Their performance properties are compared and it is demonstrated that when these antennas are made to be resonant at the same frequency, they exhibit very similar resonant properties indicating that these properties are essentially a function of the antennas height and occupied volume relative to the resonant wavelength. At the same time, certain differences in the antenna configurations that affect these resonant properties are noted.

The first antennas considered are the Koch fractal, meander line and normal mode helix configurations previous considered [2], which were shown to exhibit similar resonant behavior independent of the differences in their total wire length and geometry. These antenna configurations were converted to 3-arm folded monopoles as shown in Figure 13.

These antennas are 6 cm in height with a 6 cm horizontal arm length to the center of the geometry. The wire diameter used in modeling these antennas was 0.1 mm, which is necessary to accommodate the high degree of wire compression in the Koch fractal configuration. These antennas are resonant between 525 and 530 MHz. No attempt was made to optimize the resonant or overall performance properties of these antennas.

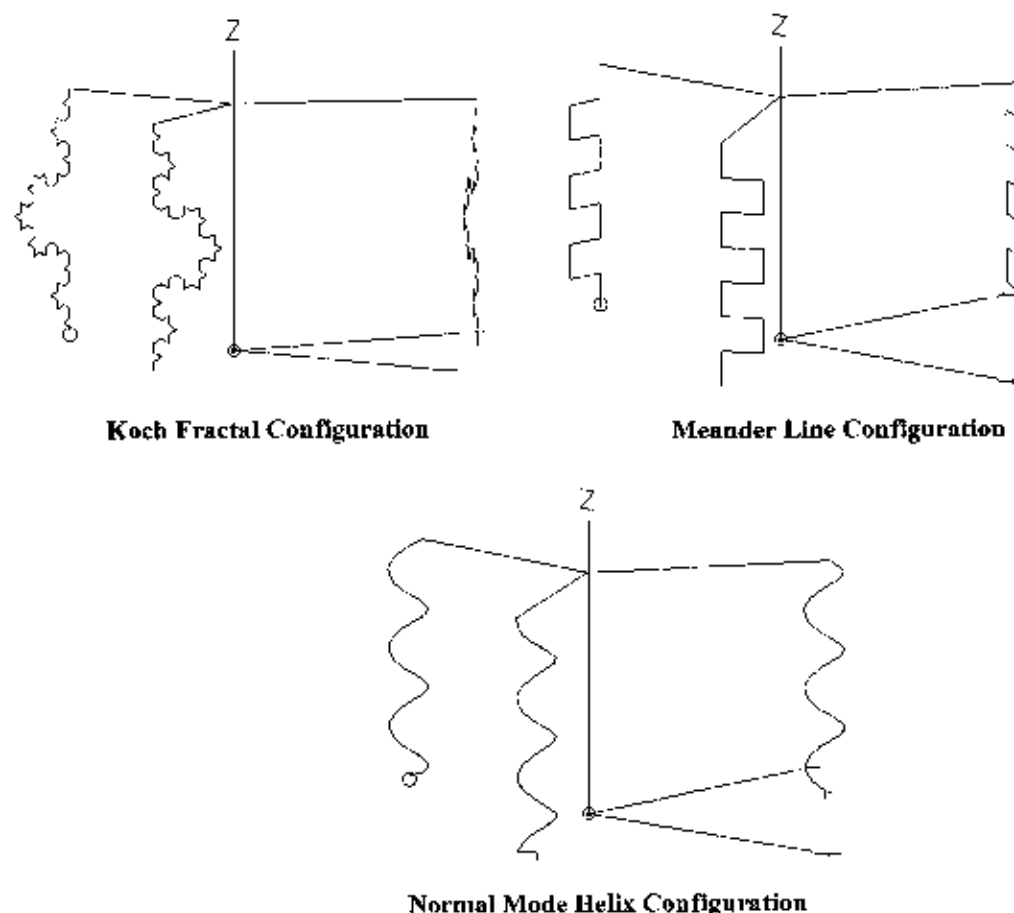


Figure 13. Geometry configuration of Koch fractal, meander line and normal mode helix folded monopole antennas.

The impedance properties of these antennas are compared in Figure 14. A table summarizing their resonant performance is presented in Table 1. Examining the performance properties of these antenna configurations it is evident that their resonant behavior is very similar, indicating that these performance properties are essentially independent of any differences in their total wire length and geometry.

Table 1. Performance Properties of the Folded Monopole Antennas Depicted in Figure 13.

Antenna	Resonant Frequency (MHz)	Resonant Resistance (Ω)	Quality Factor (Q)	Efficiency (%)
Koch Fractal	530	93.9	10.3	92.4
Meander Line	528	93.8	10.3	93.3
NM Helix	525	95	10.5	93.8

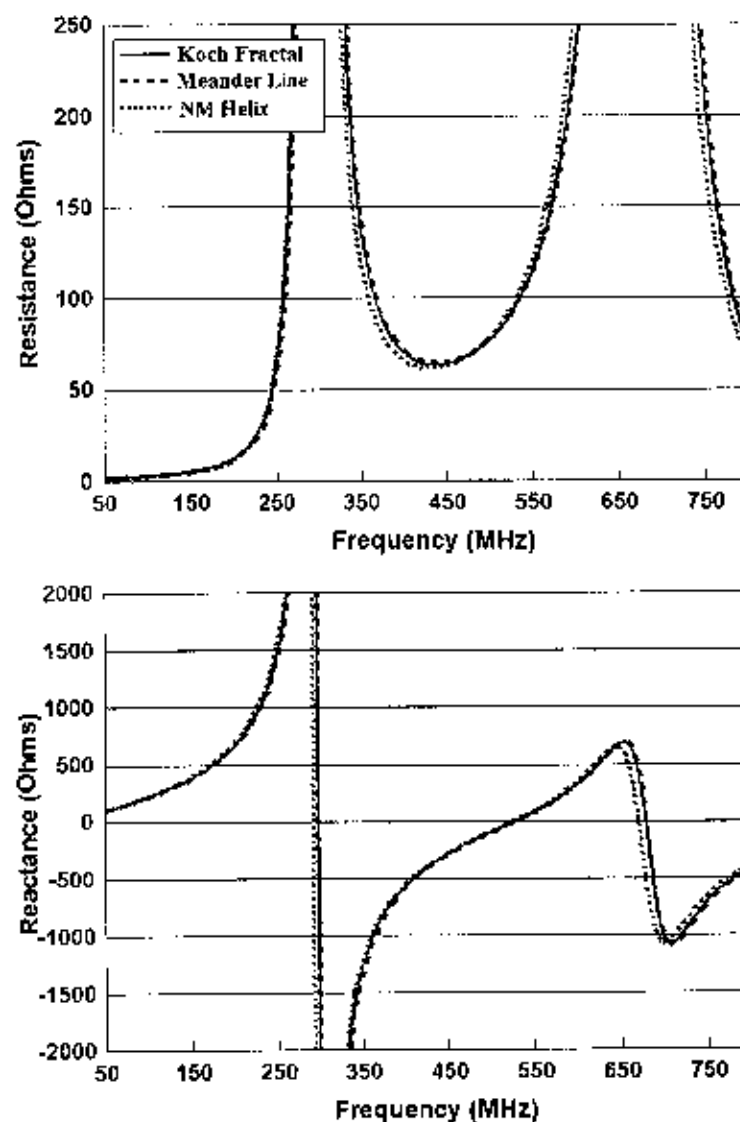


Figure 14. Input impedance properties of the Koch fractal, meander line and normal mode helix folded monopole antennas.

volume than the spherical outline of the folded spherical helix antenna. For this reason it is expected that these configurations would exhibit a lower Q .

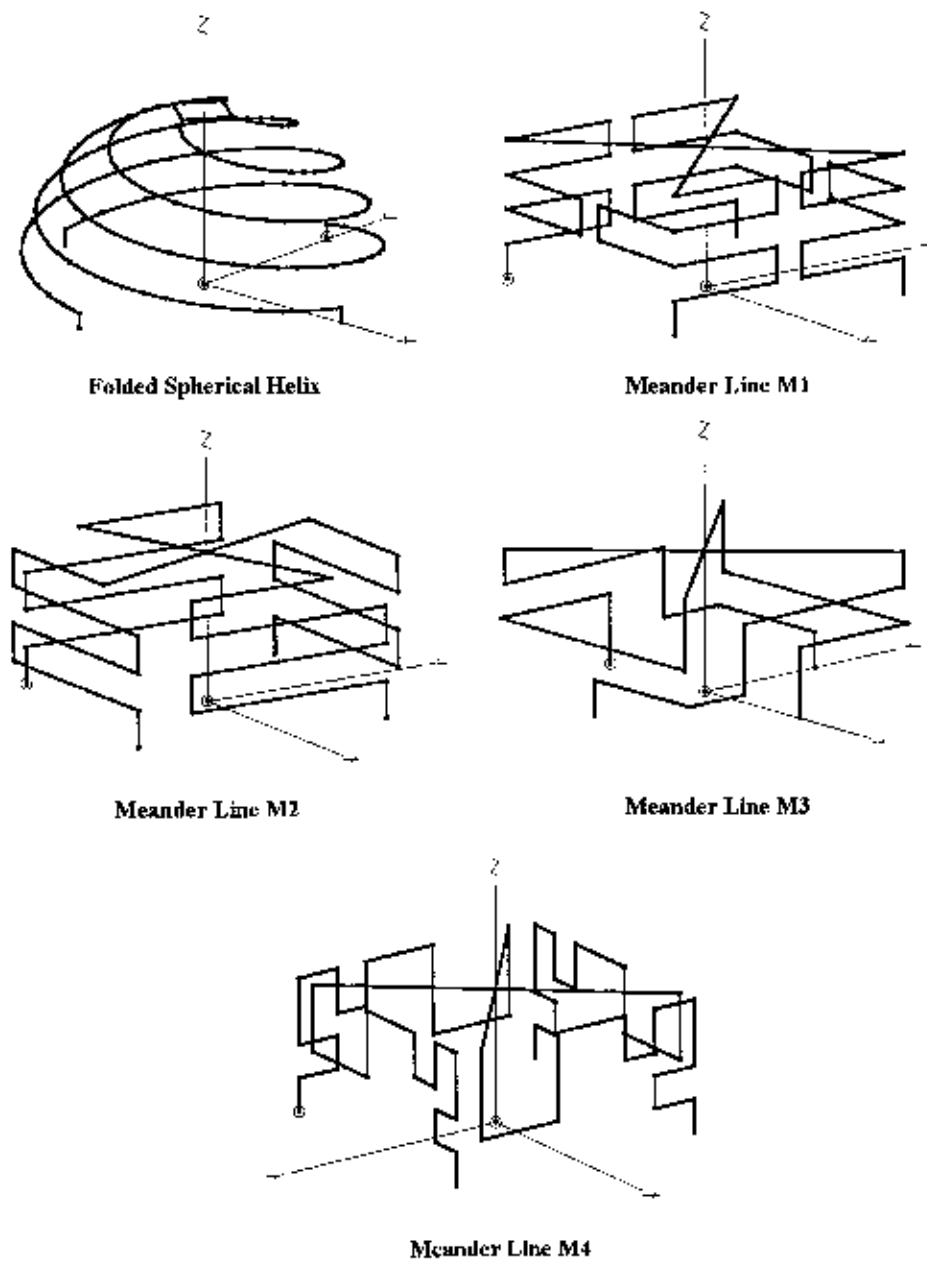


Figure 15. Geometry configuration of the folded spherical helix and the meander line folded monopole configurations M1, M2, M3 and M4.

The next set of folded monopole antennas considered is of significantly different configuration. In the configurations of Figure 13, the additional wire length added to the antenna to lower the resonant frequency is vertically oriented, with the total wire length remaining within a relatively small area of a single face of the structure. In the next set of antenna configurations, the total wire length in each arm occupies a larger area of the face or wraps around the entire antenna volume throughout multiple faces. In the previous article describing the folded spherical helix, a 4-arm configuration fitting within a sphere of 6 cm radius was presented having a resonant frequency near 300 MHz, a resonant resistance of approximately 43 Ω , and a Q of approximately 34. The 4-arm configurations presented here occupy the same physical dimensions except that they are contained within a cubic, not a spherical volume. These antennas are designed to be resonant at or near 300 MHz and their performance properties are compared as a function of total wire length and geometry.

The first set of antenna configurations is depicted in Figure 15. These antenna configurations are simply designated M1 through M4. These antennas have a wire diameter of 2.6 mm, matching that of the folded spherical helix antenna (FSH). A comparison of their impedance properties and Q is presented in Figures 16 and 17, respectively. A summary of their resonant performance properties is presented in Table 2. The total wire length indicates the total wire within the entire antenna structure.

Table 2. Performance Properties of the Folded Monopole Antennas Depicted in Figure 15.

Antenna	Total Wire Length (m)	Resonant Frequency (MHz)	Resonant Resistance (Ω)	Quality Factor (Q)	Efficiency (%)
FSH	1.30	300.3	43.1	33.8	98.7
M1	1.86	300.9	63.6	16.8	98.6
M2	1.83	300.4	56.2	17.8	98.5
M3	1.29	300.2	56.4	21.8	98.9
M4	1.56	301.1	44.3	26.4	98.3

The performance properties of these antennas do not agree as well as those of the folded monopole configurations depicted in Figure 13. The configurations in Figure 13, while having different geometries and total wire lengths, are very similar in terms of their occupied volumes and perimeters. The antennas depicted in Figure 15 have significantly different wire perimeters and location throughout the structure. Considering these factors, the resonant performance properties are reasonably similar. In all cases, the resonant radiation resistance (the total resistance including loss is indicated here) is a function of the effective height established by the wire length and geometry. The notable difference in antenna quality factor between the folded spherical helix and meander line configurations is directly attributable to the difference in their respective effective volumes. The cubic outline of the meander line geometries occupies a larger physical

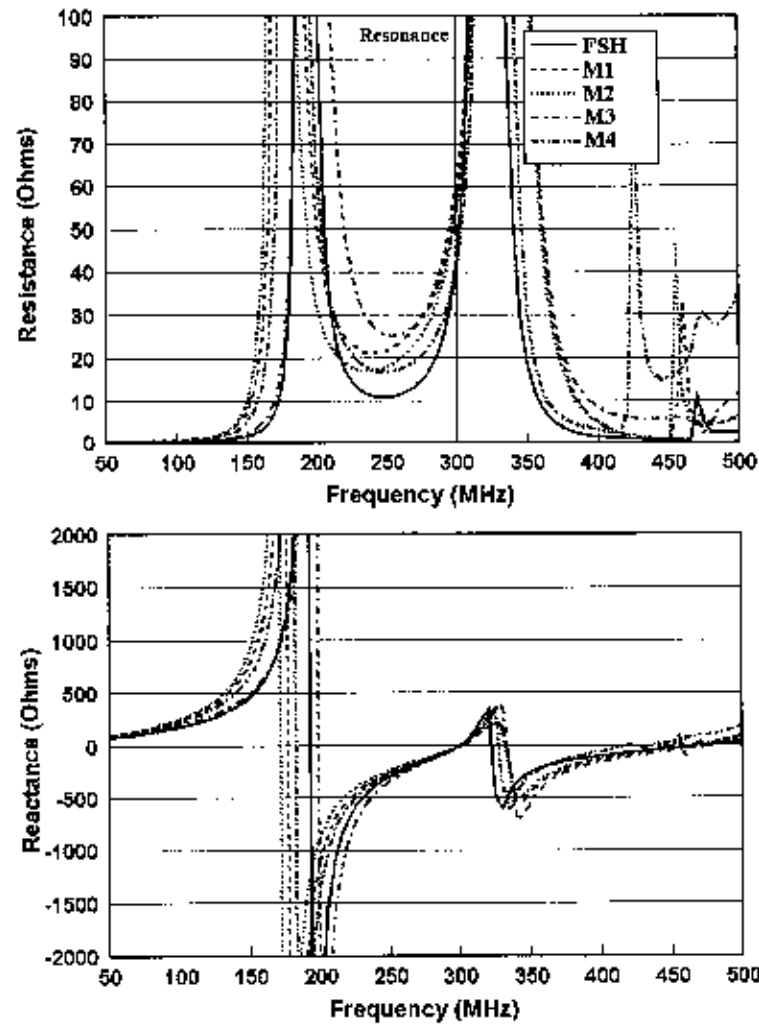


Figure 16. Input impedance properties of the folded spherical helix and the meander line folded monopole configurations M1, M2, M3 and M4.

Another point to note is that the change in height of the wire (*z-coordinate*) as a function of increasing wire length (designated $\frac{dz}{dl}$) appears to affect the resonant properties of the antenna. In most configurations studied, $\frac{dz}{dl}$ has been greater than or equal to zero. In studying configurations where $\frac{dz}{dl}$ can be less than zero (where the wire travels back towards the ground plane) significant differences in resonant performance have been noted. This has been a general observation and has not been studied extensively.

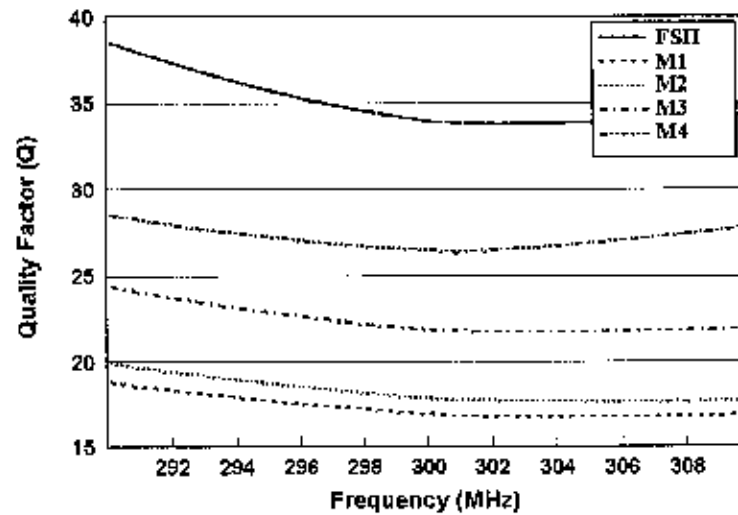


Figure 17. Quality factor (Q) of the folded spherical helix and the meander line folded monopole configurations M1, M2, M3 and M4.

In the M1, M2 and M3 configurations of Figure 15, the resonant resistance is slightly greater than 50Ω . This indicates that these antennas could be made resonant lower in frequency and they would exhibit a resonant resistance closer to 50Ω . Achieving a lower resonant resistance at a lower frequency could be accomplished in a number of ways. Obviously, increasing the total wire length would lower the resonant frequency. Alternately, the wire diameter can be decreased. Decreasing the wire diameter of compressed wire geometries generally lowers their resonant frequency. For example, consider the M2 folded meander line configuration. Decreasing the wire diameter to that of 12 gauge wire ($\approx 1.295 \text{ mm}$) reduces its resonant frequency to 278.6 MHz, where the resonant resistance is approximately 50Ω . It is very significant to note that if the wire diameter of each configuration is reduced, the decrease in resonant frequency will not necessarily be the same for each configuration. The resonant frequency is established by all physical parameters including wire diameter, geometry, wire length and height. A comparison of the relative changes as a function of reduced wire diameter is presented for all of the configurations in Table 3.

Table 3. Performance Properties of the Folded Monopole Antennas Depicted in Figure 15 as a Function of Reduced Wire Diameter.

Antenna and Wire Diameter	Resonant Frequency (MHz)	Resonant Resistance (Ω)
M1 (2.6 mm)	300.9	63.6
M1 (1.29 mm)	278.7	56.2
M2 (2.6 mm)	300.4	56.2
M2 (1.29 mm)	278.6	50
M3 (2.6 mm)	300.2	56.4
M3 (1.29 mm)	292.8	53
M4 (2.6 mm)	301.1	44.3
M4 (1.29 mm)	285.4	42.5

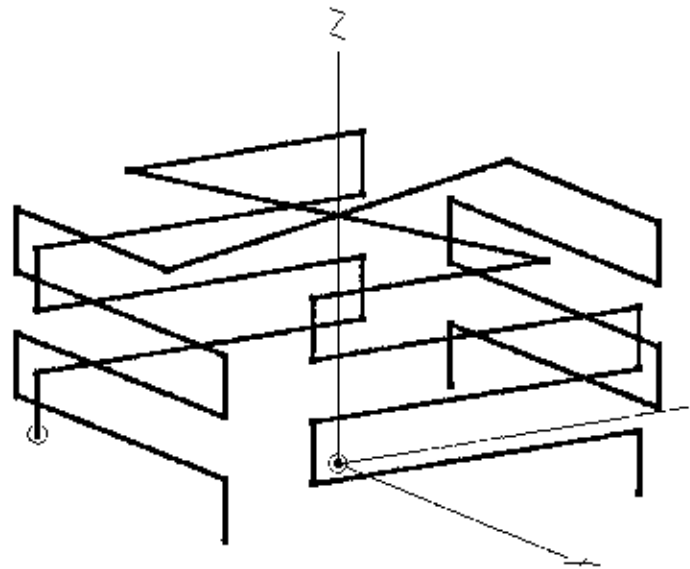
Since the antenna's resonant resistance is a function of its effective height, it is obvious that if the height of the antenna is reduced while maintaining the same resonant frequency, the resonant resistance will decrease. This was done for the M1, M2, M3 and M4 configurations having the 12 gauge wire diameter. Without a change in total wire length, a reduction in height will increase the antenna's resonant frequency. In this instance, it was desired that the antennas be resonant near 300 MHz. The height of the antennas was reduced from 6 cm to 5.5 cm with the goal of lower the resonant resistance. With the change in wire diameter and height from the original configurations, the total wire length had to be adjusted accordingly to achieve a resonant frequency near 300 MHz. A comparison of the resonant properties of these antennas is presented in Table 4.

Table 4. Performance Properties of the Folded Monopole Antennas Depicted in Figure 15 with Reduced Wire Diameter and Height.

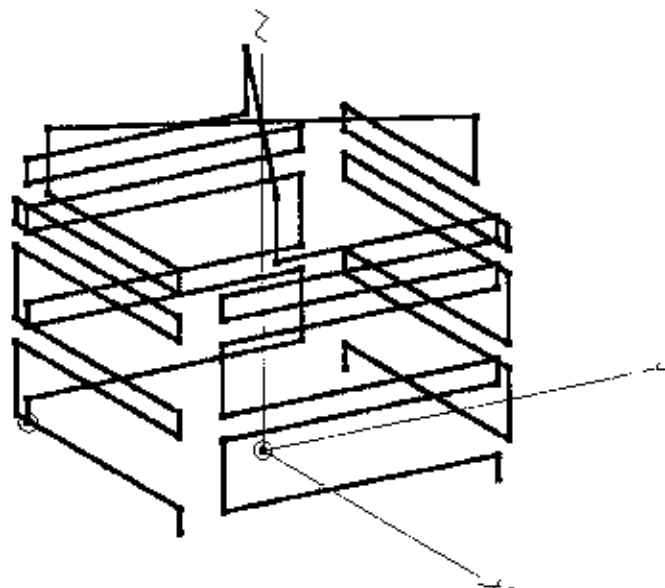
Antenna and Height	Total Wire Length (m)	Resonant Frequency (MHz)	Resonant Resistance (Ω)	Efficiency (%)
M1 (6 cm)	1.86	300.9	63.6	98.6
M1 (5.5 cm)	1.69	299.9	52.3	97.4
M2 (6 cm)	1.83	300.4	56.2	98.5
M2 (5.5 cm)	1.72	299.7	51.1	97.4
M3 (6 cm)	1.29	300.2	56.4	98.9
M3 (5.5 cm)	1.26	299.7	50.4	98
M4 (6 cm)	1.56	301.1	44.3	98.3
M4 (5.5 cm)	1.49	299.9	41.1	97

The final configuration considered is that of a reduced volume antenna. In this instance, only a single meander line configuration is considered. If the overall volume of the antenna is compressed while the height and wire diameter remain fixed, the resonant frequency of the antenna will increase and the resonant resistance will increase

correspondingly. Consider the M2 configuration with the reduced height (5.5 cm) and the reduced wire diameter (1.29 mm). If the overall diameter of the M2 configuration is reduced from 12 cm to 6 cm, as illustrated by the configurations in Figure 18, the resonant frequency increases to 433.1 MHz and the resonant resistance increases to 89.3 Ω .



Meander Line M2



Reduced Volume Configuration

Figure 18. Geometry configurations of the reduced height M2 meander line folded monopole and the reduced volume meander line folded monopole antenna.

Given that the resonant resistance of the antenna is primarily a function of the antenna's height, the total wire length in the antenna can be increased to reduce the resonant frequency to 300 MHz, where the resonant resistance should be close to $50\ \Omega$. Increasing the total wire length from 1.72 m to approximately 3.18 m reduced the resonant frequency to 322.5 MHz and the resonant resistance to $60.5\ \Omega$. At this point, adding more wire to the antenna posed a challenge and it was decided that the overall volume could be increased to lower the resonant frequency. The overall diameter of the antenna was increased to 7.6 cm and the resonant frequency decreased to 300 MHz where the resonant resistance is $49.3\ \Omega$. This configuration is depicted in Figure 19. Note that because the antenna volume is significantly less than the previous configurations, the Q increases to 28.5. As a result of the increased total wire length, the efficiency decreases to 93.1%. Note that this configuration has a lesser Q than the folded spherical helix, which occupies more volume, because of its lower efficiency. A comparison of the impedance properties of this configuration with those of the reduced height M2 configuration (of Table 4.) is presented in Figure 20.

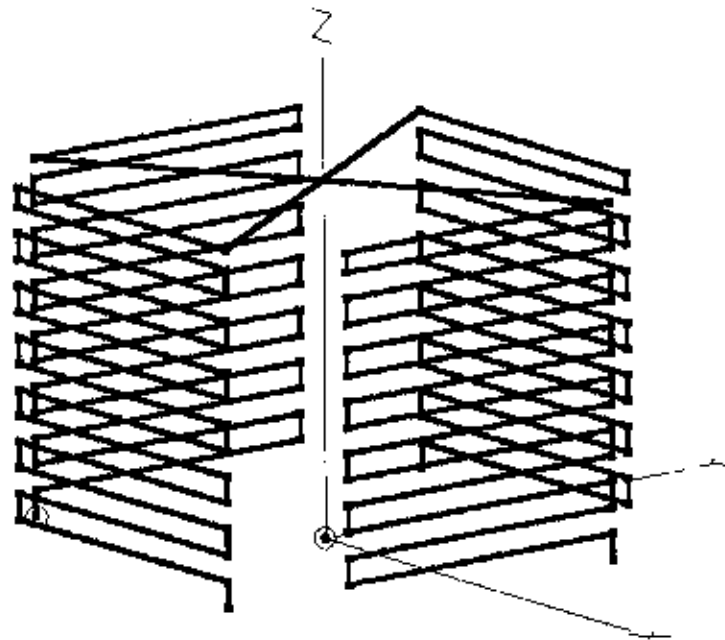


Figure 19. Geometry configuration of the final reduced volume configuration made to be resonant at 300 MHz.

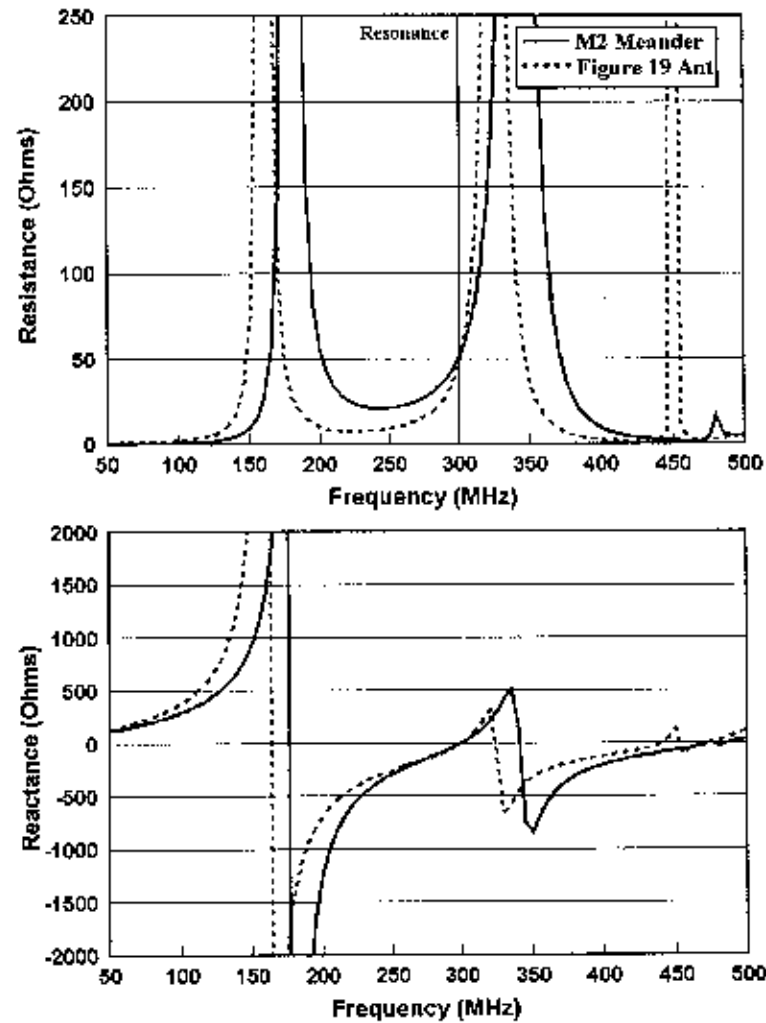


Figure 20. Input impedance properties of the reduced height M2 meander line antenna and the reduced volume antenna depicted in Figure 19.

5. REMARKS

The radiation properties of several multi-arm folded monopole antennas have been considered. The general performance properties of these antennas were shown to be a function of the antenna's height, occupied volume, total wire length, geometry and wire diameter. When multi-arm folded monopoles of the same height and occupied volume are made to be resonant at the same frequency they exhibit similar resonant performance, indicating that the resonant performance properties of these antennas are significantly a function of these physical parameters. In some instances, where the geometries are notably different, the resonant properties will vary. The performance trade-offs associated with changing height, occupied volume and wire diameter were described in some detail.

6. REFERENCES

- [1] Best, S. R., "The Performance Properties of an Electrically Small Folded Spherical Helix Antenna," *IEEE Antennas and Propagation International Symposium*, Vol. 4, pp. 18-21, June 2002
- [2] Best, S. R., "The Radiation Properties of Electrically Small Folded Spherical Helix Antennas," Accepted for Publication, *IEEE Transactions on Antennas and Propagation* Est. May 2004
- [3] Best, S. R., "On the Performance Properties of the Koch Fractal and Other Bent Wire Monopoles," *IEEE Transactions on Antennas and Propagation*, pp. 1292-1300, June 2003
- [4] Lewallen, R. EZNEC/4 Antenna Modeling Software,, <http://www.eznec.com>.
- [5] A. D. Yaghjian and S. R. Best, "Impedance, Bandwidth and Q of Antennas," *2003 APS Conference*, Vol 1, pp. 501-504, Columbus, OH, July 2003
- [6] Handelsman, D., "The Rectangle Family of Antennas, Part 2: The Asymmetrical Double Rectangle (ADR)," *ARRL QEX*, pp. 12-22, Jan/Feb 2002.
- [7] K. Fujimoto *et al*, "Small Antennas," Research Studies Press, England; John Wiley and Sons, New York, 1987.